Photoactive and UV Attenuating Nanomaterial and Heterojunction Devices

Neel M. A. Makwana

A thesis submitted to
University College London
in partial fulfilment of the requirements for the degree of
Doctor of Philosophy

Supervised by Professor Jawwad A. Darr

January 2016

Christopher Ingold Laboratories,
Department of Chemistry,
20 Gordon Street,
London WC1H 0AJ
United Kingdom

Declaration

I, Neel M. A. Makwana, confirm that the work presented in this thesis is my own. Where information has been derived from other sources, I confirm that this has been indicated in the thesis.

Neel M. A. Makwana

Abstract

This thesis focuses on the synthesis, characterisation and testing of semiconductor nanomaterials and heterojunctions, for photocatalytic and UV attenuation applications. Titanium dioxide (TiO_2) and zinc oxide (ZnO) nanomaterials were synthesised via a continuous hydrothermal flow synthesis (CHFS) process, where solutions of chemical precursors were mixed with hot, pressurised water. Samples were collected as slurries and processed to obtain dry powders.

Synthesis of TiO_2 investigated the addition of boric acid as a dopant species to determine (i) its potential to dope TiO_2 in the continuous hydrothermal process, and (ii) any effects on reaction conditions and subsequently nanoparticle properties. The powders were prepared as ceramic wafers, and tested for their ability to photocatalytically evolve hydrogen from water, in a sacrificial system.

ZnO synthesis was investigated from a scale-up perspective, comparing a mini-pilot scale CHFS reactor to a larger pilot-scale reactor already reported in literature. The observed variation in particle sizes were explained in terms of the nucleation and growth mechanisms of zinc oxide. Additionally, an investigation was carried out to explore the effects of additives in the CHFS reactor to (i) reduce ZnO particle sizes and (ii) obtain dispersions of ZnO nanoparticles. Selected materials from these experiments were investigated as UV attenuators in polymer coatings.

Heterojunction ceramic wafers of TiO_2 and WO_3 were prepared by a simple technique, reported here for the first time. The wafers displayed interesting charge transfer characteristics, and they were investigated for photocatalytic applications in the destruction of organic pollutants and disinfection of water. In these applications, the heterojunction wafers were found to have photocatalytic rates that were greater, or more beneficial than, their corresponding individual semiconductor materials.

Acknowledgements

During the last four years, whilst completing the research that is described within this thesis, a number of people have kindly provided their help, guidance and support, without which it would have been a very difficult task. I would like to take this moment to express my gratitude to the people who have supported me throughout this project.

Firstly, I would like to give special thanks to my supervisor, Professor Jawwad Darr, for his guidance, support and helpful criticism throughout the course of this work. I have very much appreciated Jawwad's encouragement to keep trying and never loose hope, even when things may have not been going so well. I would also like to thank my secondary supervisor, Professor Paul McMillan, for useful discussions on various aspects of the work. I am grateful to UCL and the EPSRC for funding this project.

I am especially grateful to many post-doctoral staff who have helped and taught me how to do science during the course of this project: Dr Robert Gruar, Dr Christopher Tighe, Dr Raul Quesada–Cabrera, Dr Rachael Hazael and Dr Ana Jorge Sobrido.

Thank you to Professor Andrew Mills (Queen's University Belfast), Professor Ivan Parkin (UCL), Professor Tony Byrne (University of Ulster) and Dr Patrick Dunlop (University of Ulster) for their discussions relating to some of the work in this thesis. Thank you also to Dr Nigel Holmes (MacDermid Autotype) for kindly evaluating some of the materials that were produced during this project.

I would like to acknowledge members of the Clean Materials Technology Group, past and present: On Ying (Eva), Josie, Sam, Sofia, Clément, Pete, Kalyani, Liam, Paul, Ian, Meggi, Dougal, Charlotte, Marco and Alistair – thank you for making my stay in the CMTG enjoyable.

I thank the support staff at the Department of Chemistry at UCL, in particular, Dr Steve Firth and Mr Martin Vickers. Without their help and training on operating various equipment, it would have been rather difficult to obtain many of the results that are

discussed in this thesis. I am also grateful to Mr Tom Bridges for his help with all things electrical when issues arose on the mini-pilot scale reactor.

Last but not least, I would like to thank my family: Manju and Ajay Makwana, my mother and father, and Priya, my sister. Your support, especially over the last four years, has been invaluable, and I shall always be grateful for all that you have done for me.

And saving the best till last – to Bhavisha – your love, patience and support has been more than I could ask for. Thank you for making life outside the lab that little bit more exciting.

Publications

Publications related to the work presented in this thesis:

1. Makwana, N. M., Tighe, C. J., Gruar, R. I., McMillan, P. F. and Darr, J. A. (2016). Pilot scale continuous hydrothermal synthesis of nano-titania; effect of size on photocatalytic activity. *Materials Science in Semiconductor Processing,* 42, 131-137.

2. Makwana, N. M., Hazael, R., McMillan, P. F. and Darr, J. A. (2015). Photocatalytic water disinfection by simple and low-cost monolithic and heterojunction ceramic wafers. *Photochemical & Photobiological Sciences*, 14, (6) 1190-1196.

3. Makwana, N. M., Quesada-Cabrera, R., Parkin, I. P., McMillan, P. F., Mills, A. and Darr, J. A. (2014). A simple and low-cost method for the preparation of self-supported TiO_2-WO_3 ceramic heterojunction wafers. *Journal of Materials Chemistry A*, 2, (40) 17602-17608.

Other publications:

4. Johnson, I. D., Lübke, M., Wu, O. Y., Makwana, N. M., Smales, G. J., Islam, H. U., Dedigama, R. Y., Gruar, R. I., Tighe, C. J., Scanlon, D. O., Corà, F., Brett, D. J. L., Shearing, P. R. and Darr, J. A. (2016). Pilot-scale continuous synthesis of a vanadium-doped LiFePO4/C nanocomposite high-rate cathodes for lithium-ion batteries. *Journal of Power Sources*, 302, 410-418.

5. Denis, C. J., Tighe, C. J., Gruar, R. I., Makwana, N. M. and Darr, J. A. (2015). Nucleation and Growth of Cobalt Oxide Nanoparticles in a Continuous Hydrothermal Reactor under Laminar and Turbulent Flow. *Crystal Growth & Design*, 15, (9) 4256-4265.

6. Lübke, M., Johnson, I., Makwana, N. M., Brett, D., Shearing, P., Liu, Z. and Darr, J. A. (2015). High power TiO_2 and high capacity Sn-doped TiO_2 nanomaterial anodes for lithium-ion batteries. *Journal of Power Sources*, 294, 94-102.

7. Lübke, M., Makwana, N. M., Gruar, R., Tighe, C., Brett, D., Shearing, P., Liu, Z. and Darr, J. A. (2015). High capacity nanocomposite Fe_3O_4/Fe anodes for Li-ion batteries. *Journal of Power Sources*, 291, 102-107.

8. Goodall, J. B., Illsley, D., Lines, R., Makwana, N. M. and Darr, J. A. (2015). Structure-property-composition relationships in doped zinc oxides: enhanced photocatalytic activity with rare Earth dopants. *ACS Combinatorial Science*, 17, (2) 100-112.

9. Jorge, A. B., Martin, D. J., Dhanoa, M. T. S., Rahman, A. S., Makwana, N., Tang, J., Sella, A., Corà, F., Firth, S., Darr, J. A. and McMillan, P. F. (2013). H_2 and O_2 Evolution from Water Half-Splitting Reactions by Graphitic Carbon Nitride Materials. *The Journal of Physical Chemistry C*, 117, (14) 7178-7185.

Table of Contents

List of Figures

List of Tables

List of Abbreviations

Abbreviation	Meaning
BPR	Back pressure regulator
BET	Brunauer Emmett Teller
CA	Citric acid
CB	Conduction band
CCM	Central collision mixer
CFU	Colony forming unit
CHFS	Continuous hydrothermal flow synthesis
CJM	Confined jet mixer
CMTG	Clean Materials Technology Group
Cs	Crystallite size
DI	Deionised
DLS	Dynamic light scattering
E. coli	*Escherichia coli*
EDX	Energy dispersive X-ray spectroscopy
EPSRC	Engineering and Physical Sciences Research Council
ESD	Equivalent sphere diameter
FQE	Formal quantum efficiency
GC	Gas chromatography
GInaFIT	Geeraerd and Van Impe Inactivation Model Fitting Tool
HiTCH	High-throughput continuous hydrothermal
HR-TEM	High-resolution transmission electron microscopy
IR	Infrared
PdI	Polydispersity index
pH	Power of hydrogen

Abbreviation	Meaning
QMUL	Queen Mary, University of London
RAMSI	Rapid automated materials synthesis instrument
RMSE	Root Mean Sum of Squared Errors
ROS	Reactive oxygen species
SA	Stearic acid
SEM	Scanning electron microscopy
SODIS	Solar disinfection
SPH	Self-supported photocatalytic heterojunction
TEM	Transmission electron microscopy
UV	Ultraviolet
UV-Vis	Ultraviolet-visible (spectroscopy)
UCL	University College London
VB	Valence band
XPS	X-ray photoelectron spectroscopy
XRD	X-ray diffraction

Chapter 1. Literature review

1.1. INTRODUCTION

The work presented in this thesis describes the results of investigations in to the use of nanomaterials, for photocatalytic and UV attenuating applications. Nanomaterials were synthesised by a continuous hydrothermal method, and were subsequently evaluated for their performance in a number of different tests. The tests encompassed the ability of nanomaterials to photocatalytically evolve hydrogen from water, to degrade organic substances and disinfect water as heterojunction devices, and to provide UV protection to substrates in the form of coatings. Accordingly, this chapter begins with a background introduction to nanomaterials and their formation under aqueous conditions, and an introduction to continuous hydrothermal flow synthesis, the primary synthesis technique used throughout this thesis. A background introduction of photocatalysis and UV attenuation follows, with an emphasis on applications of nanomaterials.

1.2. NANOMATERIALS

Nanomaterials are described as materials that have at least one dimension that is less than 100 nm. At this nanoscale, the chemical and physical properties of materials differ greatly from their bulk counterparts (i.e. at the micron or millimetre scale). Whilst the notion that the properties of a material are dependent on its size at such small scales, has been known for some time, it is only over the last two or three decades that these materials have been intensely studied (Roduner 2006). Advancements in experimental synthesis and analytical techniques have allowed scientists to synthesise such materials in a controlled way, and this has allowed a better understanding of how physical properties (e.g. size and shape) relate to function (Gasparotto et al. 2012).

Applications of nanomaterials span a wide technological space; they are found in biological fields such as cancer therapy, drug delivery and imaging; in electronic applications such as high-power magnetism, quantum computing and single electron

transistors; and in chemical applications such as lithium ion batteries, industrial catalysis and inorganic ceramic materials (Tsuzuki 2009). The focus of the work presented in this thesis, lies in the applications of inorganic nanomaterials for photocatalytic reactions and UV attenuation applications.

The following section describes nanomaterials synthesis methods, focussing on the mechanisms that occur during their formation. Subsequently, an account of the use of water as a reaction medium in nanomaterials synthesis is given, as this has been a significant focus of the work presented in this thesis.

1.2.1. Nanomaterial synthesis approaches

Nanomaterial synthesis encompasses two approaches: top-down and bottom-up (shown in Figure 1.1). Top-down methods form nanomaterials by reducing the size of bulk materials, whilst bottom-up methods form nanomaterials from smaller units, e.g. molecular level precursors. The following sections give an overview of these two approaches.

Figure 1.1 Schematic diagram showing bottom-up and top-down approaches for nanomaterial synthesis. Reprinted (adapted) from (Hong et al. 2012a).

1.2.1.1. Top-down approach

The aim of top-down nanomaterial synthesis methods is to structurally decompose bulk materials to obtain nanostructures (Koch 2003). Examples of top-down methods include mechanical grinding and milling (Prasad Yadav et al. 2012), etching (Barth et al. 2010) and lithography (Sebastian et al. 2014). Top-down methods have been used over

the last few decades in many industrial applications, e.g. for fine-scale patterning of electronic circuits in the microelectronics industry (Yu et al. 2013). Whilst top-down methods are widely used, their limitations have, in recent years, led to a larger focus on bottom-up methods. By far the biggest problem with top-down methods is the limited control over nanoscale (e.g. nanoparticle or thin film) properties. For example, lithography of a surface can lead to imperfections, and etching may introduce surface defects (Cao and Wang 2011). Since nanomaterials have large surface-to-volume ratios, the presence of such imperfections or defects can be detrimental to its properties. Top-down methods may also be extremely energy intensive, because energy is required to create new surfaces (Hornyak et al. 2009). An extensive review of top-down nanomaterials synthesis is beyond the scope of this thesis, however, there exists a number of reviews in the literature, that together provide a detailed coverage (Koch 2003; Prasad Yadav et al. 2012; Yu et al. 2013). As a consequence of the limitations of top-down methods, they are not often favoured for the synthesis of nanomaterials, especially where a high degree of control is required over the physical properties at the nanoscale.

1.2.1.2. Bottom-up approach

Bottom-up methods begin with atoms or molecules (i.e. precursors) that are reacted to form nanoparticles or thin films. The precursor may be delivered in the vapour, liquid or solid phase. Methods of synthesis include chemical vapour deposition, flame/spray pyrolysis and laser ablation in the vapour phase; sol-gel, hydro/solvo-thermal, and electrodeposition in the liquid phase; and mechanochemical or thermo-mechanical processing in the solid phase (Cushing et al. 2004; Hornyak et al. 2009). Bottom-up methods are becoming increasingly common, and are used industrially in processes such as for growth of single crystals or deposition of thin films (Cao and Wang 2011).

Since the properties of nanomaterials are so closely related to their physical characteristics such as size and morphology, which can be influenced by bottom-up synthesis methods, it is important to develop an understanding of how such materials are formed. The following section reviews the mechanisms and theories related to nanoparticle formation from a bottom-up approach.

1.2.2. Nanomaterial formation mechanisms

Nanomaterial formation from solution comprises four key stages: (i) precursor formation, (ii) nucleation, (iii) growth and (iv) aging (Jolivet et al. 2000). In 1950, LaMer and Dinegar studied the formation of sulphur sols, and subsequently proposed a model to explain the nucleation and growth that occurred (LaMer and Dinegar 1950). It was later known as the LaMer model (Figure 1.2), and has formed the basis of many others that have since been proposed. One such model is shown in Figure 1.3, which illustrates a plot of precursor concentration against time (Oskam 2006).

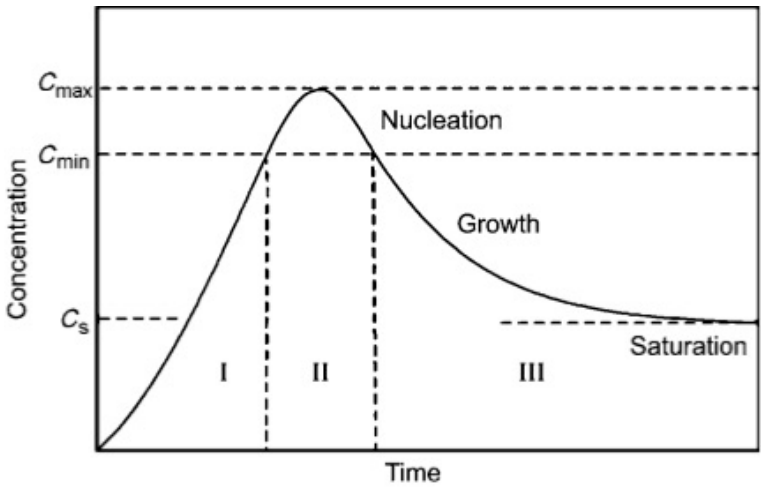

Figure 1.2 LaMer model used to describe nucleation and growth. Reprinted from (Goesmann and Feldmann 2010) with permission from John Wiley and Sons.

The first stage consists of formation of zero-charge precursor molecules that have a specific water/hydroxyl content to allow condensation to occur. When precursor molecules begin to form, and as their concentration increases, a supersaturation condition is reached (Oskam 2006). This is when, in an aqueous system, a solvent contains more dissolved solute than would exist at equilibrium (Calvert 1990). Supersaturation is an unstable state and is the driving force for crystallisation and growth. When a nucleation threshold is reached, nucleation begins, and as precursor molecules are 'used-up', the precursor concentration may fall below the nucleation threshold. At this point, growth from solution may occur, followed by aging processes. Whilst these processes generally apply to nanomaterial formation, individual synthesis

techniques and reaction conditions (e.g. temperature, pressure, etc.) may afford different control over some or all of these steps.

The following section provides a more detailed account of the steps involved in the nanomaterial formation mechanism. Figure 1.4 shows how the number and size of nanoparticles can change over the course of the formation process. References are made in the text to the regions marked in Figure 1.3 and Figure 1.4.

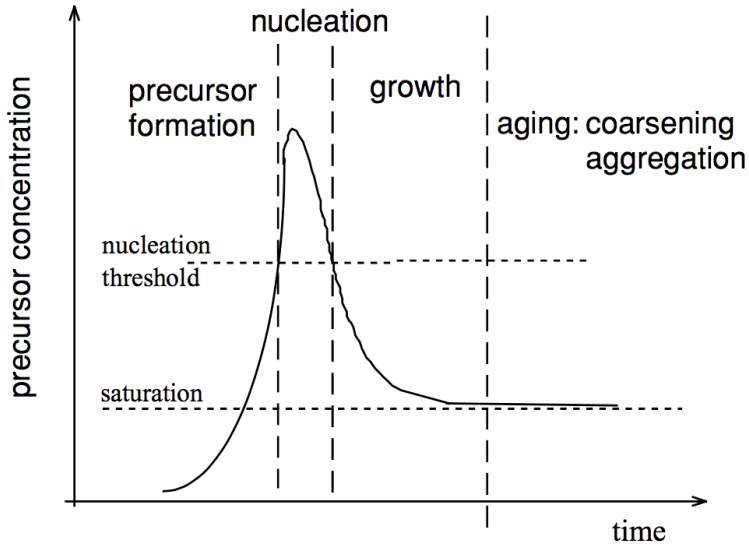

Figure 1.3 Precursor concentration against time for the processes comprising nanoparticle formation from solution. Reprinted from (Oskam 2006) with permission from Springer.

Figure removed for copyright purposes

Figure 1.4 Change in the number and size of nanoparticles as a function of time during the nucleation (regions I and II), growth (region III) and aging (IV) of nanoparticles. Reprinted from (Jolivet et al. 2000).

1.2.2.1. Precursor formation

The initial stage of nanoparticle formation consists of formation of zero-charge precursor molecules, $[M(OH)_z(OH_2)_{N-z}]^0$. This occurs by hydroxylation and hydrolysis reactions of the metal cation, which is a very fast acid-base type reaction, but the speed of formation is dependent on the route taken e.g. through the addition of a base or via thermal decomposition. Initially, the concentration of zero-charge precursor molecules is low enough such that the nucleation rate is effectively zero; this period is shown as region I in Figure 1.4.

1.2.2.2. Nucleation

The formation of zero-charge precursors leads to supersaturation, and once a nucleation threshold is reached, nucleation begins to occur. The nucleation process involves condensation of the zero-charge precursor molecules, which occurs via olation (condensation of M-OH_2 and HO-M groups) and oxolation (condensation of 2 M-OH groups), leading to the formation of solid material (region II). The rate of nucleation is a function of the precursor concentration (amongst other factors), and will continue to occur for as long as the precursor concentration is above the nucleation threshold.

The formation of solid material involves the creation of a liquid-solid surface. The Gibbs free energy required for the formation of the nuclei surface is given by:

$$\Delta G = n(\mu_S - \mu_L) + A\gamma \qquad \text{(Equation 1.1)}$$

where n is the number of molecules in the nucleus, μ_S and μ_L are the chemical potentials of the solid and liquid phases, respectively, A is the surface area and γ is the surface energy of the solid-liquid interface. The difference in chemical potentials, (μ_S - μ_L), can be written as:

$$(\mu_S - \mu_L) = -RTln\frac{C_L}{C_S} = -RTlnS \qquad \text{(Equation 1.2)}$$

where C_L is the precursor concentration in the solution, C_S is the solubility of the solid phase and S is the supersaturation, defined as the ratio between precursor concentration

and the solubility of the solid (i.e. between C_L and C_S). Assuming the nucleus is spherical, its radius is given by:

$$r = \left(\frac{3nV_m}{4\pi}\right)^{\frac{1}{3}} \quad \text{(Equation 1.3)}$$

where r is the radius of a nucleus and n is the number of precursor molecules of molecular volume V_m from which the nucleus is formed. The surface area of the nucleus is therefore:

$$A = n^{\frac{2}{3}}(36\pi V_m^2)^{\frac{1}{3}} \quad \text{(Equation 1.4)}$$

Combining equations (1.1), (1.2) and (1.4) gives:

$$\Delta G = -nRTlnS + (36\pi n^2 V_m^2 \gamma^3)^{\frac{1}{3}} \quad \text{(Equation 1.5)}$$

As nucleation occurs in a supersaturated solution, there exists a critical radius, r^*, given by:

$$r^* = \left(\frac{3\pi V_m}{4\pi}\right)^{\frac{1}{3}} = \frac{2\gamma V_m}{RTlnS} \quad \text{(Equation 1.6)}$$

Equation 1.6 shows that the radius of the critical nucleus, r^*, is smaller when supersaturation is high and the surface tension is small. Nucleated particles that have $r < r^*$ will dissolve, whilst particles with $r > r^*$ will continue to grow. The corresponding critical Gibbs free energy required to form a critical nucleus is obtained when $\delta(\Delta G)/\delta n = 0$.

ΔG^* is given by:

$$\Delta G^* = \frac{16\pi V_m^2 \gamma^3}{3(RT \ln S)^3} \quad \text{(Equation 1.7)}$$

The rate of nucleation, J_N, is a function of the critical energy and a pre-factor, J_0, which depends on the type of reaction that occurs and the frequency of collisions:

$$J_N = J_0 exp\left(\frac{-\Delta G^*}{RT}\right) \quad \text{(Equation 1.8)}$$

Equation 1.8 shows that the nucleation rate increases as the critical Gibbs free energy decreases, and therefore, as the surface energy decreases and the supersaturation increases. The presence of solid material (i.e. nanoparticle crystals) in the precipitation medium enhances the nucleation rate strongly, because supersaturation increases as the solubility of the metal oxide product decreases. Hence, as the reaction proceeds, if the concentration of the precipitating product increases, the solubility decreases and so the supersaturation increases. This causes an overall decrease in the critical Gibbs free energy required to form the critical nucleus.

1.2.2.3. Growth

When the precursor concentration goes below the nucleation threshold, the growth stage begins. Nanoparticle growth can occur by incorporation of precursor molecules that continue to form after nucleation, and the concentration of precursor molecules and number of nuclei determine the average particle size after growth. As such, the number of particles remains constant, whilst their size increases (region III). There are two mechanisms for the growth of particles: (i) diffusion limited and (ii) kinetically limited. The mechanisms are related to the speed of incorporation of atoms to existing nuclei; if it is fast, growth is diffusion limited, and if it is slow then growth is kinetically limited. The growth rate during nanoparticle formation is dependent on the mechanism by which it occurs. For diffusion limited growth, the growth rate, as a change in particle size with time, is given by:

$$\frac{dr}{r} = \frac{D(C - C_s)V_m}{r} \quad \text{(Equation 1.9)}$$

where D is the diffusion coefficient of the solute that has molar volume V_m and concentration C, and C_S is the solubility of the solid. Equation 1.9 shows that the growth

rate for diffusion limited growth is faster for smaller particles, and the corresponding size distribution may be small since small particles grow faster than large particles, creating a narrowing in the size distribution. For kinetically limited growth, the growth rate is proportional to the surface area of the particles, and therefore, larger particles would have faster growth rates. This mechanism would lead to a widening in the particle size distribution.

1.2.2.4. Aging

After nucleation and growth, aging processes may occur, which can change the size of nanoparticles whilst the amount of solid material remains the same. The two main mechanisms that occur during aging are Ostwald ripening (also referred to as coarsening) and aggregation. Ostwald ripening is the method by which smaller particles dissolve and deposit onto larger particles; here, the number of particles decreases whilst their size increases (region IV). This thermodynamically favoured process occurs because the formation of larger particles reduces the overall surface area, and since a smaller surface area has a lower surface energy, larger particles are more energetically favoured. Smaller particles have a higher probability of dissolving since they have a greater solubility than larger particles due to capillary effects, as predicted by the Gibbs-Thomson equation:

$$c_r = c_{r=\infty} exp\left(\frac{2\gamma V_m}{RTr}\right) \qquad \text{(Equation 1.10)}$$

where c_r is the solubility of a particle with radius r and $c_{r=\infty}$ is the solubility of a particle with an infinite radius. The Lifshitz-Slyozov-Wagner (LSW) theory provides a mathematical understanding of Ostwald ripening and states that for a diffusion-controlled process, the average radius of precipitated particles as a function of time (t) can be determined from:

$$\bar{r}(t) = \sqrt[3]{kt} \qquad \text{(Equation 1.11)}$$

where $\bar{r}$ is the average radius of particles and k is the Ostwald ripening rate constant, expressed as follows:

$$k = \frac{8\gamma V_m^2 c_{r=\infty}}{54\pi N_A a\eta} \qquad \text{(Equation 1.12)}$$

where N_A is Avogadro's constant, a is the hydrodynamic radius of the metal ion and η is the viscosity of solution. From equation 1.12, it can be determined that the Ostwald ripening rate is dependent on the solution viscosity, and the solubility and surface energy of the nanoparticle.

The average particle size can also increase through nanoparticle aggregation. In this process, particles attract each other and fuse to create larger particles. It can occur either at random or with preference for growth in certain crystal orientations, and is strongly dependent on the surface charge of nanoparticles (Jolivet et al. 2000). Aggregation is favoured by conditions that minimise surface electrical charge, since this allows particles to attract each other more easily than when a surface charge is present. Therefore, aggregation can be controlled to an extent by modifying experimental conditions, e.g. by the addition of surfactants.

1.2.3. Water as a reaction medium

Many chemical syntheses (such as bottom-up) rely on the use of solvents as the reaction medium. In inorganic materials syntheses, such solvents may include organic solvents such as methanol, ethanol, toluene and cyclohexane (Niederberger and Pinna 2009), or solvents such as liquid ammonia, sulphuric acid, phosphorus oxychloride and hydrogen fluoride (Holliday and Massey 1965). In many of these syntheses, the *use* of a solvent is integral to the process, but a number of options may be available as to the *choice* of solvent (Dallinger and Kappe 2007).

The use of solvents can often have many implications, such as on the environment or on the process cost. Since the development of the '12 Principles of Green Chemistry' by Paul Anastas and John Warner nearly two decades ago (Anastas and Warner 1998), there has been a large focus on developing environmentally benign chemical processes (Wei et al. 2004) and limiting the use of solvents. One of the green chemistry principles

states: 'the use of auxiliary substances (e.g. solvents, separation agents, etc.) should be made unnecessary wherever possible and innocuous when used', which has led to inherent development of 'cleaner' solvents. However, there is still a requirement to move towards limiting even the use of these solvents, for they may still have some implications for sustainability and safety.

An alternative to the use of solvents is to conduct chemical syntheses in water. Although there is no one solvent that may be applicable in every chemical process, water is regarded as the 'universal solvent' because it is able to dissolve more substances than any other liquid. The sufficient difference in the electronegativity of hydrogen and oxygen, give water a polar character, where the oxygen atom has a partial negative charge and the hydrogen atoms have a partial positive charge. Water also has a very high dielectric constant (relative permittivity) under ambient conditions ($\varepsilon_r \approx 80$). As a consequence of the polar character and the dielectric constant, water forms hydrogen bonds with adjacent molecules, is able to dissolve ionic compounds by ion solvation (forming hydration spheres), and forms complexes and hydrates. The high dielectric constant reduces the forces between ions in ionic compounds, permitting them to separate (Kerton 2009b). Other properties of water that make it a desirable solvent include its non-toxicity, low cost and it being environmentally friendly and recyclable. However, the properties of water described above are valid only at ambient conditions, because heating water causes its properties to change. For example, in geysers (hot springs), where water is naturally found at temperatures around 100 °C, minerals are able to precipitate. It is also believed that the formation of natural rock crystals is the result of processes that have occurred in hot water (Brunner 2014a). The following section describes the properties and function of water at elevated temperature and pressure.

1.2.3.1. Water at elevated temperature and pressure

The pressure-temperature behaviour of water is best shown in the form of a phase diagram (Figure 1.5). The key properties of water relating to the diagram are summarised as follows (Harvey and Friend 2004):

- A triple point (point A) at which all three phases (solid, liquid and gas) coexist in equilibrium, identified by a pressure (P_{tp}) and temperature (T_{tp}). For water, the triple point occurs at $P_{tp} = 6.12 \times 10^{-4}$ MPa and $T_{tp} = 0.01$ °C.
- A critical point (point B) at which the substance behaves as a supercritical fluid, identified by a pressure (P_c) and temperature (T_c). The critical point of water occurs at $P_c = 22.06$ MPa and $T_c = 373.95$ °C.

The lines that connect point A to B and A to C show the vapour pressure curves of the liquid phase and the solid phase, respectively. The line that connects point A to D shows how the melting point of the solid changes as a function of pressure.

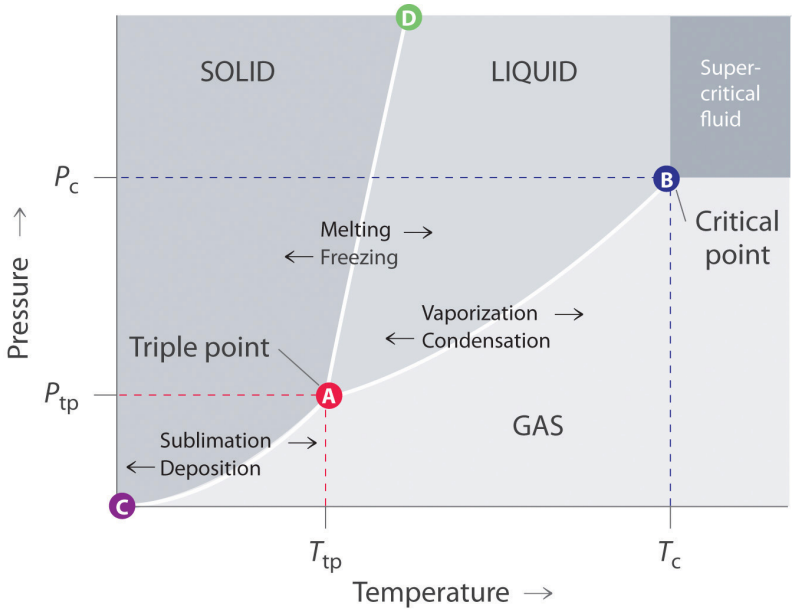

Figure 1.5 A typical phase diagram for substances that exhibit three phases (solid, liquid and gas) and a supercritical region, identifying the triple point (A) and critical point (B). Reprinted from (Larsen 2015) with permission under a creative commons licence (CC BY-NC-SA 3.0 US).

When water is heated or pressurised above ambient conditions, up to and beyond its critical point, its properties change remarkably. The density of water decreases from 998 kg m^{-3} at ambient to 322 kg m^{-3} at the critical point (Figure 1.6), and the dielectric constant decreases from approximately 80 to 5 (Figure 1.7) (Weingartner and Franck 2005). Beyond the critical point, the density of a supercritical fluid is very sensitive to changes in pressure. A solvent that is below its critical point would require a very large change in pressure to vary its density, but beyond the critical point, only a small change

is required to significantly change the density. Since solubility is related to the density of a solvent, this property enables a high degree of control over the solubility of a species (Kerton 2009a). The density of the fluid can change from liquid-like to gas-like values without any phase transition taking place (Kruse and Dinjus 2007). The sharp decrease in the dielectric constant near to and beyond the critical point (ε_r is now nearly equal to that of polar organic solvents) is thought to give water the ability to dissolve non-polar compounds (Patel et al. 2014). The solubility of organic and inorganic ionic compounds increases and decreases, respectively, as the dielectric constant of water decreases (Galkin and Lunin 2005). Control over temperature and pressure allows one to carefully tune the solubility, and hence it is an important feature when conducting syntheses in water.

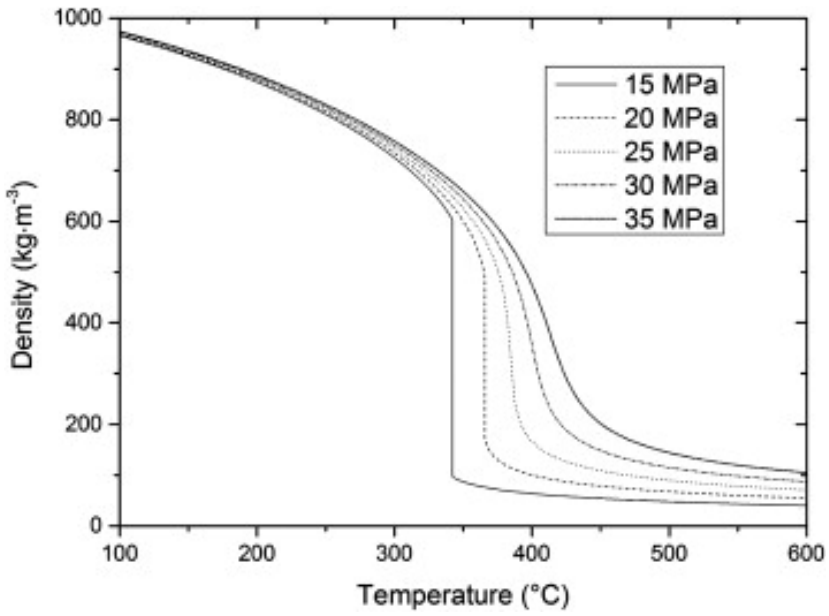

Figure 1.6 Variation in density of water as a function of temperature and pressure. Reprinted from (Yakaboylu et al. 2013) with permission from Elsevier.

Figure 1.7 Variation in dielectric constant of water as a function of temperature and pressure. Reprinted from (Fukushima 2000).

Another property of water that changes remarkably is its ionic product, which is an equilibrium constant relating to the concentration of the dissociation products of water (i.e. H^+ and OH^-), given by:

$$K_w = [H^+][OH^-] \qquad \text{(Equation 1.13)}$$

The ionic product of water (K_w) decreases from 10^{-14} mol^2 dm^{-6} at ambient conditions to 10^{-22} mol^2 dm^{-6} at the critical point (corresponding to logK_w values of –14 and –22, respectively). As shown in Figure 1.8, K_w initially increases as water is heated above ambient, and then decreases upon approaching the critical point (Galkin and Lunin 2005). The ionic product of water reaches a maximum of 10^{-11} mol^2 dm^{-6} (K_w = –11) at ca. 300 °C, which corresponds to an increase of three orders of magnitude, compared to at ambient conditions. The implication is that subcritical water has a much higher concentration of H^+ and OH^- ions (compared to at ambient). Subcritical water not only behaves as a polar solvent, but also as a self-neutralising acid-base catalyst and is able to support ionic, polar non-ionic and free radical reactions (Akiya and Savage 2002; Galkin and Lunin 2005). Figure 1.8 shows that, by increasing the pressure above P_c at or beyond

the critical point, the ionic product of water increases. Therefore, by controlling temperature and pressure, it is possible to finely control the reaction conditions.

Figure 1.8 Variation in ionic product of water as a function of temperature and pressure. Reprinted from (Fukushima 2000).

When the critical point is reached, the liquid and vapour phases of water become identical, which can be observed visually as water is heated and pressurised (Figure 1.9). Initially, a meniscus (phase boundary) exists that separates the liquid and vapour phase. However, once the critical point is reached, the meniscus disappears (Weingartner and Franck 2005). The implication of the changes in the properties of water is that it transitions from a solvent for ionic species (at ambient), to a solvent for non-ionic species (beyond the critical point) (Brunner 2014a).

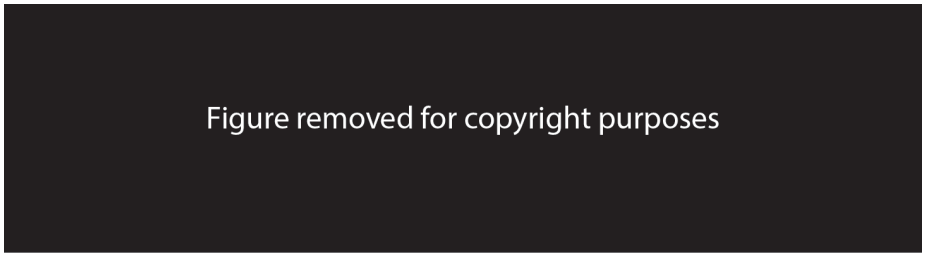

Figure 1.9 Photographs showing the disappearance of the meniscus (phase boundary) as a supercritical fluid is heated. Initially, there exists a liquid and vapour phase (a). Upon heating,

the liquid begins to expand (b), where the two phases become less distinct (c), before a single phase is formed (d). Adapted from (Kelly and Howdle 2008).

Beyond changes in the physicochemical properties of water, the structure of water also changes near to, or above the critical point. The extent of hydrogen bonding is reduced and becomes weaker, and small hydrogen-bonded clusters form with a chain structure (Kalinichev and Churakov 1999), rather than the large network found at ambient conditions (Akiya and Savage 2002). This occurs because the formation of hydrogen bonds is an exothermic process; therefore, the equilibrium constant decreases as a function of temperature (Brunner 2014b). It is believed that the breakdown of hydrogen bonding is in part responsible for the decrease in the dielectric constant, near to or above, the critical point. Since the nature of hydrogen bonding changes, there is an effect on the formation of hydration shells, because water cannot efficiently screen ions near to or beyond the critical point. For example, studies have shown that in nickel bromide under supercritical conditions, the Ni^{2+} ion (which at ambient conditions is surrounded by six water molecules) has only 2.5 water molecules associated with it, with bromide ions replacing the lost water molecules (Wallen et al. 1998). This results in strengthened cation-anion interactions and the number of ion pairs increases (Galkin and Lunin 2005).

It is clear from the above discussion that there are many appreciable changes in the properties of water under extreme conditions. These changes may be beneficial for synthesis of nanomaterials; indeed, the use of subcritical and supercritical water as a solvent and a reagent is exploited in hydrothermal syntheses. The following section describes this technique.

1.3. HYDROTHERMAL SYNTHESIS

The term ‘hydrothermal synthesis’ has been defined in many ways, all with slight variation. However, it is generally agreed that it defines a process in which a heterogeneous reaction occurs at a temperature and pressure above ambient, in aqueous media and in a closed system (Byrappa and Yoshimura 2013). Ambiguity exists regarding the term ‘hydrothermal’, since hydro- typically refers to water, but many

research studies have been conducted in solvents other than water. For this purpose, there exists the term 'solvothermal', which may refer to any solvent. Throughout the work presented in this thesis, syntheses were conducted in (hot) water only, and henceforth the work is described as hydrothermal synthesis.

Hydrothermal synthesis is an attractive method for the controlled production of materials. From a green chemistry perspective, it can operate at conditions that may be considered more environmentally friendly (Zanganeh et al. 2011) compared to other techniques e.g. solid state syntheses, where temperatures may be higher than 1000 °C. From a materials perspective, hydrothermal chemistry can produce materials that may have unique properties and be of high purity, and allow access to metastable phases, amongst others (Byrappa and Adschiri 2007). The technique has successfully demonstrated the synthesis of microporous materials (e.g. zeolites) (Cundy and Cox 2003; Cundy and Cox 2005), perovskites (Mao et al. 2003; Chen et al. 2006), metal oxides (Hayashi and Hakuta 2010), ionic conductors (Feng and Xu 2001), and inorganic-organic hybrid materials (Adschiri 2007; Namratha and Byrappa 2012). The focus here is on synthesis of metal oxides, which are the subject of this thesis. A number of reviews in the literature provide detailed accounts of other material families synthesised via hydrothermal syntheses (see above references).

In the context of metal oxide synthesis, the reactions occurring in a hydrothermal process can be summarised as two key steps: hydrolysis and dehydration (Scheme 1.1) (Adschiri et al. 1992a; Darr and Poliakoff 1999). In the hydrolysis step, hydrated metal ions are hydrolysed to form metal hydroxides, which are then dehydrated to form metal oxides. The rate of reaction is determined by the temperature, ionic product and dielectric constant of water. Since these properties differ for sub- and supercritical water, the rate can be tuned by controlling reaction conditions.

Scheme 1.1 Hydrolysis and dehydration reactions of hydrothermal syntheses leading to the formation of metal oxides.

$$Hydrolysis: \quad ML_x\,(aq.) + xH_2O \rightarrow M(OH)_x\,(s) + xHL$$

$$Dehydration: \quad M(OH)_x\,(s) \rightarrow M(O)_{x/2} + {}^{x}/_{2}\,H_2O$$

In hydrothermal processes, the key to nanoparticle production is the maximisation of supersaturation (described earlier in section 1.2.2). This can be achieved by controlling the temperature and pressure to modify the physicochemical properties of water, and hence, lead to hydrolysis of ions in solution (Byrappa and Adschiri 2007).

Conventional hydrothermal syntheses can be considered as batch reactions; products are synthesised in a group or set (called a batch), which have a defined beginning and ending. After each batch is completed, the process can be repeated, and so forth. Whilst batch hydrothermal syntheses have been used successfully for many years, they bring inherent drawbacks, such as being difficult to scale up (because of large volumes under high pressure), having slow reaction times, poor reproducibility and no (or limited) capability for high-throughput materials discovery. To overcome some of these challenges, researchers have developed continuous hydrothermal processes, which have now been used for over thirty years for the efficient manufacture of nanomaterials. The following section describes continuous hydrothermal processes, providing a review of the method and its applications.

1.4. CONTINUOUS HYDROTHERMAL FLOW SYNTHESIS

1.4.1. Introduction

Continuous hydrothermal flow synthesis (CHFS) takes many of the principles of batch hydrothermal synthesis, applying a continuous approach to materials synthesis. Hydrothermal synthesis is usually regarded as a batch-wise process, and hence may be subject to a number of limitations that affect batch processes. To overcome some of these issues, the Arai group in Japan first reported a continuous hydrothermal process in the early 1990's (Adschiri et al. 1992a; Adschiri et al. 1992b). It has since been studied by a number of groups worldwide, and each often has its own naming convention for the process. Herein, continuous hydrothermal methods in general will be referred to by the acronym CHFS, which is the name used in the Clean Materials Technology Group at University College London.

CHFS processes have successfully demonstrated the production of metal oxide nanomaterials for applications in bioceramics (Chaudhry et al. 2006; Chaudhry et al.

2008; Chaudhry et al. 2012; Lester et al. 2013), catalysis (Galkin et al. 2000; Kim et al. 2007; Kim et al. 2009a; Kim et al. 2009b; Weng et al. 2011a; Weng et al. 2011b; Weng et al. 2011c; Kim et al. 2012; Liang et al. 2015), dielectrics (Hakuta et al. 2005; Matsui et al. 2008; Hayashi et al. 2010a; Hayashi et al. 2010b), dye-sensitised solar cells (Li et al. 2013), sensing (Elouali et al. 2012; Shi et al. 2013; Naik et al. 2015), lithium ion batteries (Adschiri et al. 2001; Xu et al. 2008; Aimable et al. 2009; Shin et al. 2009; Hong et al. 2011; Hong et al. 2012b; Laumann et al. 2012; Hong et al. 2013; Nugroho et al. 2014; Lübke et al. 2015a; Lübke et al. 2015b), luminescent materials (Hakuta et al. 1999; Hakuta et al. 2003; In et al. 2007; Hobbs et al. 2009; Lin et al. 2010; Shibuki et al. 2010; Gruar et al. 2012; Hayashi et al. 2013), magnetic materials (Cote et al. 2003; Sasaki et al. 2010), photocatalysis (Thompson et al. 2009; Zhang et al. 2009b; Gruar et al. 2010; Jeon et al. 2010; Goodall et al. 2014), pigments (Lu et al. 2013), transparent conducting oxides (Fang et al. 2007; Lu et al. 2012) and UV attenuation (Goodall et al. 2015).

The CHFS process operates by mixing a flow of chemical precursors (containing the atoms of interest) with a flow of hot pressurised water, resulting in the formation of nanomaterials. The products of reaction are cooled via a heat exchanger, and typically collected as slurries, which are then processed to recover the material. Since the first reports, there have been many designs relating to CHFS type reactors. The following section reviews some of the most common designs that have been, or are currently in use.

1.4.2. CHFS reactor designs

The first reported CHFS process by Adschiri et al. (Arai group, Japan) employed two pumps, one of which was used to feed a metal salt solution, and the other a feed of distilled water. The distilled water was heated up to 763 K and fed to a mixing point, where it met the feed of the metal salt solution (at ambient temperature). The mixture then entered a reactor that was heated (up to 763 K) by an electric furnace. The residence time of the mixture in the reactor was approximately 2 minutes. The pressure of the process (30 – 35 MPa) was controlled by a back-pressure regulator (Adschiri et al. 1992a). Many of the subsequent CHFS reactors that have since been developed around the world, take inspiration from this early work.

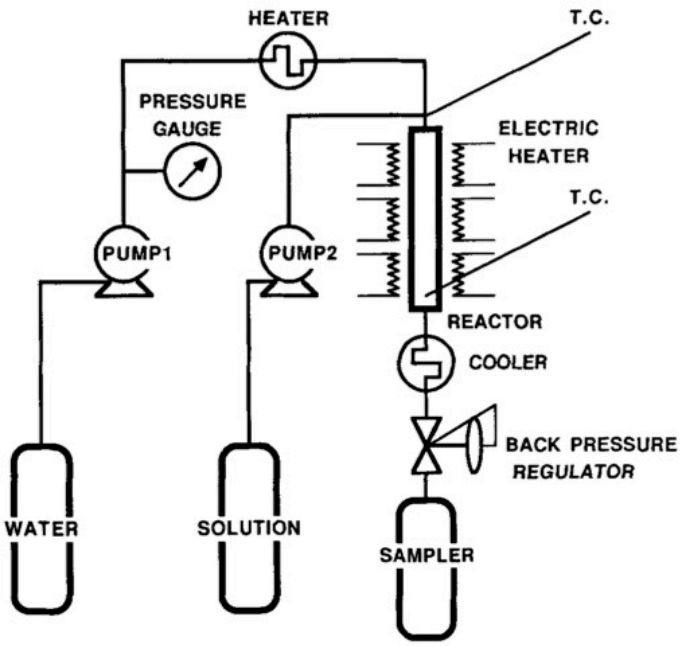

Figure 1.10 Diagram of the first reported CHFS process for the synthesis of metal oxides. Reprinted from (Adschiri et al. 1992a) with permission from John Wiley and Sons.

Since this first design, the Arai group developed the process to include additional feeds such that it was possible to have more than one precursor, which increased the synthesis capabilities of the process (Hakuta et al. 1998). For example, the synthesis of barium hexaferrite employed four pumps in total. In addition to a feed containing metal salts, a feed of potassium hydroxide was added; firstly, these two feeds mixed at ambient temperature before the addition of a hot water feed (200 °C) to pre-heat the mixture. Finally, the pre-heated mixture met a flow of supercritical water (in the range 450–500 °C). The additional feeds were necessary to allow the introduction of more than one precursor, which may have otherwise reacted undesirably if they were placed in a single feed.

Other developments have related to the mixing configuration of various feeds. Cote et al. (Teja group, USA) conducted experiments in which two scenarios were considered: cold mixing, where a metal salt was pre-mixed with potassium hydroxide prior to mixing with hot pressurised water (identical to the Arai group arrangement), and hot mixing, where the stream of potassium hydroxide was mixed with hot pressurised water, and this combined feed was then mixed with the metal salt solution (Cote et al. 2002). They found that in the hot mixing case, particle sizes of α–Fe_2O_3 were smaller than in

the cold mixing setup. It is also reported that crystal faces of α–Fe_2O_3 and Co_3O_4 particles were much more distinct in the hot mixing scenario.

Kawai-Nakamura et al. simplified the process by employing only one pump, which fed metal salt aqueous solutions through a heated (523 K) micro-tube (1.59 mm outer diameter, 100 mm length) under a pressure of 30 MPa. Products were quenched rapidly by an external water jacket and collected as slurries (Kawai-Nakamura et al. 2008). Materials that were synthesised by this process included Ag particles, Fe_2O_3, TiO_2 and ZrO_2. Whilst this simple process was successful in preparing some materials, having only one solution feed may have limited the number of individual materials synthesised. This is because, for example, the presence of a mineralizer (e.g. base) is beneficial to the synthesis of metal oxides under hydrothermal conditions, since they play a key role in nanoparticle formation (Wang et al. 2007).

The Clean Materials Technology Group (CMTG) at University College London (UCL) first began developing CHFS reactors (at Queen Mary, University of London (QMUL) from 2003) that operated at up to 50 mL min^{-1} total flow rate (described herein as the laboratory scale) (Chaudhry et al. 2006; Thompson et al. 2009). The basic design of this process is shown in Figure 1.11. Similar to the Arai group design, the process employed a number of pumps, each providing an individual feed for deionised water or precursors. However, the key difference with the CTMG design was that it did not contain a heated reactor zone; rather there was only one heater, which was used to heat the water feed up to 450 °C, prior to mixing with precursors.

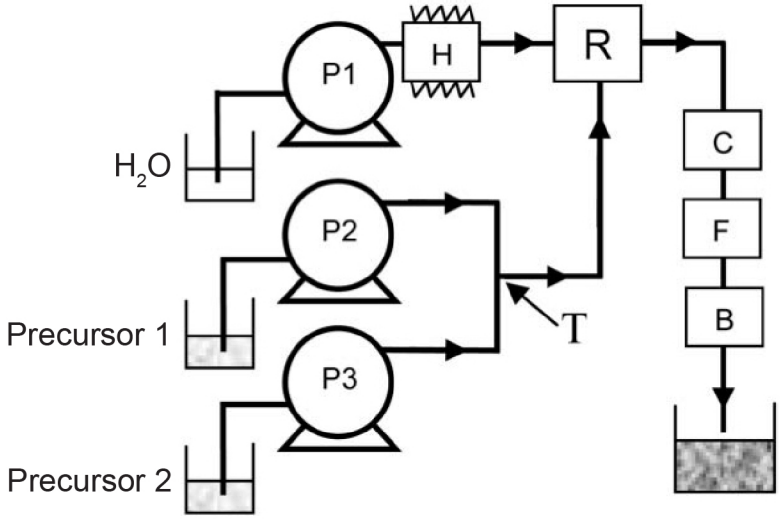

Figure 1.11 Diagram of the first developed CHFS process at the Clean Materials Technology Group at Queen Mary, University London. P1, P2 and P3: pumps, H: heater, R: reaction point, C: cooler, F: filter, B: back-pressure regulator, T: 'tee' piece mixer. Reprinted (adapted) from (Chaudhry et al. 2006) with permission from The Royal Society of Chemistry.

The CHFS designs described thus far were capable of producing up to 10 samples per day at a few grams per sample. Researchers of the Darr group at QMUL, realised that whilst this was generally far beyond the capabilities of most other nanomaterial synthesis techniques, in terms of throughput, it would still need more samples per day to be useful in combinatorial science. Subsequently, the CHFS process was developed by Professor Darr and co-workers to enable high-throughput materials discovery. A modified CHFS process was built, named the High-Throughput Continuous Hydrothermal (HiTCH) flow synthesis reactor (Figure 1.12). The capability of the HiTCH reactor was demonstrated by producing a 66-sample nanoparticle library (consisting of individual compositions of $Ce_xZr_yY_zO_2$), in less than 12 hours (Weng et al. 2009a). In the HiTCH reactor, the premixed metal salt precursor solutions (2 mL) were filled in an injector valve; when the DI water feed from pump P2 passed through the valve, it carried the precursor solution to the mixer. The valve was manually operated, such that it was possible to use the feed from P2 to flush out the system, when the injector valve was switched for filling (with precursor). Kellici et al. reported a modified version of the HiTCH reactor, which used a syringe pump instead of manual filling of the switch valve (Kellici et al. 2010). This meant that larger volumes of precursor

solution could be used, rather than the limited 2 mL of manual filling. A fully automated robotic version of the HiTCH process (Rapid Automated Materials Synthesis Instrument; RAMSI) was also developed, where metal salt precursors were automatically mixed and introduced to the reactor via a syringe pump. Products of reaction were automatically collected, cleaned and printed on a library plate, ready for subsequent processing e.g. heat-treatment and analysis (Lin et al. 2010).

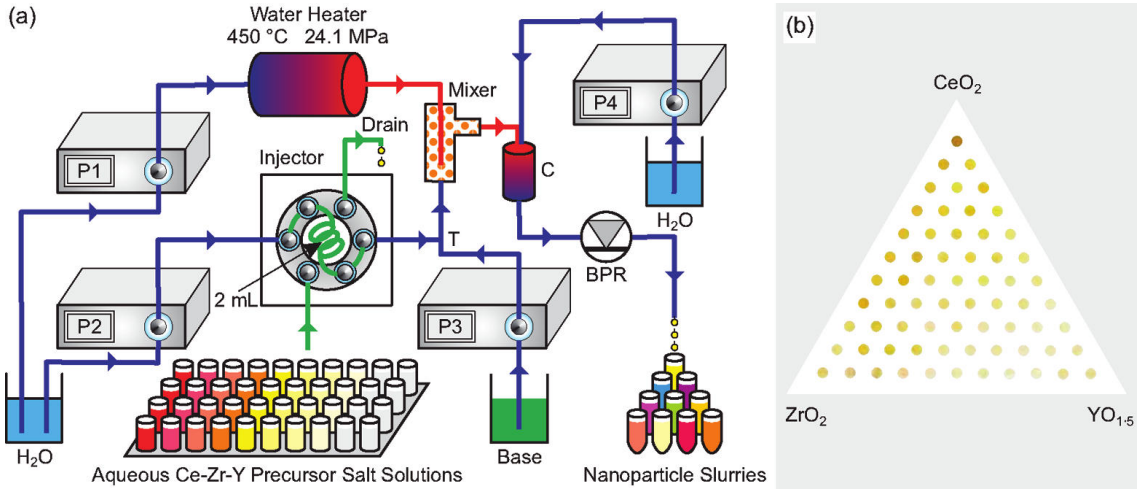

Figure 1.12 (a) Schematic diagram of the High-Throughput Continuous Hydrothermal (HiTCH) flow synthesis reactor, developed in the CMTG for the synthesis of 66 compositionally unique samples of $Ce_xZr_yY_zO_2$, prepared in less than 12 hours. (b) Image of freeze-dried powders that were heat-treated at 1000 °C and placed into a holder according to composition. Reprinted with permission from (Weng et al. 2009a). Copyright (2009) American Chemical Society.

Another important aspect of CHFS designs has been process scale up. In many of the nanomaterial synthesis routes available, scale up is often challenging, because it is difficult to obtain the same, homogeneous reaction conditions that were present at the small scale. CHFS processes have a benefit in that reaction volumes (i.e. the volume of material that is under high temperature conditions at any one time) are often very low in comparison to the total volume of the process. By employing higher capacity equipment (e.g. higher flow rate pumps), the volumetric scale, and therefore the production output, can be greatly increased. However, the increase in reaction volumes under high temperature remains low, in comparison to batch scale-up processes. This also provides safety benefits, because it limits the volume of superheated material that

may cause harm (i.e. the reaction volume), in the event of a failure. The CMTG began to investigate scale up of a CHFS process in 2009, with the development of a pilot scale process that has demonstrated the synthesis of zinc oxide, ceria-zinc oxides, iron oxide and indium oxide, amongst many other materials (some unpublished as of yet) (Gruar et al. 2013; Shi et al. 2013; Tighe et al. 2013; Gruar et al. 2015; Naik et al. 2015). The pilot scale process operated at up to 800 mL min^{-1} total flow rate, demonstrating a 20 × scale up on volumetric flow rate (compared to the laboratory scale), and allowed precursor concentrations to be increased up to 1 M. Therefore, the process was capable of producing up to 1 kg h^{-1} of dry nanomaterial powder. The scale up of the process from the laboratory scale increased material output by nearly 400 times, but with an increase in pipe diameters (from the use of larger pipe sizes) by only three times (Gruar et al. 2013). At the industrial scale (up to 4 kg h^{-1}), Hanwha Chemical Corporation Ltd. in South Korea have constructed a CHFS plant (known as SuperSyn™), in particular for the synthesis of lithium iron phosphate (known as SafEnPo®), as a material for lithium-ion batteries (Hanwha Chemical Co. 2013). It is reported that other materials have also been synthesised (Adschiri et al. 2011), however, limited information is known about this process in the literature. Another scale up process has been investigated by the SHYMAN project (University of Nottingham), with the aim of increasing output to over 100 tons per annum (Nottingham 2013).

This section has provided an overview of different CHFS process designs, suggesting that the majority of CHFS processes have been designed in a similar manner, most taking inspiration from the first reported design by the Arai group (Adschiri et al. 1992a; Hakuta et al. 1998). However, one of the unique features of different CHFS processes is the mixing point, which is the point where mixing of precursor chemicals with hot, pressurised water, occurs. The following section provides a summary of some of the different mixing point designs, that have been employed in different CHFS processes.

1.4.3. Mixing point designs

Many CHFS studies in the literature report different particle properties (e.g. composition, size, size distribution, shape, etc.), even when reaction conditions appear

to be similar. This occurs because the physical mixing of the fluids may vary, depending on the mixing point design. The primary aim of the mixing point is to induce homogeneous mixing of the different fluids, such that nanoparticle formation occurs. Whilst the desired particle properties may vary according to application, a good mixing process would allow a high rate of particle formation (to maximise yield) and limit the occurrence of blockages (which otherwise lead to downtime). It is known that the mixing in CHFS processes can affect particle properties and synthesis reproducibility (Lester et al. 2006). Mixing point designs have included tee-shaped, swirling, central collision, counter-current and co-current mixers. However, many publications related to CHFS studies limit the information they provide regarding mixing point designs; the focus is often on particle properties and applications, rather than process and mixer design. This often makes it difficult to evaluate different designs, however, a brief summary of the few designs that have been detailed now follows.

Kawasaki et al. have studied tee-shaped mixers, where the directions of different fluid flows within the tee-mixer were varied (Figure 1.13) (Kawasaki et al. 2010b). This type of mixer consisted of a tee-piece with two inlets and one outlet; the supercritical water and precursor chemicals were mixed orthogonally (Figure 1.13(a) and (b)) or directly opposing one another (Figure 1.13(c)).

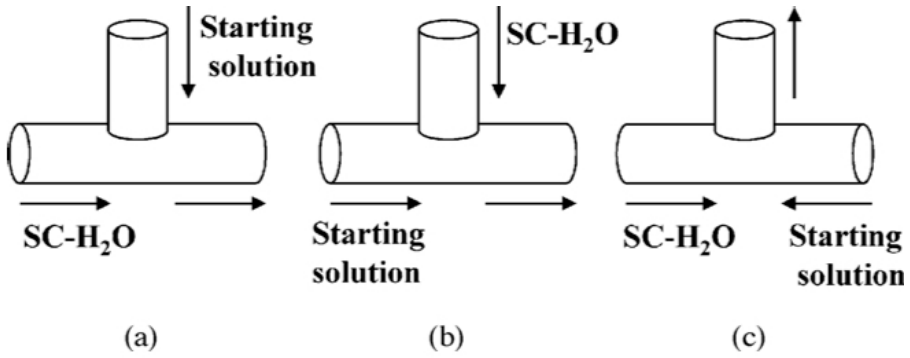

Figure 1.13 Designs of tee-shaped mixers showing the different flow directions in the (a) straight, (b) bending and (c) counter streams of the supercritical water and precursor streams. In all diagrams, the unlabelled arrow shows the flow direction of the products of reaction. Reprinted from (Kawasaki et al. 2010b) with permission from Elsevier.

The authors of this study found that decreasing inner mixer diameter and increasing flow rates, led to a decrease in the particle size of NiO. Although the different flow directions did not lead to any significant trends, the study provided a useful insight in to understanding how inner mixer diameter, flow rate and residence time affected particle properties. The same authors subsequently investigated the tee-shaped mixer for the synthesis of Fe_2O_3, NiO and CuO, and found that residence time had a great effect on the conversion efficiency of reactants to products (Sue et al. 2011).

Swirling micro mixers (Figure 1.14) have been investigated for the synthesis of NiO, and compared to tee-shaped mixers (Kawasaki et al. 2010a). In the swirling micro mixer, a supercritical water stream was split, such that two streams were created. These were set to an angle of 60° with respect to the precursor solution, and displaced (< 1 mm) with respect to the mixer's central axis. A swirling flow was created by the supercritical water streams. It is reported that swirling micro mixers produced particles with smaller size and narrower size distribution (compared to tee-shaped mixers), even when the inner diameter of the mixer was larger than that of the tee-shaped mixer. Computational fluid dynamics (CFD) simulations suggested that the swirling micro mixer had excellent mixing, which contributed to an increased heating rate of the precursor stream.

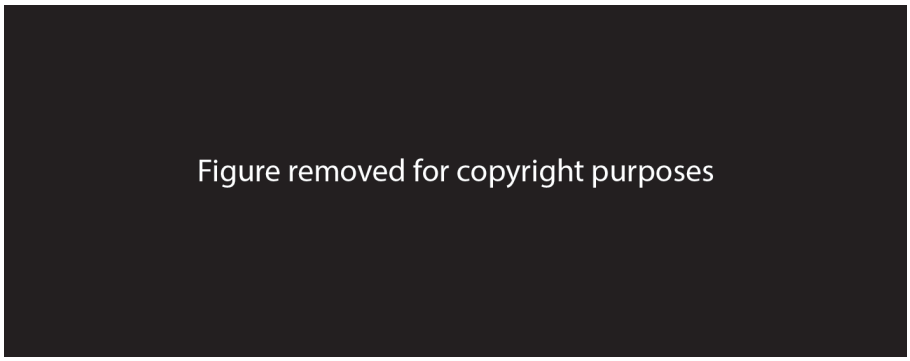

Figure 1.14 Cross-sectional designs of swirling micro mixers. Reprinted from (Kawasaki et al. 2010a).

Sue et al. developed a central collision mixer (CCM), shown in Figure 1.15 (Sue et al. 2010). The CCM was developed to minimise the contact of the precursor solution with the inner walls of the mixer; the authors suggested that in previous mixer designs, the inner walls induced heterogeneous nucleation, leading to larger particles and wider size

distributions. In the CCM, a supercritical water feed was split four ways via three tee mixers, before entering the CCM. A flow of precursor solution passed vertically downwards through the CCM, where it mixed with the supercritical water, which entered the CCM in the horizontal axis, at the central point. In comparison to a conventional tee mixer, smaller Fe_2O_3 nanoparticles were obtained, with narrower size distributions, and heterogeneous nucleation on the inner walls of the mixer was minimised.

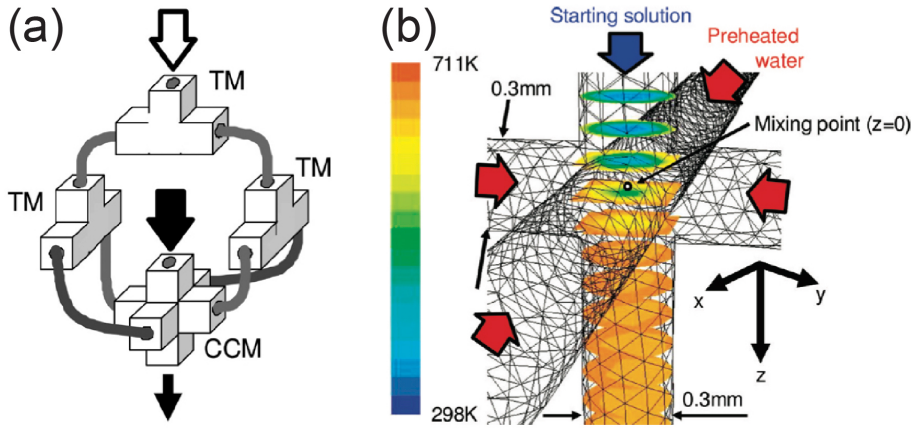

Figure 1.15 (a) Diagram of a central collision mixer. TM: tee mixer, CCM: central collision mixer. The white arrow (with black outline) indicates the flow of supercritical water, the large black arrow indicates the flow of precursor solution, and the small black arrow indicates the flow of reaction products. The lines represent the flow of supercritical water as it split from one to four streams in the tee mixers, before entering the CCM. (b) A temperature contour diagram of the CCM, showing the mixing point where the collision between precursor solution and supercritical water occurred. Reprinted (adapted) with permission from (Sue et al. 2010). Copyright (2010) American Chemical Society.

A counter-current mixer (known as a nozzle reactor), where opposing flows of supercritical water and precursor solution were mixed, was developed by Lester et al. The motivation for the development of this mixer led from studies conducted by the authors, which examined the mixing profiles in a conventional tee mixer (Lester et al. 2006). They suggested that the differences in physicochemical properties of the two feeds (i.e. supercritical water and precursor solutions) resulted in highly turbulent mixing in the tee mixer, because of the natural convection forces present. The authors concluded that the tee mixer was relatively inefficient at handling this type of mixing,

and hence a new mixer design was required (Lester et al. 2006). The counter-current mixer was a pipe-in-pipe concentric arrangement, where the inner pipe had an open-ended cone-shaped nozzle. The supercritical water was fed downwards through the inner pipe, and the precursor solution upwards through the outer pipe; where the two flows mixed, a reaction ensued, with the reaction products passing upwards in the outer pipe, around the inner pipe. Material syntheses of CeO_2 showed that there was improved reproducibility and reliability compared to the conventional tee mixer. The CMTG also evaluated the counter-current mixer for the synthesis of a number of materials, including hydroxyapatite, calcium phosphate, cerium dioxide, titanium dioxide and bismuth molybdate (Chaudhry et al. 2006; Chaudhry et al. 2008; Middelkoop et al. 2009; Thompson et al. 2009; Gruar et al. 2010; Tighe et al. 2012).

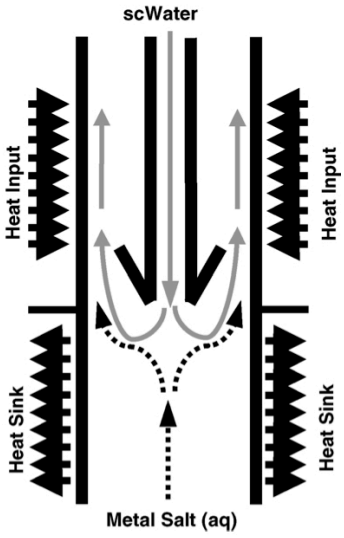

Figure 1.16 Schematic diagram of the nozzle reactor design, showing the opposing flows of supercritical water (downwards) and metal salt precursor solution (upwards). Reprinted from (Lester et al. 2006) with permission from Elsevier.

Following investigations with the counter-current mixer, Tighe et al. reported that a heat exchanger effect occurred as the product stream passed away from the mixer (Tighe et al. 2012). Consequently, the supercritical water was at a lower temperature, giving a mixing temperature that was substantially lower than the predicted value. It was also observed that the supercritical water issuing from the inner pipe penetrated far into the precursor stream, which was undesirable, because it may have led to uncontrolled nanoparticle synthesis. Consequently, the CMTG developed a co-current mixer design

(known as a confined jet mixer, CJM; (Darr et al. 2011)), where the two flows (i.e. supercritical water and precursor solutions) were fed co-currently. The mixer consisted of a pipe-in-pipe configuration, where the supercritical water flowed upwards through the inner pipe (Figure 1.17). Precursor solutions flowed into the mixer from two inlets that were initially orthogonal to the supercritical water feed. Nanoparticle formation occurred at the point where the two feeds mixed, and reaction products were carried upwards away from the mixing point (Gruar et al. 2013).

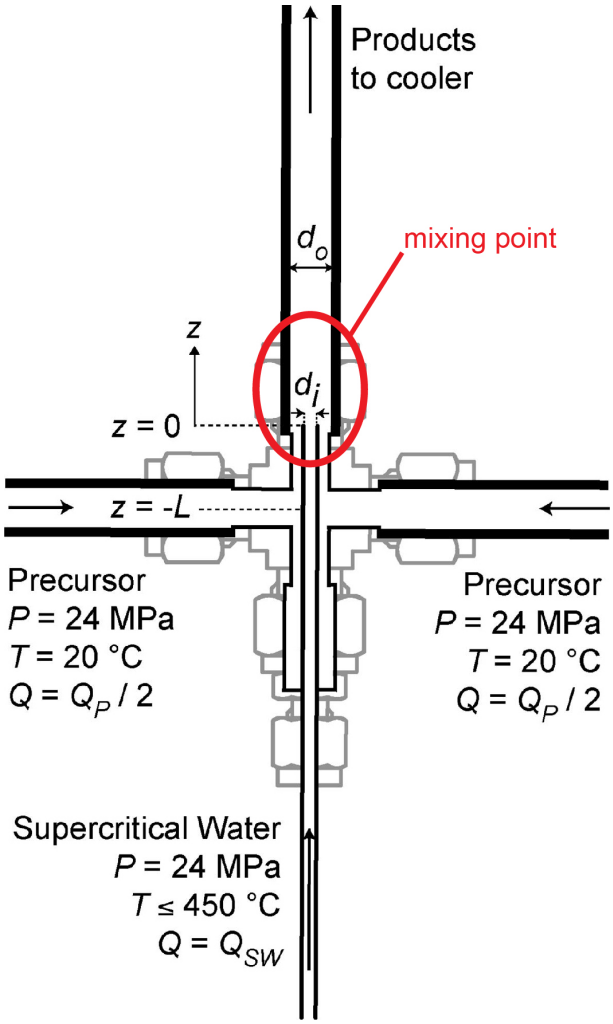

Figure 1.17 Diagram of the confined jet mixer (CJM) designed in the CMTG. The supercritical water, precursor, and reaction product feeds are indicated. Q_P and Q_{sw} are flow rates of precursor and supercritical water, respectively. *d* indicates inner (*i*) and outer (*o*) pipe diameters, and z indicates the position of the inner (supercritical water) pipe. Reprinted (adapted) with permission from (Gruar et al. 2013). Copyright (2013) American Chemical Society.

The CJM was evaluated for the synthesis of zinc oxide at two process scales. It was found that the mixer was effective for the production of nanoparticles, and that the coaxial geometry allowed synthesis at both a laboratory and pilot scale for extended durations. The mixer was scaled up from the laboratory to pilot scale by increasing its size by only three pipe diameters, which corresponded to an increase over 400 times in output. In situ temperature measurements showed that mixing occurred instantaneously as the feeds mixed, and the theoretical mixing temperature was rapidly achieved. Samples of zinc oxide prepared at the same concentrations across the two scales, were virtually indistinguishable based on microscopy and surface area analysis (Gruar et al. 2013). Throughout the work presented in this thesis, CHFS syntheses have employed the confined jet mixer. Further information on the CJM is provided in Chapter 2.

1.4.4. One-step, in-process nanoparticle surface modification

Many applications of nanoparticles require them to be dispersed in an appropriate medium (e.g. a liquid for a printable ink), which means that they must have stability against agglomeration and settling or caking. Nanoparticles have a large surface-to-volume ratio, and possess high surface energies; therefore, to minimise the surface energies, they tend to agglomerate in the absence of surface agents (Wu et al. 2008). Surface functionalising agents can be used to prevent agglomeration, by affording either steric and/or electrostatic stabilisation to particle surfaces. Steric stabilisation involves the addition of large or bulky/branched molecules to the surface of the particles, which physically prevent particles from coming together. Electrostatic stabilisation involves the addition of charged molecules to the particles surface, which creates charge repulsion between nanoparticles (Thanh and Green 2010). Surface functionalising agents have different mechanisms to stabilise nanoparticles, and therefore each is often considered on a case-by-case basis, by evaluating the material to be stabilised, the solvent, reaction conditions, etc. Some literature reports refer to these particles as surface functionalised, whilst others describe them as organic-inorganic hybrid nanoparticles.

CHFS has previously demonstrated nanoparticle surface functionalisation, in a one-step process. For the synthesis of surface functionalised $BaTiO_3$, Hayashi et al. developed a CHFS process where a surface functionalising agent (modifier) was added to the reactor at a point after the nanoparticles had formed. The modifier was added via a tee piece mixer, and mixed with the product stream before being cooled and collected (Hayashi et al. 2010b). Surface modified cobalt aluminate nanoparticles were prepared by Lu et al., by simply placing the surface functionalising agent (hexanoic acid) in the precursor solution feed (Lu et al. 2013). They found that surface modified particles dispersed well in the hexane phase of a hexane-water binary solvent system. Daschner de Tercero et al. investigated the synthesis of surface functionalised iron oxide nanoparticles via a continuous hydrothermal process (Daschner de Tercero et al. 2013a; Daschner de Tercero et al. 2013b). Their process consisted of three mixing points, where they investigated the addition of surface functionalising agents before (to the supercritical water stream), after (to the product stream) or simultaneously with iron salt solutions. They found that the choice of precursor and surface functionalising agent dictated the composition of the product, whilst the mixing regime affected particle size.

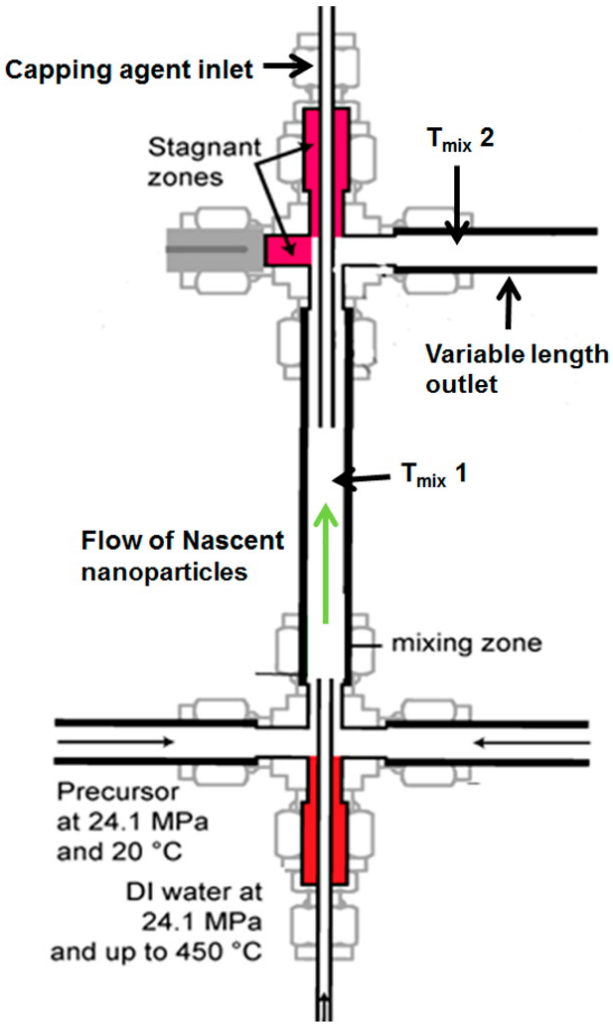

Figure 1.18 Schematic diagram of the mixer configuration used by Gruar et al., used for the surface functionalisation of iron oxide (magnetite) nanoparticles. Nanoparticles were formed in a confined jet mixer (CJM), before meeting a flow of citric acid in a counter-current geometry mixer. Reprinted with permission from (Gruar et al. 2015). Copyright (2015) American Chemical Society.

Gruar et al. (CMTG at UCL) also investigated the surface functionalisation of iron oxide nanoparticles with citric acid (Gruar et al. 2015). The authors developed a CHFS process that consisted of a co-current mixer (confined jet mixer), used for the formation of nanoparticles (as described earlier in section 1.4.3), and a counter-current mixer for the surface functionalisation step (shown in Figure 1.18). Aqueous dispersions were obtained directly from the process, with post-analysis showing a high quantity of citric acid on the surface of the particles, leading to the stabilising effect. The rate and extent of mixing between the product stream and the citric acid stream largely influenced the

dispersion stability. However, it was shown that the crystallite size was independent of the reaction conditions, suggesting that particle formation and functionalisation were two individual steps.

This section has provided an overview of continuous hydrothermal synthesis, focussing on process and mixer design. It is apparent from the discussion that these are two key aspects, which can greatly influence particle properties. Hence, the design of any CHFS process should consider these in great detail. Syntheses of materials discussed in this thesis have been prepared using the CMTG CHFS process, at two process scales. During the course of this work, an alternative mixing design was adopted for one-step surface functionalisation of particles. Details of this design are discussed in Chapter 2.

1.5. PHOTOCATALYSIS

1.5.1. Introduction

Photocatalysis is the acceleration of a photochemical reaction (photoreaction) in the presence of a catalyst, known as a photocatalyst (Mills and Le Hunte 1997). The photocatalyst has the ability to absorb photons and use their energy to lower the activation energy of the photoreaction. There are numerous applications of photocatalysis, such as water splitting (Kudo and Miseki 2009), water purification (Mills et al. 1993), water disinfection (Keane et al. 2014), CO_2 reduction (Habisreutinger et al. 2013), degradation of organics (Mills and Le Hunte 1997), self-cleaning surfaces (Banerjee et al. 2015), and air purification (Hoffmann et al. 1995). Interest in photocatalysis is particularly driven by the abundance of solar energy received from the Sun, on Earth, which can be used as an energy provider for photocatalytic reactions. Solar energy is by far the greatest energy provider on Earth, where it is already very successfully utilised by plants for photosynthesis (Scholes et al. 2011). The Earth receives more energy from sunlight in one hour than is consumed in an entire year (Lewis 2007), which suggests that efficient utilisation of sunlight would be very beneficial, especially when the reliance on fossil fuels should ideally be reduced. Solar energy consists of ultraviolet (UV), visible and infrared (IR) wavelengths of light, as shown in Figure 1.19. Outside the Earth's atmosphere, solar energy is made up of approximately 8 % UV, 39 %

visible and 53 % IR (Moan 2001). UV radiation is categorised as UVC (100 – 290 nm), UVB (290 – 320 nm) and UVA (320 – 400 nm), in order of increasing wavelength. The Earth's atmosphere is able to absorb almost all UVC radiation (100-290 nm), and there is absorption in the visible and IR region by O_2, H_2O and CO_2. Therefore, the radiation at sea level is made up of approximately 6 % UV, 52 % visible and 42 % IR (Moan 2001).

Photocatalysis was first reported in scientific literature in 1911, where Eibner discussed the effect of bleaching of Prussian blue dye, when zinc oxide was illuminated (Coronado 2013a). Following this first report, research in photocatalysis was scarce over the next 60 years. However, changes in economy in the early 1970's, such as the increase in crude oil prices, stimulated scientists to explore alternative energy sources. In 1972, Fujishima and Honda reported electrochemical photolysis of water, where a semiconductor rutile TiO_2 electrode was coupled to a platinum black counter electrode, in a biased (i.e. with electrical energy input) photoelectrochemical cell. Irradiation of the cell with UV light (< 415 nm) led to oxygen evolution at the anode, and a current flowed to the cathode (Fujishima and Honda 1972).

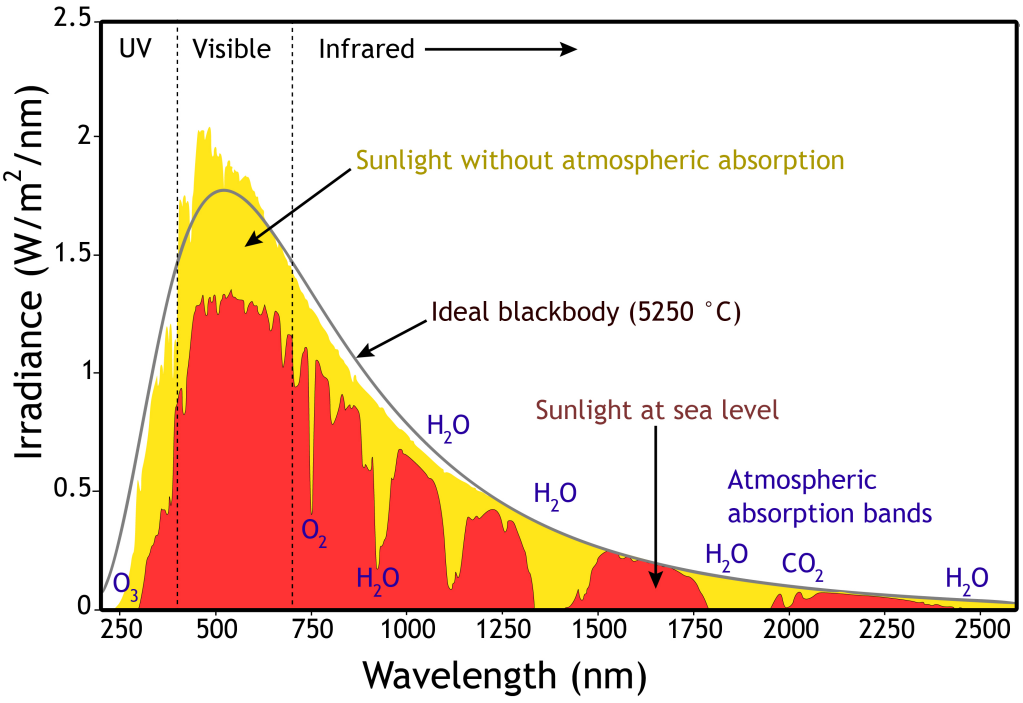

Figure 1.19 Plot of solar irradiance without atmospheric absorption (yellow; i.e. at the top of the atmosphere) and at sea level (red). Absorption bands of species in the atmosphere are indicated. Reprinted (adapted) from (Rohde 2007) with permission under a creative commons licence (CC BY-SA 2.5).

This work opened up the possibility of obtaining clean energy using abundant and inexpensive sources; sunlight and water. Despite this scientific advance, the following years remained rather dormant in terms of photocatalysis research, until 1977, when Nozik prepared a device where the design, construction and operation of a photoelectrochemical cell was greatly simplified (Nozik 1977). Nozik fused two electrodes together, creating a single-structure device known as a "photochemical diode". This was demonstrated by applying a thin film of platinum to one side of a single wafer crystal of cadmium sulphide (CdS); illumination of the CdS side resulted in hydrogen gas evolution occurring on the platinum side. This approach demonstrated that an external potential was not required to split the water molecule, and that the presence of a noble metal (e.g. platinum) could enhance photoactivity (Coronado 2013a). Since these reports, the interest in photocatalysis has grown tremendously; the number of publications has increased each decade since 1970, and there have been more publications in the last five years (2010–2015) than any preceding decade (Web of Science search based on the term "photocatalysis" as a topic).

Photocatalysts are semiconductor materials, which can absorb photons from light to produce charged species (known as excitons), that can catalyse reactions. The ability of a semiconductor to photocatalyse a reaction is related to its electronic structure. The following section describes the fundamentals of semiconductors.

1.5.2. Fundamentals of semiconductors

Semiconductors are a classification of materials that sit alongside insulators and conductors. The electronic structure of solid-state materials distinguishes them into one of these three classifications. When atoms come together to form a molecule, their atomic orbitals combine to form molecular orbitals. The molecular orbitals are high energy (antibonding) and low energy (bonding); valence electrons typically occupy bonding orbitals, in order to minimise the overall energy of the system. As the number of atoms in the molecule increases, the energy levels become closer and closer, and can be considered as a continuous band (although they actually exist as a finite number of very closely spaced energy levels). The electrons that contribute to bonding orbitals form what is known as the valence band (VB), and the unoccupied states (antibonding)

form the conduction band (CB). If the conduction and valence bands are so close that they overlap, such as in metals, some of the valence electrons can move freely through the solid; these materials are described as conductors. In other cases, the bands may be separated such that there is a forbidden region between them. The distance between the highest occupied state of the valence band, and the lowest unoccupied state of the conduction band, is known as the band gap. The size of the band gap and position of the Fermi level determines whether a material is classed as an insulator or a semiconductor; however, the distinction between these, and the size of the band gap at which a material is considered an insulator, is less precise (Coronado 2013b).

Electrons cannot possess energies that lie within the band gap region, however, in a semiconductor, if the electron is excited with an energy that is equal to or greater than the band gap, it can be promoted from the valence band to the conduction band. When the electron leaves the valence band, it leaves behind a hole. Electrons and holes are mobile species, and as such, semiconductors have interesting properties.

The Fermi level (E_F) of a solid is another important aspect when determining its electronic properties. Conductors, such as metals, have continuous bands, and the Fermi level lies within this band. On the other hand, semiconductors have fully occupied valence bands, and the Fermi level lies in the band gap. A pure (undoped) semiconductor typically has its Fermi level half way between the valence and conduction bands, and can be described as an intrinsic semiconductor (Figure 1.20(a)). If a semiconductor is doped with a foreign (impurity) atom, it can be described as an extrinsic semiconductor.

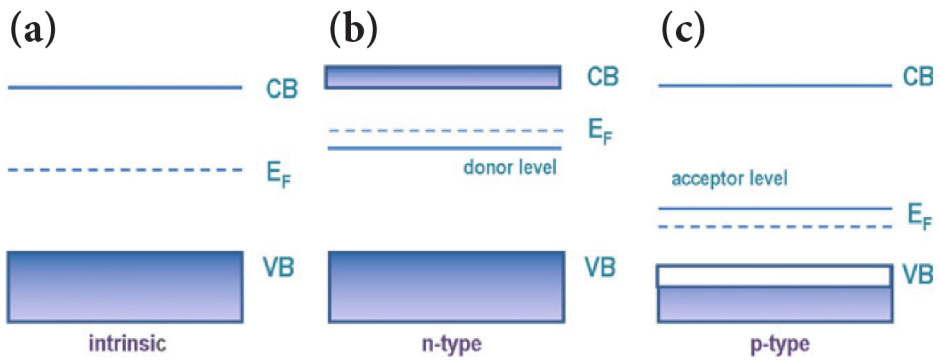

Figure 1.20 Band diagrams for (a) intrinsic and (b-c) extrinsic (doped) semiconductors ((b) n-type and (c) p-type). E_F corresponds to the Fermi level. Reprinted (adapted) from (Coronado 2013b) with permission from Springer.

Doping can be of two types: n-type or p-type, which is dependent on the type of dopant. If the dopant has extra valence electrons, the semiconductor is described as n-type, because the material contains a surplus of (negatively charged) electrons. They become the majority charge carriers, whilst holes are the minority charge carriers. The extra valence electrons are able to form donor levels close to the conduction band, and the Fermi level is shifted to higher energy (Figure 1.20(b)). Conversely, if the dopant has holes in its valence shell, the semiconductor is described as p-type, because it contains a surplus of (positively charged) holes. In this case the holes are the majority charge carriers. Acceptor levels form close to the valence band, and the Fermi level is shifted to lower energy (Figure 1.20(c)).

1.5.3. Semiconductor photocatalysis

In photocatalysis, the excitation of electrons from the valence band to the conduction band is made possible by the absorption of a photon of light with sufficient energy. The processes that take place can be explained by the aid of an appropriate diagram (Figure 1.21). When a semiconductor absorbs a photon (step 1) that possesses an energy equal to or greater than the band gap, an electron is excited from the valence band to the conduction band (step 2). The combination of the negative electron (e^-) and positive hole (h^+) is referred to as the photo-excited state of the semiconductor. Trapping sites in the crystal lattice immediately trap the charge carriers (Ohtani 2010), which can then move to the surface of the semiconductor particle (step 3), where the electron and hole

can take part in reduction and oxidation reactions, respectively (step 4). However, for a semiconductor to be efficient, the processes involving the electron and hole must compete against other electronic processes i.e. recombination (Mills and Le Hunte 1997). The electron and hole can recombine if the electron re-enters the valence band, which can occur in the bulk (step a) or at the surface (step b) of the semiconductor. These processes can be summarised as shown in Equations 1.14 and 1.15.

$$\text{Semiconductor} + h\nu \rightarrow e^-_{CB} + h^+_{VB} \qquad \text{(Equation 1.14)}$$

$$e^-_{CB} + h^+_{VB} \rightarrow \text{energy} \qquad \text{(Equation 1.15)}$$

Photoexcitation of a semiconductor and subsequent generation of excitons is a rapid process, occurring in the femtosecond scale (Hoffmann et al. 1995). The separated charges are only stable for nanoseconds, before they recombine, and such energy is therefore lost, either by radiative or non-radiative energy release (Coronado 2013b).

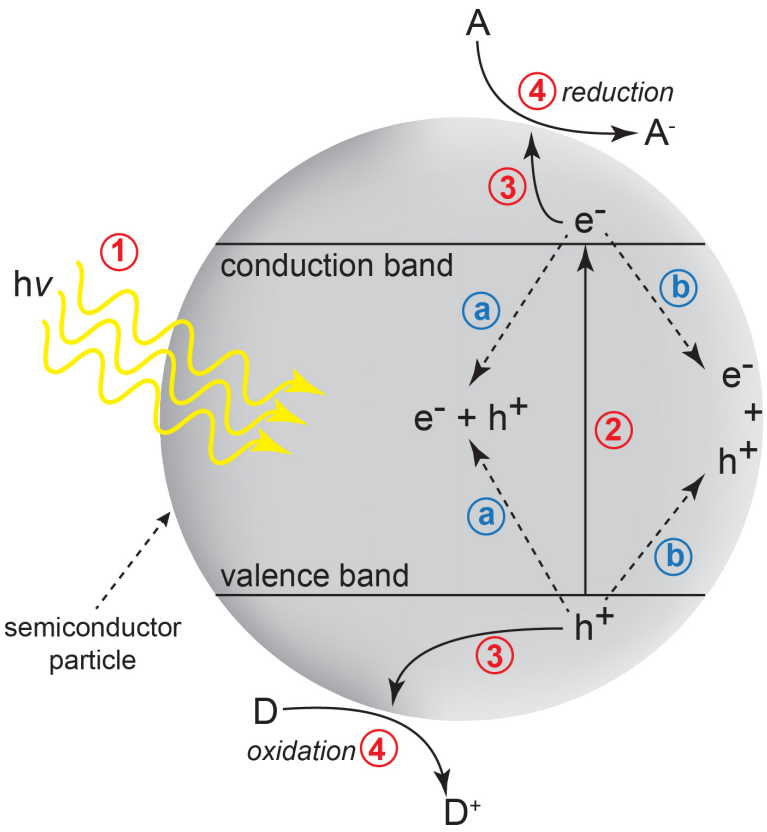

Figure 1.21 Schematic diagram showing the charge carrier processes that may occur on a semiconductor particle upon absorption of a photon. A description of each step is provided in the text.

For a material to be a photocatalyst, it must satisfy a number of conditions. The band positions of the semiconductor must be of appropriate energy, such that they are complimentary to the redox potentials of the reaction in question. The top of the valence band must be more positive than the oxidation potential, whilst the bottom of the conduction band must be more negative than the reduction potential. For a semiconductor to be excited by incident light radiation, its band gap must be smaller than the wavelength of light it is to be excited by. In theory this means, for excitation by solar light incident on the Earth's surface, the band gap must be less than ≈ 4 eV to absorb photons from the UVB region of solar light (wavelength > ≈ 300 nm). However, materials with band gaps as large as this may be inefficient in photocatalysis, because only a small proportion of photons from solar light have these or higher energies.

A number of inorganic materials have been investigated for their ability to act as photocatalysts, some of which are shown in Figure 1.22. As an example, the redox potentials of water splitting are also shown. Water splitting is the process in which the water molecule is split to produce hydrogen and oxygen. It has reduction and oxidation potentials for hydrogen and oxygen generation at 0.00 and +1.23 V, respectively, versus the normal hydrogen electrode. Therefore, a semiconductor must have a minimum band gap of 1.23 eV (ignoring any overpotential), and its valence and conduction bands must straddle the redox potentials (as described earlier), in order to photocatalytically split water. Many of the semiconductors shown in Figure 1.22 have valence band positions that are more positive than the oxidation potential, so photocatalytic oxygen generation using these materials is generally feasible. However, a smaller number of semiconductors (from those shown) have conduction band positions that are more negative than the reduction potential. Consequently, not all semiconductors are able to photocatalytically reduce water to evolve hydrogen. To efficiently utilise lower energy photons (solar light consists of ca. 6 % UV and 52 % visible light (400-750 nm), with the remainder being infrared), the semiconductor band gap must be less than ≈ 3 eV. Not all of the semiconductors shown meet this criteria, so whilst they may be able to photocatalytically evolve hydrogen and/or oxygen from water, strategies to modify their electronic properties are desirable.

Besides the electronic requirements that semiconductors must fulfil to act as photocatalysts, other properties are also required; the materials must be: chemically stable under illumination in their respective environment, non-toxic, and cheap to produce. For example, cadmium sulphide fulfils the electronic requirements, but photocorrodes under illumination to form Cd^{2+} ions (which are toxic) (Meissner et al. 1986).

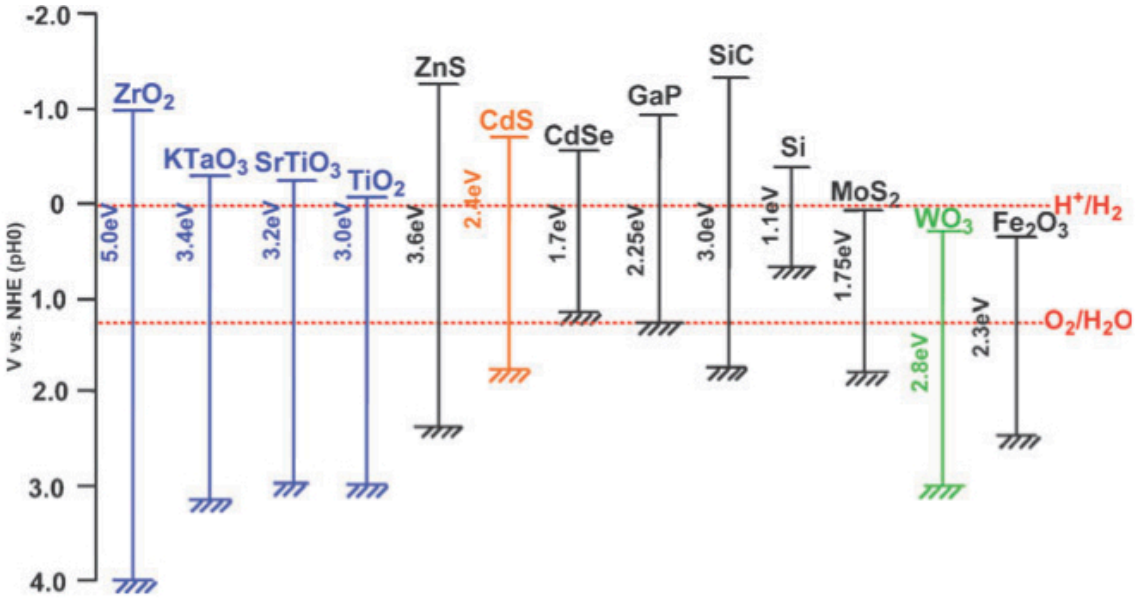

Figure 1.22 Band gap energy, and position of valence and conduction bands for a number of semiconductors on a potential scale (V) *versus* the normal hydrogen electrode (NHE). The potentials of hydrogen and oxygen generation from water are shown as an example. Reprinted from (Kudo and Miseki 2009) with permission from The Royal Society of Chemistry.

Of all the different semiconductors available, titanium dioxide is one of the most widely researched because it has a high photoactivity (under UV irradiation), is photostable, relatively inexpensive and abundant, and environmentally friendly (Hashimoto et al. 2005; Xu et al. 2014). However, one major drawback of TiO_2 is its relatively large band gap, at ≈ 3.2 eV (anatase). This means that it can only absorb photons from UV light or higher energies ($\lambda < 400$ nm; constituting only a small proportion of solar light). Since the electronic properties of a semiconductor (and therefore the absorption of photon energy, excitation of electrons, and the separation and migration of electrons and holes to the surface of the semiconductor) are dependent on the structural properties of the material, numerous studies have been conducted in an attempt to modify band

positions and band gaps, in an effort to improve photoactivity. Some of these strategies are discusses in the following section.

1.5.4. Strategies to improve photocatalytic performance

In principle, the photocatalytic performance of a material may be higher if there is greater light absorption or if charge carrier recombination is reduced. The following section describes some of the strategies that have been investigated, to improve photocatalytic performance of materials.

1.5.4.1. Metal and non-metal ion doping

Doping of semiconductor photocatalysts involves the incorporation of impurity atoms into the crystal structure of the material, to alter its electronic properties. Dopants may be metal or non-metal ions, and as discussed earlier, the valency of the dopant with respect to the semiconductor atom, determines whether it is n-type or p-type. Dopants can act as electron or hole traps, which can be beneficial since they may extend charge carrier lifetimes (Carp et al. 2004). The implication is that, a greater number of charge carriers may be available to participate in a photocatalytic reaction, and hence, the overall rate may be enhanced. For photocatalytic applications, doping, and in particular non-metal ion doping, has been intensively studied since Asahi et al. reported nitrogen doping of TiO_2 (Asahi et al. 2001). The authors reported that $TiO_{2-x}N_x$ showed band gap narrowing, extending light absorption to higher (visible light) wavelengths, with enhanced photoactivity over undoped TiO_2. Many non-metal ions have also been studied, showing similar effects with enhanced photocatalytic activity (over analogous undoped materials), for various applications. Metal ion dopants such as 3d transition metals, noble metals and lanthanides have also been investigated, and found to enhance photoactivity. However, it is also reported that metal ion dopants can act as charge recombination centres, lowering photocatalytic efficiency (Banerjee et al. 2014). In both cases, the origin of enhanced photoactivity, and how it relates to the presence of a dopant, is not always well understood, likely because a number of factors may contribute to such effects (Osterloh 2008; Liu et al. 2010).

The synthesis methods of doped materials are a key factor, since they may affect the overall structure (e.g. crystallinity, morphology, etc.) of the materials, and hence, their electronic properties. For example, Anpo et al. synthesised Cr-doped TiO_2 via ion implantation and impregnation. They found that the ion implantation method resulted in a red shift of the UV-visible absorbance profile of the samples, which increased as the Cr dopant concentration increased. However, the absorbance profile of Cr-doped TiO_2 prepared via impregnation, did not show the same red shift; rather, a new absorbance shoulder-like band was observed (Anpo 2003). The authors reported that only Cr-doped TiO_2 prepared via ion implantation was effective to increase the rate of photocatalytic decomposition of NO. Hence, this example may serve to highlight why it is important to have fine control over reaction conditions. Although there are many conflicting reports in the literature regarding doped photocatalysts, research within this area is developing, in an effort to further understand these materials and the unique properties they possess. It is hoped that this understanding will help to develop highly active photocatalysts, that may one day be viable for large scale commercialisation.

1.5.4.2. Optimising material properties

The physical properties of a material, in particular at the nanoscale, have a large impact on its photocatalytic activity. Such material properties include particle size and morphology, surface area and material quality (crystallinity/defects) (Djurišić et al. 2014). When particle size decreases, the corresponding surface area increases. In general, a larger surface area provides an increased number of active sites for adsorption and reactions to occur. However, materials with large surface areas are often associated with an increased number of crystalline defects, which can act as charge recombination centres (Carp et al. 2004). A compromise between surface area and crystallinity must be sought, in order to increase photocatalytic activity. If the particle size is reduced such that it is comparable to or smaller than the Bohr radius (exciton diameter), the excitons (electrons and holes) become spatially confined. They are not easily separated, and therefore they may be more susceptible to recombination. Additionally, quantum size effects are observed, where the band gap of a material begins to increase below a certain critical particle size. A blue shift in the absorbance profile occurs because energy levels

become discrete and are quantized. Such effects would be detrimental to the overall photocatalytic activity (Hernández-Alonso 2013).

The shape of nanoparticles may also influence photocatalytic activity, because certain crystal facets may be more reactive than others. If such facets were preferentially exposed, their available surface area would increase; consequently, an enhancement in activity may be expected. McLaren et al. investigated the shape and size effects of zinc oxide on photocatalytic activity (McLaren et al. 2009). They reported a method for tailoring the growth of zinc oxide nanoparticles along the $\langle 0001 \rangle$ direction, obtaining hexagonal plate-like crystals and hexagonal rods, at either extreme. The plate-like particles had larger terminal polar (001) and $(00\bar{1})$ faces, and displayed more than five times higher photoactivity than the rods (for the degradation of methylene blue dye). The results suggested that the polar faces were more active for photocatalysis, than the (100) and (101) non-polar surfaces perpendicular to them. Again, this example highlights the need for control over reaction parameters, such that material properties can be carefully tuned.

1.5.4.3. Coupling semiconductors: homo- or heterojunction photocatalysts

An alternative strategy to improving photocatalytic activity, which does not necessarily require a materials physical or electronic properties to be altered, is to couple two (or more) semiconductors together. These arrangements are described as homo- or heterojunctions, and are advantageous over single semiconductors because they can promote electron-hole separation, and keep oxidation and reduction reactions at physically separated sites (Liu et al. 2010; Jang et al. 2012). When two semiconductors are brought together, they form a junction at their interface, and can display interesting electronic properties, depending on the band properties of each semiconductor. If the semiconductors are made from similar material, they form a homojunction; if they are different materials, they form a heterojunction.

There are three main types of semiconductor-semiconductor heterojunction architectures, as shown in Figure 1.23. The following describes the positions of the CB and VB for each semiconductor, along with the direction of electron and hole transfer, when both semiconductors are irradiated. In a type I (straddling gap) heterojunction,

the CB of semiconductor B is more negative than that of A, and the VB of semiconductor B is more positive than that of A. In this scenario, electrons and holes migrate and from B to A, where they accumulate. Hence, there may be no improvement in charge carrier separation or photocatalytic activity (Marschall 2014). However, this type of junction is common, for example in a double heterojunction laser, which is composed of a layer of GaAs (semiconductor A) sandwiched between two layers of AlGaAs (semiconductor B). This confines charge carriers to GaAs (since it has the smaller bandgap), which means there are more electron-hole pairs available for laser amplification (Alferov 2000). In a type II (staggered gap) heterojunction, the CB of semiconductor B is more negative than the CB of A, and the VB of semiconductor A is more positive than the VB of B. Subsequently, an energy gap between the semiconductors is formed. This gap drives the charge carriers across the junction; electrons migrate from the more negative CB to the more positive CB, while holes migrate from the more positive VB to the more negative VB, i.e. electrons migrate from B to A, and holes migrate from A to B (Fresno 2013). This type of heterostructure promotes electron-hole separation, since the charge carriers are physically separated, and can lead to enhanced photocatalytic activity. A type III (broken gap) heterojunction is similar to a type II, except that there is no overlap between the bands of semiconductors A and B, and the difference in band positions is more pronounced.

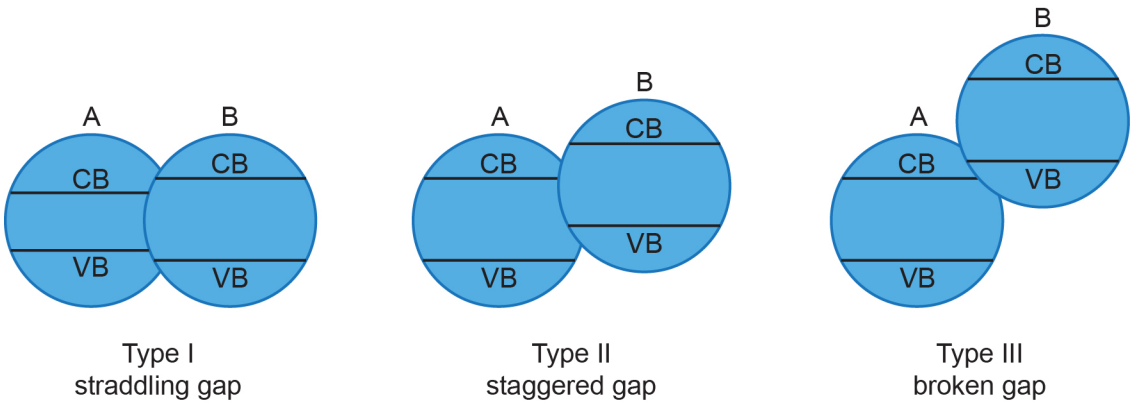

Figure 1.23 Schematic diagrams showing positions of the conduction (CB) and valence (VB) bands in type I, II and III semiconductor-semiconductor heterojunctions.

The most common heterojunctions in the literature are type II staggered gap junctions, particularly because this architecture promotes efficient charge separation. These types

of junctions were first described by Serpone et al. in 1984, for a CdS–TiO_2 system (Serpone et al. 1984). The authors investigated hydrogen evolution by decomposition of H_2S, by irradiating the heterojunction system with visible light ($\lambda > 400$ nm). Under visible light, only CdS (band gap = 2.4 eV) was able to generate excitons. They found that whilst CdS was able to directly reduce water to evolve hydrogen, electrons excited to the CB of CdS were also able to migrate to the CB of TiO_2 (and subsequently reduce water). Since this first report, type II heterojunction semiconductors have been extensively studied, which are highlighted in a number of recent reviews (Jang et al. 2012; Wang et al. 2013; Lee and Jang 2014; Yuan et al. 2014; Moniz et al. 2015).

p-n junctions (shown in Figure 1.24) are another form of type II semiconductor-semiconductor heterojunction, where the diffusion of electrons and holes creates a space-charge region at the interface. Electrons migrate to the CB of the n-type semiconductor, and holes migrate to the VB of the p-type semiconductor. An electrical potential develops, which directs electrons and holes in separate directions. The conventional silicon solar cell is an example of a p-n (homo)junction device, where the two semiconductors are made from doped silicon. One semiconductor is p-type silicon, whilst the other is n-type silicon (Chapin et al. 1954). Since the two doped structures of silicon have different electronic properties when they are coupled, an energy gap between the band levels is formed. Electrons migrate from the CB of p-type silicon to the CB of n-type silicon, whilst holes migrate from the VB of n-type silicon to the VB of p-type silicon. This effect promotes charge carrier separation.

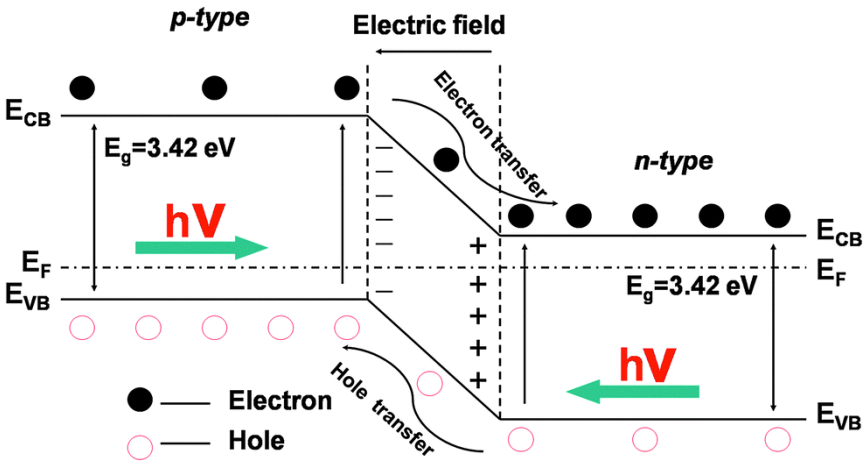

Figure 1.24 Schematic diagram of a type II p-n heterojunction, showing band structure, electron-hole separation and development of electrical potential at the interface. Reprinted from (Wang et al. 2014) with permission from The Royal Society of Chemistry.

As well as semiconductor-semiconductor heterojunctions, there also exists semiconductor-metal heterojunctions (Figure 1.25). Under irradiation, electrons migrate from the higher to lower Fermi level, to align the Fermi levels of the two materials. A space-charge region (called the Schottky barrier) forms at the interface. In a typical case, when metal particles are deposited on the surface of an n-type semiconductor (e.g. Pt particles on TiO_2), the electrons flow from the semiconductor to the metal. The metal behaves as an electron trap, thereby promoting charge separation. This type of system may also be described as photocatalytic enhancement via the use of a co-catalyst (e.g. Pt) on a semiconductor, which is common practice with many oxide photocatalysts (in particular, for water reduction, where the conduction bands of many metal oxides are not sufficiently negative to reduce water alone).

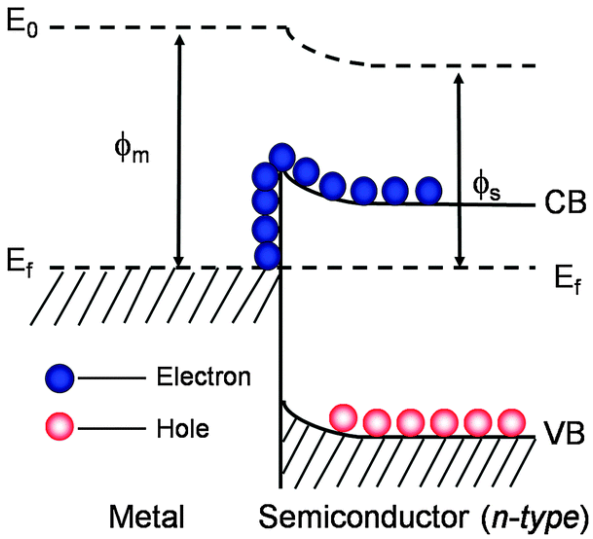

Figure 1.25 Schematic diagram of a semiconductor-metal heterojunction. Electrons are shown to transfer from the CB of the semiconductor to the Fermi level of the metal (a common case when an n-type semiconductor is used). Reprinted from (Wang et al. 2014) with permission from The Royal Society of Chemistry.

This section has served to highlight the benefits of coupling semiconductors together, enhancing charge separation and photocatalytic activity. By carefully selecting semiconductors that have complimentary and appropriate band positions (or Fermi levels, in the case of metals), with respect to each other and to the redox potentials of the reaction in question, it may be possible to exploit heterojunctions in a number of applications.

1.6. UV ATTENUATION

1.6.1. Protection from UV light

As discussed previously, sunlight is an abundant source of energy, which may be utilised on Earth for photo-driven catalytic applications. However, UV light is able to decompose and degrade organic compounds, which can discolour dyes and pigments, and may lead to loss of critical properties in polymers or plastics, such as mechanical strength (Zayat et al. 2007). In biological systems, such as humans, UV light can also cause erythema (redness, commonly known as sunburn), premature aging and cancers of the skin (Hacham et al. 1991). Thus, there is a need to provide protection against UV radiation (Juzeniene and Moan 2012), e.g. via the use of materials that are able to absorb, or attenuate, energies of UV wavelengths. Typically, these UV protecting materials can be organic or inorganic based, and under ideal conditions they would absorb all UV wavelengths, while remaining transparent in the visible region (Mahltig et al. 2005). Although there is no single material that exhibits this ideal behaviour, a number of organic compounds and inorganic materials are used in combination as sunscreens, either in cosmetics (for application on the skin) or on substrates, where they work to reduce exposure to harmful UV light.

1.6.2. UV absorbers and attenuators

Organic compounds that are used to provide protection against UV light, work by absorbing specific wavelengths of light. These compounds can provide absorption of UVA radiation (benzophenones and dibenzolymethanes) or UVB radiation (cinnamates, para-aminobenzoic acid, salicylates or camphor derivatives), and are typically used in combination to provide a broad UV absorption (Serpone et al. 2007). Whilst they are effective in reducing UV exposure, they are known to induce allergic reactions in humans when used in sunscreens (Wong and Orton 2011), and they also have the potential to degrade in the presence of light (Kockler et al. 2012). An alternative is to use inorganic materials, which work by scattering or reflecting UV and/or visible light. Inorganic materials typically have a lower potential for irritating skin (Serpone et al. 2007), and they can be used together to provide broad UV

attenuation (Smijs and Pavel 2011). Materials such as TiO_2 and ZnO have received a great deal of interest for use as UV attenuators, because they have suitable optical properties. Traditionally, these materials were used as micron-sized particles, which meant that sunscreens were opaque in appearance (because of visible light scattering) and therefore, they were not cosmetically acceptable. However, recent advances in synthesis of nanomaterials has made these materials commercially attractive, because smaller particles typically transmit in the visible region, giving them a transparent appearance (Smijs and Pavel 2011).

1.6.3. Applications of UV absorbers and attenuators

Beyond sunscreens, UV absorber or attenuator materials are widely used in many applications, which are often unnoticed because of their transparent appearance. Natural wood is susceptible to damage, because lignin (in wood) can absorb UV light, leading to radical induced depolymerisation of lignin and cellulose. Over time, the surface of wood can become rough and change colour, giving an undesirable appearance and physical breakdown of the surface. Therefore, wood coating products (e.g. varnishes) are available that contain ingredients to protect from UV damage (Aloui et al. 2007). In museums and galleries, artwork is often exposed to natural or artificial light for long periods of time. As a result, pigments in paint may fade and loose their colour. Since it may not always be possible to apply a coating directly to a painting (because of the risk of damaging the work permanently), one solution is to place the work in a glazing, such as glass or plastic. The glazing may be coated with a UV absorber or attenuator, which would be transparent to the eye but opaque to damaging UV radiation. Piegari and Polato reported a coating for glass glazing, that also reduced the reflectivity of the glass, thereby improving the view for the observer, compared to uncoated glass (Piegari and Polato 2003). In the automotive industry, plastic components are widely used (for example, fascia panels), which are exposed to solar light for very long periods. Therefore, coatings are applied either to the windscreen or window glass or directly to the plastic, that can provide protection against UV light (Morimoto et al. 1999).

These applications highlight the importance of protection against UV light in a number of different scenarios. Whilst there are a number of organic compounds that are used as UV absorbers, their drawbacks mean there is an emphasis to develop inorganic material UV attenuators. Since the size and morphology of particles affects their optical properties, continued advancements in synthesis strategies may be very beneficial.

1.7. HYPOTHESES

This introductory chapter has served to introduce subjects relevant to the overall outcomes of this thesis. Nanomaterial formation has been discussed, with an overview of syntheses using water as the reaction medium. Subsequently, this progressed to discuss continuous hydrothermal synthesis, where reactions are conducted in hot, pressurised water. Finally, a background introduction of photocatalysis and UV attenuation was given.

The hypotheses of this thesis can be described as follows:

i. To investigate the synthesis of titanium dioxide nanomaterials via continuous hydrothermal methods, for photocatalytic water splitting applications. The aim here is to determine whether doped titanium dioxide can be prepared (via CHFS), and the effects of reaction conditions on the materials properties (e.g. size, morphology, etc.). The materials will then be evaluated for their photocatalytic performance in water splitting, to evolve hydrogen in a sacrificial system. The results obtained here will allow correlations to be made between particle properties and photocatalytic performance, and to determine how such properties can be controlled via CHFS synthesis.
ii. To investigate synthesis of zinc oxide, following a mass-based scale up (i.e. increasing concentration), on a newly built mini-pilot scale CHFS reactor. The materials will be characterised to determine the effects of concentration scale up on material properties. The results of similar experiments at the pilot scale, are already presented in the literature, therefore, comparisons will be made to determine the scalability of CHFS zinc oxide synthesis. Changes in physical properties of the materials will be related to known mechanisms of zinc oxide formation.

iii. The synthesis of zinc oxide will be extended to evaluate the surface functionalisation of these materials, in a one-step process within the CHFS reactor. These experiments will be conducted using a novel mixing process, which allows the introduction of an additional reagent feed after nanoparticles have formed. In these experiments, the additional feed will consist of surface functionalising agents. Experiments will also be conducted to determine whether zinc oxide particle sizes can be reduced via a new CHFS approach (literature reports suggest zinc oxide in a CHFS process is typically larger than 50 nm). Zinc oxide nanomaterials will be evaluated for their ability to act as UV attenuators.

iv. To investigate the preparation of heterojunction semiconductors via a simple powder pressing technique. Semiconductor powders will be pressed together to form ceramic wafers, and their properties will be characterised. The wafers will be investigated for their ability to enhance the rate of photocatalytic reactions, in particular, degradation of organic compounds and disinfection of water.

In summary, this thesis will explore the synthesis of semiconductor nanomaterials via a continuous hydrothermal method, and investigate the effects of changing reaction conditions on particle properties. Materials will be evaluated for their performance in a number of photocatalytic tests. It is hoped that, through the work presented in this thesis, the benefits of CHFS synthesis of nanomaterials and applications of such materials in heterojunctions for photocatalysis will be realised, opening up new research avenues for future development.

Chapter 2. Experimental methods

2.1. INTRODUCTION

This chapter discusses the experimental techniques that have been used throughout the work presented in this thesis. A description of the continuous hydrothermal flow synthesis (CHFS) reactor is given at two process scales, followed by an overview of synthesis methodologies and sample processing, and materials characterisation techniques. The aim of this chapter is to give an account of the common techniques that have been applied throughout the thesis work. However, each chapter contains a description of the materials synthesis and testing relevant to the work contained within that chapter.

2.2. CONTINUOUS HYDROTHERMAL FLOW SYNTHESIS (CHFS)

Professor J. A. Darr and Dr P. Boldrin first built the CHFS process in the Clean Materials Technology Group (CMTG) at Queen Mary, University of London, in 2003 (Boldrin 2008). Since then, the process has undergone many modifications, as described in Chapter 1 and in the works of others (Gruar 2012). The following sections provide an account of the process as it was used in this work, and the modifications that were carried out during, and for, the work described in this thesis.

2.2.1. Mini-pilot scale reactor design

The mini-pilot scale reactor was built in collaboration with Dr Robert Gruar, where I was involved in the construction and commissioning of the process. The reactor was a scale-up of the older laboratory scale process that was the first scale of the CHFS process in the CMTG. In summary, the laboratory scale reactor had a total output of approximately 50 mL min^{-1} of nanoparticle slurry, typically producing a few grams of material per day. The aim of the new lab-scale process (hereafter referred to as mini-pilot scale reactor) was to increase nanoparticle production up to 100 grams of material

per day, by increasing the volumetric (up to 320 mL min^{-1}) and mass (by using higher precursor concentrations) output of the CHFS process.

A schematic diagram of the mini-pilot scale reactor in a three-pump configuration is provided in Figure 2.1 (a photograph is shown in Figure 2.2). The process was constructed from Swagelok 316L stainless steel seamless tubing and fittings, ranging from sizes ⅛″ to ¾″. This design meant that maintenance of the system was easier as specialist fittings (i.e. custom made) were not required.

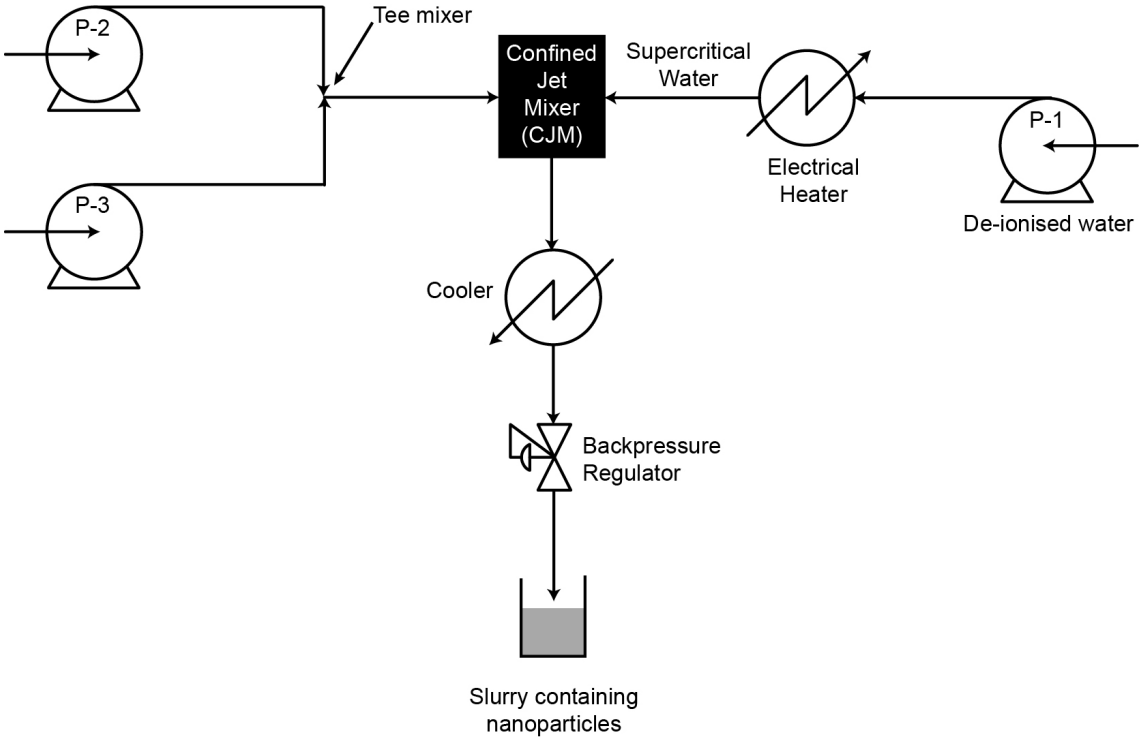

Figure 2.1 Schematic diagram of the laboratory scale reactor in a three-pump configuration.

Each pump (Milton Roy model PrimeRoyale K) was configured to provide an independent feed of water or chemical precursor to the CHFS process, which allowed each feed to be modified (for example, in terms of concentration, flow rate or additive), independently of each other. This allowed the reactor to be operated in a high-throughput nature, with the possibility of synthesising a large number of samples, at a range of different conditions during a given experimental run.

Each pump was connected to two storage vessels; one being a 100 litre tank which was connected in series to each pump, and a second being 1-litre conical vessels, which were

connected to each pump independently. For each pump, the storage vessels were piped with ½″ tubing (and ¼″ tubing for the 1-litre conical vessels) to a three-way ball valve, which allowed the selection of feed from either vessel to the pump. Each feed line then connected to a pulsation dampener (Pipehugger Phr-TW; Liquid Dynamics, Stockport, UK), pressure relief valve (Parker HPRV; relief pressure 276 bar), pressure gauge and non-return valve assembly before feeding into the reactor system. The role of the pulsation dampener was to reduce pulsations occurring in flow from the pumps. The pressure relief valves ensured pressure did not exceed 276 bar in the reactor in occurrence of a pipe blockage, while the pressure gauges allowed independent monitoring of the pressure within each feed line. The non-return valve assembly (assembled from Swagelok fittings) was used to prevent backflow in the event of pump failure. Pump P-1 was used exclusively to feed deionised water (> 10 MΩ resistivity) through an electrical heater (custom built and described in section 2.2.2), before entering the reactor mixing point. Pumps P-2 and P-3 were typically used to feed aqueous metal ion and auxiliary reagents (e.g. base), respectively, at ambient temperature, which premixed in a tee-piece prior to entering the reactor mixing point. In the mixing point (described in section 2.2.4), the feed of hot, pressurised water (from P-1) was mixed with the flow of premixed reagents (from P-2 and P-3). The products of reaction from the mixing point then flowed through a pipe-in-pipe heat exchanger, which rapidly reduced the temperature of the mixture to less than 50 °C. Finally, the mixture passed through a back-pressure regulator (BPR; Tescom model 26-1762-24-194, obtained from Emerson Process Management Regulator Technologies, Inc., South Lanarkshire, UK), which was responsible for maintaining reactor pressure at 240 bar, before being collected in an appropriate vessel.

2.2.2. Heater design

The deionised water feed from P-1 passed through a custom-built electrical heater, to pre-heat the feed up to 450 °C under a pressure of 240 bar. The design of the heater was similar to that previously used in the CMTG for the laboratory scale reactor. Some components of the electrical heater are shown in Figure 2.3.

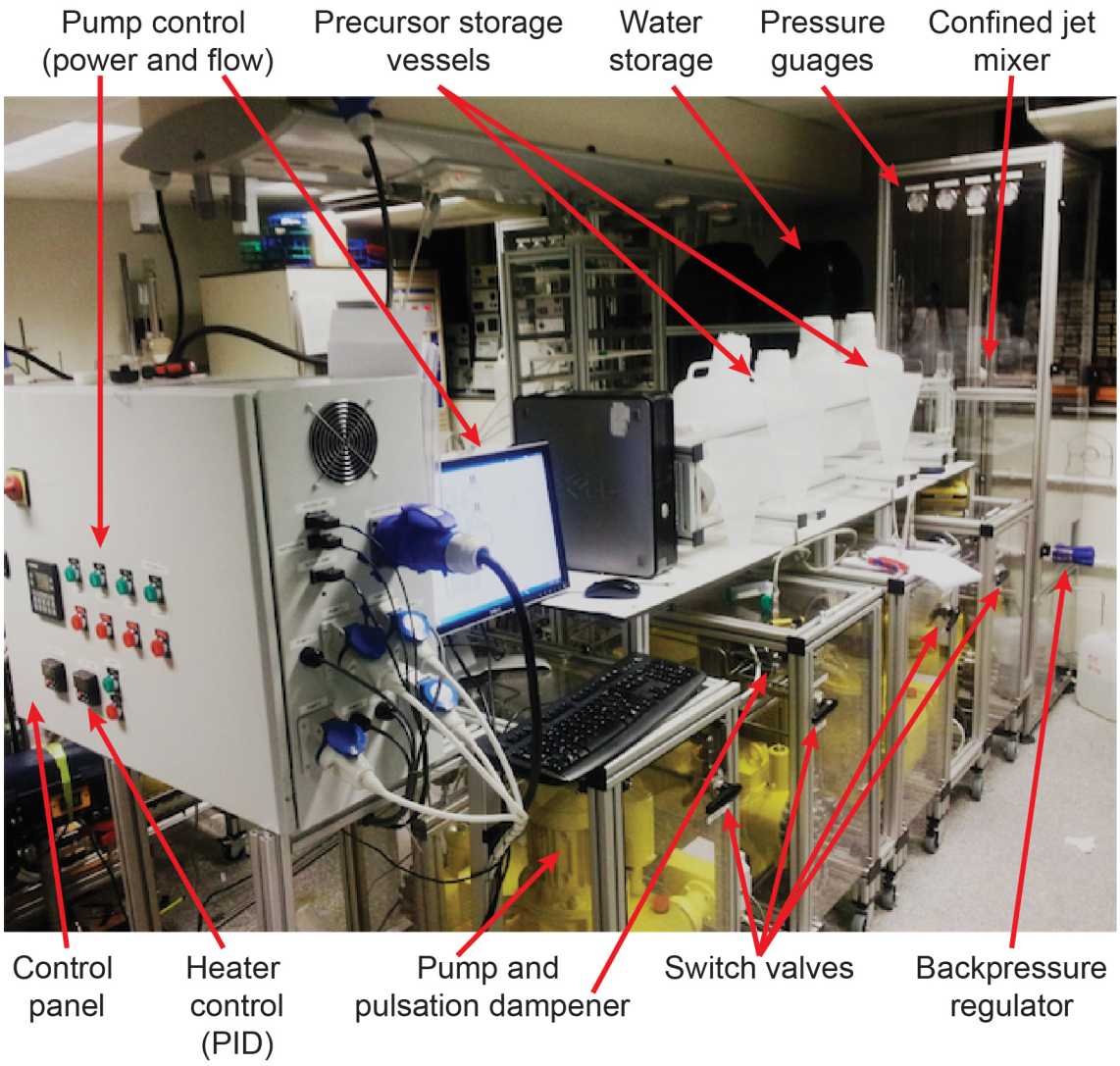

Figure 2.2 Annotated photograph of the mini-pilot scale CHFS process.

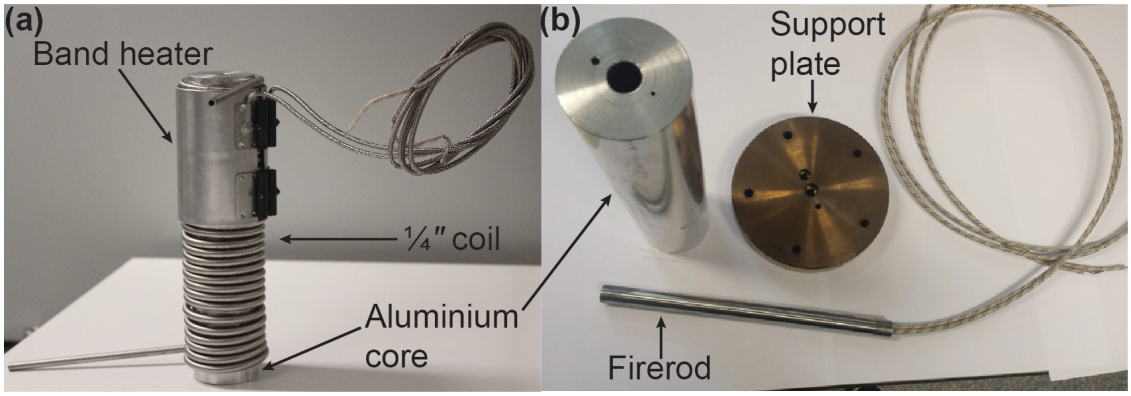

Figure 2.3 Heater construction showing (a) the ¼" stainless steel coil wrapped around an aluminium core, with a band heater placed over the coil, and (b) a typical Watlow firerod that was inserted within the aluminium core and held in place with support plates.

The heater consisted of a 9¼″ (length) by 2″ (diameter) aluminium core with a ½″ diameter hole bored in the centre to a depth of 8″. A 6 metre length of ¼″ stainless steel tubing was coiled tightly around the aluminium core, to ensure sufficient contact between the coil and the core. A ½″ 2000 W cartridge heater (Firerod J8A–15210, Watlow) was inserted in to the aluminium core, and 3 × 500 W band heaters (Mineral Insulated Band Heater MB2J1JN1–E60, Watlow) were placed around the coil. The entire heater was insulated in a microtherm flexible insulating quilt (RS Components) and high temperature ceramic blanket insulation. Two heaters with a combined power output of 7 kW were connected in series. A J type thermocouple in the bottom of one heater allowed the internal temperature of the heater to be monitored, with an alarm function on the control unit programmed to terminate electrical power if the temperature exceeded 460 °C. A second thermocouple, placed in a tee-piece (perpendicular to the flow of water) beyond the output of the second heater, was used to monitor the temperature of the water and automatically control power to the heaters.

2.2.2.1. Modified heater design

It was found after a small number of heating – cooling cycles, heater failure began to occur, resulting in electrical fuse blowout and loss of power. Inspection of the heater assembly revealed the outer protective sheath of the cartridge heater leads had frayed and exposed the internal wiring, leading to a short-circuit (shown in Figure 2.4).

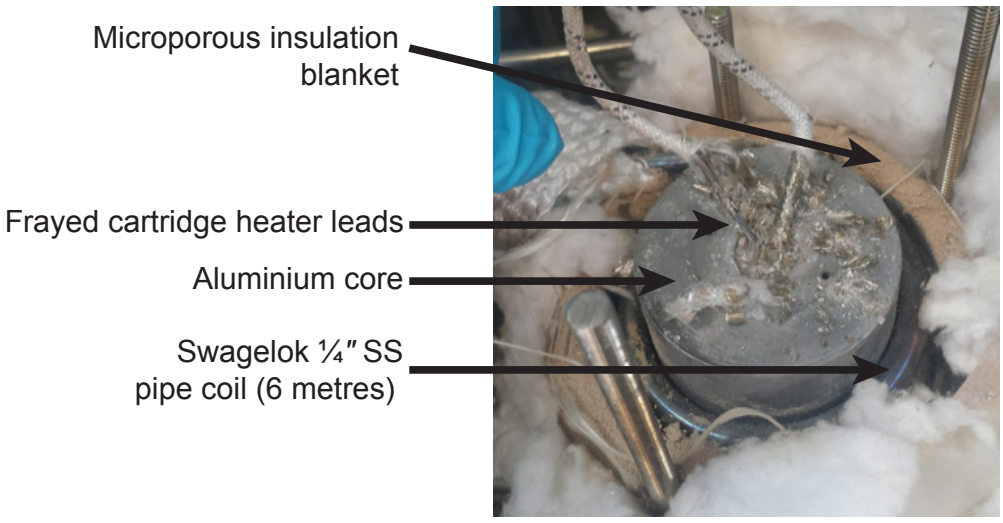

Figure 2.4 Photograph to show frayed cartridge heater leads that resulted in heater failure.

The electrical leads of the cartridge and band heaters were encased in high temperature fibreglass rated to 450 °C. It was likely that through conduction the leads were being heated, to a point where the fibreglass began to fray and internal wiring was exposed. The fibreglass leads were used previously in the smaller scale CHFS laboratory systems where they did not present an issue, but the cartridge heaters operated at lower power (1000 W) and consequently had a lower watt density.

To prevent heater failure, ⅝″ diameter 2000 W cartridge heaters (Firerod L8A80–L10J48T, Watlow; the hole in the aluminium core was widened to ⅝″ diameter) were used, where the internal wiring was encased in mineral insulation rated to 815 °C. The larger diameter was required since the maximum permissible current in ½″ diameter cartridge heaters was 7 amps; 2000 W drew 8 amps and hence, the diameter was increased. The heater support plates were modified, such that the mineral insulated leads were able to pass vertically through the plates before the Teflon leads were connected to heater power.

2.2.3. Pilot scale reactor design

The pilot scale process was designed and built by Dr Robert Gruar, Dr Christopher Tighe and Professor Jawwad Darr, and operated in a similar manner to the mini-pilot scale process, albeit on a larger scale. Typically, the pilot scale process operated at up to 800 mL min^{-1}, with the capability to produce a kg of material per hour, significantly scaling up synthesis over any previous CHFS process. Like the mini-pilot scale process, the pilot scale process was constructed from Swagelok 316L stainless steel seamless tubing and fittings, the dimensions of which are provided in Table 2.1. Full details of the process can be found in the literature and relevant supplementary information (Gruar et al. 2013).

2.2.4. Confined Jet Mixer (CJM)

The mixing point of the CHFS process was where chemical precursors were mixed with hot, pressurised water. In this work, a co-current reaction point configuration was used on both the mini-pilot and pilot scale processes. The patented co-current reaction point (hereafter referred to as confined jet mixer, CJM), which was designed and evaluated by

Professor Jawwad Darr, Dr Christopher Tighe and Dr Robert Gruar (Darr et al. 2011), introduced the precursors and hot water in a co-axial geometry (shown in Figure 2.5). The products of reaction were carried away from the CJM in an upward direction, towards the heat exchanger. Across all CHFS process scales, the CJMs were constructed in an identical manner but with different tubing and fitting sizes (summarised in Table 2.1). In general, the feed issuing from the heaters was passed upward into a cross union by means of a bored-through union fitting, and terminated above the precursor inlet annuli. The pre-mixed precursor feed was fed in to the cross union symmetrically, through the inlets perpendicular to the hot water inlet. Tubing was connected to the cross union which allowed the reaction products to flow towards the heat exchanger.

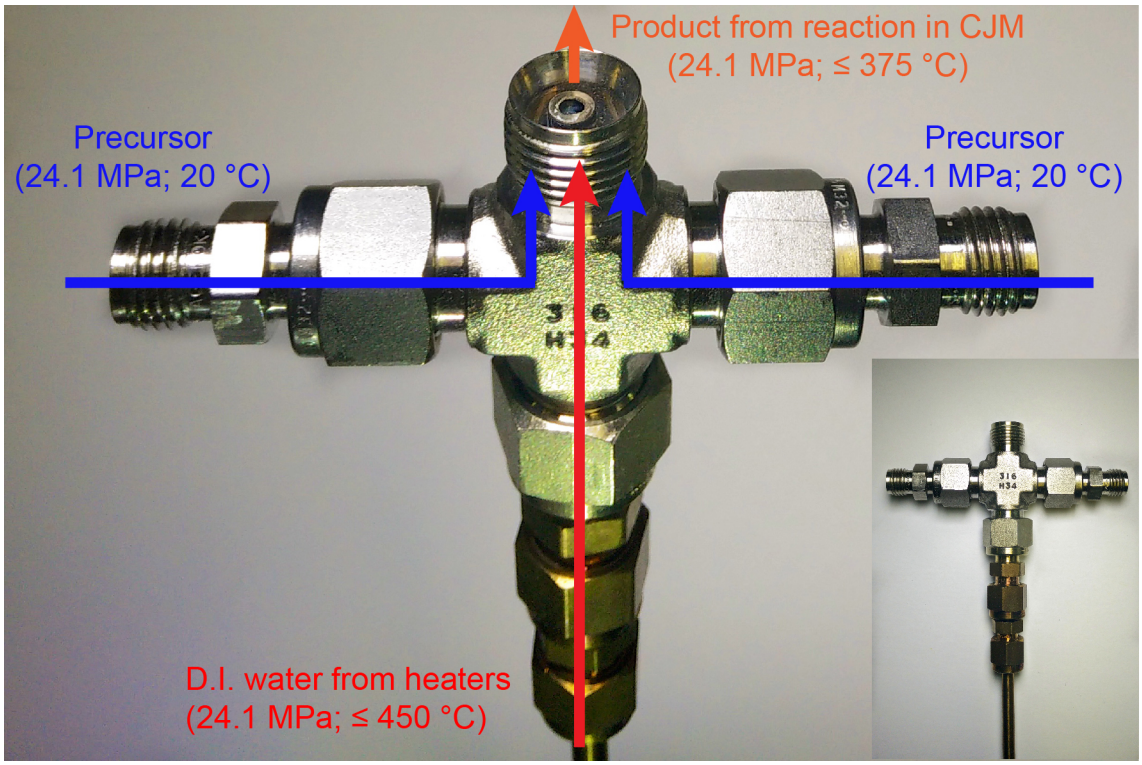

Figure 2.5 Annotated photograph of a typical confined jet mixer (CJM) showing the flows of hot, pressurised water, ambient temperature precursors and product stream issuing from the CJM. The inset photograph shows a side view of the CJM.

2.2.4.1. Single confined jet mixer arrangement

In a three-pump configuration, the CHFS process (at the mini-pilot and pilot scale) was fitted with a single CJM (Figure 2.7(a)). This configuration allowed the synthesis of a

range of materials, where it was possible to vary a number of process parameters and investigate the effects on material properties.

2.2.4.2. Double confined jet mixer arrangement

A modification to the mini-pilot scale process was made, to allow the addition of a fourth pump, where its feed entered the process at a point immediately following the reaction point (Figure 2.6). The feed from fourth pump was introduced to the process through a second CJM (CJM-2), that was placed directly above the first CJM (CJM-1); see Figure 2.7(b). The outlet (product stream) from CJM-1 formed the inlet of CJM-2, with the feed from pump P-4 fed in to the cross union (of CJM-2) symmetrically, through the inlets perpendicular to the product stream inlet. The products issuing from CJM-2 then passed to the pipe-in-pipe heat exchanger, before being collected.

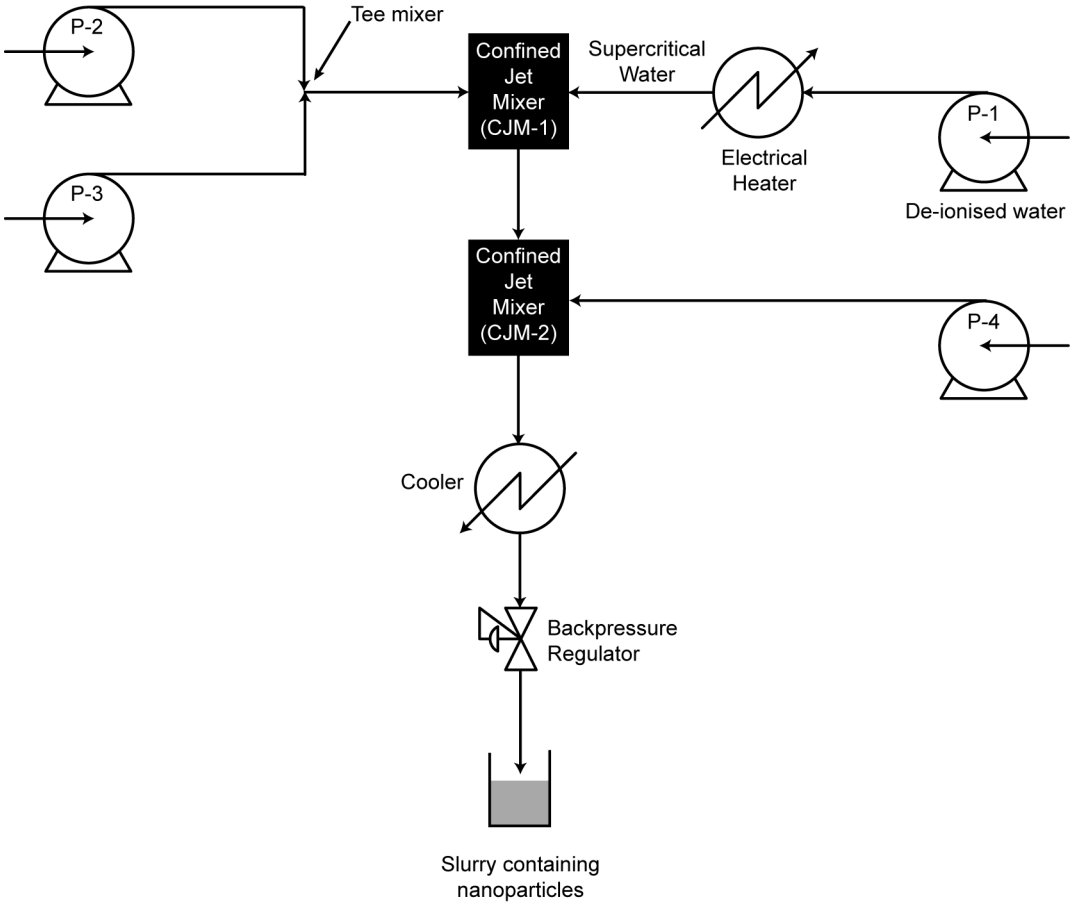

Figure 2.6 Schematic diagram of the laboratory scale reactor in a double confined jet mixer, four-pump configuration.

This configuration allowed the addition of additives to the process, after the initial nanoparticle formation occurred in CJM-1. Since the feed from P-4 was at ambient temperature, the temperature of the product stream from CJM-1 was lowered as it met the additive feed in CJM-2 (in addition to being lowered via convection). This meant that it was possible to add organic-based reagents, which may have otherwise been unstable at the higher temperature typically encountered in CJM-1.

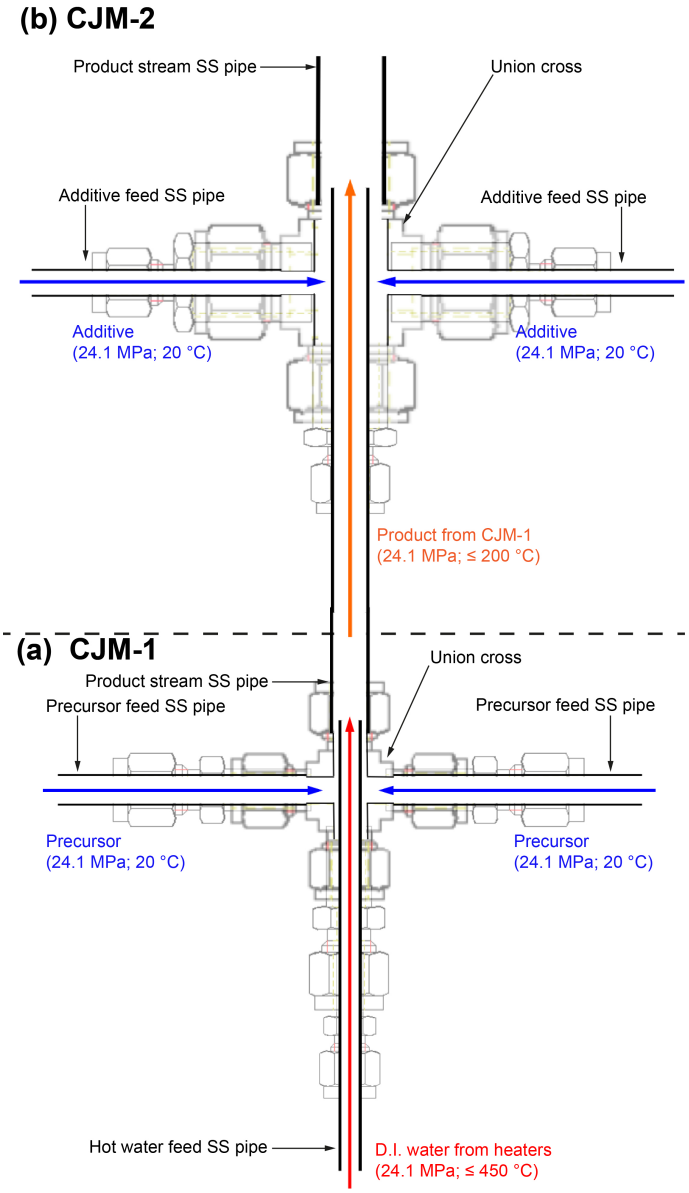

Figure 2.7 Schematic diagram of confined jet mixers (a) CJM-1 used at the mini-pilot and pilot scale for nanoparticle synthesis and (b) CJM-2 used at the mini-pilot scale for addition of an additive to a product stream. The dashed line is provided for clarity only to show the distinction between the two mixers. In the single CJM arrangement only CJM-1 was used; in this case the product steam flowed directly to the pipe-in-pipe heat exchanger (not shown).

2.2.4.3. Confined jet mixer dimensions

The confined jet mixers used in the mini-pilot (single and double arrangement) and pilot scale processes (Figure 2.7) had the same basic design but differed in dimensions of fittings and tubing. Table 2.1 provides the dimensions relevant to the work presented in this thesis. In all configurations, the product stream consisted of ⅜″ diameter tubing. Since the union cross for CJM-2 (mini-pilot scale) and CJM-1 (pilot scale) was ¾″, it was necessary to use a reducer fitting after the union cross, to allow the diameter to be reduced from ¾″→⅜″, as indicated in Table 2.1.

Table 2.1 Dimensions of tubing and fittings for confined jet mixers at different process scales.

Process scale	**Mixer**	**Component**			
		Hot water/inlet feed	**Precursor/additive feed**	**Union cross**	**Product stream**
Mini-pilot	CJM-1	3/16″	¼″	⅜″	⅜″
	CJM-2	⅜″	¼″	¾″	¾″→⅜″
Pilot	CJM-1	¼″	¼″	¾″	¾″→⅜″

2.2.5. Materials synthesis

A typical CHFS synthesis consisted of a number of individual runs, in which various parameters were modified to investigate the effects of reaction parameters on the material properties. Reaction parameters included composition and concentration of precursor, concentration ratio of precursors, flow rates, heater temperature, and, in the case of the four pump double CJM configuration, the composition, concentration and flow rate of the additive. At the beginning of each synthesis, pre start-up checks were conducted to ensure the CHFS process was within specification for the flow rates and safe to operate, and that there was sufficient supply of water and storage for products and waste. Following the pre start-up checks, the CHFS process was powered to begin the start-up procedure. Each pump was allowed to prime at ambient pressure for 5 minutes, before pressurising the system via the backpressure regulator. Under system

pressure, the total output flow rate was measured to ensure correct calibration (each pump was calibrated if necessary), and each fitting was inspected for leakage. Once these checks were completed, power to the heaters was established; the PID controlled the heating cycle. When the desired temperature was reached, precursor solutions were placed in the conical storage vessels, and the relevant three-way valves were switched to allow the pumps to draw from the conical precursor storage vessels. When the product was collected at the outlet of the CHFS process, the three-way valves were switched back to the water storage tank to flush out each feed line and the reactor tubing with water. The procedure was then repeated as necessary to collect remaining samples. As a precaution, to prevent contamination, products were collected from the outlet approximately two minutes after the first appearance of the slurry at the outlet point.

2.2.6. Sample processing

Each sample was collected as a nanoparticle-laden slurry that was allowed to settle over a period up to 12 hours; the supernatant layer was then decanted. If the quantity of settled nanoparticles was less than 100 mL, they were transferred to centrifuge tubes for cleaning. The samples were centrifuged at 4500 rpm for 5 minutes on a Sigma 4K15 centrifuge fitted with a rotor containing four buckets, each with a capacity of 7 × 50 mL centrifuge tubes. The supernatant was replaced with deionised water before re-suspending the sample using a VWR VM-3000 vortex mixer. This process was repeated a minimum of three times until the conductivity of the supernatant gave a reading below 50 μS. The material was then freeze-dried. For quantities greater than 100 mL, the samples were transferred to dialysis membranes with an appropriate molecular weight cut-off. The membranes were sealed and placed in an appropriate vessel containing deionised water. The vessel was stirred continuously to ensure sufficient transfer of ions was achieved rapidly. The conductivity of the water was monitored and it was replaced at regular intervals. When the measurement remained stable at below 500 μS, the samples were removed from the dialysis membranes and centrifuged to consolidate the material, which was then freeze-dried.

2.2.6.1. Freeze drying

Cleaned samples were freeze dried to obtain dry powders for characterisation. Samples were placed in centrifuge tubes and covered with Parafilm M®. Small perforations were made in the covering to facilitate water removal during the sublimation stage. The tubes were placed in trays in a Virtis Genesis 35XL freeze drier, and were frozen to –40 °C with a condenser compartment cooled to –60 °C. Freeze drying was conducted under vacuum (1.3×10^{-7} MPa), typically for a period of 22 hours.

2.3. MATERIALS CHARACTERISATION TECHNIQUES

The following section details the materials characterisation techniques that have been applied throughout the work in this thesis. Where more than one approach was used for a particular technique, the chapters to which each approach refers to, is identified.

2.3.1. Powder X-ray diffraction (XRD)

Powder X-ray diffraction was used to determine the phase composition of each sample. XRD patterns presented in Chapter 3 were obtained on a Bruker D4 Endeavor diffractometer using Cu-Kα radiation (λ = 1.541 Å), over the 2θ range 10 – 80° with a step size of 0.05° and a count time of 2 s per step. Samples were ground to obtain a fine powder that was mounted in a PMMA flat-plate specimen holder. The Bruker D4 instrument was fitted with a 64-position sample auto-changer, to enable high-throughput data collection.

Diffraction data presented in Chapters 4, 5 and 6 were collected on a Stoe Stadi P diffractometer using Mo-Kα radiation (λ = 0.709 Å) in transmission geometry, over the 2θ range 2 – 40° with a step size of 0.5° and a count time of 5 s per step. Powder samples were mounted within transparent films for analysis.

The phase composition was identified by comparison of collected patterns to standard reference patterns available in the Joint Committee on Powder Diffraction Standards (JCPDS) database or the Inorganic Crystal Structure Database (ICSD), found within the Diffrac^{plus} Eva™ software. For selected samples, the crystallite size was estimated from given reflections using the Scherrer equation:

$$d = \frac{K \times \lambda}{\beta \times cos\theta} \quad \text{(Equation 1.1)}$$

where d is the crystallite size (nm), K the Scherrer constant (0.9), λ the wavelength of incident radiation, β the width of the peak (FWHM) and θ the Bragg angle of the peak.

2.3.2. Brunauer-Emmett-Teller (BET) surface analysis

Brunauer–Emmett–Teller (BET) surface area measurements were carried out (using N_2 gas adsorption) in a Micrometrics ASAP 2420 instrument. Powder samples were degassed under vacuum at 150 °C for 12 h, weighed, and then adsorption isotherms were measured. The crystallite size was estimated using the BET equivalent sphere diameter approximation:

$$ESD\ (nm) = \frac{6000}{SA_{BET} \times \rho} \quad \text{(Equation 1.2)}$$

where ESD is the equivalent sphere diameter (nm), SA_{BET} the BET surface area ($m^2\ g^{-1}$) and ρ the density of the sample ($g\ cm^{-3}$).

2.3.3. Raman Spectroscopy

Raman spectra were obtained on a Raman microscope system (Renishaw inVia™) with a laser (Ar^+) excitation wavelength of 514.5 nm. The Raman microscope was calibrated against silicon at 520 cm^{-1}. The output laser power was 100 % (80 mW) and each scan was performed for 10 seconds at a spectral resolution of 1 cm^{-1}.

2.3.4. Infrared (IR) spectroscopy

FTIR spectra were recorded on a PerkinElmer Spectrum RXI (with Spectrum v5.3.1 software) in transmission geometry. Spectra were obtained over the wavenumber range 4000 – 400 cm^{-1}, with 64 scans and a spectral resolution of 4 cm^{-1}.

2.3.5. Dynamic light scattering (DLS)

DLS measurements were conducted on a Malvern Zetasizer Nano (ZEN3600). Samples were prepared as described in the text (Chapter 5). Samples were diluted with solvent to 0.1 wt% and placed in disposable cuvettes with a nominal path length of 1 cm. Each measurement was conducted using a backscatter geometry and the intensity of light scattered by the sample was measured at an angle of 173°. Measurements of hydrodynamic diameter are given as an average of 25 measurements of 10 s duration each. Measurements were recorded as the average hydrodynamic diameter and measured polydispersity.

2.3.6. Electron microscopy

Selected samples were analysed by transmission, high-resolution and scanning electron microscopy, as described. In all cases, particle analysis was conducted using ImageJ software (version 1.48v; http://imagej.nih.gov/ij/).

Samples were prepared for TEM by dispersing the particles via ultrasonication in methanol, for approximately 5 minutes. A few drops of the resulting solution were pipetted onto carbon film grids (300 mesh; Agar Scientific, UK), and the solvent allowed to evaporate, prior to imaging.

2.3.6.1. Transmission electron microscopy (TEM)

Transmission electron microscopy (TEM) images presented in Chapter 4 were obtained on a JEOL 100cx microscope (100 keV accelerating voltage) equipped with a CCD camera (GATAN) for digital imaging.

2.3.6.2. High-resolution transmission electron microscopy (HR-TEM)

High-resolution transmission electron microscopy (HR-TEM) images presented in Chapter 3 were obtained using a Philips CM200 FEG HR-TEM (200 keV accelerating voltage) at the Leeds EPSRC Nanoscience and Nanotechnology Research Equipment Facility at University of Leeds (funded by EPSRC Grant EP/F056311/1).

HR-TEM images in Chapter 5 were obtained on a JEOL JEM-2100 TEM (200 keV accelerating voltage) equipped with a CCD camera (GATAN) for digital imaging. Energy dispersive X-ray spectroscopy (EDX) was conducted on the JEOL JEM-2100 TEM fitted with an Oxford Instruments X-Max^N 80 T Silicon Drift Detector (SDD). Analysis was conducted using the AztecTEM software.

2.3.6.3. Scanning electron microscopy (SEM)

Field emission scanning electron microscopy (FE-SEM) images were obtained on a JEOL JSM-6700F microscope (5 keV accelerating voltage). Powder samples were gold coated prior to imaging, using a sputter coater fitted with a gold target. Alternatively, suspensions of samples (already dispersed in water) were mixed with 50 vol% methanol and drop-coated on to fragments of silicon wafers. The solvent was allowed to dry, leaving a thin film on the silicon wafers for imaging.

2.3.7. UV-Visible absorption spectroscopy

UV-visible absorption spectra presented in Chapter 3 were obtained using a deuterium-tungsten halogen light source, an optical fibre assembly and a USB 2000+ UV-vis spectrometer, all supplied by Ocean Optics (Florida, USA). Data was collected using *SpectraSuite*™ software.

UV-Visible spectra presented in Chapter 5 were obtained using a PerkinElmer Lambda 950 UV/Vis/NIR spectrophotometer. Samples were measured as dry powders, coatings or dispersions. Dry powders were measured using an integrating sphere setup. As dispersions, powders were dispersed in water at 0.02 wt% and sonicated for 10 minutes. Absorbance was measured using a UV optical glass cuvette (1 cm path length).

2.3.8. X-ray photoelectron spectroscopy (XPS)

X-ray photoelectron spectroscopy (XPS) measurements were collected using a Thermo Scientific™ K-Alpha™+ spectrometer, using Al-K_α radiation with constant pass energy of 50 eV. Data was analysed using CasaXPS™ software (version 2.3.16).

Chapter 3. Pilot plant scale continuous hydrothermal synthesis of nano-titania; effect of size on photocatalytic activity

3.1. AIMS AND OUTLINE

The aim of this chapter was to investigate the synthesis of nano-TiO_2 via CHFS with the addition of additives, to induce doping and/or effects on nanoparticle size and surface area. In photocatalysis, such effects have been widely studied, however there are limited reports of such investigations via CHFS. The TiO_2 samples were characterised by a range of techniques, and assessed for their ability to photocatalytically evolve hydrogen from water, in a sacrificial system.

3.2. INTRODUCTION

The need for a clean, safe, and abundant energy source as an alternative to fossil fuels is one of the major challenges facing the current generation. Solar energy is widely accepted as one of the most attractive future contributors towards the ever-increasing global demand for energy. However, solar energy is diurnal, intermittent, and can vary in intensity from day-to-day, and electrical energy is not, at present, stored widely in domestic homes in large amounts. This highlights the need for a technology that harnesses the abundance of sunlight, to produce a fuel (energy source) that can be stored and is available when it is required most, potentially locally. One solution is the use of hydrogen as a fuel for energy production, which is sustainable as its combustion yields only water. The majority of hydrogen is currently produced by steam reforming, which is both costly and environmentally harmful, with CO_2 produced as a by-product. An alternative strategy for the production of hydrogen is to use a photocatalytic water splitting process that converts solar to chemical energy, by separating hydrogen (and oxygen) from water (Equation 3.1):

$$H_2O \rightarrow H_2 + \tfrac{1}{2}O_2 \qquad \Delta G = +237 \text{ kJ mol}^{-1} \qquad \text{(Equation 3.1)}$$

One of the most popular photocatalysts for this process is titanium dioxide (TiO_2), which is highly stable, non-toxic and cheap to produce. These properties have made it one of the most widely studied photocatalytic materials for a range of applications such as air and water purification (Mills et al. 1993), self-cleaning glass (Mills et al. 2003), and photodegradation of organic pollutants (Chatterjee and Dasgupta 2005). Titanium dioxide, in its anatase polymorph, has a band-gap of approximately 3.2 eV, allowing it to absorb photons of wavelengths $\lambda < 400$ nm, corresponding to the ultraviolet (UV) portion of light and higher energy photons. This is a drawback since the solar radiation that reaches the Earth's atmosphere consists of ca. 6 % UV and 52 % visible light (with the remainder largely consisting of infrared radiation), leading to very low maximum photocatalytic efficiencies for UV absorbing photocatalysts. A common strategy to achieve photocatalysis under visible light is to attempt band engineering of wide band gap semiconductors (such as TiO_2) through the introduction of dopant (metal or non-metal) ions into the semiconductor lattice. Non-metal ion dopants can create an upward shift of the valence band edge, narrowing the band gap and shifting the light absorption into the visible region (Ni et al. 2007). TiO_2 doped with anions such as nitrogen (Asahi et al. 2001; Livraghi et al. 2008; Dunnill and Parkin 2011; Hu et al. 2011), sulphur (Umebayashi et al. 2002; Dunnill et al. 2009; Dunnill et al. 2010), and boron (Begum et al. 2008; Lu et al. 2008; Grabowska et al. 2009; Lu et al. 2010; Carmichael et al. 2013) have shown enhancement in photocatalytic activity under UV and/or visible light; however, the long term stability of these dopants is often in question.

In addition to metal or non-metal doping, the crystallite size, morphology, phase composition and the presence of exposed facets, can significantly affect overall photocatalytic efficiency and activity (Li and Liu 2011). Therefore, the relationship between nanoparticle synthesis conditions for semiconductors and their effect on particle properties, and consequently photoactivity, are of utmost importance. In some common synthesis routes it is often difficult to demonstrate a high degree of particle size control, since reactions may be slow or require high temperatures, which can give poorly defined products. Additionally, in some synthesis processes, there may be a need to post-treat materials, which can result in uncontrolled particle growth or agglomeration and a loss of surface area. Therefore, methods that can offer well-defined

nanoparticles are of interest to be able to better understand structure-composition-property relationships.

Continuous hydrothermal flow synthesis (CHFS) offers a rapid way of preparing nanoceramics in a single-step process with well-defined properties. The process also offers potential as a high-throughput method (Weng et al. 2009a; Parker et al. 2010; Quesada-Cabrera et al. 2013) in which many unique samples can be rapidly generated in a short time, previously demonstrated in the synthesis of doped nanomaterials (Weng et al. 2009b; Goodall et al. 2015). Furthermore by virtue of being a continuous process, it is also scalable, as has been shown in recent literature (Gruar et al. 2013; Tighe et al. 2013). The CHFS process mixes aqueous metal salts (mixed with other reagents such as pH modifiers in flow) with a stream of supercritical water in an engineered confined jet mixer, which is described earlier in Chapter 2. Upon mixing with the superheated water, the metal salt(s) in the reagents experience a sudden change in conditions, resulting in rapid hydrolysis and dehydration, resulting in crystallisation of nanomaterials, typically as oxides. The nanoparticle slurry is then cooled to room temperature in flow before being collected at the exit of the process (after a backpressure regulator, BPR, which maintains pressure in the system). By altering synthesis conditions in the confined jet mixer, it is possible to achieve some control over particle properties e.g. crystallite size, morphology, surface area, faceted growth etc., (Gruar et al. 2013; Shi et al. 2013; Denis et al. 2015). Nano-TiO_2 has previously been synthesised by continuous hydrothermal methods (Kawasaki et al. 2009; Thompson et al. 2009; Zhang et al. 2009a; Zhang et al. 2009b; Malinger et al. 2011; Mi et al. 2012) and these materials have been investigated for the photocatalytic degradation of organic species (such as model dyes). However, there are no reports of any studies concerning photocatalytic sacrificial water splitting for such materials made via CHFS.

Herein, CHFS was employed for the synthesis of nano-TiO_2 particles. The addition of varying amounts of boric acid in the reagent feed was investigated to determine, (a) whether boron doping can be induced by CHFS, and/or, (b) the effects of addition of boric acid on the reaction pH and therefore the crystallite size (and surface area). The as-synthesised nano-TiO_2 samples were characterised by a number of techniques, and

assessed for their ability to photocatalytically split water (in a sacrificial system) for hydrogen evolution.

3.3. EXPERIMENTAL METHODS

3.3.1. Chemicals and materials

Titanium(IV) oxysulfate ($TiOSO_4 \cdot xH_2O$; ≥29 % Ti (as TiO_2); ≤17 % free acid (as H_2SO_4)) and potassium hydroxide pellets (KOH; ≥85 %) were supplied by Sigma-Aldrich (Dorset, UK). Boric acid (H_3BO_3) was supplied by Fluka Analytical. Ethanol (absolute) and HCl (~36 %) (Fisher Scientific, Leicestershire, UK) were used in the preparation of sacrificial solutions. Compressed air, nitrogen (oxygen free) and high-purity hydrogen gases (BOC, Surrey, UK) were used in the operation of the gas chromatograph. All chemicals and gases were used as received. Deionised (DI) water (10 MΩ) was used throughout.

3.3.2. Continuous hydrothermal synthesis of nano-TiO_2

All samples were prepared on the pilot scale CHFS reactor, which is described in Chapter 2. A tee-piece junction was used to premix the aqueous solution of titanium oxysulfate containing a specific amount of dissolved boric acid (total metal salt concentration of 0.5 M; details provided in Table 3.1) with a second solution of potassium hydroxide (0.7 M), before the combined flow met a flow of supercritical water (at 400 °C and 24.1 MPa) in the confined jet mixer, whereupon rapid crystallisation of the nanoparticles occurred. The products of each reaction were cooled in flow via a water jacket cooler and collected at the exit of the process, where the pH was also measured. The slurries were dialysed in deionised water, centrifuged and washed before being freeze-dried (further details in Chapter 2). The samples were collected as off-white powders and labelled according to the nominal concentration of boric acid used in the reagents (in mol%), as shown in Table 3.1.

Table 3.1 Details of experimental conditions and products obtained from continuous hydrothermal flow synthesis reactions [a]

[H_3BO_3]/mol%	**0**	**0.5**	**1**	**1.5**	**2**	**2.5**	**3**	**5**	**7**	**10**
Cs/nm	5.0	7.8	12.9	17.2	10.3	14.1	9.7	6.5	5.4	5.0
SA/m^2g^{-1}	245	182	129	112	150	123	167	235	270	233
ESD/nm	6.3	8.5	12.0	13.8	10.3	12.6	9.3	6.6	5.7	6.6

[a] NB: the flow rates were fixed for all syntheses at 400 mL min^{-1} (Pump 1), 200 mL min^{-1} (Pump 2) and 200 mL min^{-1} (P-3), generating a reaction point temperature of 305 °C. The total metal salt concentration was fixed at 0.5 M and KOH was used at 0.7 M throughout.

Key: Cs = crystallite size, SA = BET surface area, ESD = equivalent sphere diameter.

3.3.3. Materials characterisation

The crystalline phase of each sample was identified by powder X-ray diffraction (XRD; Bruker D4 instrument), and crystallite sizes were estimated using the full width at half maximum (FWHM) of the anatase (101) peak, by application of the Scherrer equation. The surface area and equivalent sphere diameter (ESD) of each sample was determined via Brunauer–Emmett–Teller (BET) surface area measurements. Samples were also characterised via Raman, UV-vis and X-ray photoelectron spectroscopy and high resolution transmission electron microscopy (HR-TEM) (at the University of Leeds). Further details on these techniques can be found in Chapter 2 of this thesis.

3.3.4. Preparation of TiO_2 ceramic wafers

Samples of each powder (0.3 g) were pressed into 25 mm diameter circular wafers using a powder pressing technique, similar to that described in the literature (Elouali et al. 2010). Briefly, the powder was placed in a stainless steel die (Compacting Tooling Inc., Philadelphia, USA) and pressed at a pressure of 200 bar, in the extraction ram of a non-end-loaded piston cylinder (Patera and Holloway 1978) (Depths of the Earth Company, Arizona, USA), as shown in Figure 3.1. Previous work by Elouali et al. determined that

0.3 g was the minimum required mass of powder, to prepare a robust ceramic wafer that was able to withstand handling (Elouali et al. 2010). The ceramic wafers were heat-treated in an air atmosphere at 300 °C for 3 hours. A single side of each wafer was coated with a platinum co-catalyst, using a sputter coater fitted with a platinum target (35 mA for 4 min).

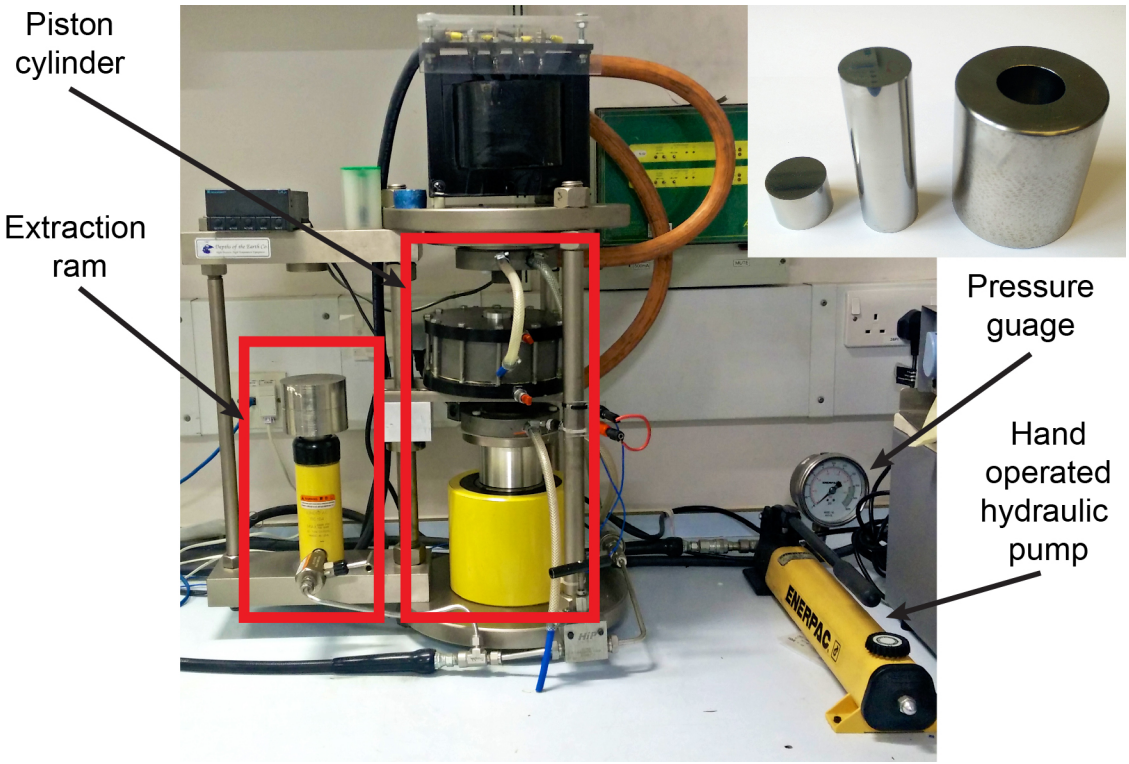

Figure 3.1 Photograph of piston cylinder press identifying the extraction ram used to prepare ceramic wafers in this work. The piston cylinder part was not used. The inset image shows the stainless steel die.

3.3.5. Photocatalytic hydrogen evolution testing

The photocatalytic activities of each ceramic wafer were measured using a photo-reduction reaction in a sacrificial solution, under UV and visible light irradiation from a 75 W xenon light source (Photon Technology International, West Sussex, UK), illustrated in Figure 3.2. Briefly, a silica double-walled glass reactor was filled with 50 mL of a sacrificial solution (consisting of 1:1 EtOH:H_2O containing 0.1 M HCl), with cooling water (20 °C) circulated through the outer glass wall of the reactor by a chiller (ThermoHake K75). The reactor was sealed to the outside atmosphere using a rubber

septum, which also allowed the ceramic wafer to be suspended in the solution, with the non-Pt coated surface facing the light source. The solution was kept under continuous stirring, and 250 µL of gas was removed from the headspace every 15 minutes for two hours, and analysed via gas chromatography.

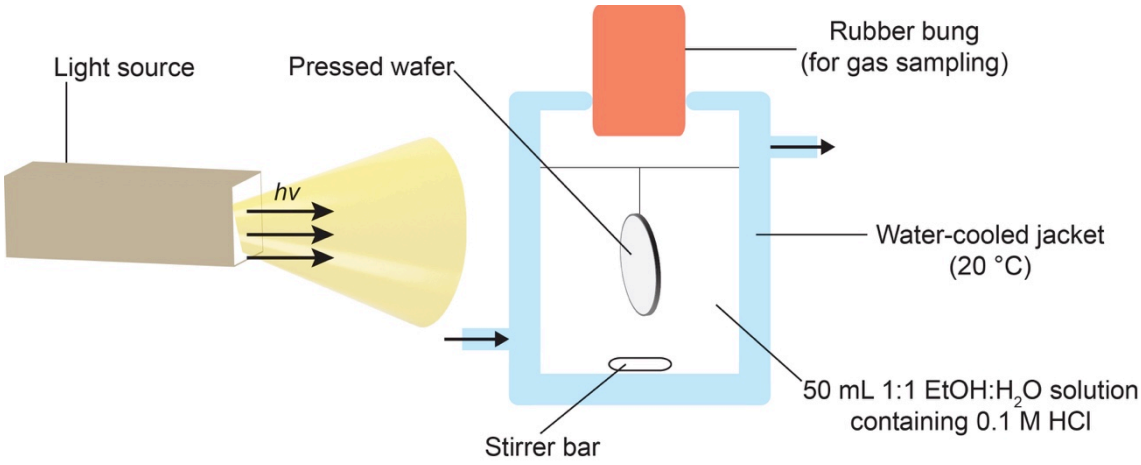

Figure 3.2 Schematic diagram of the experimental setup used for photocatalytic hydrogen evolution testing.

3.4. RESULTS AND DISCUSSION

3.4.1. Materials characterisation

Powder XRD patterns (Figure 3.3) revealed peaks for anatase TiO_2 for all samples (which were in good agreement with JCPDS pattern 21-1272 for anatase TiO_2), in agreement with results from previous studies on synthesis of TiO_2 via CHFS (Thompson et al. 2009; Zhang et al. 2009a; Zhang et al. 2009b). Whilst the peak positions did not shift between samples, the width of diffraction peaks did vary, depending on reaction conditions. This initial observation suggested that the boron anion might not have doped within the TiO_2 lattice via CHFS, but that the crystallite size (or strain) in the particles may have varied. When an impurity ion is introduced into a host lattice, the strain that the impurity ion imposes (on the host lattice) may cause the lattice to expand or contract. This change may often be observed as shifts in XRD peak positions (Bryan and Gamelin 2005).

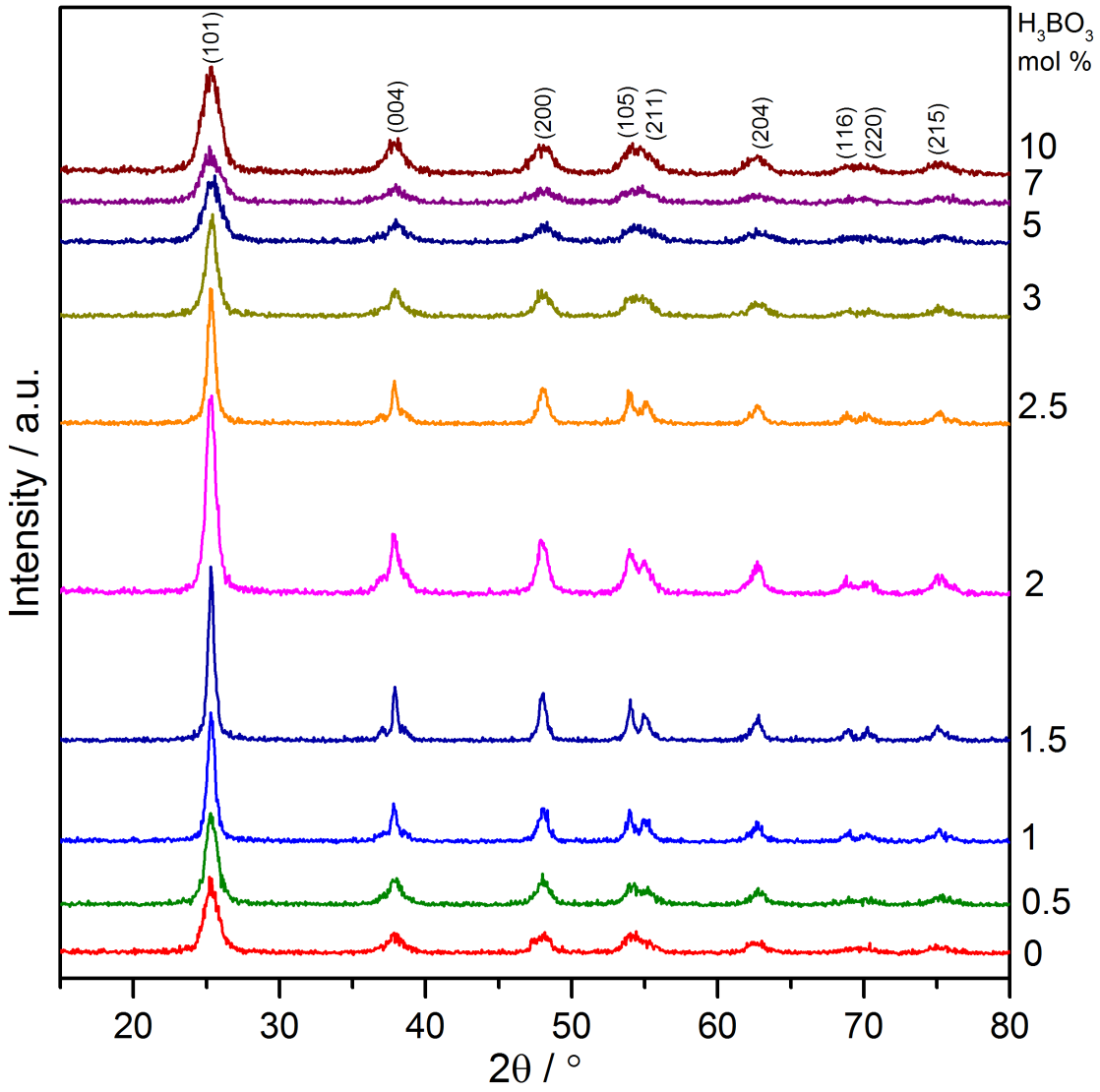

Figure 3.3 Powder X-ray diffraction (XRD) patterns of CHFS synthesised TiO_2. Diffraction peaks are indexed to the anatase structure of TiO_2. Data collected using Cu-Kα radiation (λ = 1.541 Å).

The variation in pH for each sample, measured at the point of sample collection, is shown in Figure 3.4. In the absence of boric acid, the titania sample slurry was obtained at pH 1. However, on addition of boric acid, the pH of the slurry began to increase, reaching a maximum of pH 9 at ca. 1.5 mol% boric acid. Thereafter, further addition of boric acid led to a decrease in pH, reaching pH 1 again at 10 mol% boric acid.

To determine the effects of the pH on the TiO_2 crystallite size, the diameter of crystallites was estimated by application of the Scherrer equation to the powder XRD

data (peak widths at half maximum). BET surface area was also measured and an equivalent sphere diameter (ESD) estimated. Figure 3.4 shows that as the pH of the product increased, the corresponding average crystallite size increased, whilst the surface area decreased. Conversely, as the pH decreased (beyond addition of 1.5 mol% boric acid) the crystallite size decreased, and surface area increased. This trend has also been reported for TiO_2 nanoparticles prepared by other methods (Mahshid et al. 2007; Ibrahim and Sreekantan 2010; Devi et al. 2014). At 7 and 10 mol% boric acid, the crystallite size appeared the same but the surface area decreased by ≈ 40 m^2g^{-1}; this difference may be attributed to the error associated with and assumptions made when calculating crystallite sizes using the Scherrer equation.

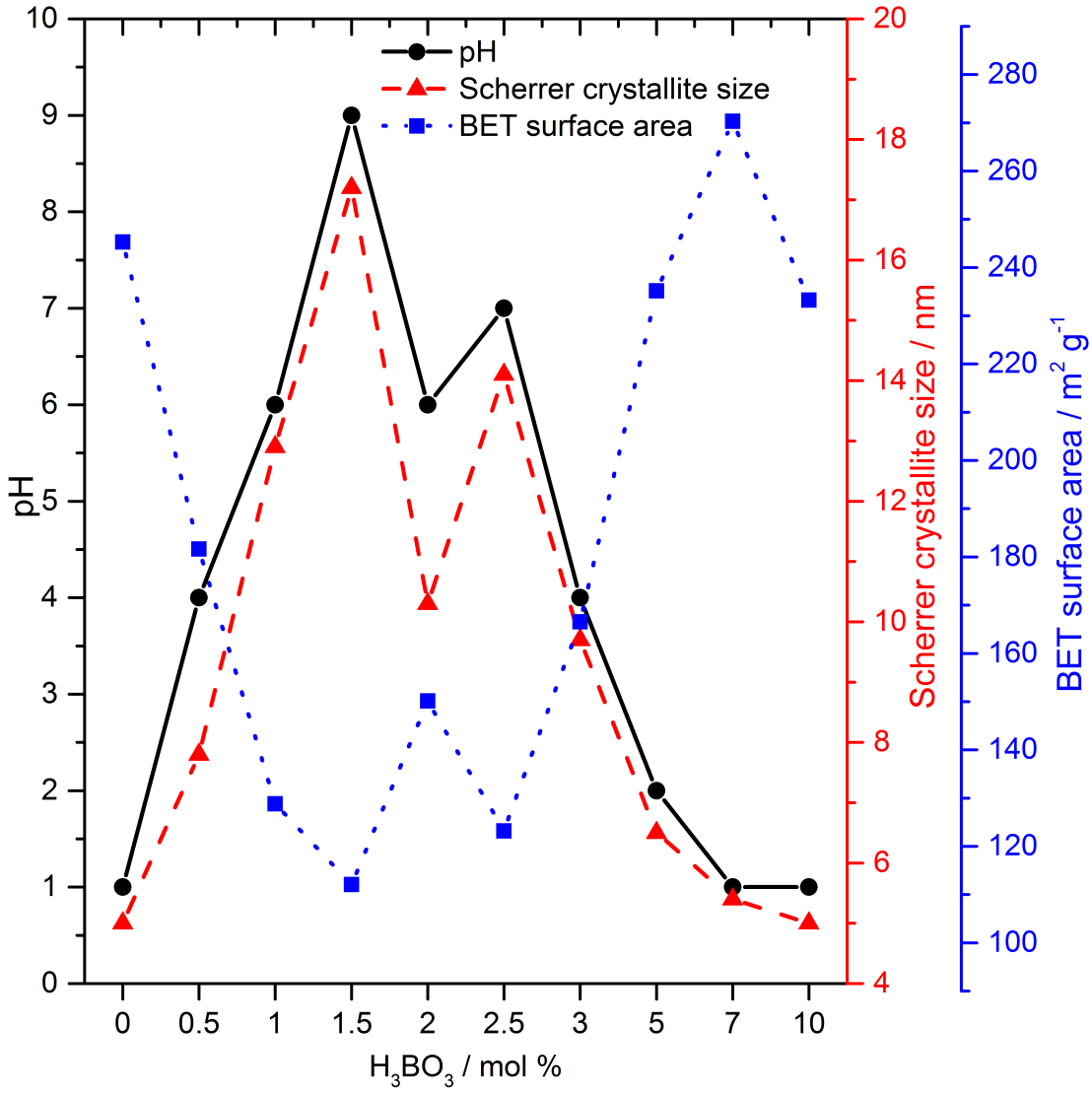

Figure 3.4 Variation in pH of collected slurry (●), crystallite size (▲) and BET surface area (■) for CHFS synthesised TiO_2.

The correlations between the product slurry pH and the amount of boric acid used in the reagents was rather complex as there were a number of chemical species present, all or some of which may have affected the overall product pH. For example, there were species from the precursors (e.g. sulphuric acid or related species), and the newly formed particles would have also contained a large number of hydroxide ions on their surface, which were in equilibrium with solution boron species.

The concentration of hydroxide ions in solution could be related to the relative degree of condensation of monomeric titanyl (TiO^{2+}) units in solution (Bavykin et al. 2007). Herein, the total metal ion concentration (referring to both titanium and boron) remained at 0.5 M, thus, as the concentration of boric acid was increased, the concentration of $TiOSO_4$ was effectively reduced. Bavykin et al. state that aqueous solutions of $TiOSO_4$ contain chains of $–Ti^{2+}–O–Ti^{2+}–O–$ (Bavykin et al. 2007), however, at low $TiOSO_4$ concentrations, monomeric titanyl species are also present (Comba and Merbach 1987). Furthermore, the degree of condensation may affect the quantity of OH^- ions released into solution, which may affect pH. The hydrolysis of both Ti species occurs differently; under certain conditions, the hydrolysed chains would be expected to form the largest particles, compared to the monomeric titanyl species in solution (Bavykin et al. 2007).

The observed changes in pH (and therefore size of titania nanoparticles) may also be related to the concentration of free boric acid. Initially, at low concentrations, boric acid molecules may have reacted with hydroxide ions (Wofford et al. 1998), forming the basic tetrahydroxyborate anion, $[B(OH)_4]^-$, which would explain the initial increase in pH of the product slurry for boric acid levels from 0 to 1.5 mol%. However, at levels greater than 1.5 mol%, an excess of free boric acid in solution may have been sufficient to decrease the pH and, eventually, the product slurry became strongly acidic. Depending on the initial conditions (particularly pH and concentration of the $TiOSO_4$ precursor), the relative number of monomeric and long chain Ti species in solution would have changed, which in turn would have affected the concentration of hydroxide ions in solution. This may partly explain why pH was slightly raised (rather than continuing to decrease with increasing boric acid concentration) when going from

2.0 to 2.5 mol% boric acid. Thereafter, beyond 3 mol% boric acid, the pH remained low due to an excess of the free acid.

The calculated BET equivalent sphere diameter (Table 3.1) for each sample correlated well with the trend in powder XRD crystallite size. The results show that the pH directly affected the crystallite size of CHFS made TiO_2 nanoparticles, and the change in surface area was related to this change in size.

Raman spectroscopy was used to further characterise the structure of the CHFS samples (Figure 3.5). Anatase has six distinct Raman bands: $3E_g$ (144, 197 and 639 cm^{-1}), $2B_{1g}$ (399 and 519 cm^{-1}) and A_{1g} (513 cm^{-1}) (Zhang et al. 2009a).* The Raman spectra confirmed the samples had the anatase TiO_2 crystal structure, in agreement with observations made from powder X-ray diffraction data. In comparison to TiO_2 prepared in the absence of boric acid (0 mol%), the E_g band ≈ 150 cm^{-1} appeared to initially shift to lower wavenumbers as the crystallite size increased, and then towards higher wavenumbers again as the crystallite size decreased. The position of the E_g band appeared at very similar wavenumbers for samples 0, 7 and 10 mol% H_3BO_3, where the crystallite size for these samples was calculated to be in the range 5–6 nm. The shift observed in the position of the E_g band is attributed to a phonon confinement effect in nano-crystals, which has been reported previously (Zhu et al. 2005; Zhang et al. 2009a; Venkatasubbu et al. 2012).

* For reference, the Raman bands of rutile TiO_2 are: E_g (446 cm^{-1}), B_{1g} (144 cm^{-1}), B_{2g} (827 cm^{-1}) and A_{1g} (610 cm^{-1}) (Balachandran and Eror 1982), and those of brookite TiO_2 are: $6B_{1g}$ (133, 159, 215, 320, 415 and 502 cm^{-1}), $4B_{2g}$ (366, 395, 463 and 584 cm^{-1}), B_{3g} (452 cm^{-1}) and $6A_{1g}$ (127, 154, 194, 247, 412 and 640 cm^{-1}) (Tompsett et al. 1995).

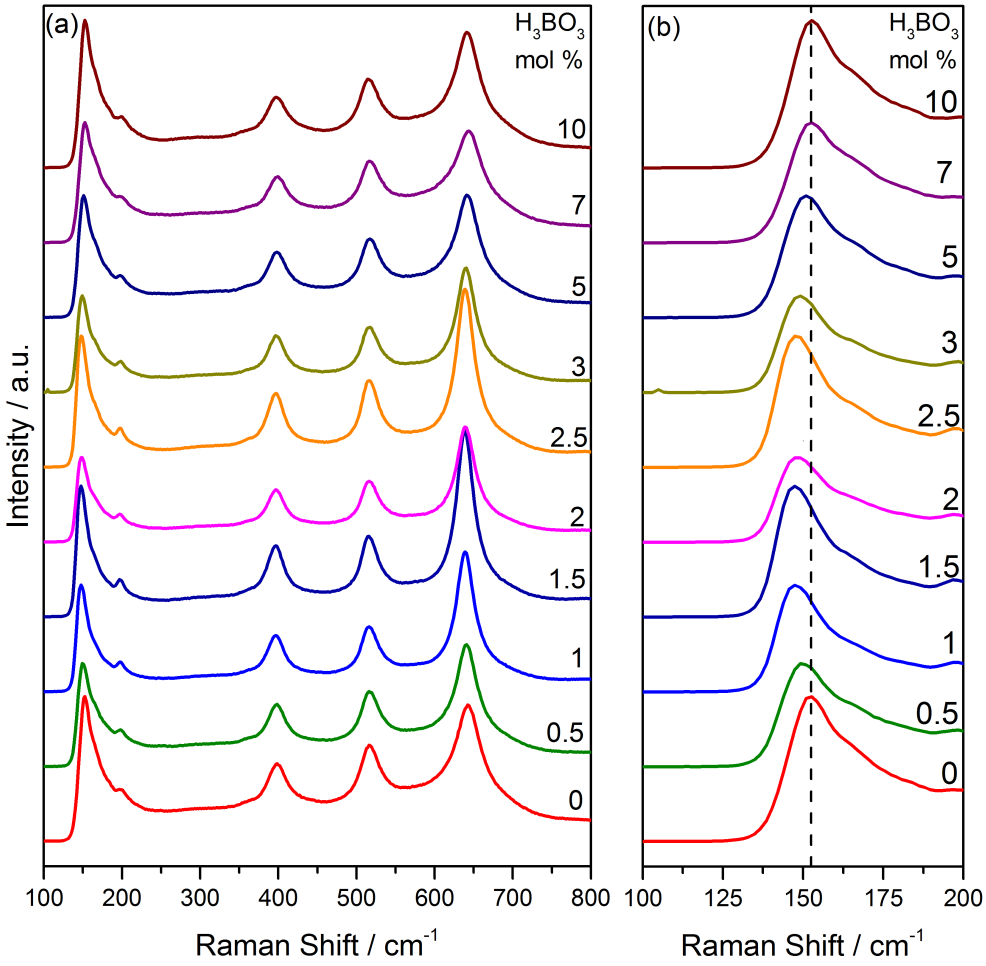

Figure 3.5 (a) Raman spectra of as-prepared nano-TiO_2 samples and (b) a close-up view of the E_g band of anatase at ≈ 150 cm^{-1}, showing the shift in band position as nanoparticle size varied.

UV-visible absorbance spectra (shown in Figure 3.6) showed negligible change in the absorbance profile of any CHFS TiO_2 sample. It is expected that boron doping of TiO_2 would have enhanced the visible light response (i.e. a red shift in the absorbance profile) as described in the literature (Lu et al. 2008; Xu et al. 2009; Lu et al. 2010; Carmichael et al. 2013). The absence of this shift in the spectra for any of the CHFS TiO_2 samples suggested that the boron anion was not doped within the TiO_2 lattice.

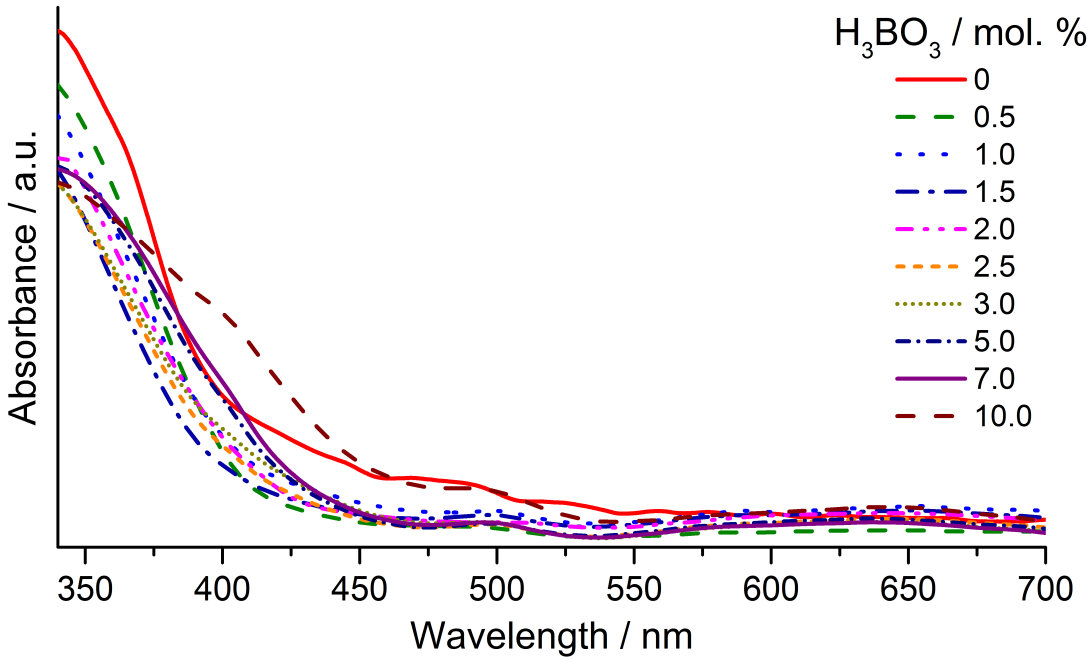

Figure 3.6 UV-visible absorbance spectra for pilot plant CHFS TiO_2 samples.

X-ray photoelectron spectroscopy (XPS) was used to determine the nature of chemical states in the TiO_2 samples. A representative survey spectrum (Figure 3.7) contained peaks for titanium, oxygen and carbon states. However, the presence of boron chemical states, which usually appear in the range ≈ 185–195 eV, was not observed. This suggested that the samples did not contain any boron surface species. Studies investigating kinetics of the dehydration of boric acid have shown, at temperatures above 300 °C (at ambient pressure), the reaction began only after approximately 5 minutes and went to completion after approximately 45 minutes (Balcı et al. 2012). This suggests that the dehydration of boric acid required a longer timescale than provided within the CHFS process (the order of a few seconds), and hence may explain why boron doping was not achieved.

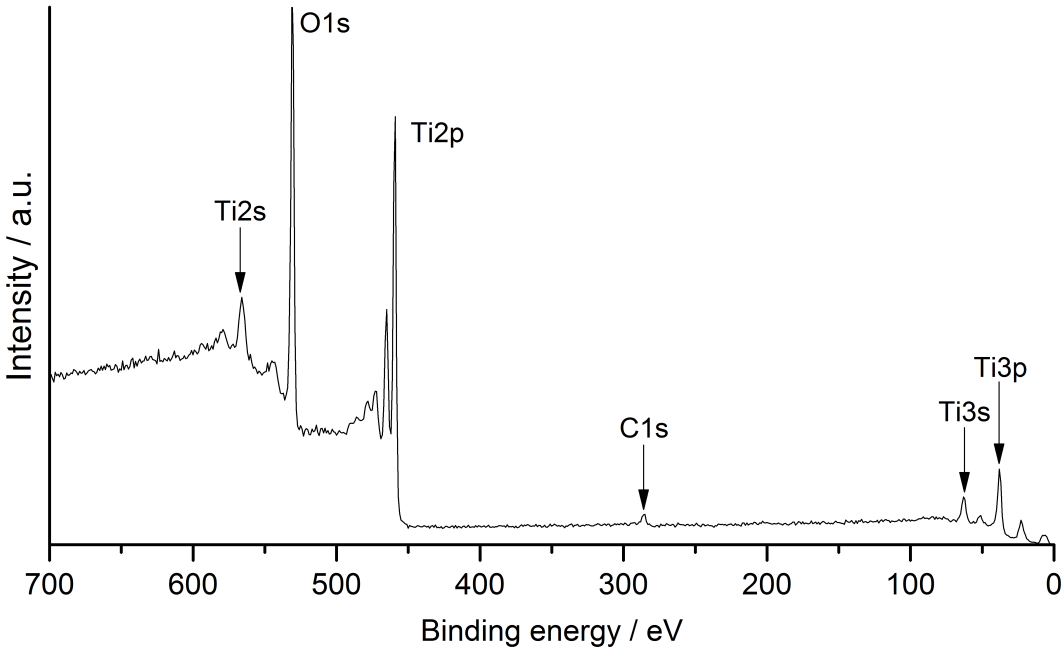

Figure 3.7 X-ray photoelectron spectroscopy (XPS) survey scan showing chemical states present in TiO_2 samples.

Figure 3.8 shows HR-TEM images for a TiO_2 sample prepared with 1.5 mol% boric acid. The images show roughly spherical agglomerated particles with an anatase (101) lattice spacing of 0.35 nm (Figure 3.8(a)), in agreement with literature values for CHFS TiO_2 of 0.355 and 0.356 nm (Figure 3.8(b)) (Zhang et al. 2009a; Goodall et al. 2014).

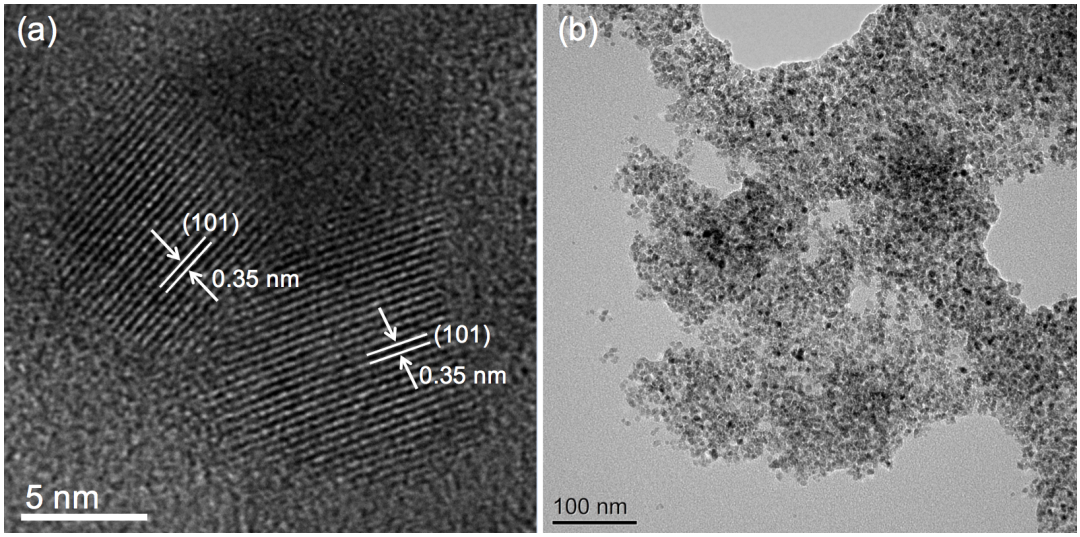

Figure 3.8 HR-TEM images of TiO_2 prepared via CHFS (a) with 1.5 mol% H_3BO_3 and (b) with 10 mol% H_3BO_3.

3.4.2. Photocatalytic hydrogen evolution

The heat-treated, pressed wafers of each titania sample were investigated for hydrogen evolution under a UV-visible light source (xenon lamp). One side of each wafer was coated with a layer of platinum co-catalyst. As discussed in Chapter 1, the conduction band of TiO_2 is not sufficiently high to reduce water at an appreciable rate alone. Therefore, co-catalysts are typically used to enhance the rate of hydrogen evolution. Figure 3.9 shows a typical experimental setup, where the platinum coated side of the TiO_2 wafer is visible, with the uncoated, TiO_2 side facing the light source. During the experiments, gas bubbles were observed to evolve from the wafers, most apparent at the edges. Elouali reported similar observations using commercial and CHFS TiO_2 wafers, and attributed the effect to an increased surface area at the edges of the wafers, which is likely to be higher in comparison to the face of the wafers (Elouali 2012).

Figure 3.9 Photograph of a platinum coated TiO_2 wafer evolving hydrogen bubbles during the photocatalytic hydrogen evolution experiments. The xenon lamp is to the right of the glass reactor, out of the frame of the image (Photo credit: O Usher, UCL MAPS faculty).

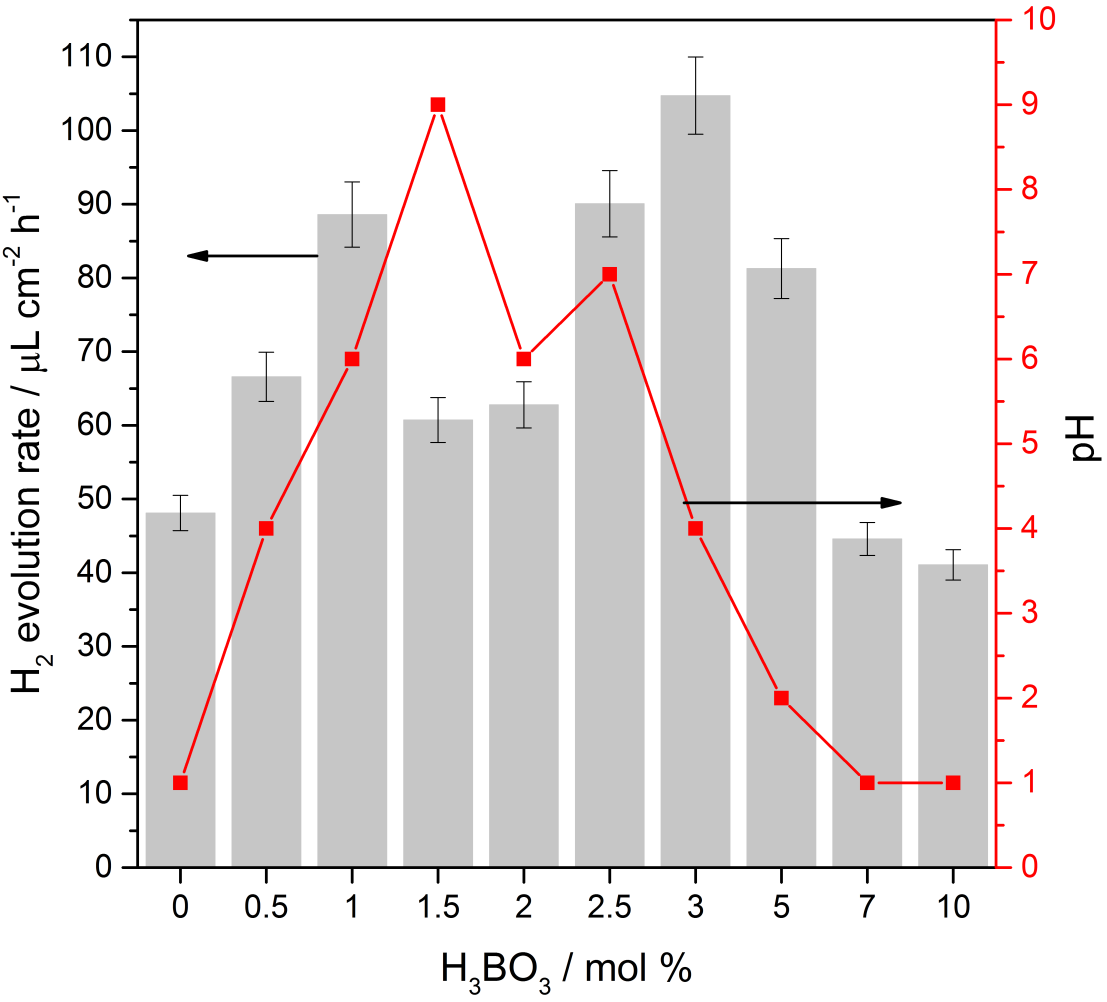

Figure 3.10 Variation in hydrogen evolution rate and pH (of the product slurry of as-prepared samples) for nano-TiO_2 samples.

Figure 3.10 shows the hydrogen evolution rate for each TiO_2 sample, in comparison with the pH of the as-prepared sample. On addition of boric acid, the pH initially increased from 1 to 6 in the product slurry, correlating to an increase in the hydrogen evolution rate. However, beyond pH 6 (1 mol% boric acid) the hydrogen production rate decreased, whilst the pH increased (pH 9; 1.5 mol% boric acid). Overall, it appears that mildly acidic or neutral conditions of the product slurry (where TiO_2 nanoparticles were synthesised with crystallite sizes in the range 9–12 nm and surface areas 150–200 $m^2 g^{-1}$) gave the highest hydrogen evolution rates of all samples. It emerges that there is a compromise between the crystallite size and surface area, and that neither extremes of each parameter (such as small crystallite size or high surface area) was ideal for

hydrogen evolution by such nanomaterials. In similar work conducted by Elouali on hydrogen evolution by TiO_2 ceramic wafers in a sacrificial system, it was found that the hydrogen evolution rate for commercial TiO_2 samples was nearly an order of magnitude higher than those reported in the present work (TiO_2 PC50: 548.1 μL cm^{-2} h^{-1} and P25: 612.1 μL cm^{-2} h^{-1})†. Elouali also synthesised TiO_2 via CHFS (4–6 nm particles with surface area ≈ 270 m^2 g^{-1}) where the hydrogen evolution rate was 68.0 μL cm^{-2} h^{-1} (Elouali 2012). This result compares well to the TiO_2 sample prepared in this work with 5 mol% H_3BO_3 where the size and surface areas of the particles are similar (within error). The higher evolution rates achieved for commercial TiO_2 samples may be attributed to the optimised synthesis procedures for such materials, which have been prepared by optimised methods. In the current work, one of the aims was to determine how particle size might be controlled via CHFS synthesis methods, and therefore, further optimisation of process conditions may lead to higher photocatalytic rates.

Kočí et al. studied the effect of TiO_2 crystallite size on the photocatalytic reduction of CO_2, where they found that the photocatalytic rate increased as crystallite size increased from 4.5–14 nm. However, beyond 14 nm, the photocatalytic rate decreased (Kočí et al. 2009). In the present work, the sample that gave the largest crystallite size (1.5 mol% H_3BO_3), had a hydrogen evolution rate that was towards the lower end of those measured for the sample series. Lin et al. synthesised anatase TiO_2 nanoparticles by a metal-organic chemical vapour deposition method (Lin et al. 2006). They reported that, for the photocatalytic oxidation of 4-chlorophenol, the photocatalytic rate was higher for particles with crystallite sizes between 9.2–11.6 nm than those that were 17–24 nm. Similar results were obtained by Jang et al. for the degradation of methylene blue, where the authors observed an increase in photocatalytic rates as TiO_2 particle size decreased from 30–15 nm (Jang et al. 2001).

The results from these studies suggest that reducing TiO_2 particle size can be beneficial for a number of photocatalytic applications. The results obtained for CHFS prepared TiO_2 nanomaterials have demonstrated the ability to control reaction parameters within the CHFS process, and it is believed that further optimising synthesis conditions or

† The work presented by Elouali quotes hydrogen evolution rates in units of μmol H_2 h^{-1}, but these are converted here for ease of comparison.

investigating the role of additives in CHFS, may contribute towards preparing materials with higher photocatalytic efficiencies in the future.

3.5. CONCLUSIONS

Nano-TiO_2 samples were prepared using a continuous hydrothermal method for photocatalytic hydrogen evolution from water. The addition of boric acid as a reagent was investigated, and whilst boron doping in the titania was not observed, the boric acid significantly affected the reaction pH and consequently the properties of the nanoparticles. It is suggested that boron doping was not achieved because of the requirement for a long reaction time for dehydration of boric acid; the reaction time obtained in the CHFS process was on the order of a few seconds. Powder X-ray diffraction and Raman spectroscopy confirmed that all samples were anatase TiO_2, with crystallite sizes in the range 5–17 nm. pH measurements of the nanoparticle slurries from the CHFS process showed a direct relationship between pH and crystallite size; as pH increased, the average crystallite size also increased. Increasing the concentration of boric acid led to an increase in the pH of the product, up to a boric acid concentration of 1.5 mol%. Above this concentration, the pH generally decreased. Photocatalytic hydrogen evolution measurements (as ceramic wafers) suggested that the highest photocatalytic activities were achieved with samples prepared under mildly acidic or neutral conditions. Further optimisation of reaction conditions may provide new insights for future materials discovery. The findings of this study have demonstrated that control of crystallite size can be readily achieved, via CHFS synthesis of nanomaterials at pilot plant scale, by carefully controlling reaction conditions. Other nanomaterial properties may be further controlled by incorporating other additives in the one-step synthesis process, where it may be possible to achieve morphology control or to preferentially crystallise nanoparticles with exposed facets, which may prove beneficial for photocatalytic applications. The role of additives (i.e. surfactants) in the CHFS process is investigated in Chapter 5, for the synthesis of zinc oxide, as a strategy to control particle size and shape.

Chapter 4. Continuous hydrothermal synthesis of nano-zinc oxide

4.1. AIMS AND OUTLINE

The aims of this chapter are to investigate the mass-based scale up of zinc oxide nanoparticles, on the mini-pilot scale continuous hydrothermal flow synthesis (CHFS) reactor in the Clean Materials Technology Group at University College London. Gruar et al. previously conducted similar experiments on both the laboratory and pilot scale processes (Gruar et al. 2013). In this work, comparisons are made to the results already presented from that work in the literature. The following discussion attempts to explain the similarities and differences between the two process scales, in terms of the size and morphology properties of zinc oxide nanoparticles.

4.2. INTRODUCTION

Zinc oxide is a multifunctional material; it has a variety of physical and chemical properties that have led to numerous applications (Kołodziejczak-Radzimska and Jesionowski 2014) such as in electronics, cosmetics and gas sensors (Fan and Lu 2005). Many of these properties rely on the nano-size of zinc oxide, since nanomaterials display unique properties in comparison to their bulk counterparts (Namratha and Byrappa 2012). Therefore, synthesis of high quality nano-zinc oxide is important, especially in industrial processes. Nano-zinc oxide has been synthesised by a number of different methods, e.g. spray pyrolysis (Mani and Rayappan 2014), hydrothermal (Dem'yanets et al. 2006), chemical vapour deposition and highly controlled photolithography (Fan and Lu 2005; Goodall et al. 2015). However, the majority of techniques that are described in the literature concern batch processes conducted on a small laboratory scale. Whilst these processes may be adequate in synthesising small quantities of material, scaling up such processes often remains a challenge (Tighe et al. 2013), in particular when considering commercialisation. When processes are scaled up there may be limited control over particle properties or batch-to-batch variations,

because particle formation mechanisms may not be identical across different process scales. These differences are attributed to the difficulties in achieving stable and uniform reaction environments (Tsuzuki 2009). Additionally, scaled-up processes may be intensive in energy, raw materials and labour, and may generate large amounts of waste. To overcome some of these challenges, researchers have been exploring continuous hydrothermal methods, which were first developed in the early 1990s in Japan (Adschiri et al. 1992a; Adschiri et al. 1992b), for the preparation of high quality inorganic nanomaterials.

In continuous hydrothermal methods (referred to as continuous hydrothermal flow synthesis, CHFS), a stream of hot, pressurised water is mixed with a stream of aqueous metal ions (at room temperature), resulting in rapid hydrolysis and dehydration reactions. These reactions occur because of the rapid change in the environment experienced by the metal ions, and leads to the formation of metal oxide particles.

In this chapter, the scale up synthesis of nano-zinc oxide is investigated, where the effects of increasing precursor concentrations on particle size and morphology are reported. The purpose of the investigation was to identify any similarities and differences between CHFS processes at different scales, i.e. a comparison between the mini-pilot scale and the larger pilot scale process.

4.3. EXPERIMENTAL METHODS

All experiments discussed in this chapter were conducted on the mini-pilot scale CHFS reactor as described in Chapter 2. The syntheses were conducted in collaboration with Dr Robert Gruar. All materials characterisation and data analyses were conducted independently.

4.3.1. Chemicals and materials

Zinc nitrate hexahydrate ($[Zn(NO_3)_2 \bullet 6H_2O]$, reagent grade, 98 %) and potassium hydroxide pellets (KOH, ≥ 85 %) were supplied by Sigma-Aldrich (Dorset, UK). All chemicals were used as received. Deionised (DI) water (10 MΩ) was used throughout.

4.3.2. Synthesis and characterisation

Zinc oxide nanoparticles were synthesised on the mini-pilot scale reactor, investigating the effects of a mass-based scale up. The CHFS reactor was used in a three-pump configuration, where all pumps were operated at a pressure of 24.1 MPa. Pump 1 was used to feed a flow of DI water (80 mL min^{-1}) through an electrical heater with a set-point temperature of 450 °C. Pump 2 and Pump 3 (40 mL min^{-1} each) were used to feed flows of zinc nitrate and KOH (both at ambient temperature), respectively, to a tee-piece mixer where the two feeds mixed. The combined metal salt and base flow then met a flow of supercritical water in a confined jet mixer, whereupon a rapid crystallisation occurred. Further details on the CJM are given in Chapter 2. The concentrations of zinc nitrate and KOH began at 0.1 M, and were simultaneously increased by 0.1 M increments for each subsequent experiment, up to a maximum concentration of 1.0 M. The products of CHFS reactions were cooled in-flow and collected as white slurries. Each sample was allowed to settle for up to 3 hours, before dialysing and freeze-drying the concentrated slurries as described in Chapter 2. The freeze-dried samples were obtained as white powders.

ZnO samples were characterised by powder X-ray diffraction (XRD), transmission electron microscopy (TEM) and scanning electron microscopy (SEM). A description of these techniques is provided in Chapter 2.

4.4. RESULTS AND DISCUSSION

4.4.1. CHFS synthesis of zinc oxide and comparison to other process scales

The CHFS experiments for the synthesis of zinc oxide (ZnO) on the mini-pilot scale reactor were conducted to understand the similarities and differences to ZnO prepared at the laboratory scale and pilot scale, and to investigate mass based scale-up.

The yields of freeze-dried ZnO product were in the range 36–71 %, with the samples prepared at concentrations above 0.5 M giving yields towards the higher end of this range. Loss of product during the sample cleaning process may partially account for the

lower yields. The lower yields at lower concentrations may be accounted for in terms of the degree of supersaturation during the reaction.

Powder X-ray diffraction patterns, shown in Figure 4.1, were indexed to the hexagonal wurtzite structure of ZnO, and were in good agreement with ICSD reference pattern 26170. The patterns were consistent to those obtained previously by Gruar et al. on the pilot scale process, where the total flow rate was 700 mL min^{-1} (except for the sample prepared at 0.1 M, where the total flow rate was 800 mL min^{-1}) (Gruar et al. 2013).

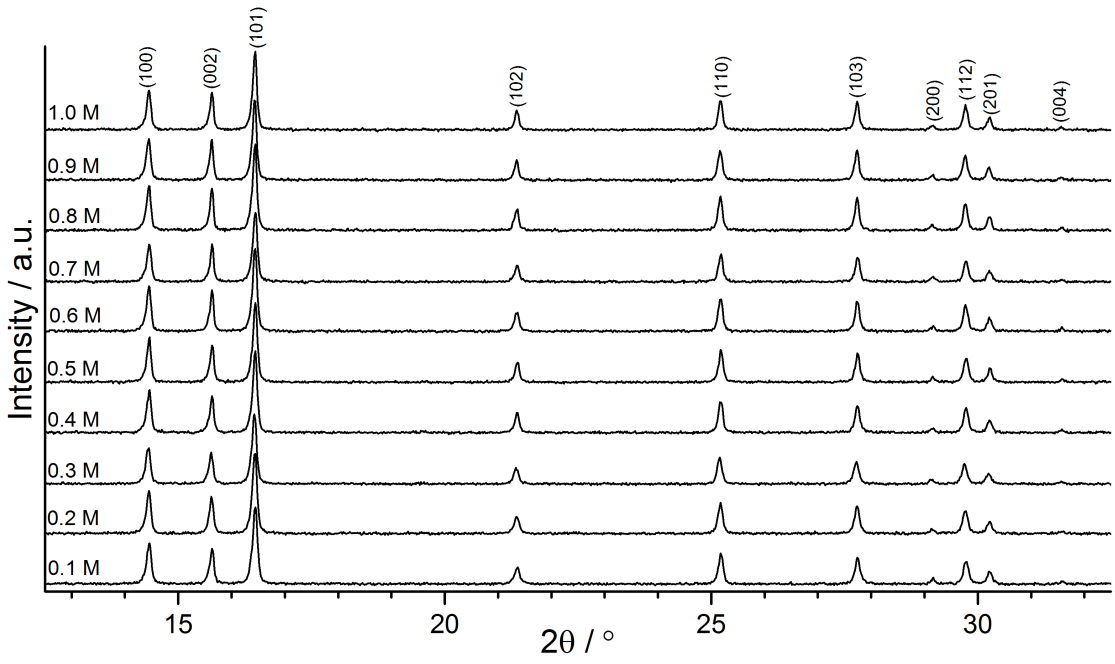

Figure 4.1 Powder X-ray diffraction patterns for CHFS produced zinc oxide at precursor concentrations in the range 0.1 – 1.0 M. Data collected using Mo-Kα radiation (λ = 0.709 Å).

The crystallite size for each sample was inferred from application of the Scherrer equation on the (100) diffraction peak. Crystallite size estimates were in the range 40 – 50 nm (Figure 4.2), and there was little variation when increasing the precursor concentration. At the laboratory scale, where the synthesis of ZnO was investigated as a mass-based (precursor concentration up to 0.2 M) and a volumetric-based (total flow output up to 40 mL min^{-1}) scale-up, the crystallite size estimates were in the range 30 – 40 nm. The difference between the size ranges at the different process scales is rather small, given the laboratory process only achieved $\frac{1}{5}^{th}$ of the precursor

concentration used at the mini-pilot scale. This suggests that with careful consideration of reaction parameters, the scale-up synthesis of ZnO with near-identical properties from the laboratory to mini-pilot scale, can be readily achieved.

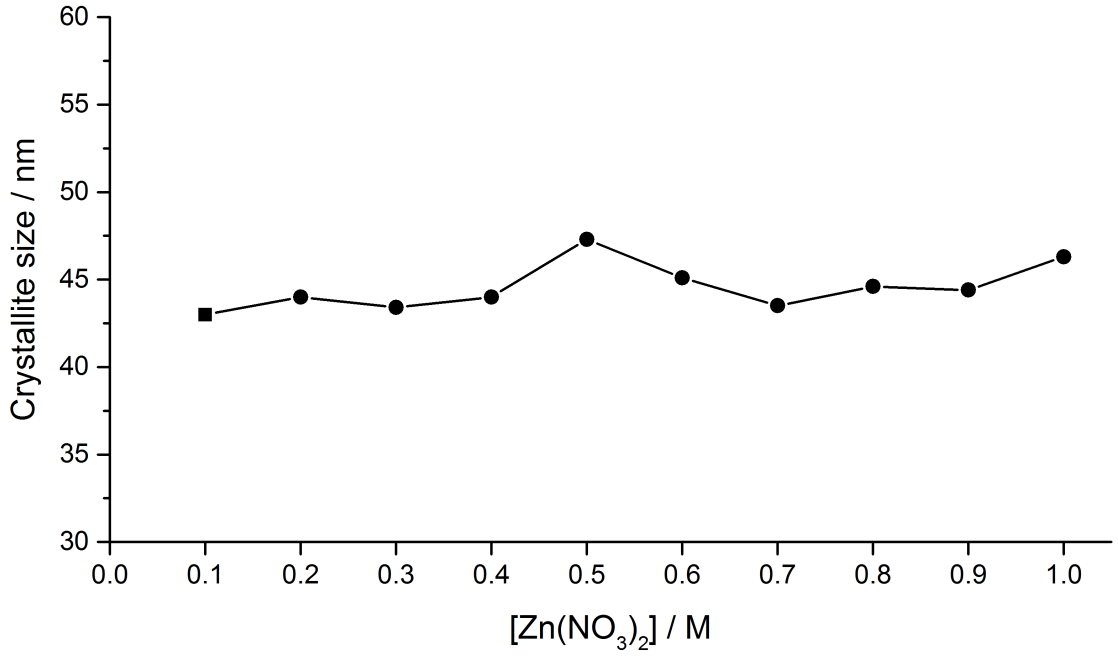

Figure 4.2 Comparison of the crystallite size obtained from application of the Scherrer equation on the (100) diffraction peak as a function of precursor concentration.

Zinc oxide is known to crystallise in a number of different morphologies, which can be controlled by tuning growth rates along different growth directions (Wang 2004; Baruah and Dutta 2009b). ZnO has three fast growth directions: $\langle 2\bar{1}\bar{1}0\rangle$ ($\pm[\bar{1}2\bar{1}0], \pm[2\bar{1}\bar{1}0], \pm[\bar{1}\bar{1}20]$), $\langle 01\bar{1}0\rangle$ ($\pm[01\bar{1}0], \pm[10\bar{1}0], \pm[\bar{1}\bar{1}00]$) and $\pm[0001]$, some of which are shown in Figure 4.3. The fast growth directions exist as a result of the need to stabilise high-energy facets (Goodall et al. 2015). Differences in the growth rates of these directions can lead to particle anisotropy, which is known to have an effect on the peak intensities in the powder X-ray diffraction patterns, because of the anisotropic grain size of the crystallites (Ariosa et al. 2011). Laudise and Ballman state that the (0001) face is not stable under hydrothermal conditions, and it has been observed that growth in the $\langle 0001\rangle$ direction (corresponding to the *c*-axis) is twice as fast as growth in the $\langle 10\bar{1}0\rangle$ direction (Laudise and Ballman 1960). Masuda et al. have investigated morphology control in ZnO in solution, and have shown that intensities of

the (0002) and (10$\bar{1}$0) diffraction peaks can directly relate to the particle shape achieved. Where the intensity of the (0002) peak was much greater than the (10$\bar{1}$0) peak, electron microscopy showed growth of long, hexagonal particles, which were probably caused by elongation in the *c*-axis (Masuda et al. 2007; Masuda and Kato 2008).

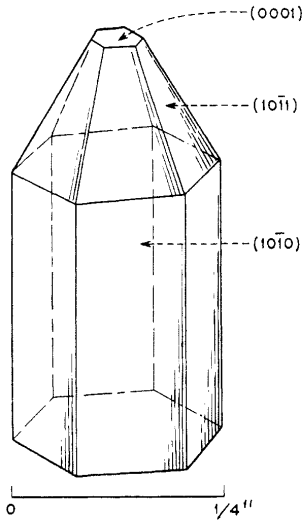

Figure 4.3 Diagram to show selected growth facets of zinc oxide. Reprinted with permission from (Laudise and Ballman 1960). Copyright (1960) American Chemical Society.

Calculating the relative ratio between the intensities of these peaks, can give an approximation as to the isotropy of particles likely to be produced. Figure 4.4 shows the intensity ratio between the (0002) and (10$\bar{1}$0) diffraction peaks (which correspond to the (002) and (100) diffraction peaks, respectively, in Figure 4.1) for the samples prepared on the mini-pilot plant. Across the sample range, a slight variation in the ratios was observed, in the range 0.84 – 1.01. ZnO samples prepared on the pilot scale process under analogous conditions gave (0002)/(10$\bar{1}$0) peak intensity values below 0.60, suggesting a high degree of anisotropic growth, which was confirmed by the rod-like particles observed by electron microscopy (Gruar et al. 2013). In the case of the present work, whilst the intensity ratios only varied in a narrow range, a slight increase was observed beyond 0.5 M. This may suggest that the extent of growth was greater at the higher concentrations; to confirm whether this was the case, selected samples were analysed via electron microscopy.

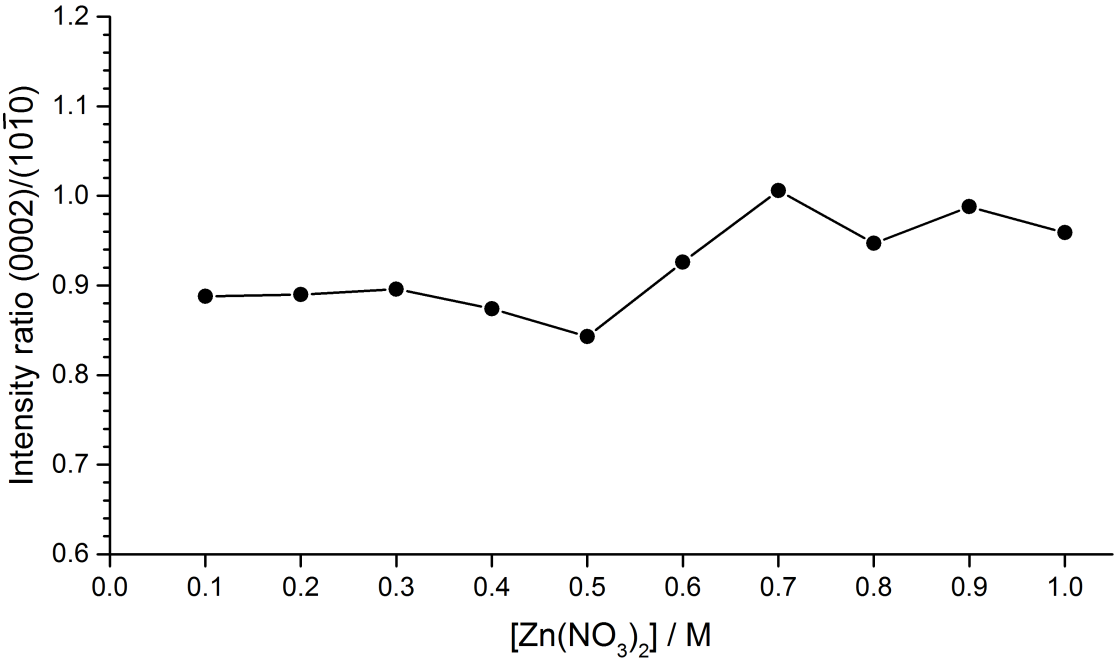

Figure 4.4 Variation in the (0002)/(10$\bar{1}$0) diffraction peak intensity values as a function of precursor concentration.

Figure 4.5 shows TEM images of selected ZnO samples. At the lower concentrations (0.1 and 0.5 M; Figure 4.5(a–d)), the images showed polygonal shaped particles of various sizes. However, at the higher concentrations (0.7 and 1.0 M; Figure 4.5(e–h)), in addition to polygonal shaped particles, rod-like particles were also observed. This correlates well with the data presented in Figure 4.4, where an increase in the (0002)/(10$\bar{1}$0) peak intensity values is calculated at the higher concentrations. These results suggest that anisotropic growth began to occur within the continuous hydrothermal process for the synthesis of zinc oxide as the concentration was increased. Gruar et al. previously made a similar observation in the case of the pilot scale CHFS process (Gruar et al. 2013).

To provide a quantitative treatment of the TEM images obtained, a series of particle size measurements were conducted to obtain representative size distributions. In each case, the diameters of approximately 300 particles were measured for each sample. At concentrations of 0.7 and 1.0 M, the lengths of approximately 100 rod-like particles were also measured. The size distribution plots are shown in Figure 4.6.

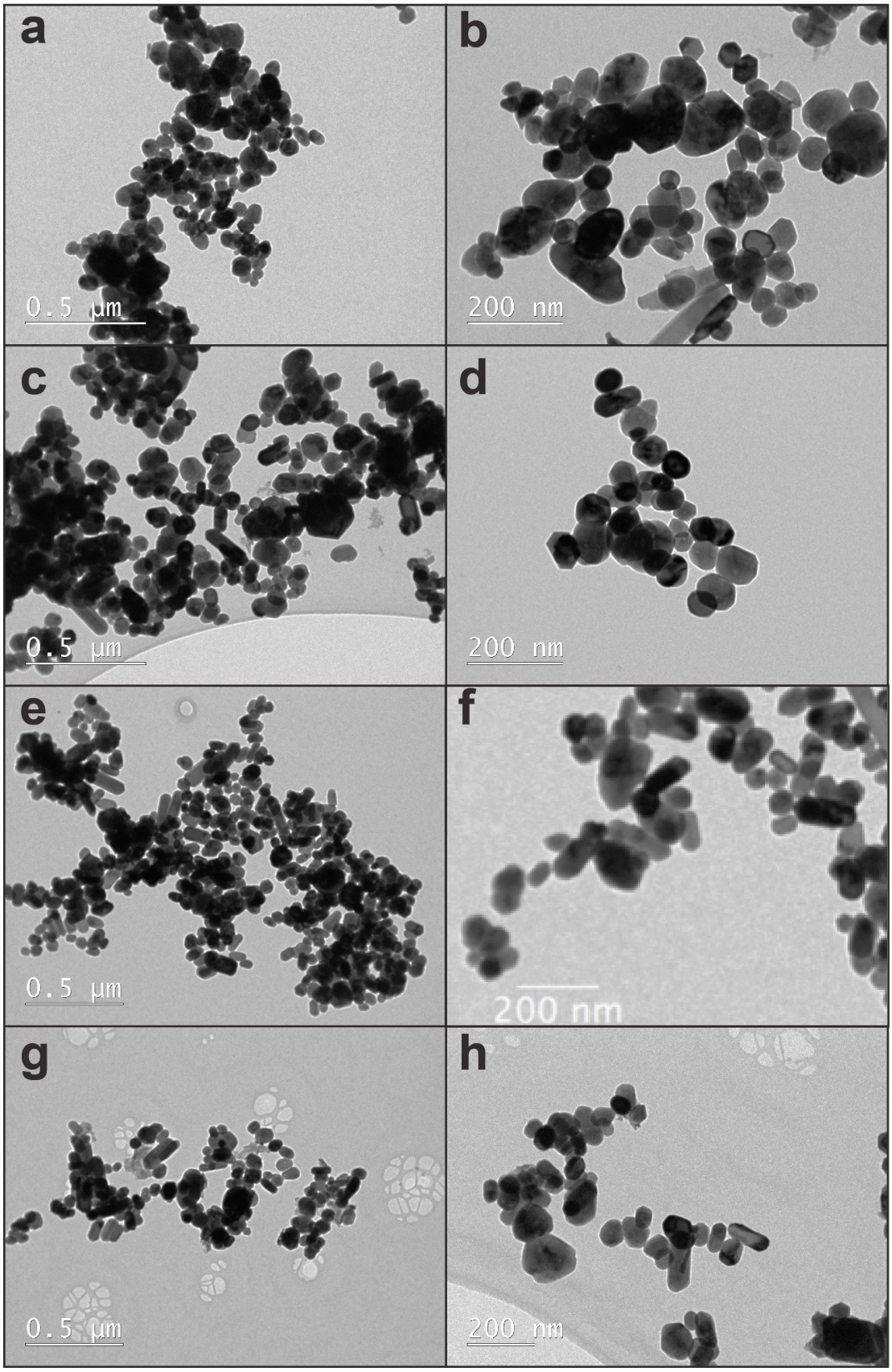

Figure 4.5 TEM images of ZnO nanoparticles synthesised by CHFS at precursor concentrations: (a) and (b) 0.1 M, (c) and (d) 0.5 M, (e) and (f) 0.7 M, and (g) and (h) 1.0 M.

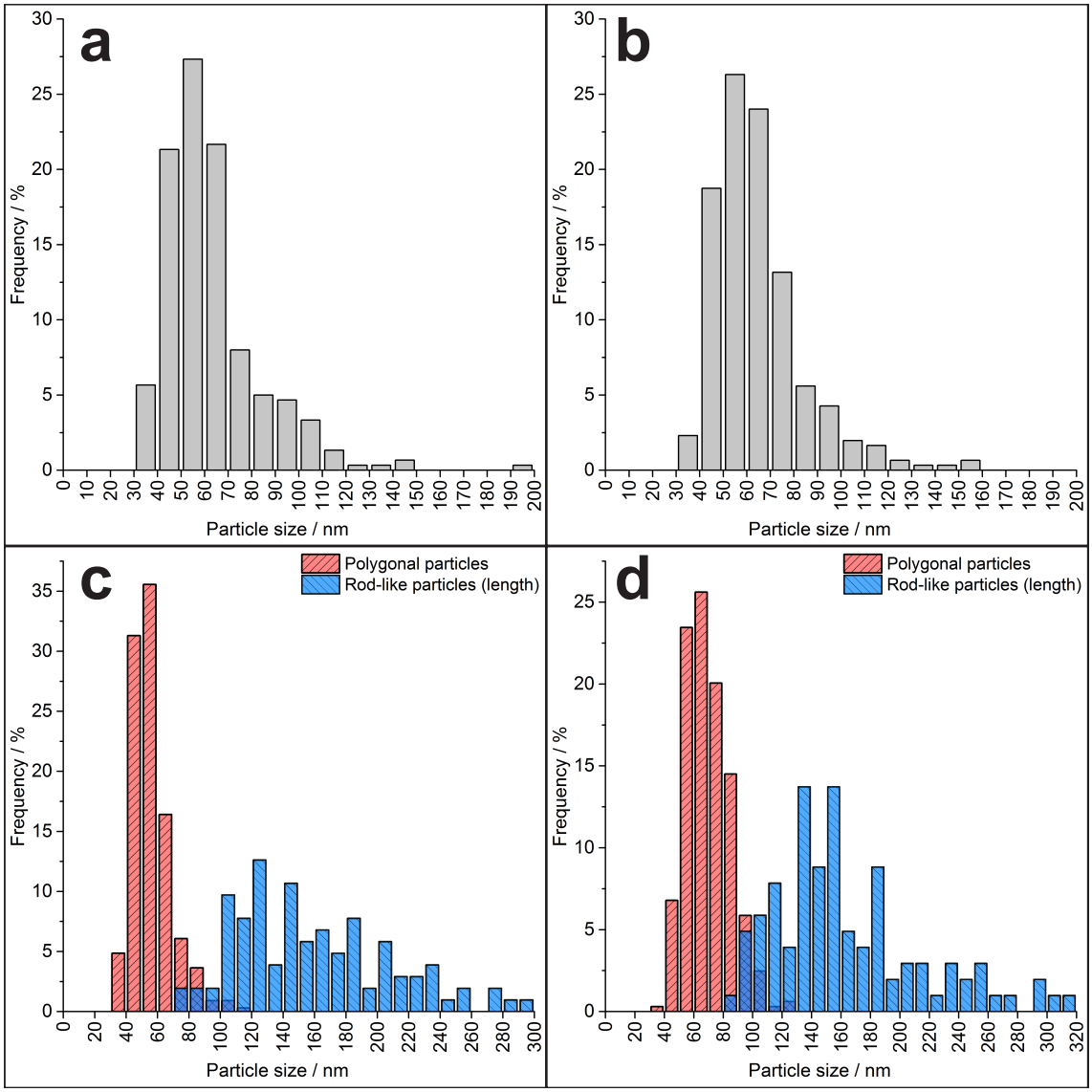

Figure 4.6 Particle size distributions obtained from the measurement of particles presented in TEM images for selected ZnO samples. Approximately 300 polygonal shaped particles were measured for samples prepared at (a) 0.1 M, (b) 0.5 M, (c) 0.7 M and (d) 1.0 M. Additionally, approximately 100 rod-like particles were measured for samples prepared at (c) 0.7 M and (d) 1.0 M.

Figure 4.6 shows the size distribution plots for selected ZnO samples. An initial observation of the distributions for samples prepared at 0.1 and 0.5 M (Figure 4.6(a) and (b)) shows that the distributions are similar; indeed this is confirmed by the particle size averages obtained: 63.0 ± 20.9 nm at 0.1 M, and 64.8 ± 19.4 nm at 0.5 M. At the pilot

scale, Gruar et al. obtained average particles sizes of 51.84 ± 13.84 nm and 103.72 ± 40.10 nm, at 0.1 M[‡] and 0.5 M, respectively (Gruar et al. 2013). At the mini

-pilot scale, the small difference between average particle sizes at these concentrations suggests that particles were formed with less growth from solution. In contrast, at the pilot scale, the large difference suggests that solution mediated growth occurred, which led to larger particle sizes at the higher concentrations. In the CHFS process, the physicochemical properties of supercritical water present an environment in which a high supersaturation of precursor molecules is achieved (described in Chapter 1). This results in relatively rapid nucleation of nanoparticles under most circumstances. At higher precursor concentrations, when the concentration of precursor molecules decreases below the nucleation threshold, it is likely that growth from solution occurs. At the lower concentrations, it may be less likely for this to occur since the concentration of precursor molecules would naturally be lower. This may explain why larger particles are observed at higher concentration.

Table 4.1 Particle size measurements for selected ZnO samples prepared at the mini-pilot scale.

Sample (Precursor concentration)	**Particle size property / nm**				
	Average	**Standard deviation**	**D_{10}**	**D_{50}**	**D_{90}**
0.1 M	63.1	20.9	42.9	58.3	92.1
0.5 M	64.8	19.4	45.9	61.1	88.9
0.7 M (polygonal)	56.1	12.9	42.5	53.9	73.0
0.7 M (rod-like)	159.6	49.5	105.4	149.3	231.7
1.0 M (polygonal)	69.4	15.5	52.4	68.2	89.4
1.0 M (rod-like)	154.8	52.0	106.2	153.4	240.8

[‡] The average particle size for ZnO synthesised at the pilot scale at 0.1 M was conducted at a total flow rate of 800 mL min^{-1}. The remaining samples were prepared at a total flow rate of 700 mL min^{-1} (Gruar et al. 2013).

For samples prepared at 0.7 and 1.0 M, in addition to measuring the diameters of approximately 300 polygonal shaped particles, the lengths of approximately 100 rod-like particles were also measured; size distributions shown in Figure 4.6(c) and (d). It was necessary to treat the polygonal and rod-like particles as two separate distributions, because otherwise the polygonal distributions would have been skewed and unrepresentative. For polygonal shaped particles, particle size averages were obtained as: 56.1 ± 12.9 nm at 0.7 M and 69.4 ± 15.5 nm at 1.0 M.

Average lengths for rod-like particles were 159.6 ± 49.5 nm at 0.7 M and 154.8 ± 52.0 nm at 1.0 M; there is little variation in these values. However, one obvious difference is that rod-like particles have far greater standard deviations than polygonal shaped particles; this is also observed in the wide size distributions for rod-like particles in Figure 4.6(c) and (d). A detailed assessment of the growth of ZnO nanoparticles is provided later in section 4.4.2.

D values of D_{10}, D_{50} and D_{90} are used to describe particle size distributions; they report the particle size below which 10 %, 50 % and 90 % of the population lies, respectively. The D values for selected samples are given in Table 4.1. The values obtained for the polygonal and rod-like particles do not show large differences when comparing samples, suggesting that increasing precursor concentration does not affect the shape of the size distributions. To further investigate the morphologies of the ZnO nanoparticles, selected samples were investigated via scanning electron microscopy (SEM), shown in Figure 4.7. At 0.1 M and 0.5 M (Figure 4.7(a–d)), particles showed polygonal morphology. However, at the highest concentration of 1.0 M (Figure 4.7(e–f)), rod-like particles were also observed. The observations from SEM correlate well with those from TEM.

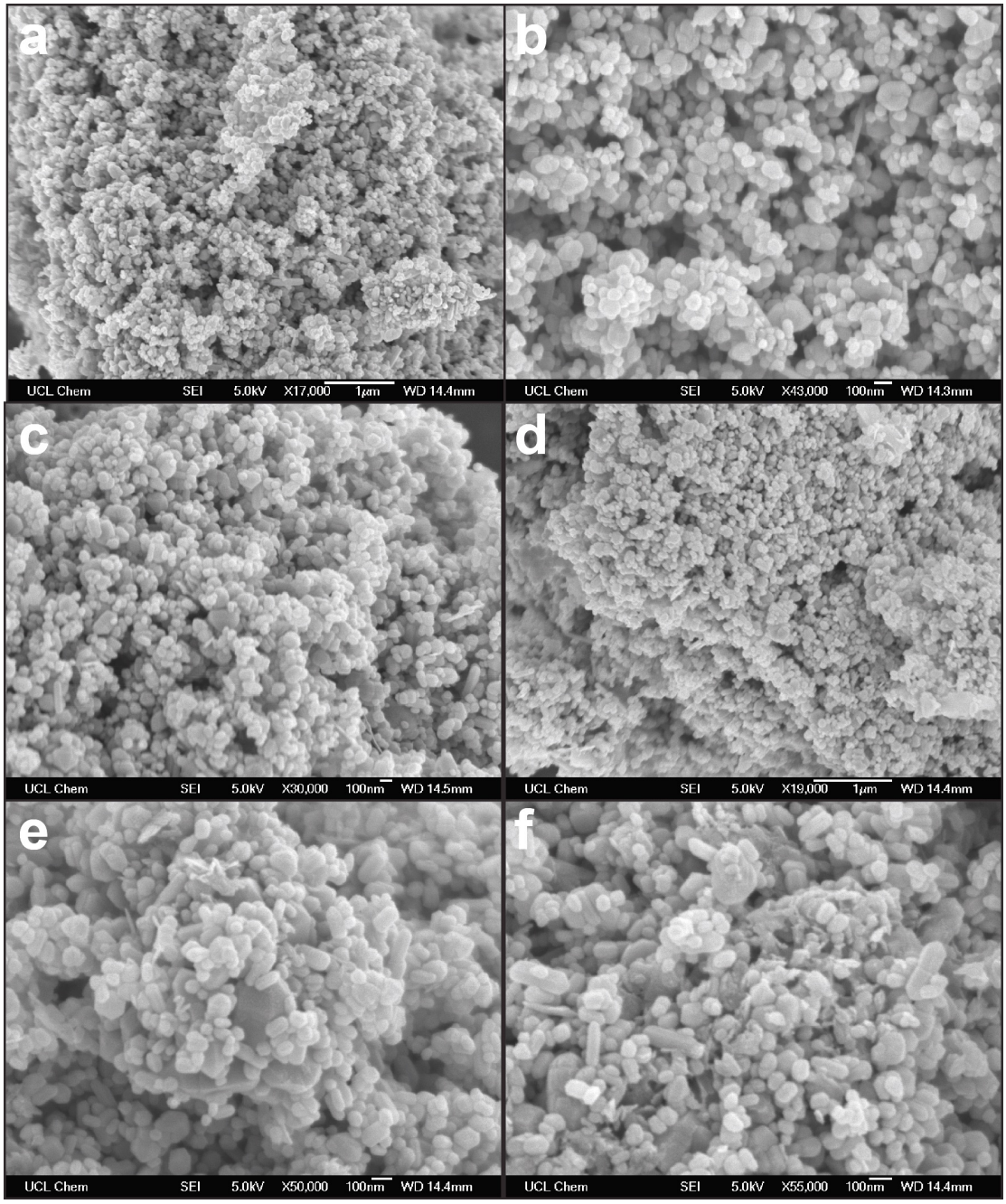

Figure 4.7 SEM images of ZnO nanoparticles synthesised by CHFS at precursor concentrations (a) and (b) 0.1 M, (c) and (d) 0.5 M, and (e) and (f) 1.0 M.

The nanoparticles observed in the TEM and SEM images can be described as agglomerates, where a number of primary particles come together and interact via either weak van der Waals interactions or potentially chemical bonds. In general, the particles are well defined and may not necessarily be fused together, suggesting that it should be possible to overcome particle-particle interactions, via post-treatment methods such as

use of a chemical agent (e.g. a surfactant). Nanoparticles have a tendency to agglomerate because their high relative surface area gives them a high surface energy; by forming agglomerates the relative surface energy can be reduced. Agglomerates consist of primary particles and can lead to the formation of aggregates through growth and sintering processes (Thanh et al. 2014). Furthermore, a number of aggregates may come together to form agglomerates. Since particle sizes can have a direct effect on the particles' properties, it is important to be able to understand the nucleation and growth mechanisms of nanoparticles.

4.4.2. Nucleation and growth mechanisms of zinc oxide

The formation of metal oxide particles under aqueous conditions is dominated by factors that affect their nucleation, growth and aging processes (described in Chapter 1) (Oskam 2006). Since these processes can affect particle properties, it is important to have an understanding of how reaction conditions are related to the formation of the particles. The following section describes the formation of zinc oxide nanoparticles, a well-studied process under hydrothermal conditions (Li et al. 1999; Demianets and Kostomarov 2001; Demianets et al. 2002; Callahan et al. 2011; Zhang et al. 2011; Nicholas et al. 2012; Liang et al. 2014).

The reactions that occur in the hydrothermal synthesis of ZnO nanoparticles can be summarised as follows. Upon mixing of the zinc salt solution with a mineraliser (e.g. potassium hydroxide), an insoluble zinc hydroxide is formed:

$$Zn^{2+} + 2OH^- + 2H_2O \rightarrow Zn(OH)_2 + 2H_2O \qquad \text{(Equation 4.1)}$$

The attraction of ions to $Zn(OH)_2$ leads to the formation of growth units:

$$Zn(OH)_2 + 2OH^- \rightarrow [Zn(OH)_4]^{2-} \qquad \text{(Equation 4.2)}$$

Demianets et al. stated that the $[Zn(OH)_4]^{2-}$ growth unit can dissociate to form $[ZnO_2]^{2-} + 2H^+$, where $[ZnO_2]^{2-}$ is another growth unit (Demianets et al. 2002). It has been suggested that clusters are formed by the dehydration reaction of growth units (Li et al. 1999) as shown in Equation 4.3:

$$[Zn(OH)_4]^{2-} + [Zn(OH)_4]^{2-} \rightarrow Zn_2O(OH)_6^{4-} + H_2O \qquad \text{(Equation 4.3)}$$

When the size of the cluster reaches a critical size, a nucleus is formed, and consequently the ZnO crystal precipitates:

$$[Zn_xO_y(OH)_z]^{(z+2y-2x)-} \text{ (nucleus)} + [Zn(OH)_4]^{2-} \qquad \text{(Equation 4.4)}$$

$$\rightarrow [Zn_{x+1}O_{y+1}(OH)_{z+1}]^{(z+2y-2x+2)-} + H_2O$$

The subscripts x, y, z represent the numbers of Zn^{2+}, O^{2-} and OH^- in the crystal, respectively. Li et al. suggested that the stacking of polyhedra by sharing the corners, edges or faces of a polyhedron, forms the ZnO crystal. Within the crystal, polyhedra are connected by sharing O^{2-}, and at the interface, the terminal vertex is an OH^-. Therefore, these terminal OH^- groups are denoted in the structure of the cluster (Equation 4.4), but since their numbers are very low in comparison to the number of ions within the crystal, the cluster is simply represented as ZnO (Li et al. 1999).

In alkaline solutions, the hydrothermal growth of zinc oxide is known to occur with distinct facets: two monohedra, (0001) and $(000\bar{1})$ ($+c$ and $-c$ planes, respectively); six hexagonal prismatic faces, $(10\bar{1}0)$ *m* planes; and six hexagonal pyramid faces, $(10\bar{1}1)$ *p* planes (Demianets et al. 2002; Callahan et al. 2011). These planes are identified in Figure 4.8. The facets have independent growth rates, which may vary under various synthesis conditions, leading to particle anisotropy.

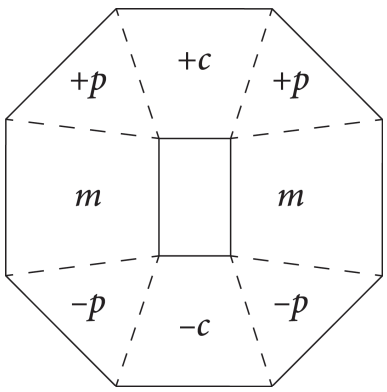

Figure 4.8 Schematic drawing of a cross-section of a representative zinc oxide crystal showing different growth facets.

Zinc oxide is a polar crystal that has its polar axis along the *c*-axis. Each crystallographic plane has a unique surface energy that will interact differently with ions in solution. The Zn^{2+} based growth units, which have tetrahedral geometry, are slightly polarised because of the displacement of the Zn cation (Yin et al. 2005), and they may bond together differently depending upon their coordination number (i.e. the number of points of attachment available for bonding). The corner of a growth unit may bond to three growth units, the edge may bond to two growth units, and the face may bond to one growth unit. This suggests that the fastest growth rate is for the crystallographic planes where corners are present, and slowest where faces are present.

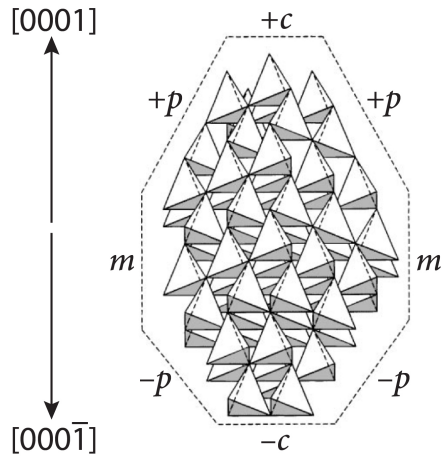

Figure 4.9 Diagram of the ZnO crystal structure represented by the coordination of Zn^{2+} growth unit tetrahedra. Reprinted (adapted) from (Li et al. 1999) with permission from Elsevier.

Figure 4.9 shows that a different type of element (corner, edge or face) of the tetrahedral unit is present at the interface for each crystallographic plane. In the ⟨0001⟩ direction (+*c* axis), each tetrahedron has a corner present, whilst in the ⟨000$\bar{1}$⟩ direction (–*c* axis) a face of each tetrahedron is present. In the hexagonal prismatic direction (*m* planes), half of the tetrahedra have a corner present, whilst the other half has a face present. In the hexagonal pyramid direction (+*p* and –*p* planes), half of the tetrahedra have corners and edges, whilst the other half have faces and edges, present at the interface. Accordingly, the growth rate is fastest in the +*c* direction and slowest in the –*c* direction (Li et al. 1999).

The +*c* and –*p* surfaces are terminated by Zn^{2+} ions, and the –*c* and +*p* surfaces are terminated by O^{2-} ions; consequently, these surfaces have polarity. It is believed that the polarisation and the presence of high coordination corners, makes the +*c* direction preferential for bonding of growth units. Hence, ZnO typically forms particles with elongation in the *c* direction, often yielding structures such as rods, needles and prisms (Masuda and Kato 2008).

For the ZnO samples prepared at the pilot scale, Gruar et al. stated that preferential growth was related to the ratio of growth units to the number of nucleates formed. The morphology change was attributed to the rapid formation of insoluble zinc species (i.e. growth units), and their rapid increase in concentration under the given reaction conditions (Gruar et al. 2013). At the mini-pilot scale, it is believed that a similar mechanism of growth occurs. Across the range of concentrations, the size distributions for polygonal particles were relatively similar (within one standard deviation of the mean), suggesting that similar growth processes were observed. It is only at the higher concentrations that preferential growth in the +*c* direction occurred, which may be related to the larger number of growth units in solution. At the mini-pilot scale it appeared that the critical size that a cluster must have formed, before ZnO precipitated, was in the range 20–30 nm, because at all concentrations, the minimum measured particle size was within this range. CHFS syntheses typically have short reaction times (because of the short residence time in the reactor), which may explain why the growth of ZnO particles is limited in comparison to other hydrothermal processes.

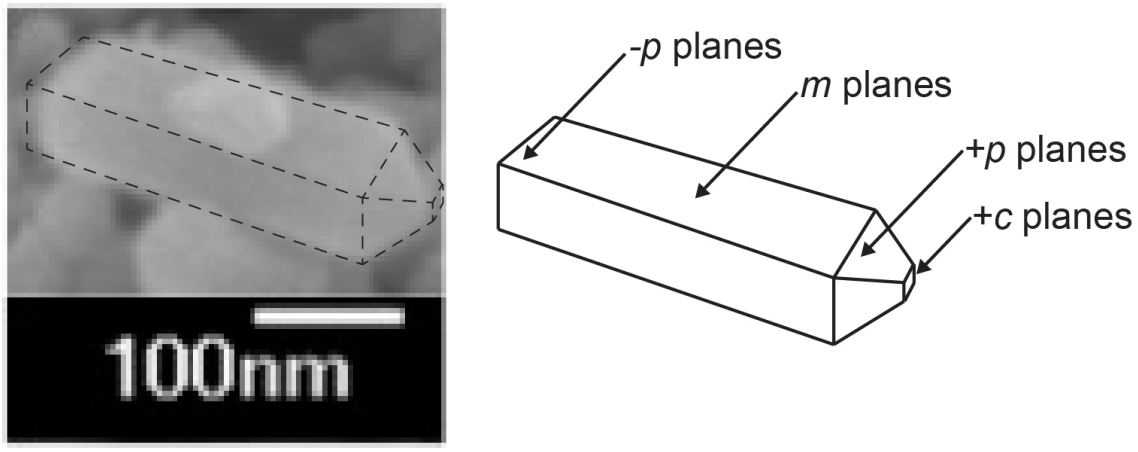

Figure 4.10 SEM image of rod-like zinc oxide nanoparticle showing evolution of fast growth planes, as identified in the schematic diagram (cf. Figures 4.3, 4.8 and 4.9).

The growth of ZnO nanoparticles at the higher precursor concentrations showed evolution of the fast growth planes as described earlier, shown in Figure 4.10. A number of prismatic faces were observed (in the horizontal plane of the image) terminated by pyramidal faces. Whilst a number of these rod-like particles were observed at the higher concentrations, the majority of particles appeared polygonal shaped, unlike at the pilot scale, where there appears to be a larger proportion of rod-like particles at nearly all concentrations. These reactions demonstrate that whilst CHFS scale-up is readily achievable, in the case of nano-zinc oxide, the reaction conditions must be carefully chosen, in order to synthesise particles with identical characteristics between the process scales. However, despite these limitations, which may be material dependent, the overall aim of scaling CHFS processes is successfully achieved in comparison to other synthesis techniques.

4.5. CONCLUSIONS

In summary, this chapter has shown that CHFS processes can be readily scaled, with the synthesis of zinc oxide used as a system to evaluate the similarities and differences between the mini-pilot and pilot scale reactors. It was shown that up to a precursor concentration of 0.5 M, particles appeared to have similar size and morphology; however, at higher concentrations, a degree of particle growth was observed. Zinc oxide is known to have high-energy facets that give it fast growth directions, namely in the +*c* direction. The particle growth observed yielded rod-like particles, which may be the evolution of growth in this direction. In comparison, literature on similar experiments conducted at the pilot scale, suggested that particle growth was more pronounced, and hence a mass-based scale up (at least of zinc oxide) would require careful consideration of reaction conditions. It is suggested that these differences may have occurred as a result of small differences present in the particle nucleation and growth phases, to which zinc oxide may be very sensitive. Nevertheless, this does not mean that other material compositions may be limited in the same way, which would require detailed evaluations. The work has demonstrated that scale-up of CHFS processes is readily achievable, and although particle sizes of ZnO were larger at the pilot scale than the mini-pilot scale, further investigations may prove to be beneficial in determining how reaction conditions between the two process scales are related.

Chapter 5. Surface functionalisation and particle size control of zinc oxide via CHFS

5.1. AIMS AND OUTLINE

The aim of the work presented in this chapter was to investigate the synthesis of surface functionalised zinc oxide via in process and post synthesis methods, and to develop techniques that were able to impart particle size control via CHFS synthesis. Results previously described in Chapter 4 and in the literature, showed that it was possible to synthesise zinc oxide nanoparticles via CHFS, with average particles sizes in the range 50 – 70 nm, dependent upon precursor concentration. The investigations that followed were aimed at reducing the size of zinc oxide nanoparticles, and to functionalise their surface so as to obtain nanoparticle dispersions. The ZnO materials were evaluated for their ability to act as UV attenuators in functional coatings.

5.2. INTRODUCTION

There is a growing interest in synthesis methods that are able to produce dispersed nanoparticles, since they can help to limit nanoparticle agglomeration. In many applications, agglomeration should be limited, because it can prevent access to the unique properties of nanoparticles. Many different methods have been reported for surface functionalisation of nanoparticles, both as one-step and two-step processes. One-step processes are preferred, because they are able to directly produce dispersed nanoparticles, and they may provide better control over particle agglomeration than a two-step process. However, one potential drawback of current one-step processes is that they tend to be batch-type, and hence they may suffer from the limitations of such (which have been described in Chapter 1). In particular, scale up of such processes may be difficult.

In this work, the synthesis of surface functionalised zinc oxide nanoparticles, in a one-step CHFS process, was investigated. The CHFS process that was used for the synthesis of zinc oxide nanoparticles in Chapter 4 was further developed, to allow surface

functionalisation to occur immediately after nanoparticles are formed. A second mixing point (confined jet mixer, CJM) was used to allow a feed of capping agent to mix with the nanoparticle slurry, whilst also lowering the mixing temperature. In Chapter 4, the mass-based scale up of zinc oxide via CHFS, typically obtained particles with sizes greater than 50 nm. In certain applications of zinc oxide, such as UV attenuation, it is beneficial to reduce particle size, because optical properties (amongst others) are dependent on particle size. Therefore, in an effort to reduce the particle size of ZnO synthesised via CHFS, a novel seeding approach was investigated. A TiO_2 sol was used as a seeding agent, to provide nucleation sites for ZnO formation. TiO_2 sols have previously been used in CHFS processes for the synthesis of perovskite structure titanate materials (Hakuta et al. 2005; Matsui et al. 2008; Hayashi et al. 2010a), but there are no known reports of their use as seeding agents.

The zinc oxide samples were then formulated as UV curable coatings, which were coated on polyester films and UV cured. The coatings were evaluated for their performance as UV light attenuators.

5.3. EXPERIMENTAL METHODS

All nanoparticle synthesis experiments discussed in this chapter were prepared on the mini-pilot scale CHFS reactor, the design and operation of which are described in Chapter 2.

5.3.1. Chemicals and materials

Zinc nitrate hexahydrate ($[Zn(NO_3)_2 \bullet 6H_2O]$, reagent grade, 98 %), citric acid (99 % assay), titanium(IV) bis(ammonium lactato)dihydroxide (50 wt% in solution; referred to as TiBALD) and potassium hydroxide pellets (KOH, ≥ 85 %) were supplied by Sigma-Aldrich (Dorset, UK). Polymeric surfactants (Solsperse™ 41000, Solsperse™ 44000, Solplus™ D570 and Solplus™ J945) were obtained from Lubrizol Limited (Derby, UK). Photomer 4017 (1,6-hexanediol diacrylate, an acrylate monomer), Photomer 6690 (a hexafunctional aliphatic urethane acrylate oligomer), Omnirad TPO (2,4,6-trimethylbenzoyl-diphenyl phosphine oxide, a type I photoinitiator) and Omnirad 73 (2-hydroxy-2-methyl-1-phenylpropanone, a type I photoinitiator) were obtained from

IGM Resins B.V. (The Netherlands). All chemicals were used as received. Deionised (DI) water (10 MΩ) was used throughout.

5.3.2. In process surface functionalisation

Surface functionalised zinc oxide nanoparticles were synthesised on the mini-pilot scale reactor, which was used in a four-pump configuration with the double confined jet mixer (CJM) arrangement. The second CJM acted as a surfactant-containing quench. Pump 1 was used to feed a flow of DI water through an electrical heater, with a set-point temperature of 450 °C. Pump 2 and Pump 3 were used to feed flows of zinc nitrate and KOH (both at ambient temperature), respectively, to a tee-piece mixer and then to the first CJM (CJM-1) where a rapid crystallisation occurred. Pump 4 was used to feed an aqueous flow of a surface functionalising agent to a second CJM (CJM-2), where the feed met the product stream (containing nanoparticles) from CJM-1. A summary of synthesis conditions is provided in Table 5.1 and Table 5.2. The products of reaction were further cooled in-flow (pipe-in-pipe heat exchanger) and collected as slurries. Surface functionalised nanoparticles were cleaned via dialysis, otherwise samples were cleaned and dried as described earlier in Chapter 2.

Table 5.1 Synthesis conditions for zinc oxide synthesised with a flow of citric acid (as a surface functionalising agent) in CJM-2. [a]

Sample	**Additive** [b]	**Additive conc. / mol%**
ZnO/CA0 [b]	–	–
ZnO/CA1	Citric acid	1.0
ZnO/CA5	Citric acid	5.0
ZnO/CA7.5	Citric acid	7.5
ZnO/CA10	Citric acid	10.0
ZnO/CA10[pH]*	Citric acid	10.0

[a] All samples were prepared using 0.5 M $Zn(NO_3)_2$ and 0.5 M KOH, except the sample marked * which used 0.75 M KOH.

[b] For sample ZnO/CA0, a flow of DI water was fed via Pump 4 instead of surfactant.

Samples prepared with citric acid were labelled according to the mol% of citric acid (e.g. ZnO/CA5 corresponded to 5 mol% citric acid; Table 5.1). Samples prepared with polymeric surfactants were labelled according to the surfactant used and its vol% (e.g. ZnO/C0.1 corresponded to Solsperse™ 44000 at 0.1 vol%; Table 5.2). The flow rates were fixed for all syntheses at 80 mL min^{-1} (Pump 1), 40 mL min^{-1} (Pump 2), 40 mL min^{-1} (Pump 3) and 160 mL min^{-1} (Pump 4). A theoretical reaction point temperature of 335 °C was achieved in CJM-1 and 187 °C in CJM-2.

Table 5.2 Synthesis conditions for zinc oxide synthesised with a flow of polymeric surfactants in CJM-2.

Sample	**Surfactant [b]**	**Surfactant conc. / vol%**
ZnO/A [b]	–	–
ZnO/B0.1	Solsperse™ 41000	0.1
ZnO/B0.5	Solsperse™ 41000	0.5
ZnO/B1.0	Solsperse™ 41000	1.0
ZnO/C0.1	Solsperse™ 44000	0.1
ZnO/C0.5	Solsperse™ 44000	0.5
ZnO/C1.0	Solsperse™ 44000	1.0
ZnO/D0.1	Solplus™ D570	0.1
ZnO/D0.5	Solplus™ D570	0.5
ZnO/D1.0	Solplus™ D570	1.0
ZnO/D2.0	Solplus™ D570	2.0
ZnO/E0.1	Solplus™ J945	0.1
ZnO/E0.5	Solplus™ J945	0.5

[a] All samples were prepared using 0.2 M $Zn(NO_3)_2$ and 0.5 M KOH.

[b] For sample ZnO/A, a flow of DI water was fed via Pump 4 in substitution of a surfactant.

5.3.3. Zinc oxide size control via a seeding approach

The synthesis of zinc oxide via a new two-step seeding approach was conducted on the mini-pilot scale reactor. The first step comprised the synthesis of the seed material, a dispersed TiO_2 sol. The sol was then used in the second step for the seeded synthesis of zinc oxide.

5.3.3.1. Synthesis of TiO_2 sol

The TiO_2 sol was synthesised using a four-pump mini-pilot scale CHFS configuration with the double CJM arrangement, where all pumps were operated at a pressure of 24.1 MPa. Pump 1 was used to feed a flow of DI water (80 mL min^{-1}) through an electrical heater, with a set-point temperature of 450 °C. Pump 2 and Pump 3 (40 mL min^{-1} each) were used to feed flows of TiBALD (0.3 M) and KOH (0.18 M), respectively, at ambient temperature to a tee-piece mixer, and then to CJM-1 where the combined feed met a flow of supercritical water. The product stream from CJM-1 met a flow of TiBALD (0.3 M) that was fed via Pump 4 (160 mL min^{-1} at ambient temperature) in CJM-2. The slurry was cooled in-flow, collected and stored until use (without further processing).

Table 5.3 Synthesis conditions for seeded ZnO nanoparticles synthesised with a TiO_2 sol acting as a seeding agent. The KOH concentration was 0.4 M for all experiments.

Sample	**[$Zn(NO_3)_2$] / M**	**[TiO_2 sol] / M**	**TiO_2 sol / mol%**
ZnO-1	0.2	–	–
ZnO/Ti-1	0.19	0.00125	0.65
ZnO/Ti-2	0.18	0.0025	1.40
ZnO/Ti-3	0.16	0.005	3.00
ZnO/Ti-4	0.14	0.0075	5.10

5.3.3.2. Seeded synthesis of zinc oxide

Seeded zinc oxide samples were synthesised using a three-pump configuration with a single CJM. Pump 1 was used to feed a flow of DI water (80 mL min^{-1}) through an

electrical heater with a set-point temperature of 450 °C. Pump 2 was used to feed a combined flow of a chosen zinc nitrate and TiO_2 sol concentration (40 mL min^{-1}) and Pump 3 was used to feed a flow of KOH (both at ambient temperature), to a tee-piece mixer where the two feeds mixed (see Table 5.3 for precursor concentrations). The combined feed then met a flow of supercritical water in a CJM. The concentration of metal salt (Pump 2) was up to 0.2 M with the TiO_2 sol added at up to 5.10 mol%. KOH was used at 0.4 M throughout. Synthesis conditions are provided in Table 5.3.

5.3.4. Combined nanoparticle seeding and in process surface functionalisation

Syntheses were carried out to surface functionalise the seeded zinc oxide nanoparticles that were prepared using a TiO_2 sol (described in section 5.3.3.1) in process with surface functionalising agents. The synthesis was carried out similarly to that described in section 5.3.3.2, except the mini-pilot scale reactor was used in a four pump configuration. Pump 4 was used to feed a flow of a Solplus™ D570 to CJM-2, where it met the product stream (zinc oxide) from CJM-1. The concentration of the TiO_2 sol was varied (as before) and the concentration of the surfactant remained constant. A summary of the synthesis conditions is provided in Table 5.4.

Table 5.4 Synthesis conditions for zinc oxide synthesised with a TiO_2 sol (acting as a seeding agent) and a polymeric surfactant (Solplus™ D570).

Sample	**[$Zn(NO_3)_2$] / M**	**[TiO_2 sol] / M**	**TiO_2 sol / mol%**
ZnO-1a	0.2	–	–
ZnO/Ti-1a	0.19	0.00125	0.65
ZnO/Ti-2a	0.18	0.0025	1.40
ZnO/Ti-3a	0.16	0.005	3.00
ZnO/Ti-4a	0.14	0.0075	5.10
In all experiments listed here, a flow of surfactant (Solplus D570) at 0.5 vol% was pumped to CJM-2 via pump 4.			

5.3.5. Post synthesis surface functionalisation, formulation preparation and coating

Post synthesis surface functionalisation of zinc oxide samples, prepared as described in section 5.3.3.2, was investigated by the addition of ZnO powder to a solvent-surfactant system. The mixtures were subsequently prepared as UV curable formulations that were coated on glass substrates.

ZnO powder (0.33 g) was added to a mixture of 1,6-hexanediol diacrylate (HDDA; Photomer 4017) solvent (0.55 g) and Solsperse™ 41000 (surfactant) (0.12 g). The mixture was sonicated for 10 minutes and then stirred at 750 rpm for 1 hour. The resulting mixture was a milky white liquid. The zinc oxide dispersion was added to a mixture (3.00 g) of 70:30 wt% Photomer 6690:Photomer 4017 (oligomer:monomer), and stirred at 1000 rpm for 15 minutes on a bench top stirrer. A 60:40 wt% mixture (0.25 g) of Omnirad TPO:Omnirad 73 (photoinitiators) was added to the formulation, and stirred for a further 10 minutes at 1000 rpm. The final formulation contained 10 wt% zinc oxide. The formulation was doctor-bladed on to a glass substrate, and cured under UV light (254 nm) for 5 minutes. Cured films were subsequently delaminated for imaging.

5.3.6. Formulation and UV cured coatings at MacDermid Autotype

5.3.6.1. Zinc oxide (seeded) dispersion preparation (UCL)

Powder zinc oxide samples ZnO-1 and ZnO/Ti-4 were dispersed (post synthesis), and provided to Dr Nigel Holmes at MacDermid Autotype (Wantage, Oxfordshire, UK). Zinc oxide powder (ZnO-1: 30 wt% and ZnO/Ti-4: 15 wt%) was added to a solvent-surfactant mixture of HDDA (Photomer 4017) and Solsperse™ 41000. The surfactant was added at 35 wt% with respect to the mass of zinc oxide powder. The dispersion was stirred at 1000 rpm for 1 hour using a bench-top stirrer (IKA).

5.3.6.2. Formulation and coating preparation (MacDermid Autotype)

Dr Nigel Holmes prepared UV curing formulations and subsequently coated the formulations on polyester film. A stock lacquer consisting of a 70:30 wt% mixture of

Ebecryl 5129 (oligomer) and 1,6-hexanediol diacrylate (monomer) was prepared. The dispersed zinc oxide formulations were added to the lacquer at varying quantities, and Irgacure 2020 (a photoinitiator mixture of α-hydroxy benzophenone and bis-acyl phosphine oxide) was also added to each formulation. Table 5.5 provides details on each formulation, where samples are labelled according to the sample number of the ZnO powder sample and the ZnO wt% in the formulation, i.e. NH-4-1.6 identifies a formulation prepared using ZnO sample ZnO/Ti-4 with 1.6 wt% ZnO in the coating.

Table 5.5 Coating formulation preparation identifying the ZnO sample and wt% used to prepare each formulation.

Formulation	**ZnO sample**	**ZnO wt%**
NH-0-0	None (control)	0
NH-1-2.7	ZnO-1	2.7
NH-1-1.1		1.1
NH-4-1.6	ZnO/Ti-4	1.6
NH-4-0.6		0.6

Each formulation was laminated between sheets of an untreated polyester film (Kodak) and adhesion treated grade of polyester film (Melinex 715). The coating was cured by passing the laminate beneath two 300 W in^{-1} medium pressure mercury lamps (operating at 100 % output and line speed of 10 m min^{-1}).

Dr Nigel Holmes subsequently conducted a number of measurements on the cured coatings. The thickness of coatings was measured using an Avantes interferometer, and haze and light transmission measurements were conducted on a Gardner Pacific Haze-Gard apparatus. The hardness of the coatings was measured using a JIS pencil test with an applied load of 1 kg. Pencil hardness varies from 9B (softest) to 9H (hardest). Five attempts were made to scratch the surface of each coating with 2H, 3H and 4H pencils.

Solvent resistance was determined by subjecting the coatings to 50 double-rubs with a paper towel soaked in methyl ethyl ketone (MEK).

The coatings were then provided to UCL where UV-visible spectroscopy measurements were conducted.

5.3.7. Materials characterisation

Zinc oxide samples prepared via CHFS were characterised by powder X-ray diffraction (XRD), high-resolution transmission electron microscopy (HR-TEM) and energy dispersive X-ray spectroscopy (EDX), scanning electron microscopy (SEM), UV-visible spectroscopy and dynamic light scattering (DLS). A description of these techniques is provided in Chapter 2.

5.4. RESULTS AND DISCUSSION

5.4.1. In process surface functionalisation of ZnO with citric acid

The following section reports the results of an investigation of the in-process surface functionalisation of ZnO nanoparticles, using citric acid as a capping agent. Citric acid was added to the process in CJM-2, after the formation of nanoparticles had occurred in CJM-1. This allowed citric acid to be added at a lower temperature, since the product stream had begun to cool as it flowed away from CJM-1. The concentration of citric acid was varied from 0–10 mol% relative to the zinc nitrate concentration, and samples were collected as white slurries. Nanoparticles readily settled out and yields were in the range 1–50 %; as citric acid concentration increased, the product yield decreased.

Figure 5.1 shows the powder X-ray diffraction patterns obtained of the ZnO samples. All samples were indexed to the hexagonal wurtzite structure of ZnO, in good agreement with ICSD reference pattern 26170. Crystallite sizes calculated for each sample using the Scherrer equation were in the range 24–30 nm (data not shown). In Chapter 4, zinc oxide prepared at an identical precursor concentration (0.5 M for zinc nitrate and KOH) but in a three-pump configuration, gave a larger crystallite size of 47 nm. In this work, the flow of DI water or citric acid solution (aq.) in CJM-2, which

was at ambient temperature, lowered the temperature of the product feed from CJM-1 when the two flows mixed. Hence, the residence time for the product stream from CJM-1, was lower in the double CJM reactor than it was in the single CJM reactor; indeed, this was confirmed by residence times of 0.76 s and 4.16 s, respectively.

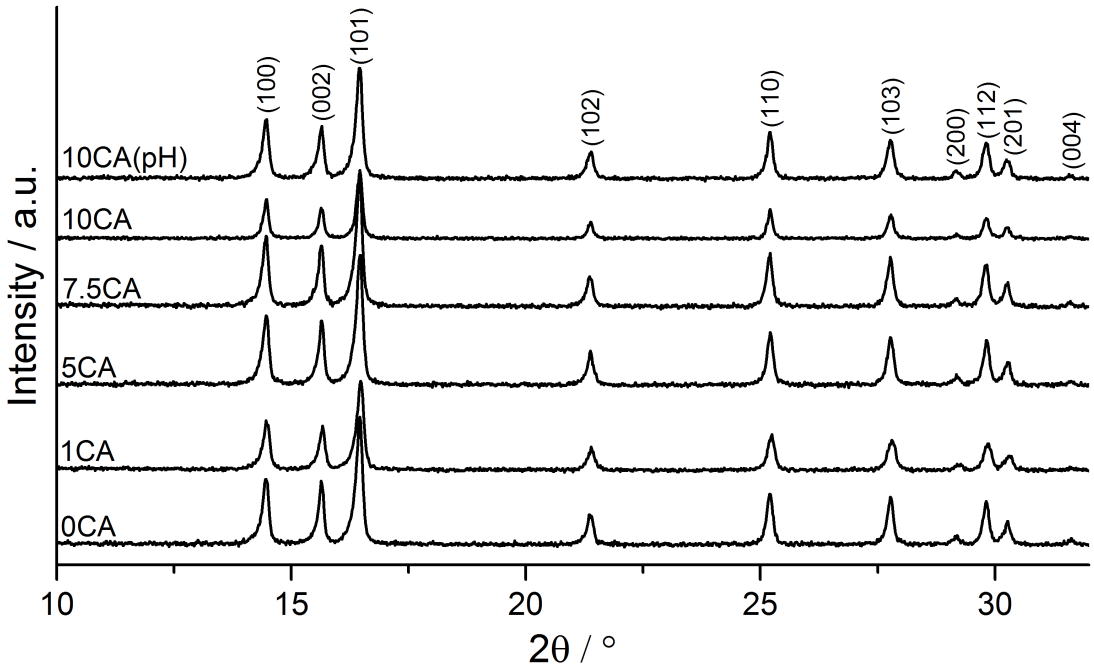

Figure 5.1 Powder X-ray diffraction patterns of zinc oxide prepared with citric acid used as a surface functionalising agent. Data collected using Mo-Kα radiation (λ = 0.709 Å).

It is likely that the lower residence time was responsible for the smaller crystallite sizes obtained in the double CJM reactor. Sample ZnO/CA0 was observed by high resolution transmission electron microscopy (Figure 5.2). Particle size measurements (approximately 300 particles) were conducted to obtain a representative particle size distribution (Figure 5.3).

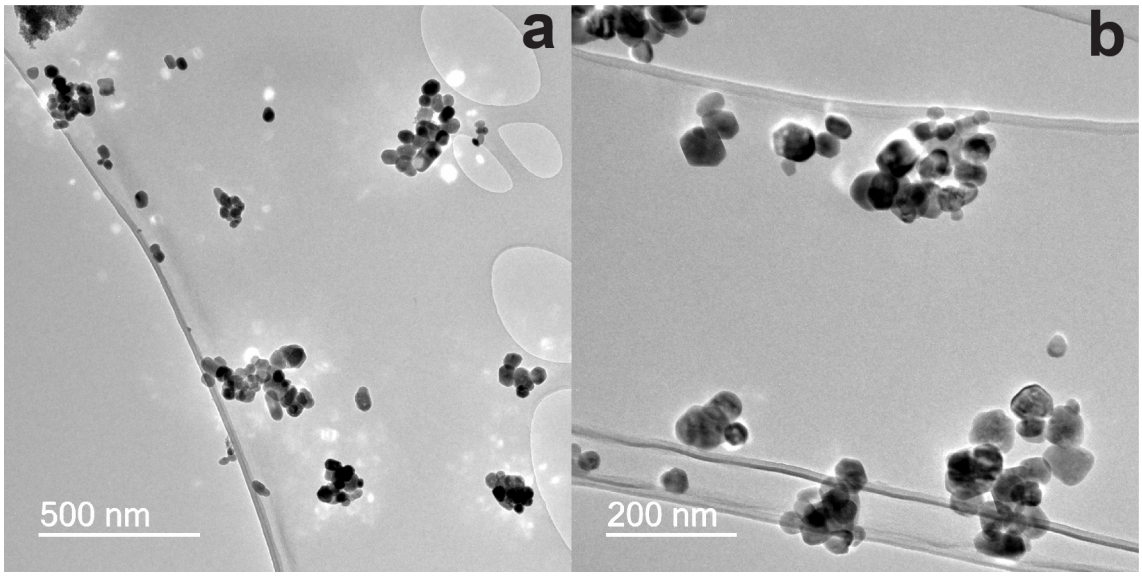

Figure 5.2 HR-TEM images of ZnO nanoparticles (sample ZnO/CA0) synthesised by CHFS in a four-pump configuration with a double CJM arrangement. Zinc nitrate and potassium hydroxide were both maintained at 0.5 M and a flow of DI water (at ambient temperature) was mixed with the product stream in CJM-2.

Sample ZnO/CA0 had an average particle size of 45.2 ± 19.1 nm and D_{10}, D_{50} and D_{90} values of 29.1, 41.8 and 63.2 nm, respectively, with a 50 % product yield. The sample discussed in Chapter 4 had an average particle size of 64.8 ± 19.4 nm and D_{10}, D_{50} and D_{90} values of 45.9, 61.1 and 88.9 nm, respectively, with a 70 % product yield. It is clear from this data that whilst the lower residence time limited particle growth, it also reduced the product yield, suggesting that, following particle nucleation, the growth stage was shorter in the double CJM reactor, and hence, less precursor material was consumed in the reaction. This may also explain why the average particle size was lower.

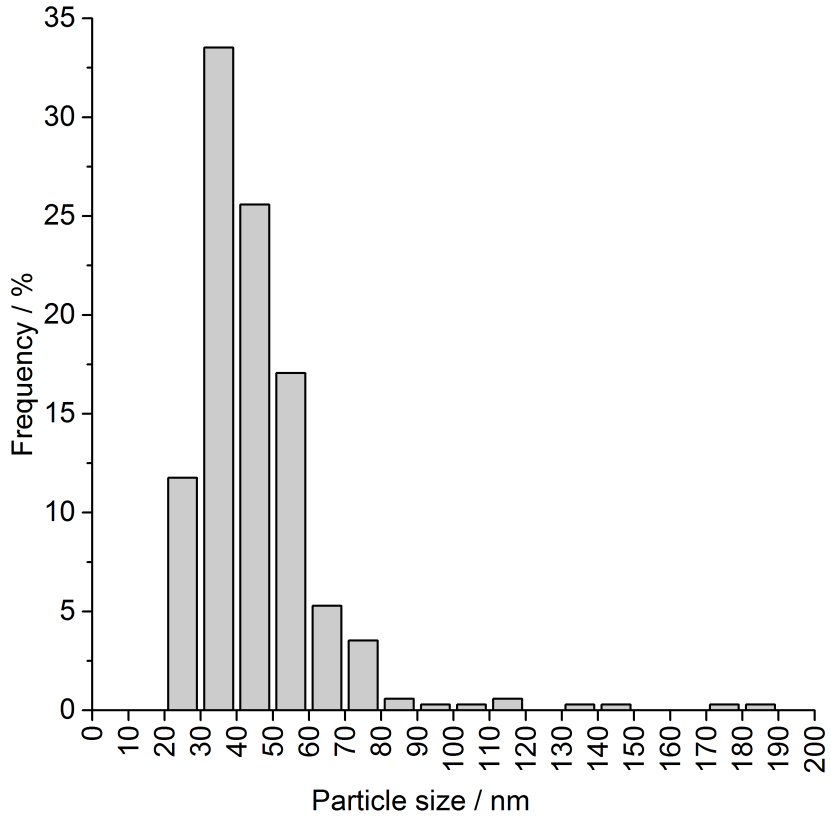

Figure 5.3 Particle size distribution obtained from the measurement of approximately 300 particles presented in TEM images for sample ZnO/CA0.

On the addition of citric acid as a surface functionalising agent, product yields were substantially lower (1 – 47 %) in comparison to sample ZnO/CA0. Although ZnO was synthesised under identical conditions (i.e. in CJM-1) for each sample (except ZnO/CA10[pH]), addition of citric acid at increasing concentration would have decreased the pH of the product stream. Solubility of ZnO increases as pH decreases; hence it is likely that ZnO dissolved in solution, giving lower product yields. At all citric acid concentrations used in this study, ZnO readily settled out, which suggested that even if surface functionalisation had occurred, it was not sufficient to stabilise particles. In an effort to increase product yield at the highest citric acid concentration (10 mol%), the concentration of potassium hydroxide was increased to 0.75 M (from 0.5 M), to increase the pH of the product stream before it mixed with citric acid. Indeed, the product yield increased as expected, but again, settling out readily occurred. Gruar et al. have demonstrated in-process surface functionalisation of iron oxide with citric acid in a CHFS process (Gruar 2012; Gruar et al. 2015), albeit with a different engineering

configuration (citric acid was added via counter-current flow to the product stream from the CJM, rather than a co-current flow such as that used herein). Iron oxide nanoparticles were obtained as fine dispersions and it was found that the concentration of citric acid and the residence time, largely affected the dispersion of the nanoparticles. The mixing temperature at the point where the iron oxide nanoparticles mixed with citric acid was reported in the range 216 – 277 °C, which was significantly higher than the mixing temperature used in this work (≈187 °C).

The absence of particle stabilisation in this work may be a result of a number of factors: the mixing temperature may have been too low to enable citric acid to bind to ZnO (although iron oxide has been functionalised previously at only 95 °C (Sahoo et al. 2005)), inadequate mixing (the feed issuing from CJM-2 (where mixing of ZnO and citric acid occurred) was characterised by transitional flow, i.e. between laminar and turbulent), or the incompatibility of citric acid with the surface of zinc oxide. However, given that product yields were below average, and any effort to increase them may have affected other properties of ZnO (because of complex reaction conditions), it was decided to further investigate surface functionalisation with polymeric surfactants.

5.4.2. In process surface functionalisation of ZnO with polymeric surfactants

A CHFS experiment was conducted to investigate the surface functionalisation of ZnO nanoparticles using a range of polymeric surfactants. The aim of the study was to determine the effects of such surfactants on the stability, dispersibility and morphology of ZnO nanoparticles. Surfactants were added as aqueous solutions that were fed in to CJM-2, to allow them to mix with the product stream issuing from CJM-1. Zinc oxide nanoparticles were synthesised under identical conditions for each experiment, where zinc nitrate and potassium hydroxide were used at 0.2 and 0.5 M, respectively, throughout. The surfactant was used at up to three concentrations: 0.1, 0.5 and 1.0 vol%. The concentration of zinc nitrate was reduced in comparison to that described in section 5.4.1 to increase reaction pH and product yield.

Samples were collected as white slurries with pH in the range 5–7, and were cleaned via dialysis and/or centrifugation (as described in Chapter 2). The addition of Solsperse™

44000 and Solplus™ D570 surfactants in CJM-2, resulted in partially dispersed zinc oxide. Other surfactants (Solsperse™ 41000 and Solplus™ J945) did not yield samples that were dispersed; ZnO readily settled out and yields appeared to decrease as surfactant concentration increased. A number of factors may be responsible for the absence of surface functionalisation, such as the concentration of surfactant (there may have been only partial coverage or collapse of the polymeric layer), or surfactant incompatibility under CHFS reaction conditions (in the case of Solsperse 41000, which, under ambient conditions, has the ability to disperse ZnO as described later).

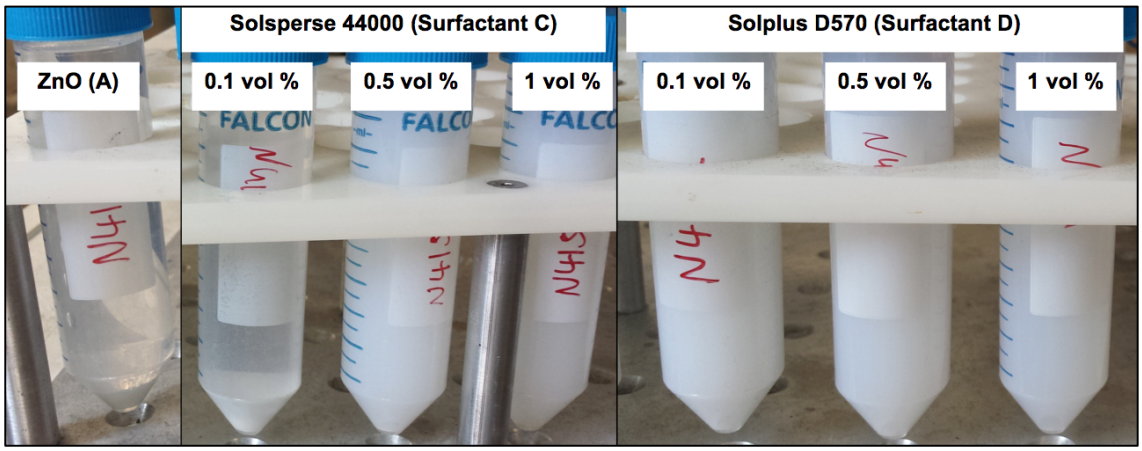

Figure 5.4 Photograph of selected zinc oxide samples 24 hours after collection, prepared with an aqueous flow of surfactant in CJM-2. For comparison, pure ZnO is also shown. Solsperse™ 44000 partially dispersed ZnO at 0.5 and 1.0 vol%, whilst Solplus™ D570 also partially dispersed ZnO at 0.1 vol%.

Figure 5.4 shows the appearance of selected samples 24 hours after collection. As expected, zinc oxide prepared in the absence of a surfactant (with DI water in CJM-2) settled out readily. At the three concentrations investigated, Solsperse™ 44000 effectively dispersed ZnO at 0.5 and 1.0 vol%, and Solplus™ D570 effectively dispersed ZnO at all three concentrations used. Visually, after a 24-hour period there did not appear to be any settling. Dynamic light scattering (DLS) was used to determine the hydrodynamic diameter (Z-average) size in the dispersions, as shown in Figure 5.5, for samples prepared with Solplus™ D570 at 0.1 and 1.0 vol% over a 15-hour period. There is a small, gradual decrease in the hydrodynamic diameters over time suggesting that larger particles settled out slowly. However, the results confirmed that it was possible to

obtain ZnO dispersions via the addition of aqueous surfactants in CJM-2. To improve the quality of the dispersion, further experiments would be required to optimise the synthesis conditions. Another parameter that is obtained via DLS measurements is the polydispersity index (PdI), which gives a measure of the dispersity of a sample. Samples that have a polydispersity index less than 0.1 are regarded as monodisperse, whilst values above 0.5 may indicate the presence of very large agglomerates. For the samples analysed herein the average PdI values were less than 0.25, indicating a degree of polydispersity.

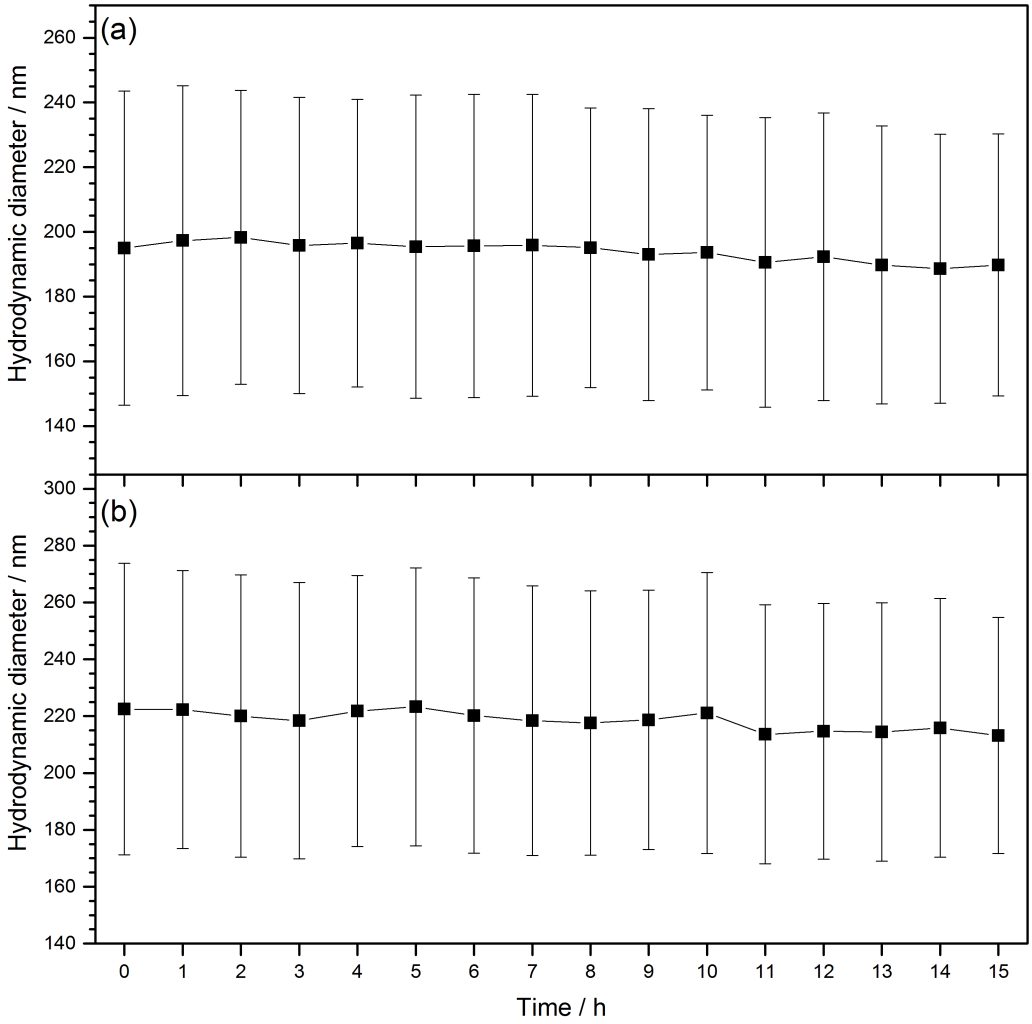

Figure 5.5 Variation in hydrodynamic diameter over a 15-hour period for ZnO synthesised with surfactant (Solplus™ D570) at (a) 0.1 and (b) 1.0 vol%. Error bars show the polydispersity measured at each point.

Selected samples were investigated via scanning electron microscopy (SEM), to observe the effects of surfactants on particles (Figure 5.6). Where there was a flow of DI water (ambient temperature) in CJM-2, ZnO nanoparticles appeared polygonal and highly agglomerated, similar to that described earlier in Chapter 4. Solsperse™ 44000 appeared to induce the formation of microspheres, which had a stratified structure. There were small breaks in the structure where small agglomerates of nanoparticles were observed (Figure 5.6(d)), which were confirmed as ZnO via energy dispersive spectroscopy (data not shown). It appears that ZnO nanoparticles were encapsulated within the microspheres, which imparted stabilisation to ZnO. During imaging, a fog-like appearance was observed when the electron beam was focussed on a microsphere for a prolonged period, which may suggest that polymerisation of adventitious carbonaceous material began to occur. In the case of Solplus™ D570, particles appear fairly dispersed. This result was promising since it supported the observations of dispersion made of the sample slurries following collection (Figure 5.4).

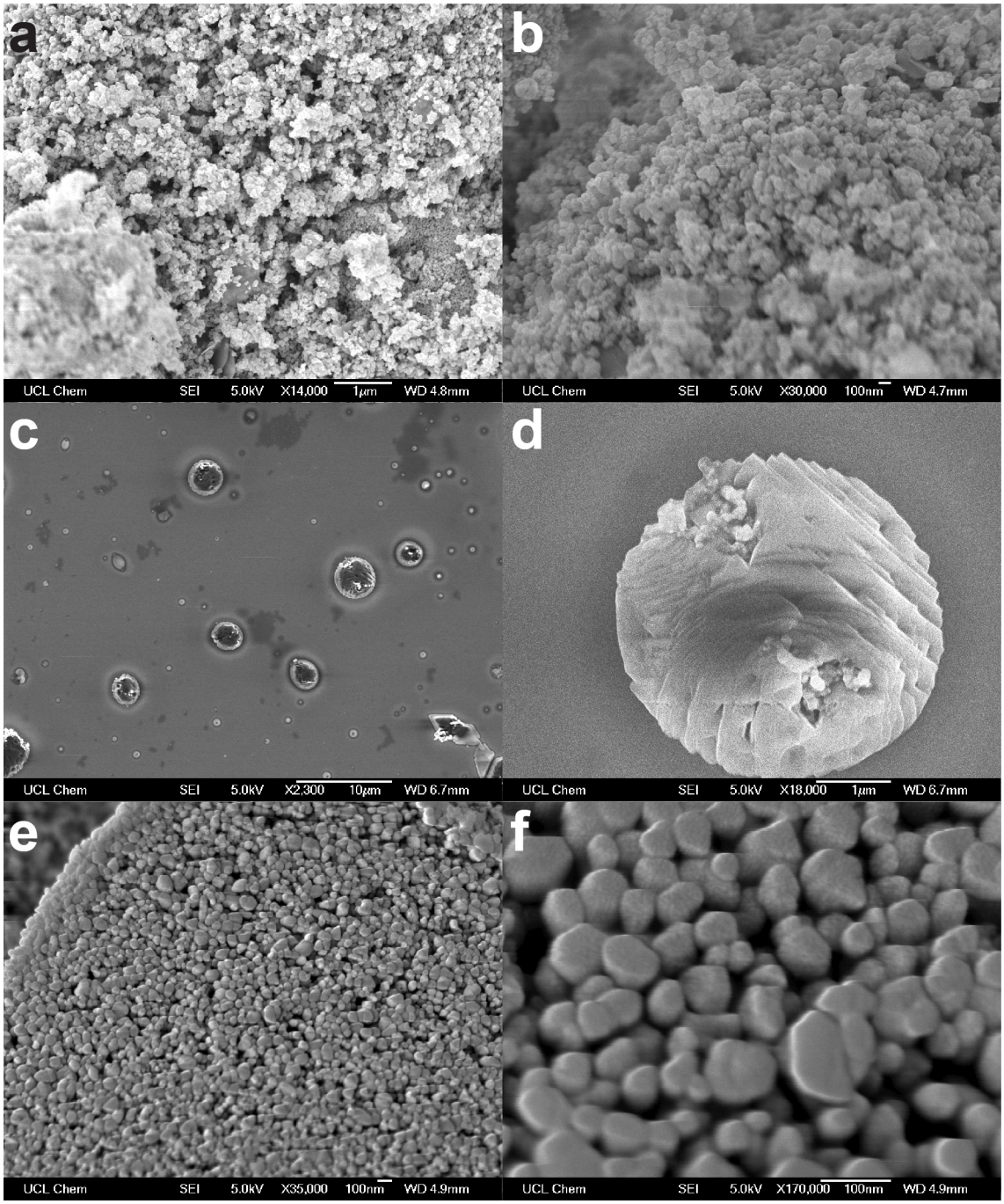

Figure 5.6 SEM images of ZnO nanoparticles synthesised in a double CJM configuration with a flow of: (a) and (b) water, (c) and (d) Solsperse™ 44000 (0.5 vol%), (e) and (f) Solplus™ D570 (1.0 vol%), in CJM-2.

5.4.3. Zinc oxide size control via a seeding approach

The results discussed in Chapter 4 and earlier in section 5.4.1 showed that zinc oxide was prepared in the CHFS reactor with a minimum average particle size of

approximately 50 nm. Whilst this was sufficiently small, particles below 50 nm may significantly improve the optical effects of ZnO, which would be very beneficial not only in improving functionality, but also for many aesthetic reasons (e.g. in coating applications to limit haze and increase transparency). To further reduce the particle size of ZnO prepared via CHFS, one approach would have been to reduce the residence time within the reactor. However, this may have negatively impacted on the product yield, as it was observed earlier with sample ZnO/CA0 (section 5.4.1). Another approach would have been to lower the reaction temperature; however, this would have potentially affected particle properties such as crystallinity.

A nanoparticle seeding approach, which has previously been reported in batch hydrothermal syntheses but not for continuous hydrothermal (Baruah and Dutta 2009a; Henley et al. 2010), was used to provide nucleation sites for nanoparticle formation. In this approach, the seed material was a fine dispersion of titanium dioxide nanoparticles, which were pre-formed in the CHFS reactor. The TiO_2 seed material was mixed with zinc nitrate that met a flow of potassium hydroxide, as previously described. It was important for the seed material to be a fine dispersion so as to prevent settling of the material within the CHFS reactor, which may have otherwise led to blockages. The concentration of the seed material was varied to determine the effects of such.

5.4.3.1. TiO_2 sol as a seeding agent

A TiO_2 sol was prepared in a four-pump arrangement with a double CJM configuration. In CJM-1, a flow of TiBALD and KOH met a flow of supercritical water, resulting in nucleation of TiO_2 nanoparticles. The product stream issuing from CJM-1 then met a flow of TiBALD in CJM-2, wherein it was likely that the lower mixing temperature allowed ligands from TiBALD, to bind to the surface of the TiO_2 nanoparticles, affording stability against settling. The powder X-ray diffraction pattern of the TiO_2 sol (Figure 5.7) was indexed to the anatase structure of TiO_2, in agreement with TiO_2 prepared via CHFS shown in this thesis (Chapter 3) and by others (Thompson et al. 2009; Zhang et al. 2009a; Zhang et al. 2009b; Lübke et al. 2015b).

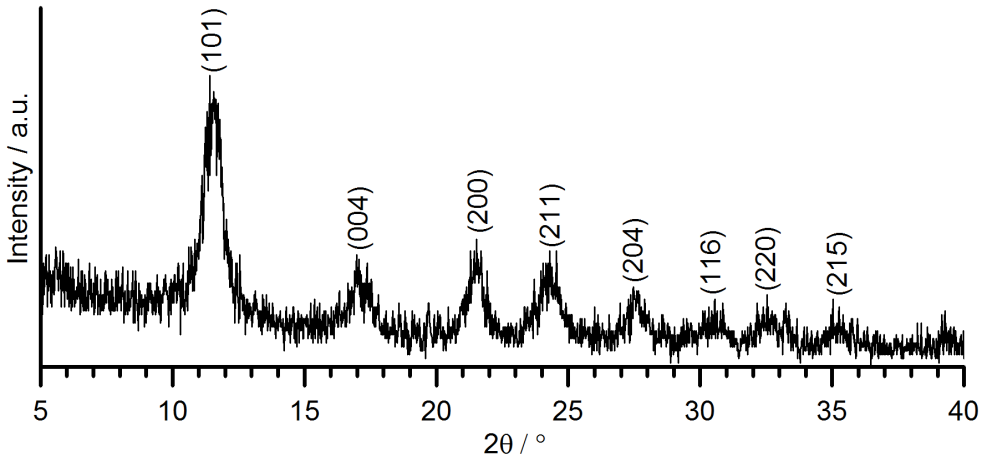

Figure 5.7 X-ray diffraction pattern of TiO_2 sol as prepared in the CHFS process. Data collected using Mo-Kα radiation (λ = 0.709 Å).

Upon visual inspection, the TiO_2 sol did not appear to settle, remaining as a fine dispersion even after a period of more than 6 months. Hydrodynamic diameter measurements were obtained for a period of 60 hours, shown in Figure 5.8. There did not appear to be any significant changes in the hydrodynamic diameter, suggesting that the sol was indeed a stable dispersion. No further processing of the TiO_2 sol was required prior to use.

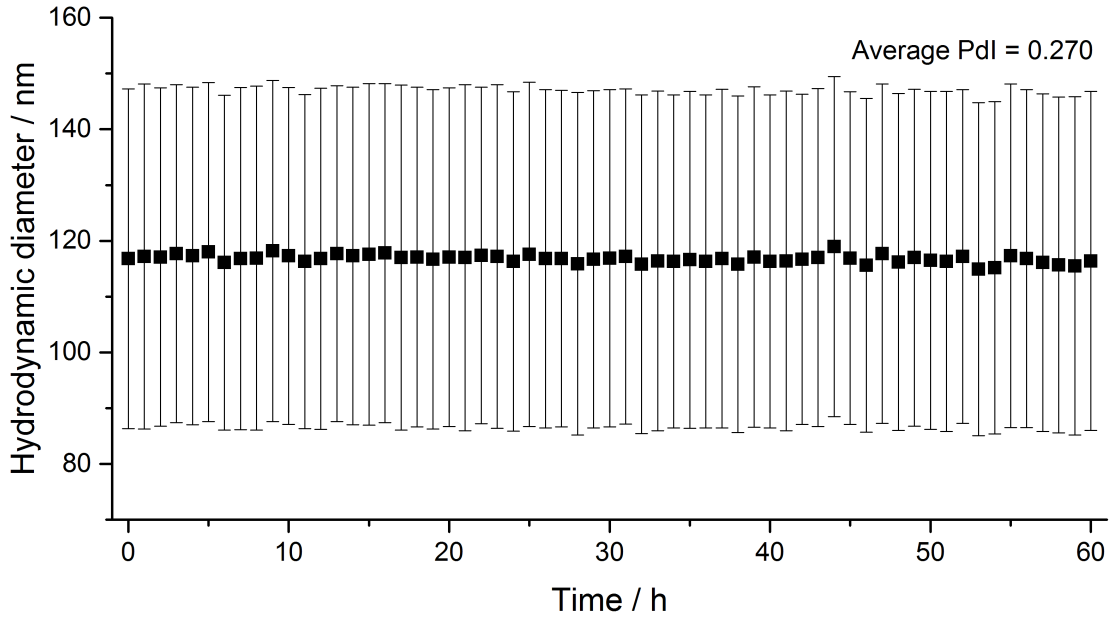

Figure 5.8 Hydrodynamic diameter of as-prepared TiO_2 sol over a 60-hour period.

5.4.3.2. Synthesis of seeded zinc oxide

Seeded zinc oxide was synthesised using the TiO_2 sol as a seeding agent at various TiO_2 concentrations. As a general trend, as the concentration of the TiO_2 sol was increased, it was found that peaks in the powder X-ray diffraction patterns became broader (Figure 5.9), suggesting that crystallite sizes were decreasing. Interestingly, the presence of TiO_2 peaks was not observed in the powder XRD patterns.

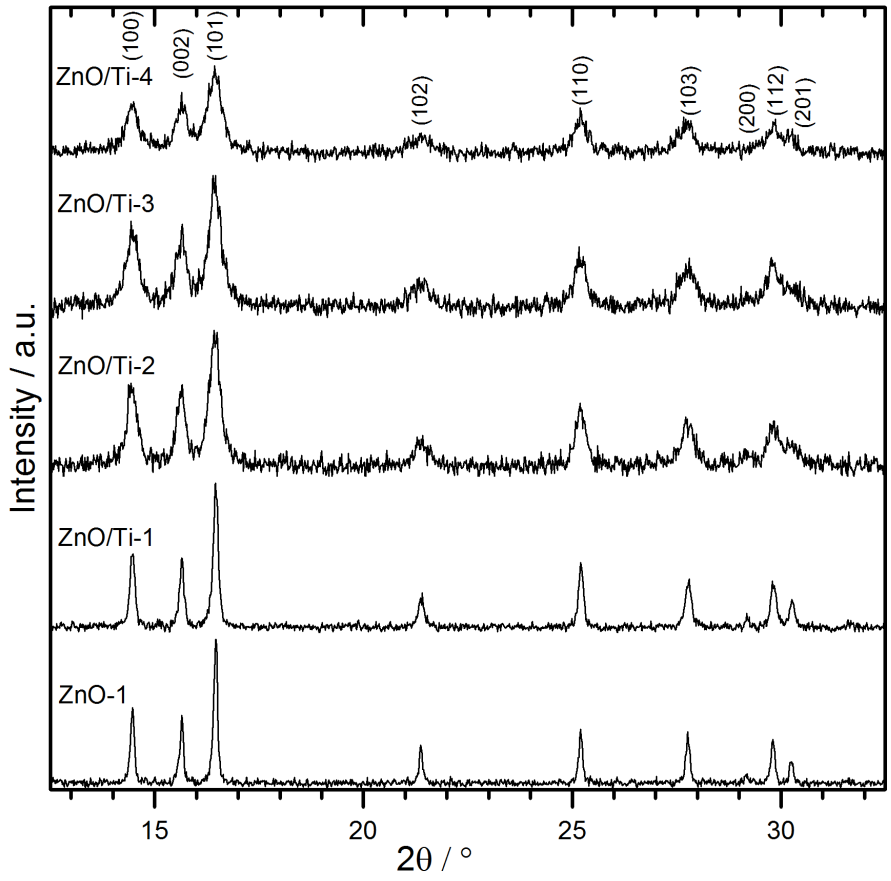

Figure 5.9 Powder X-ray diffraction patterns for seeded zinc oxide prepared via the CHFS process (via a seeding approach, where a TiO_2 sol was used at increasing concentrations (see Table 5.3 for reaction conditions)). Data collected using Mo-Kα radiation (λ = 0.709 Å).

The crystallite size for each sample was inferred from application of the Scherrer equation, using the full width half maximum value of the (100) diffraction peak (Figure 5.10). In agreement with observations from the powder X-ray diffraction patterns, crystallite size estimates decreased from ca. 42 to 10 nm as the concentration of the TiO_2 sol was increased. This suggested that it would be possible to reduce the average size of

ZnO by varying the concentration of the TiO_2 sol. Additionally, only relatively small concentrations of the sol were required to have a large impact on the crystallite size.

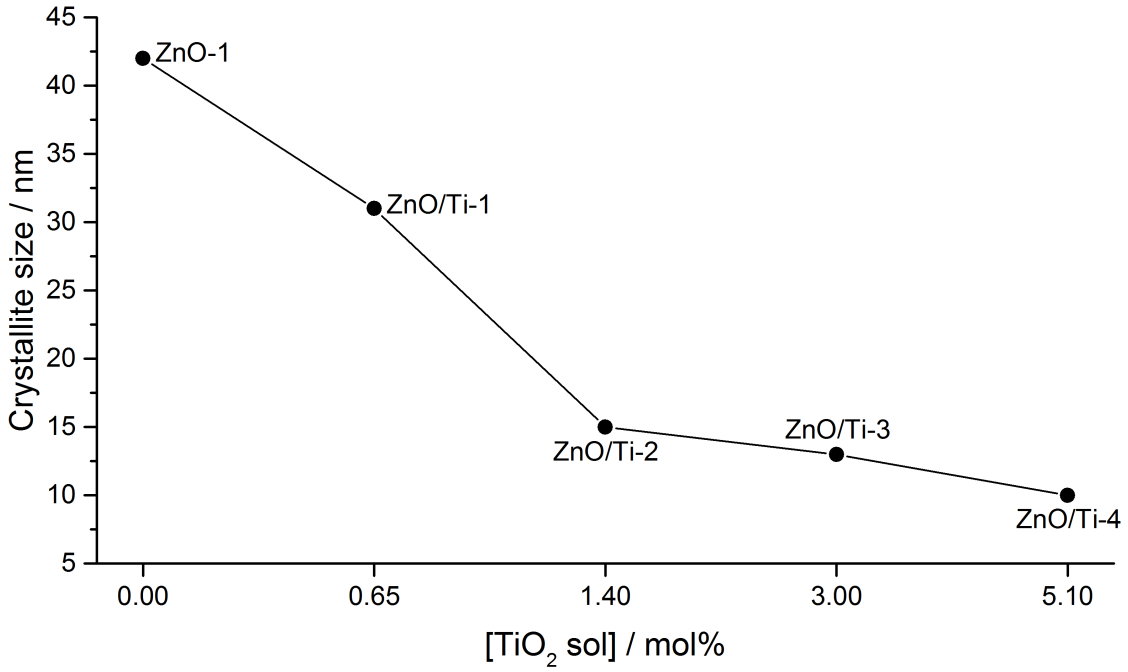

Figure 5.10 Comparison of the crystallite size obtained from application of the Scherrer equation on the (100) diffraction peak for ZnO samples (prepared using a TiO_2 sol as a seeding agent) versus the TiO_2 sol concentration used in the initial CHFS synthesis.

Selected samples were observed by HR-TEM to determine effects of the TiO_2 sol concentration on size and morphology (Figure 5.11). The images generally showed polygonal shaped particles that were highly agglomerated, similar to those observed in Chapter 4. However, there also appeared to be a number of significantly smaller particles, which may have been the TiO_2 sol (as seen in Figure 5.11(c)). Energy dispersive X-ray (EDX) spectroscopy was conducted on sample ZnO/Ti-3, and suggested the presence of titanium (as an oxide) at approximately 7 at% (Figure 5.12(a)). Elemental mapping using EDX showed that titanium (oxide) was dispersed across the sample, although some regions were more concentrated (Figure 5.12(b)).

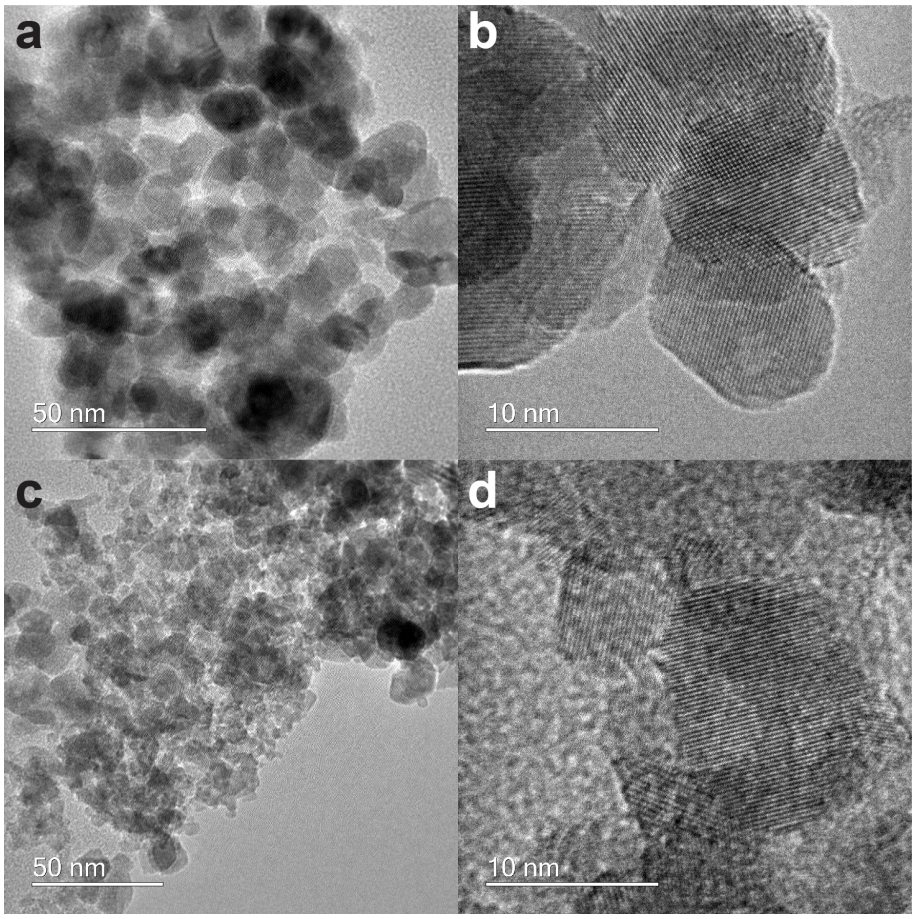

Figure 5.11 HR-TEM images of ZnO nanoparticle samples (a) and (b) ZnO/Ti-2, and (c) and (d) ZnO/Ti-4, synthesised by CHFS with the addition of a TiO_2 sol used as a seeding agent.

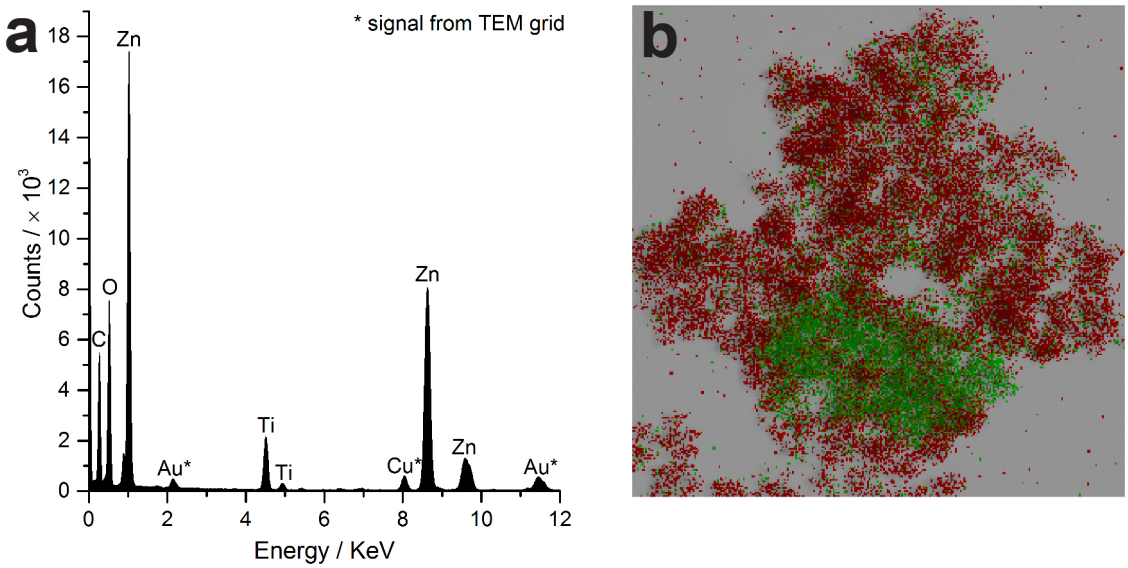

Figure 5.12 (a) Energy dispersive X-ray (EDX) spectrum and (b) elemental composition map of sample ZnO/Ti-3. Zinc is represented by the red colour, and titanium by the green colour.

Light absorption properties of the ZnO samples were investigated using UV/vis spectroscopy. Figure 5.13 and Figure 5.14 show the UV/vis spectra obtained for the ZnO samples as powders (diffuse reflectance), and as 0.02 wt% dispersions in water (transmission), respectively. As powders, the spectra showed very little variation as the ZnO particle size decreased (as the TiO_2 sol concentration increased). Typically, a blue shift in the absorbance profile would be expected with decreasing particle size; this was possibly observed at $\lambda \approx 375$ nm, but the effect was not very pronounced. This may be interpreted (possibly incorrectly) as there being little change with particle size. However, diffuse reflectance measurements are prone to the light scattering effect of particles, which may 'hide' any presence of a blue shift. Therefore, it was necessary to obtain measurements of UV/vis absorbance via dispersions, because scattering is negligible in dispersed media. As dispersions (Figure 5.14), there were clear variations in the absorbance profiles. Zinc oxide prepared in the absence of any TiO_2 sol (sample ZnO-1), showed a typical absorption profile, with a sharp cut-off at approximately 370 nm. Whilst the addition of TiO_2 at the lowest concentration (0.65 mol%; sample ZnO/Ti-1), did not greatly change the absorption profile, the absorbance maximum greatly increased in the range 250-370 nm. The crystallite size had decreased for this sample (from 42 nm for sample ZnO-1 to 31 nm for sample ZnO/Ti-1), and therefore, in theory, a blue shift in absorbance would have been expected. However, the unexpected increase in absorbance may have resulted from the presence of TiO_2 (a reference spectrum of CHFS TiO_2 is shown). As the TiO_2 sol concentration was increased (and crystallite size decreased), a decrease in absorbance was observed.

A report in the literature showed that UVA absorbance of ZnO nanoparticles decreased as particle sizes were reduced below 40 nm (Goh et al. 2014). The authors reported detrimental effects on the UVA/UVB absorbance ratio, as a broad exciton-related peak at 360-370 nm disappeared. Similar observations are made herein, where the change in absorbance profile shape appears to also be related to the exciton-related peak. Another feature of the spectra obtained in this work, is that absorbance in the visible region ($\lambda > 400$ nm) appears to decrease as particle size decreased. Since smaller particles scatter less light than larger particles, a smaller absorbance at these wavelengths may be expected. In terms of aesthetics, it is beneficial to have minimum absorbance in the visible, because this would give higher transparency in applications where it is desired,

e.g. in sunscreens or UV attenuating coatings. There appears to be a compromise between zinc oxide particle size and UVA absorbance; however, the results suggest that synthesising ZnO with the TiO_2 sol was beneficial in two aspects: reducing particle size and increasing UV absorbance (relative to ZnO prepared without the sol).

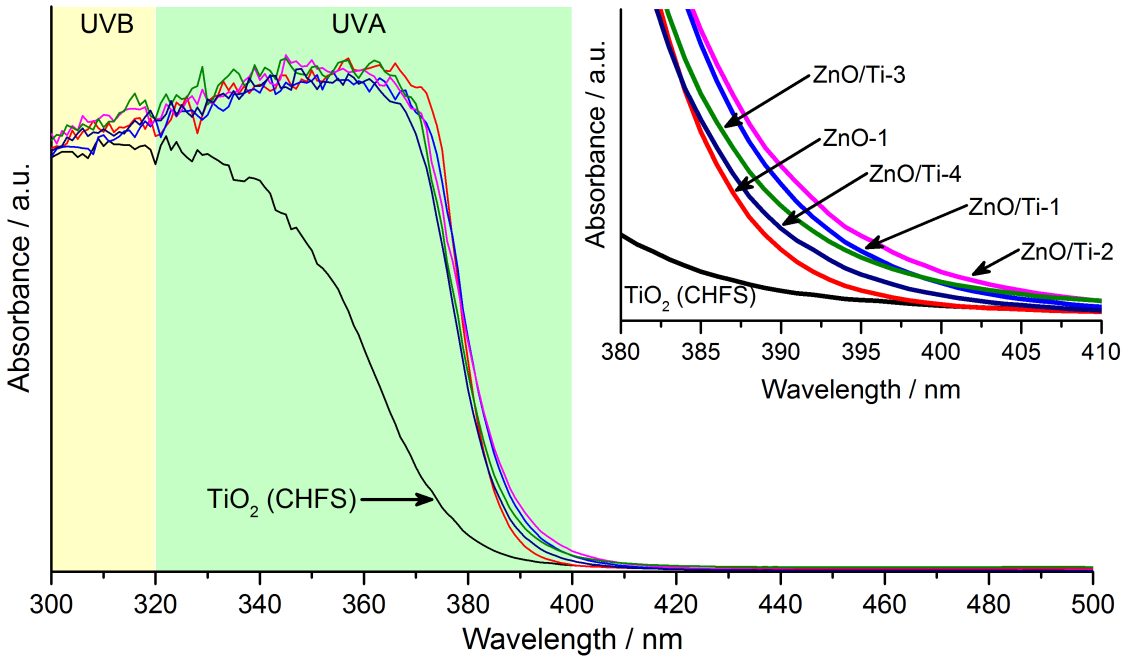

Figure 5.13 UV/Vis spectra of seeded ZnO samples as powders. Samples were prepared using a TiO_2 sol as a seeding agent in the CHFS synthesis.

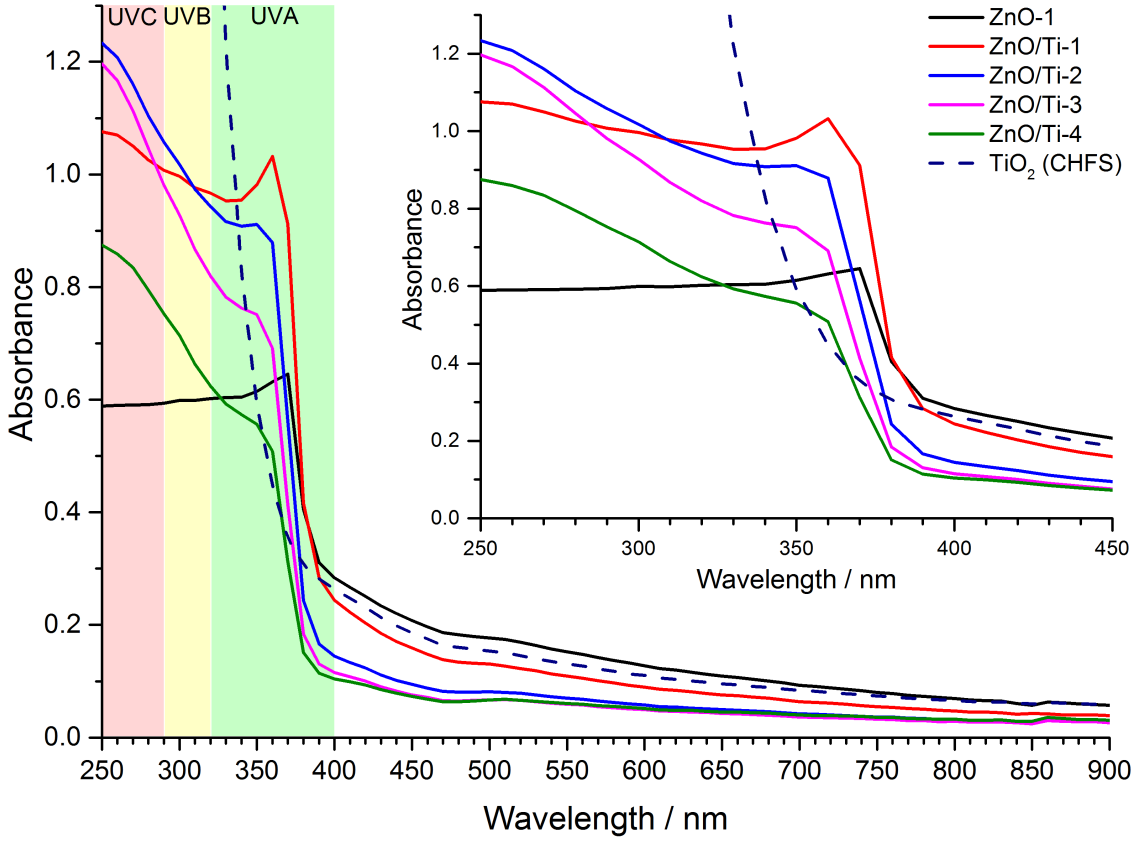

Figure 5.14 UV/Vis spectra of seeded ZnO samples as 0.02 wt% dispersions in water. The ZnO samples were prepared using a TiO_2 sol as a seeding agent in the CHFS synthesis.

5.4.4. Zinc oxide (seeded) synthesis with in process surface functionalisation

Whilst the zinc oxide samples prepared in the presence of a TiO_2 sol seeding agent (described in section 5.4.3) showed benefits in terms of optical properties, as-synthesised particles appeared highly agglomerated. Applications in UV attenuation, such as sunscreens or UV protection, would require a highly dispersed material in order to maximise optical effects, amongst others properties. The ZnO samples were prepared with the addition of a surfactant (Solplus™ D570; 0.5 vol%) in CJM-2, similarly to that described earlier in section 5.4.2. Samples were obtained as white slurries that were cleaned via dialysis, and stored as aqueous dispersions (hard settling was not observed).

Samples were investigated via SEM (shown in Figure 5.15) and the particles appeared agglomerated, but with a 'shell' formed around small agglomerates. This 'shell', which appeared consistently, may provide evidence of the surfactant coverage on particles.

Indeed, the field-of-view developed a fog-like appearance if the electron beam was focused on one region for a prolonged period (similar to that described in section 5.4.2), which may suggest that formation of adventitious carbonaceous material began to occur under the beam. For samples ZnO-1a, ZnO/Ti-1a and ZnO/Ti-2a, particles appeared polygonal shaped, similar to that observed previously for CHFS ZnO (in Chapter 4). Particle size distributions (Figure 5.15 (c), (f), (i)) showed that the average particle size decreased as the TiO_2 sol concentration increased, which correlated with the trend in crystallite sizes of similar ZnO samples (prepared without the surfactant). Although polygonal shaped particles were observed at low TiO_2 sol concentrations, at the higher sol concentrations (samples ZnO/Ti-3a and ZnO/Ti-4a), rod-like particles were observed (Figure 5.15 (j), (k) and Figure 5.16). ZnO samples prepared under similar conditions, but without a surfactant in CJM-2 showed only polygonal shaped particles at all TiO_2 sol concentrations (see Figure 5.11 shown earlier). The presence of rods may be explained as follows: at higher TiO_2 sol concentrations, there may have been a greater number of nucleation sites for ZnO, compared to at the lower TiO_2 sol concentrations. A larger number of nucleation sites may have resulted in a larger number of ZnO nuclei, and consequently, they may have had a small average crystallite/nuclei size. The nuclei at lower TiO_2 sol concentrations may have had a larger average size, because there may have been a smaller number of nucleation sites. When the surfactant was added in CJM-2, there may have been two possible events: the surfactant may have bound selectively to certain ZnO facets, or the surfactant may have increased the solubility of zinc in solution. The driving force for particle growth may have been greater at the higher TiO_2 sol concentrations, in an effort to reduce the high surface energy (because of smaller particles). In the case of surfactant bound to zinc oxide, it may have directed growth in the $+c$ direction (fast growth direction of ZnO, as discussed in Chapter 4), yielding rod-like particles.

A particle size distribution of sample ZnO/Ti-3a (Figure 5.16 (d)) showed that the length of the measured rods varied largely (in the range 20–180 nm), whilst the size distribution of their widths was narrow; nearly 90 % of the particles that were measured had widths in the range 10-20 nm. In comparison, the data presented in Chapter 4, showed that rods were much larger for non-seeded ZnO (70–320 nm), and they were only observed at precursor concentrations above 0.5 M. Herein, the rods were obtained

at lower concentration, and only in the presence of the TiO_2 sol and surfactant together. As discussed in section 5.4.2, rod-like particles were not observed with the surfactant alone. This work suggests that surface functionalisation of zinc oxide is achievable in a one-step process within the CHFS reactor. Further experiments would be beneficial to determine the extent to which the length of rods may be controlled.

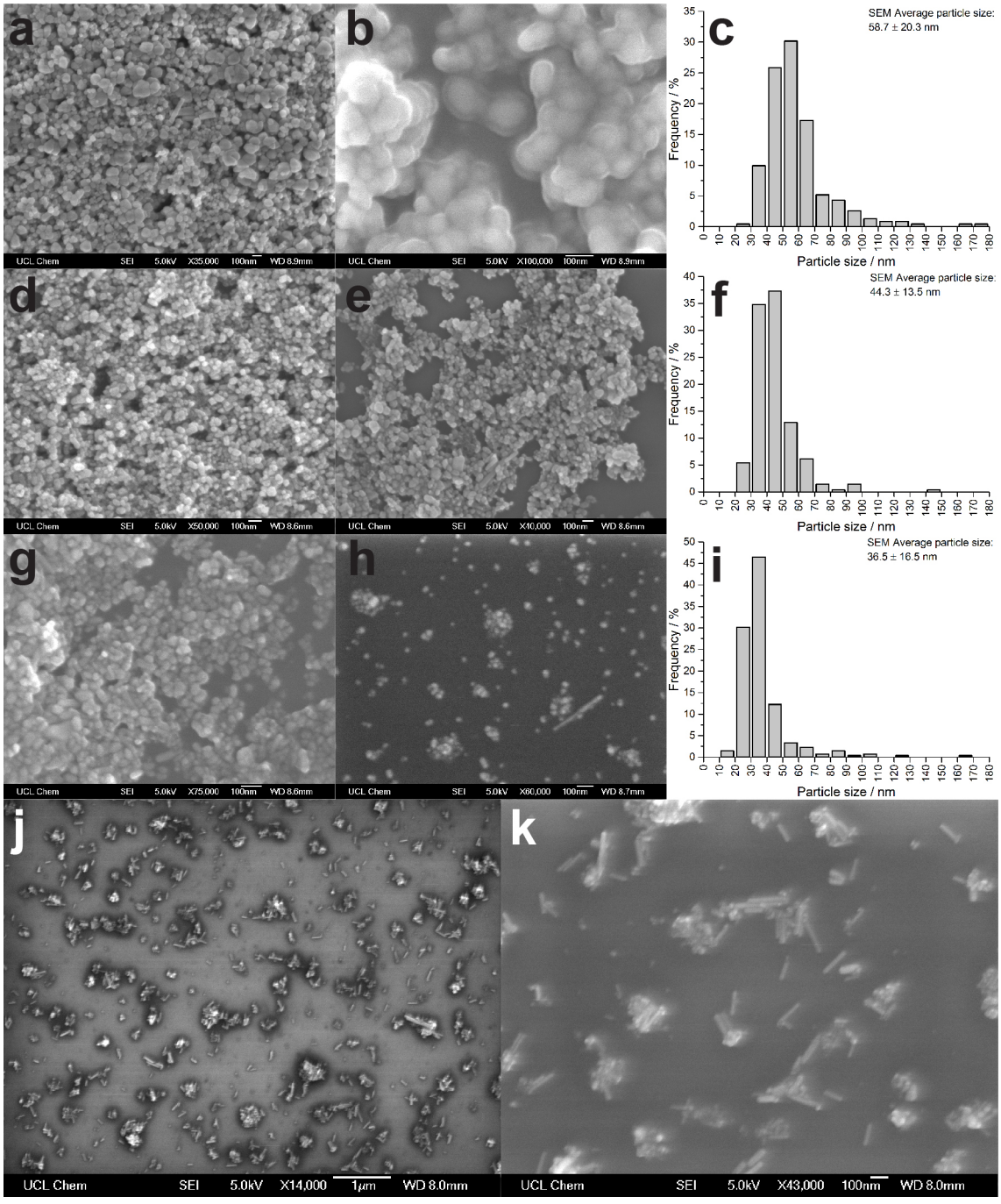

Figure 5.15 SEM images and particle size distributions for zinc oxide samples prepared with a TO_2 sol (as a seeding agent) and Solplus™ D570 (surfactant) in CJM-2. The images shown are

for samples (a-c) ZnO-1a, (d-f) ZnO/Ti-1a and (g-i) ZnO/Ti-2a. SEM images (j-k) show rod-like particles observed for sample ZnO/Ti-3a.

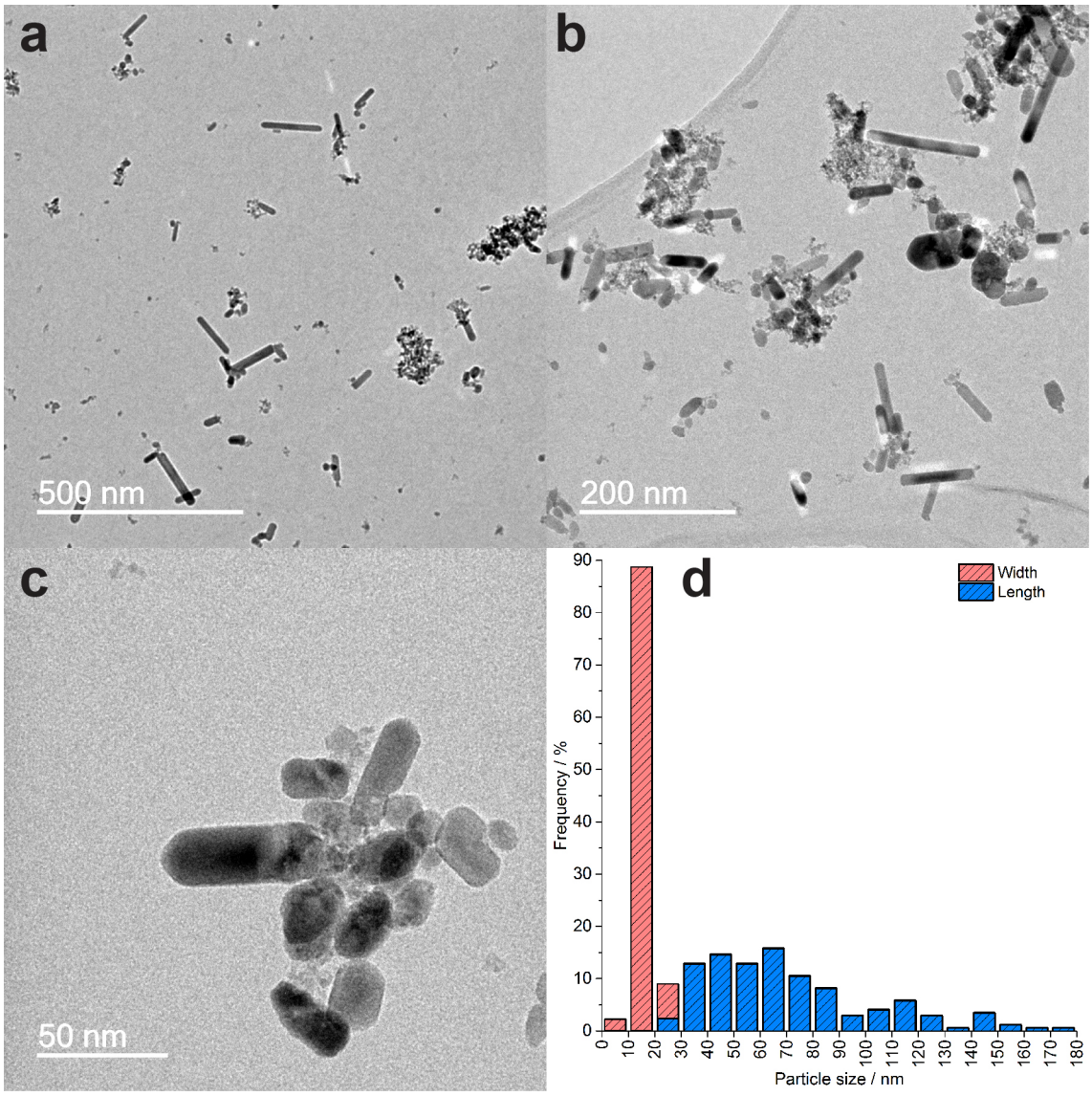

Figure 5.16 HR-TEM images (a-c) and size distribution (d) of zinc oxide sample ZnO/Ti-3a, prepared using a TiO_2 sol (as a seeding agent) and Solplus™ D570 (surfactant) in CJM-2.

5.4.5. Post synthesis surface functionalisation of zinc oxide

The zinc oxide samples were dispersed in 1,6-hexanediol diacrylate (HDDA) solvent with Solsperse™ 41000 (surfactant). The mixtures were then prepared as polymer formulations via the addition of an oligomer, monomer and photoinitiator. The final formulations contained 10 wt% ZnO. Hydrodynamic diameters of each formulation

were measured via DLS, as shown in Figure 5.17. In agreement with other size measurements, it was found that the hydrodynamic diameter decreased, as the concentration of the TiO_2 sol used in the synthesis increased. Formulations were then doctor-bladed on to glass slides and UV cured (254 nm), where they hardened in less than 5 minutes. Glass slides were chosen as the substrate (despite the poor adhesion of the coatings to glass), because it allowed the coatings to be readily delaminated for analysis.

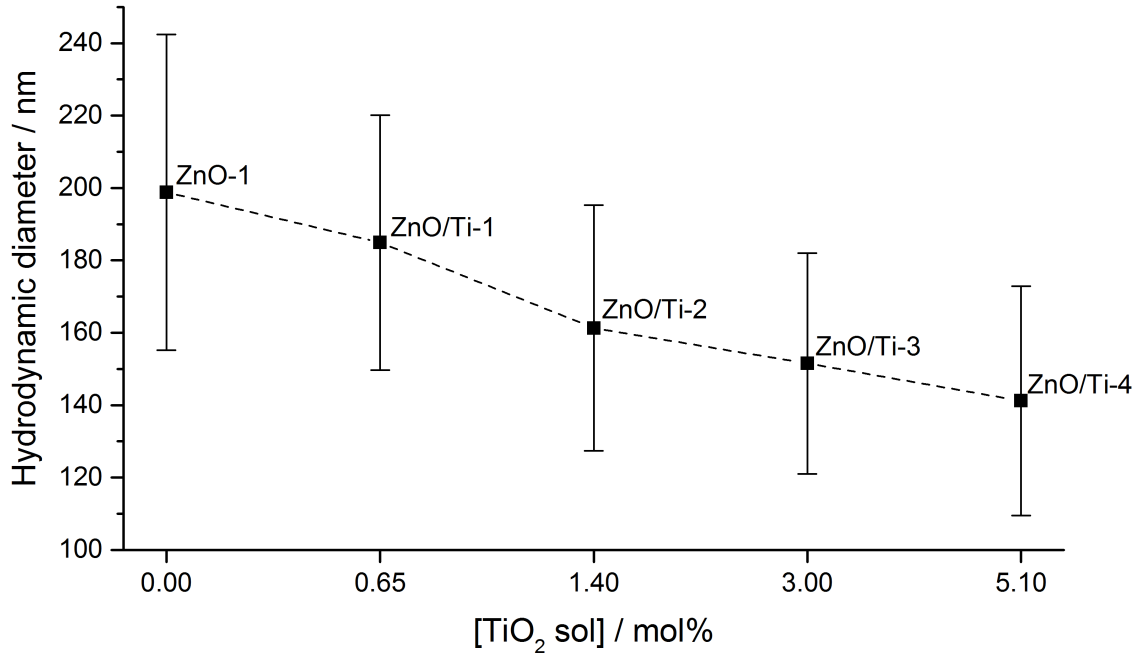

Figure 5.17 Hydrodynamic diameters of coating formulations prepared from zinc oxide samples (synthesised using a TiO_2 sol as a seeding agent) versus the TiO_2 sol concentration used in the initial CHFS synthesis.

Figure 5.18 shows an SEM image of a UV cured coating. Particles can be observed, which appear to be in a large matrix. The clarity of the particles was obscured by the polymer coating; when the electron beam was focussed on a particular region, the image appeared to brighten up (like that observed in the centre of the image). This is suggested to be from the formation of adventitious carbonaceous material (i.e. the polymer). This image is similar to reports in the literature of UV cured coatings (Huang and Hsieh 2010).

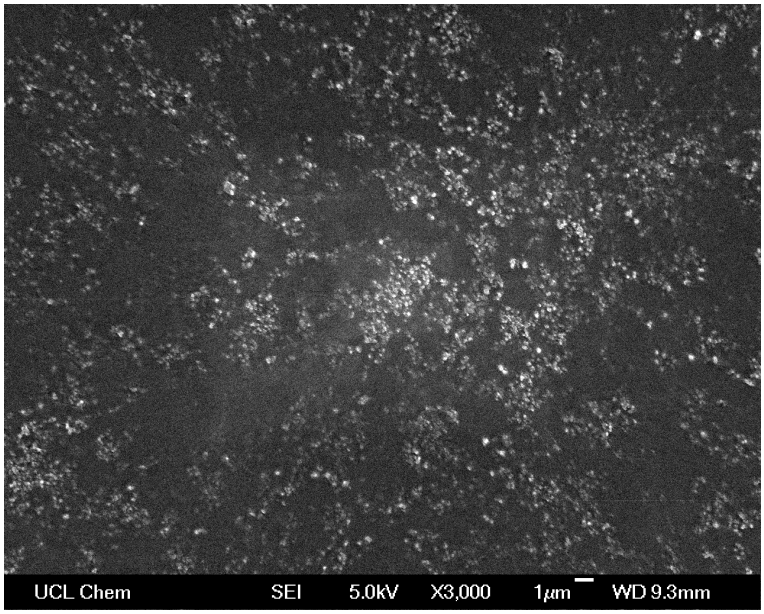

Figure 5.18 SEM image of a UV cured coating prepared from a coating formulation prepared from zinc oxide (synthesised using a TiO_2 sol as a seeding agent).

5.4.6. Formulation and UV cured coatings at MacDermid Autotype

Zinc oxide dispersions of samples ZnO-1 and ZnO/Ti-4 were provided to Dr Nigel Holmes at MacDermid Autotype (Wantage, Oxfordshire, UK), where formulations were prepared, coated and UV cured on polyester film. The aim of this preliminary study was to determine the properties of coatings prepared using ZnO, that were synthesised using the TiO_2 sol seeding method (described earlier in section 5.4.3). The dispersions showed some signs of soft settlement, but the solid material was readily dispersed when stirred. Although this was not ideal, the dispersions did not show any signs of caking, which is when solid material forms large clumps and becomes very difficult to re-disperse. Further optimisation of the dispersion procedure in the future, may help to prevent even soft settlement.

The formulations were prepared via the addition of an oligomer, monomer and photoinitiator to the dispersions, and they did not show any significant settling after 48 hours. The coatings on polyester film were prepared via a hand coating technique, since only small volumes of ZnO dispersions were provided for this initial study.

Figure 5.19 shows how the thickness, light transmission and haze varied with each sample. Given that the coatings were prepared by a hand coating technique, it was difficult to control the thickness precisely; hence there was a large variation between the different samples. The ideal thickness of such coatings is in the range 5-10 μm, and although the coatings in this study were slightly thicker, future studies with machine-prepared coatings would allow for better thickness control. Huang and Hsieh prepared UV cured ZnO coatings containing up to 20 wt% ZnO, with average thickness of 4 μm (Huang and Hsieh 2010). Of course, the thickness of a coating would impact on its light transmission and haze properties. The transmission of the uncoated and coated (not containing ZnO) polyester film was 90.9 ± 0.5 % and 91.2 ± 0.1 %, respectively. This result showed that the formulation alone (i.e. without ZnO) had very little effect on the light transmission properties. Likewise, the haze of these coatings was very similar (0.8 ± 0.3 % and 1.2 ± 0.3 % for the uncoated and coated (not containing ZnO) polyester film, respectively). Upon the addition of sample ZnO-1 to the formulation at 2.7 wt% (NH-1-2.7), the transmission decreased to 87.5 ± 0.9 %. However, reducing the ZnO loading to 1.1 wt% (NH-1-1.1) yielded an improvement in the transmission (89.9 ± 0.3 %). Coatings prepared from formulations containing sample ZnO/Ti-4, which had the smaller average particle size, gave a similar trend; the light transmission improved as the ZnO loading in the coating was reduced (from 1.6 to 0.6 wt%). Overall, the light transmission for the smallest average size ZnO particles was better than the light transmission for the larger ZnO particles (sample ZnO-1), even when the loading was higher (coating NH-4-1.6 versus NH-1-1.1). The haze measurements of the coatings improved as (i) the ZnO particle size was reduced, and (ii) the ZnO loading was reduced. The uncoated polyester film and the coating that did not contain ZnO, had haze values of 0.8 ± 0.3 % and 1.2 ± 0.3 %, respectively. Ideally, the ZnO coatings should have similar haze values to these reference values, however, given that the procedures were not optimised and the coatings were prepared via a hand coating technique, improvements may be gained through further work.

The hardness of the coatings was evaluated using a pencil test, where attempts were made to scratch the surface of the coating using 2H, 3H and 4H pencils. The results showed that all coatings passed the test with the 2H and 3H pencils. The 4H pencil was able to make 4 scratches each for the coatings prepared from formulations NH-1-2.7

and NH-1-1.1, and hence, they failed this test. Coatings prepared from sample ZnO-5 (NH-5-1.6 and NH-5-0.6) passed the 4H test. These results may be related to the coating thickness, and hence a meaningful comparison is difficult, because the thickness varied across all coating samples. There did not appear to be any significant differences in the curing behaviour of the coatings, arising from the presence of ZnO. Since ZnO is a UV absorber, it can affect the degree of cure of the formulation, which can reduce the hardness of the coating.

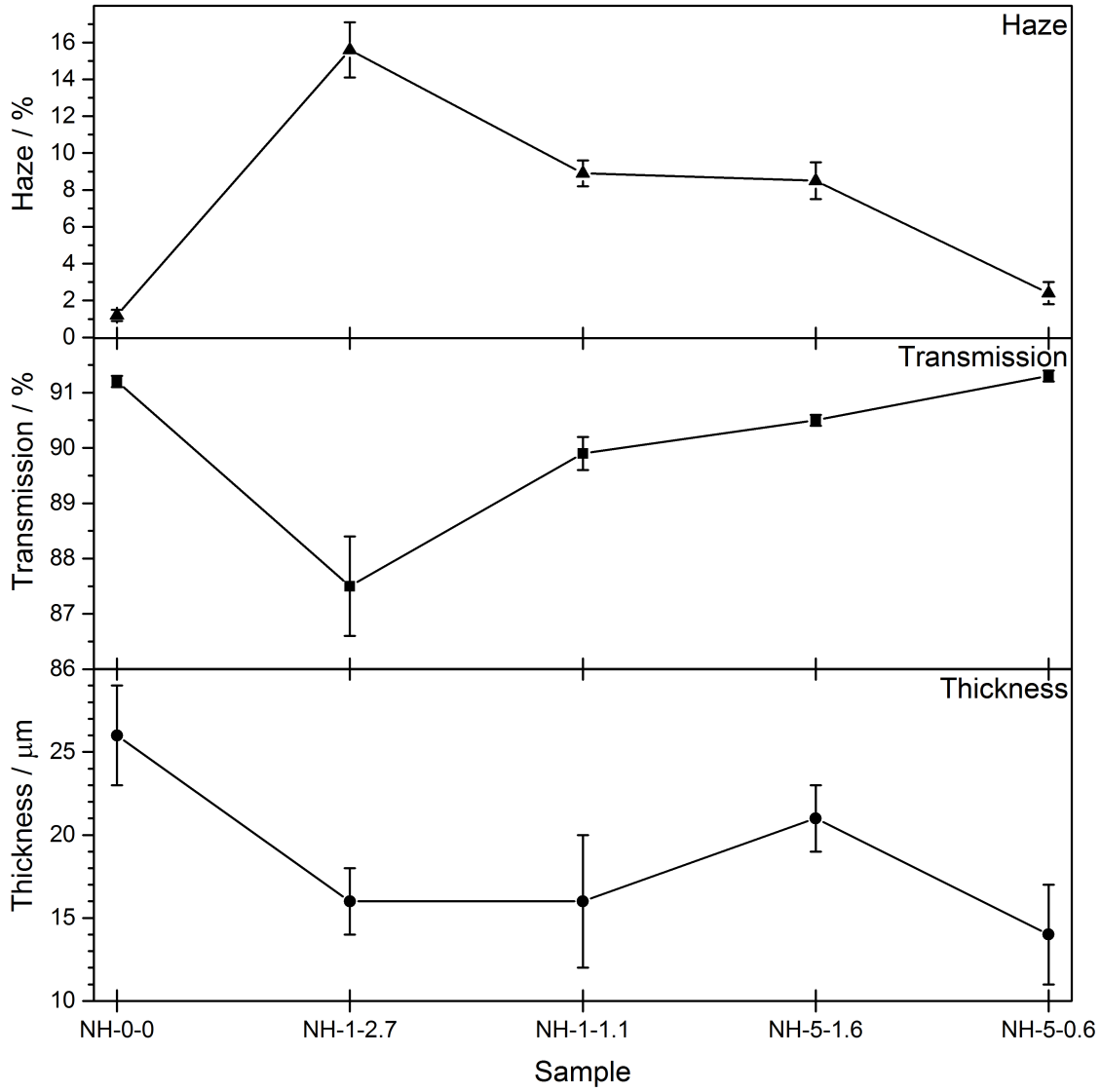

Figure 5.19 Variation in thickness, transmission and haze of each UV cured coating on polyester film.

To further assess the degree of cure in the coating, a solvent resistance test was carried out. Each coating was subjected to 50 double rubs with a paper towel soaked in methyl ethyl ketone. In all cases, there were no signs of coating removal from the polyester film.

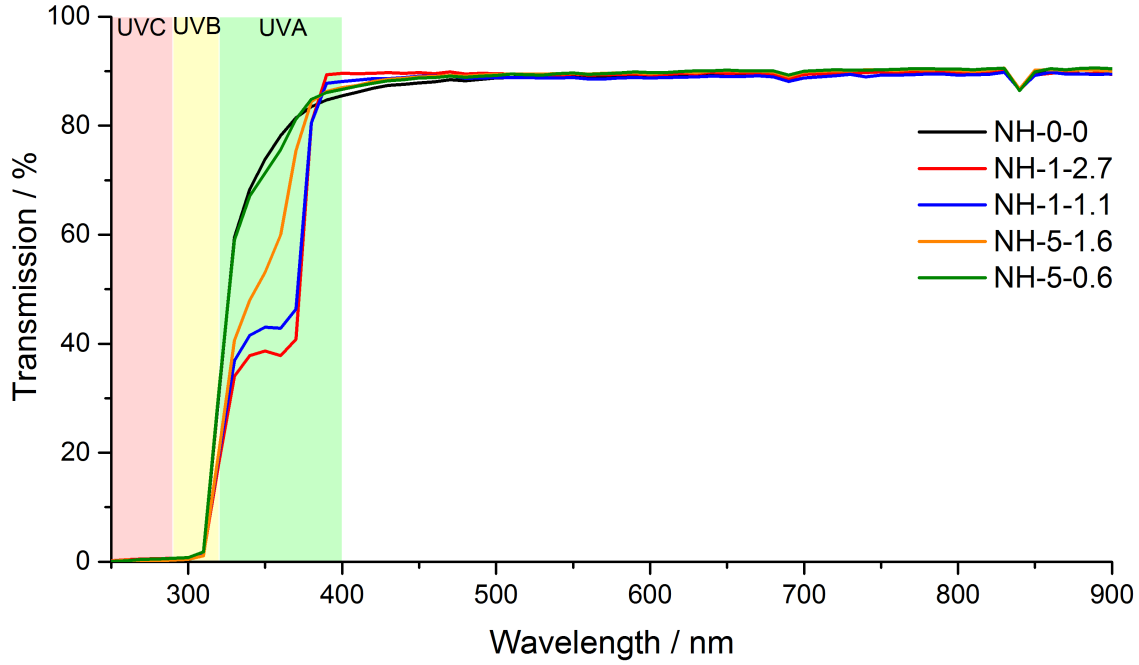

Figure 5.20 UV-visible transmission spectra of each UV cured coating on polyester film.

The UV-Vis transmission spectra of the UV cured samples were measured at UCL (shown in Figure 5.20). All ZnO coatings showed ≈ 90 % transmission at wavelengths > 400 nm, which was comparable to a coating that did not contain ZnO (NH-0-0). The coatings that contained the larger zinc oxide particles (NH-1-2.7 and NH-1-1.1) showed better absorbance in the UVA region than the smaller zinc oxide particles (NH-4-1.6 and NH-4-0.6). This result correlated with the UV-Vis absorbance spectra shown earlier (Figure 5.14), where the smaller ZnO particles showed lower absorbance in the UVA region. In both particle size cases, reducing the ZnO loading was detrimental to the optical properties; transmission in the UVA region increased slightly.

The preliminary results discussed here have shown that it was possible to prepare UV cured coatings, containing ZnO synthesised in a CHFS process. The coatings showed good hardness and solvent resistance, with an enhanced UV absorption in the UVA

region, compared to a coating that did not contain ZnO. Whilst the optical properties of the coatings can be improved, the results shown herein are encouraging for a preliminary study. Further studies using automated techniques (i.e. via machine coating) to prepare coatings are underway, and they may prove beneficial in having better control over the properties of the films (in particular the thickness).

5.5. CONCLUSIONS

In conclusion, CHFS has been used to prepare surface functionalised zinc oxide nanoparticles. In process surface functionalisation using citric acid as a capping agent, did not yield functionalised nanoparticles under the reaction conditions employed. The presence of citric acid is thought to have lowered reaction pH, resulting in low product yields, because of the pH sensitivity of ZnO. However, it was shown that using the double CJM arrangement was successful in reducing particle size alone, by comparisons made to data presented earlier in Chapter 4. In-process surface functionalisation was then investigated using polymeric surfactants, where partially coated particles were obtained. A seeding approach was investigated, with the aim of reducing ZnO particle size. A TiO_2 sol was used to provide nucleation sites for ZnO formation, and results suggested that when the concentration of the sol was increased, smaller ZnO particles were obtained. UV-Vis absorbance measurements showed that the samples prepared with the TiO_2 sol (without surfactant) had enhanced UV absorption, particularly in the UVA region. This property of the samples would be very beneficial in applications such as UV attenuation, where maximum UVA absorption is desirable.

The seeding method for synthesis of ZnO was used with a double CJM arrangement, with a surfactant meeting the product stream in CJM-2. Dispersed nanoparticles were obtained, and SEM measurements suggested a size reduction as the TiO_2 sol concentration increased. It was also found that at higher sol concentrations, and with a surfactant in CJM-2, the morphology of samples changed from polygonal shaped particle to narrow rod-like particles. The ZnO samples prepared with the sol were then made up as formulations that could be coated on a substrate, and subsequently UV cured. Samples were provided to MacDermid Autotype, where ZnO coatings were prepared on polyester film. It was found that all coatings were physically robust, and

that coatings that contained the larger ZnO particles (prepared using the TiO_2 sol) gave better UV absorbance. These preliminary studies were successful in demonstrating the ability of CHFS ZnO to act as UV attenuators. Further scale up work is now continuing with these samples, at MacDermid Autotype.

Overall, this chapter has shown that CHFS can be employed as a technique to prepare surface functionalised and seeded zinc oxide nanoparticles, with some control over size and shape. In future experiments, reaction conditions can be optimised, such that greater control over particle properties can be achieved. Nevertheless, CHFS is demonstrated as a versatile process for ZnO nanomaterials synthesis.

Chapter 6. Simple and low-cost preparation of self-supported TiO_2–WO_3 ceramic heterojunction wafers for photocatalysis

6.1. AIMS AND OUTLINE

The purpose of this chapter was to investigate the charge transfer characteristics, and photocatalytic properties, of heterojunction pressed ceramic wafers. Reports of such simple structures are very rare in the literature, despite their ease of preparation. Elouali et al. have previously investigated the photocatalytic properties of single layer pressed ceramic wafers, which were prepared from commercial TiO_2 powders (Elouali et al. 2010). The investigations described herein extended this work to monolithic ceramic wafers prepared from TiO_2 and WO_3 as a heterojunction. The photocatalytic performance of the wafers was investigated for the degradation of stearic acid, a model organic pollutant.

6.2. INTRODUCTION

Solar energy harvesting devices, including heterojunction solar cells and semiconductor photocatalysts, effectively harness part of the Sun's energy via efficient formation and separation of photogenerated excitons (Fujishima and Honda 1972; Kudo and Miseki 2009; Abe 2010; Pandey and Holmes 2010; Cowan and Durrant 2013; Heeger 2013). Earlier reports in the literature focused on selecting and tuning semiconductors (e.g. by addition of dopant atoms (Asahi et al. 2001; Zaleska 2008)) with appropriate band gaps for light absorption, and selecting band edge positions relevant to the targeted reduction and oxidation processes. However, for a single material, it is difficult to combine the desired characteristics of efficient light absorption in the required wavelength range, while matching the redox potentials and minimizing recombination and trapping processes. Recently, researchers have begun to develop photoelectrochemical devices consisting of two or more coupled semiconductor materials, as thin films or particles, using materials with complementary band edge positions. These arrangements

substantially reduce the occurrence of the back reaction (i.e. electron–hole recombination) (Kubacka et al. 2012; Maeda 2013; Rawal et al. 2013; Wang et al. 2013). Therefore, architectural design of such solar driven devices based on coupled semiconductor systems, is critical for developing high photocatalytic efficiencies.

In a heterojunction photocatalytic system, photogenerated electrons and holes at different sides of the junction can participate in a variety of surface oxidation reactions, including organic pollutant degradation (Do et al. 1994; Dunnill et al. 2012; Liu et al. 2012; Quesada Cabrera et al. 2012), oxidation of water to O_2 (Wang et al. 2012), or the removal of harmful bacteria or organisms (Akhavan et al. 2009; Akhavan 2010), that are typically coupled with the concomitant reduction of oxygen to water at the opposing (often dark) junction. Because of efficient vectorial charge separation, heterojunction photocatalysts or devices can display superior performance compared to analogous single semiconductor systems (Jang et al. 2012).

It is important to develop efficient, reliable and cost-effective methods to produce such coupled photoelectrochemically active systems. Heterojunction photocatalytic materials consisting of multiple layered or composite semiconductors, or on different crystal facets (Yu et al. 2014) have been prepared using a range of synthesis methods, some of which can be laborious, often involving multiple steps (e.g. ion-exchange precipitation reactions (Bessekhouad et al. 2004; Bessekhouad et al. 2005; Wang et al. 2012)) and taking many hours to complete, or requiring expensive and specialised equipment or precursors (such as chemical vapour deposition (Quesada Cabrera et al. 2012), sol-gel synthesis (Dunnill et al. 2012; Scanlon et al. 2013), and batch hydrothermal synthesis (Cao et al. 2013; Zhao et al. 2013; Huang et al. 2014)). Often, in the case of layered heterojunction photocatalytic materials, a substrate layer is required upon which the heterojunction is deposited/fabricated, and although it may not take part in the photocatalytic reaction, it can be considered an additional cost in the process. Therefore, simpler, inexpensive synthesis routes based on readily available and sustainable precursors and elements to form robust, self-supported, semiconductor heterojunction photocatalytic systems, are desirable.

Recently, Elouali et al. reported a simple and inexpensive method of producing self-supporting wafers of photocatalytically active TiO_2 powders, using a cold-pressing

technique (Elouali et al. 2010). Here, the simple method has been extended to prepare self-supported photocatalytic heterojunction (SPH) wafers, using commercially available TiO_2 and WO_3 powders. The resulting wafers incorporated a relatively stable charge-transfer heterojunction between the TiO_2 and WO_3 layers, and showed enhanced photocatalytic performance for the degradation of stearic acid, a well-known organic pollutant, compared to a pure TiO_2 wafer.

6.3. EXPERIMENTAL METHODS

6.3.1. Chemicals and materials

Industrial grade titanium dioxide PC50 (anatase) was obtained from Cristal Global (Stallingborough, UK) and tungsten(VI) oxide (99.8 % metals basis) was obtained from Alfa Aesar (Lancashire, UK). Stearic acid (reagent grade, 95 %) was obtained from Sigma-Aldrich (Dorset, UK). Deionised (DI) water (> 15 MΩ resistivity) was used for the preparation of solutions throughout.

6.3.2. Preparation of TiO_2–WO_3 ceramic wafers

Ceramic wafers were prepared by pressing powders in a circular 25 mm diameter stainless steel die (Compacting Tooling Inc., Philadelphia, USA) at a pressure of 200 bar, in the extraction ram of a non-end-loaded piston cylinder press (Patera and Holloway 1978) (Depths of the Earth Company, Arizona, USA), following a similar procedure reported in the literature (Elouali et al. 2010). It was found that an even powder distribution was important for the preparation of thin and robust wafers. To prevent the powder from sticking to the die, Mylar® sheets cut to size were placed on each die surface and a razor blade was used to level the powder surface. This aided in achieving a uniform thickness whilst minimising wafer fracture. For the preparation of the TiO_2–WO_3 wafers (illustrated in Figure 6.1(a)), TiO_2 (0.3 g) was first placed in the die and levelled to create an even surface, followed by the addition of WO_3 (0.7 g) on top of the TiO_2 layer. After pressing, the ceramic wafers were heat-treated in air at 500 °C for 6 hours to enhance their robustness. As shown in Figure 6.1(b), some cracking occurred

at the edges of the WO_3 layer; however, the bulk of the wafers remained intact throughout testing and handling.

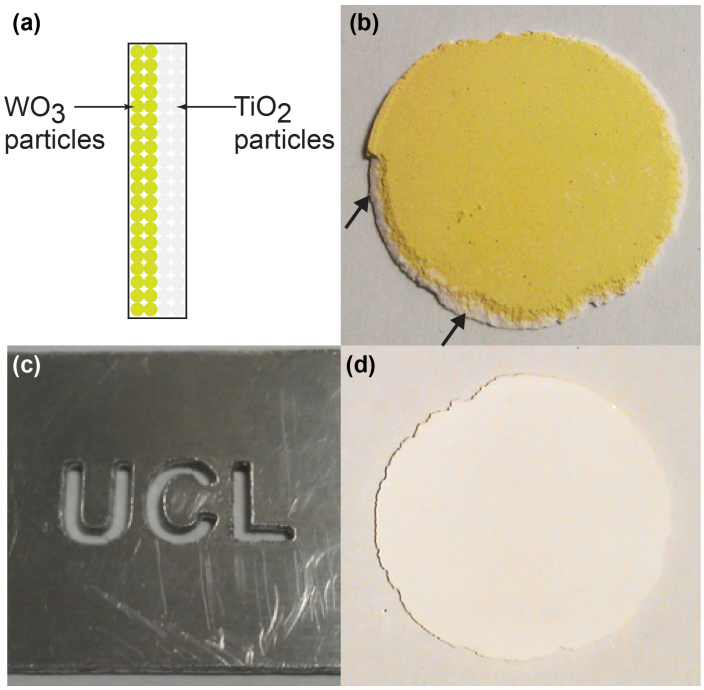

Figure 6.1 (a) Illustration depicting the preparation of TiO_2–WO_3 ceramic wafers, (b) shows the WO_3 side of a ceramic wafer, where flaking was observed at the edges (indicated by the arrows), exposing the underlying TiO_2 layer, and (d) shows the TiO_2 side of a ceramic wafer. (c) shows a photograph of a CNC-milled aluminium 'UCL' lettering template used to investigate the charge transfer directionality of the heterojunction wafers.

6.3.3. Investigation of heterojunction charge-transfer

In a typical experiment, the ceramic wafer was placed in a sacrificial solution consisting of 1:1 EtOH:H_2O containing 0.1 M HCl. The TiO_2 surface was irradiated with simulated solar light using a 75 W xenon light source (Photon Technology International, West Sussex, UK) fitted with an AM 1.5G filter (Newport Spectra-Physics Ltd., Oxfordshire, UK; spectral output shown in Figure 6.2(a)) with a lamp to sample distance of 14 cm. In experiments to determine the directionality of electron transfer pathways, a region of the TiO_2 surface of the ceramic wafer was masked for selective photoirradiation of the surface. A template prepared from a 1 mm sheet of aluminium via CNC milling was milled with the lettering 'UCL' (Figure 6.1(c)) to investigate the electron transport pathways through the ceramic wafer. The template was placed directly on the TiO_2

surface of the ceramic wafer, and photoirradiation was carried out exactly as mentioned earlier.

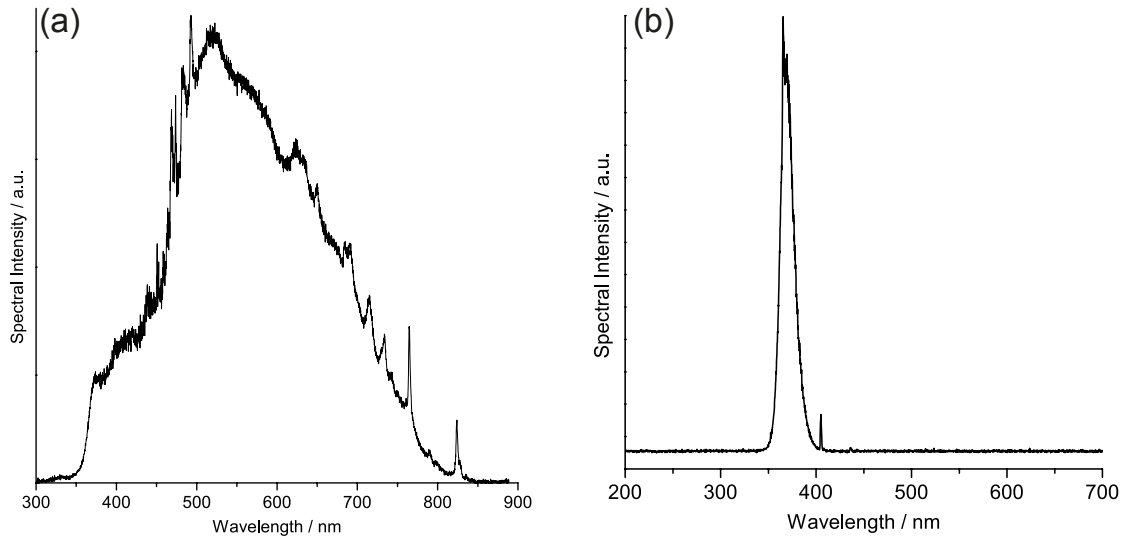

Figure 6.2 Spectral output of (a) 75 W xenon light source and (b) 2 × 8 W 365 nm UV lamp, used for photoirradiation throughout this work.

6.3.4. Stearic acid (SA) photocatalytic degradation tests

The photocatalytic performance of each pressed wafer was determined by the photocatalytic degradation of SA, by the amount of evolved CO_2 monitored by FTIR spectroscopy at regular intervals. Stearic acid (50 μL (10 μL for sample A2b; wafer configurations discussed later in section 6.4.2), 0.05 M in $CHCl_3$) was placed on the centre of the wafer surface of interest, and the solvent was allowed to evaporate. The coated wafer was placed in a gastight glass cell fitted with KBr windows, and the internal atmosphere of the cell was purged with argon gas to remove traces of CO_2. The wafer was placed with the irradiated surface (as indicated in Figure 6.10) facing upwards, so that the surface was under direct UVA irradiation from 2 × 8 W 365 nm UV lamp (Uvitec, Cambridge, UK; spectral output shown in Figure 6.2(b)). The IR spectrum through the gas cell was measured at regular intervals (PerkinElmer Spectrum RXI with Spectrum v5.3.1 software). To ensure no contamination from atmospheric CO_2, the sample chamber in the IR instrument (within which the gas cell was placed for measurement) was purged with argon gas for 5 minutes prior to each measurement. A series of control experiments were carried out under irradiation; (i) an empty gas cell,

(ii) a TiO_2 wafer in the absence of stearic acid, and (iii) stearic acid on a glass substrate, to confirm that the presence of atmospheric CO_2 did not interfere with the measurements.

6.3.5. Ceramic wafer characterisation

Following photoirradiation, oxidation states were determined via X-ray photoelectron spectroscopy (XPS). Heterojunction ceramic wafers were investigated by powder X-ray diffraction and field-emission scanning electron microscopy (FE-SEM). As-prepared ceramic wafers were cracked to expose the cross-sectional interface between the TiO_2 and WO_3 layers, and all samples were gold coated prior to imaging. Image analysis was performed using ImageJ software (version 1.48v). Further details are provided in Chapter 2.

6.4. RESULTS AND DISCUSSION

6.4.1. Investigation of heterojunction charge-transfer

When a TiO_2–WO_3 SPH wafer was placed in a sacrificial electron donor solution and photoirradiated on the TiO_2 side only, a gradual dark blue colouration occurred on the non-illuminated (i.e. 'dark'), WO_3 side within 45 minutes. Consideration of the expected conduction and valence band positions of TiO_2 and WO_3 (Figure 6.3) would lead to the conclusion that in the SPH wafers, photogenerated electrons in the conduction band (CB) of TiO_2 were shuttled across the heterojunction and into the CB of WO_3, whereas the photogenerated holes would have reacted irreversibly with the sacrificial electron donor, ethanol. Therefore, the electrons would have accumulated in the conduction band of WO_3 where W^{6+} in the WO_3 crystal lattice may have been reduced to W^{5+}, causing a dark blue colouration that intensified with increasing irradiation time.

Indeed, as the photoirradiated wafers retained their colour for several hours when dried, it was possible to confirm, by X-ray photoelectron spectroscopy (XPS), the presence of W^{5+} species as being responsible for the colour change (Figure 6.4; peak fitting accounted for W^{5+} species only). The two major $4f_{7/2}$ and $4f_{5/2}$ peaks centred at 35.61 and 37.79 eV were assigned to W^{6+}, and the two smaller $4f_{7/2}$ and $4f_{5/2}$ peaks centred at 34.45

and 36.59 eV were assigned to W^{5+}. The reoxidation of W^{5+} to W^{6+} by oxygen in air was very slow, with the original, yellow/green colour of the WO_3 only fully reappearing after approximately 1 week following photoirradiation.

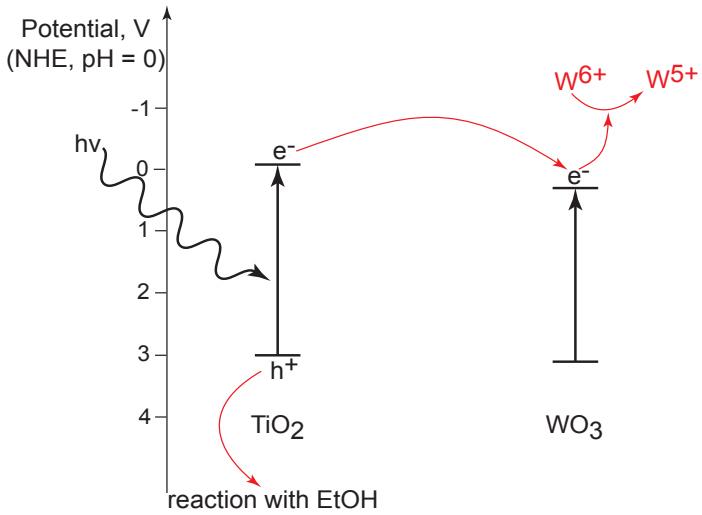

Figure 6.3 Conduction and valence band positions of TiO_2 and WO_3 with arrows showing the proposed mechanism of electron and hole transfer (and subsequent reduction of W^{6+} species), when photoirradiating the TiO_2 side only.

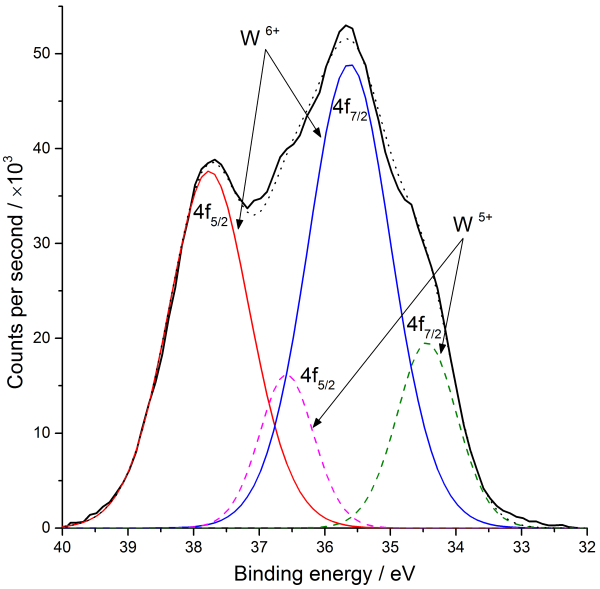

Figure 6.4 X-ray photoelectron spectrum showing the presence of W^{5+} reduced states on the WO_3 surface, following photoirradiation (75 W xenon lamp) of the TiO_2 surface of a TiO_2–WO_3 self-supported photocatalytic heterojunction wafer. Peak fitting accounted for W^{5+} only.

Following the onset of irradiation at the TiO_2 side, the first observation of the light induced colour change at the WO_3 surface occurred within 2 minutes. Over a period of 45 minutes, the WO_3 surface changed rapidly from light green to dark blue (Figure 6.5).

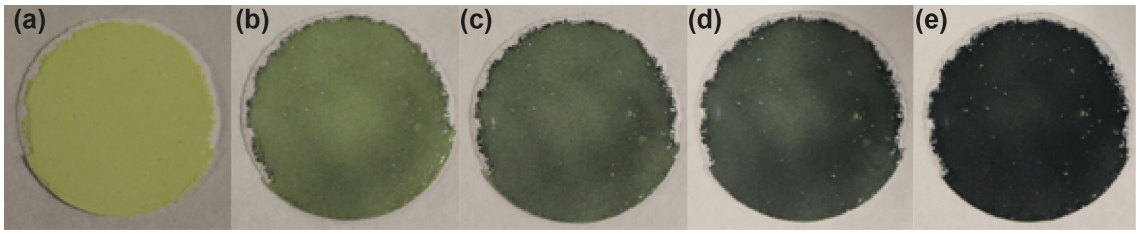

Figure 6.5 Photographs showing the colour change occurring on the WO_3 surface after photoirradiating the TiO_2 surface of a TiO_2–WO_3 wafer at time intervals of (a) 0, (b) 2, (c) 5, (d) 15 and (e) 45 minutes.

When the test was repeated with direct irradiation of the WO_3 surface, a colour change was only observed at the edge of the wafer, where some TiO_2 was exposed due to a small amount of flaking of the WO_3 layer (Figure 6.6(a); the flaking occurred as a result of the large micron size WO_3 powder having poor granular adhesion, and non-optimised pressing procedure). This confirms that the electrons responsible for the colour change were photogenerated in the TiO_2, transported across the heterojunction and accumulated in the WO_3 CB, where they reduced W^{6+} to W^{5+}. In both cases, with irradiation of either the TiO_2 or WO_3 side, the TiO_2 surface always remained white in appearance (Figure 6.6(b)).

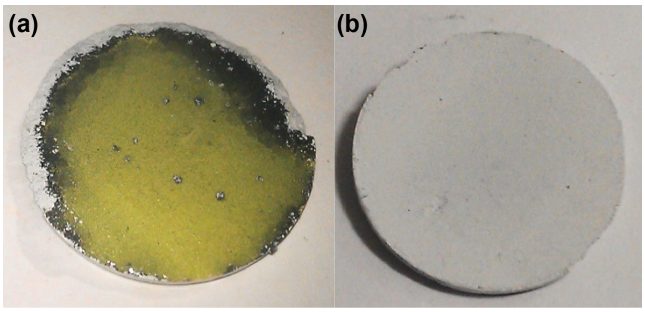

Figure 6.6 Photographs showing (a) the colour change that occurred on the edge of the WO_3 side of a TiO_2–WO_3 wafer after irradiating the WO_3 surface, and (b) the TiO_2 surface after photoirradiation of either surface.

When the wafer was irradiated with visible light only (obtained by placing a UV 420 nm cut-off filter, Optivex™, between the lamp and sample) no colour change in the WO_3 side was observed, suggesting that the effect could only be produced via UV irradiation of the TiO_2 surface. Although it might be expected that visible light irradiation of the WO_3 surface should result in appearance of a blue colour due to the reduction of W^{6+} to W^{5+}, this process appeared to be very slow, implying the trapping of the photogenerated holes on the WO_3 by the ethanol was much less effective than it was for TiO_2, and a colour change on the WO_3 side was not observed on the timescale of the irradiation (ca. 1 hour) performed herein. While thin films of TiO_2–WO_3 are known for photocatalytic and photochromic applications (He et al. 2002; He et al. 2003; Higashimoto et al. 2008; Djaoued et al. 2013), the interaction between each semiconductor is often gained through layered growth, to form good electronic contact between the materials. In contrast, here, a stable interface with excellent electronic contact was formed between the TiO_2 and WO_3 powders solely through the application of high-pressure pressing (the heat treatment was used only to strengthen the wafers, and previous studies have shown the electronic contact is present even before heat-treatment).

To demonstrate the directionality of electron transfer through the ceramic wafer, an aluminium mask with the letters 'UCL' milled out was placed on the TiO_2 side to partially block the light irradiation (Figure 6.7). Two possible outcomes of irradiation were identified, depending on the directionality of electron transfer. If electron transfer through the wafer was to occur in an approximate straight line, it was expected that the blue colour that develops on the WO_3 surface would take the shape of the template, i.e. in the form of the 'UCL' lettering. Conversely, if electron transfer was to occur in random orientations, it was expected that the blue colour would develop randomly across the entire surface of the WO_3.

The outcome showed rapid darkening of the WO_3 side with the 'UCL' lettering from the mask appearing with little distortion (Figure 6.8). This observation indicated that charge transfer across the heterojunction, and through the wafer, occurred approximately normal to the illuminated TiO_2 surface with little spreading. This may indicate that the carrier mean path followed a line of least resistance between the photoactivated sites and

the WO_3/air interface. This would be considered beneficial to photocatalytic applications because shorter electron transfer pathways lead to more efficient overall photocatalytic processes (Kudo and Miseki 2009; Maeda 2011).

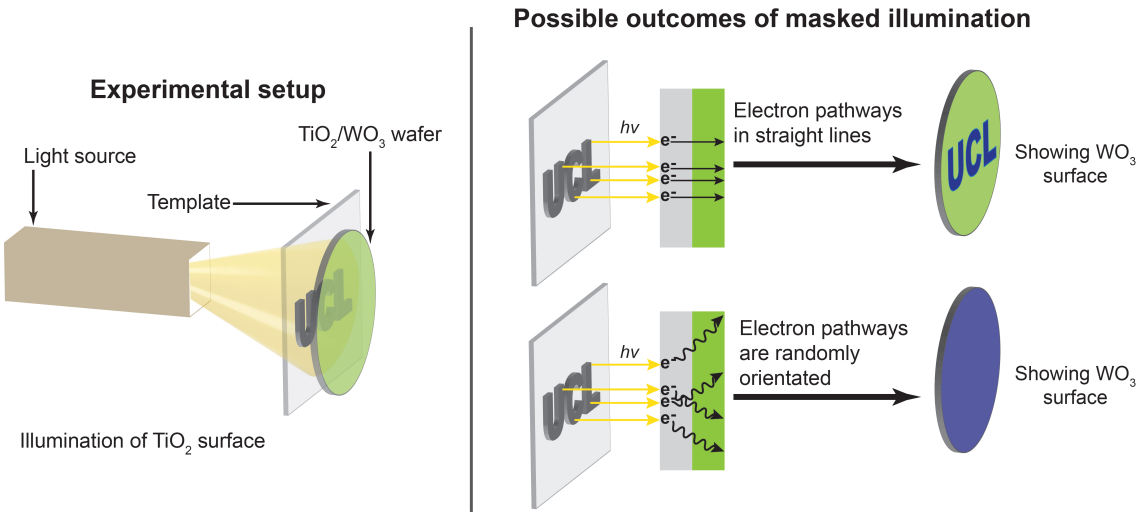

Figure 6.7 Diagram showing the experimental setup and possible outcomes, when photoirradiating a TiO_2–WO_3 ceramic wafer with an aluminium mask placed between the xenon light source and the wafer.

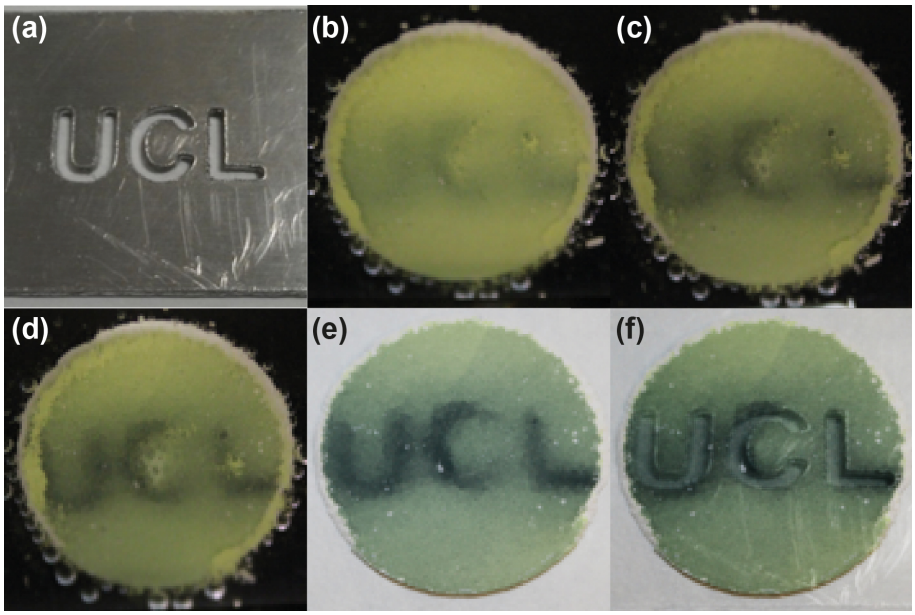

Figure 6.8 Photographs showing the appearance of the 'UCL' lettering on the WO_3 surface, after photoirradiating the TiO_2 surface of a TiO_2–WO_3 wafer with an aluminium mask (shown in (a)), placed between the xenon light source and the wafer. The photographs of the wafer

show time intervals of (b) 5, (c) 15, (d) 25 and (e) 35 minutes. Image (f) shows an overlay of the aluminium mask on a TiO_2–WO_3 wafer showing the 'UCL' lettering.

6.4.2. Stearic acid degradation experiments

To assess the photocatalytic activity of a self-supported TiO_2–WO_3 SPH compared to a pure TiO_2 ceramic wafer, a stearic acid (SA) degradation test was employed under UVA (365 nm) irradiation. Stearic acid is used as a typical model compound for the hydrophobic, wax-like organic pollutants that may coat internal and external surfaces. The degradation of stearic acid is a mineralization process (Mills and Wang 2006) which proceeds to form carbon dioxide and water, as shown in Equation 6.1:

$$CH_3(CH_2)_{16}CO_2H + 26O_2 \xrightarrow{semiconductor;\ hv \geq E_{bg}} 18CO_2 + 18H_2O \qquad \text{(Equation 6.1)}$$

This process can be followed using FTIR spectroscopy to monitor the disappearance of stearic acid. However, the technique is not practical for studying the pressed powder wafers used here. Therefore, as a method of assessing the efficacy of the reaction, the amount of CO_2 released in to the gas phase was monitored by FTIR.

A TiO_2–WO_3 SPH wafer coated on one side with SA, was placed inside a gastight IR glass cell and illuminated with UVA light (365 nm; UV irradiance at the sample surface was ca. 0.59 mW/cm^2). The FTIR spectrum of the headspace above the sample was measured at regular intervals, in order to follow the increase in evolved CO_2. Figure 6.9 shows a typical set of IR absorbance spectra obtained, in which there is the emergence of peaks in the range 2250-2400 cm^{-1}, which correspond to the asymmetric and symmetric stretching modes of CO_2 (Mills and Wang 2006). The integrated area under the CO_2 absorbance peak for each IR spectrum, which is proportional to the concentration of CO_2 in the gas phase, was plotted as a function of irradiation time**.** Control experiments carried out in the absence of a photocatalyst and UVA light, confirmed that CO_2 detected within the gas cell was evolved through the photocatalysed degradation process.

Figure 6.10(a)–(c) identifies which surface of the TiO_2–WO_3 SPH wafer was coated with stearic acid and which surface was illuminated. Also shown are the expected electron-hole transfer pathways (e^- and h^+ with arrows) in each irradiation scenario. The CO_2 evolution profiles obtained over the course of the degradation of SA are shown in Figure 6.11.

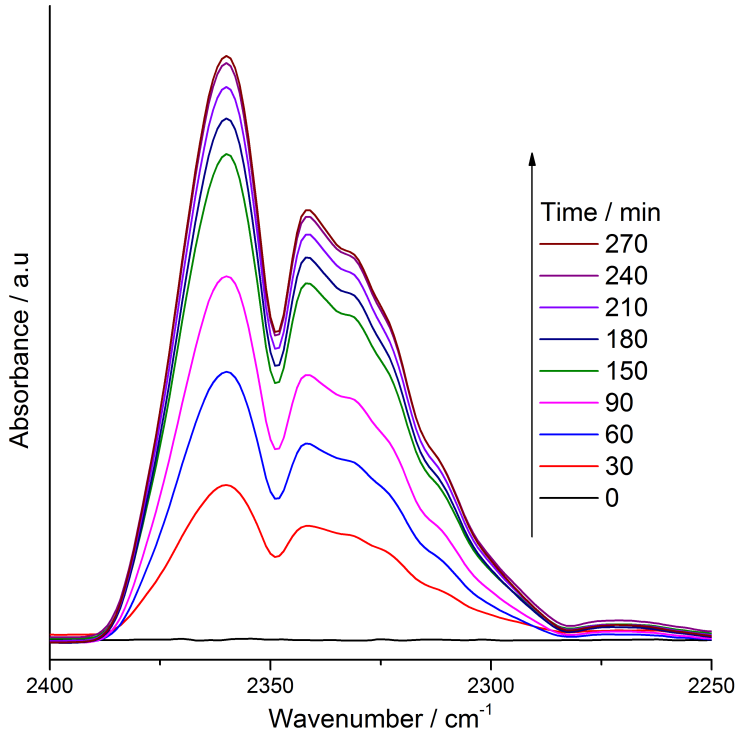

Figure 6.9 Typical infrared absorption spectra obtained for the evolution of CO_2, during the photodegradation of stearic acid on TiO_2–WO_3 wafers under UVA (365 nm) light irradiation.

Sample A2 (TiO_2–WO_3 SPH wafer with SA on the TiO_2 side) exhibited a rate of CO_2 generation eight times that of a pure TiO_2 ceramic wafer (sample A1). For samples A1 and A2, the photogenerated holes are able to effect, either by direct or an indirect electron transfer mechanism, the oxidative degradation of SA. The lower CO_2 evolution rate of sample A1, may be attributed to a less efficient vectorial separation of the photogenerated electrons and holes, and so a greater rate of electron-hole recombination occurring within the pure TiO_2 wafer and on its surface. Conducting the degradation experiment with smaller amounts of SA showed that the degradation rate was independent of the quantity of SA present, as shown for sample A2b (a TiO_2–WO_3 SPH wafer with 10 μL of 0.05 M SA in $CHCl_3$ solution on the TiO_2 side). Sample A3

(SPH with SA on WO_3 side and irradiation on the TiO_2) appeared slightly more effective than sample A1 for SA degradation. Kim et al. have shown that WO_3, when photoexcited, can generate hydroxyl radicals via reductive decomposition of H_2O_2 that is produced by reduction of O_2 on WO_3 (Kim et al. 2010). Thus, it is also likely herein that photogenerated electrons on the surface of WO_3 generate H_2O_2, which can act as a secondary source of hydroxyl radicals that are effective in aiding photocatalytic SA oxidation. The photogenerated holes would then be able to oxidise surface adsorbed H_2O to O_2. In contrast, a TiO_2–WO_3 SPH with SA and UVA light on the WO_3 surface yielded very little CO_2.

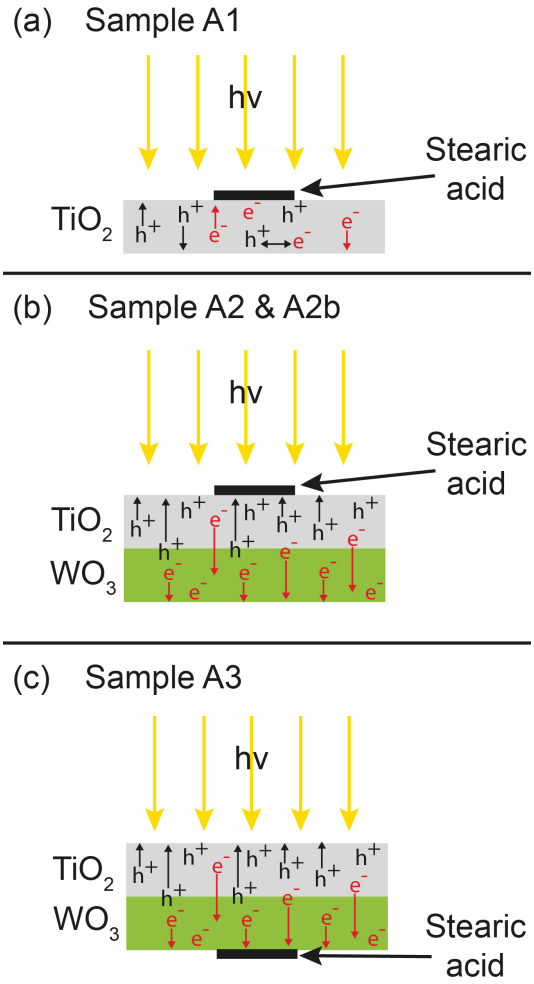

Figure 6.10 Schematic diagrams illustrating sample configuration and identifying the surface containing stearic acid (SA) and subjected to UVA irradiation as: (a) ceramic wafer of TiO_2 only, SA and UVA irradiation on the same surface, (b) self-supported photocatalytic heterojunction (SPH) wafer of TiO_2–WO_3 with SA and UVA irradiation on the TiO_2 surface, and (c) SPH wafer of TiO_2–WO_3 with SA on the WO_3 surface and UVA irradiation on the TiO_2

surface. e^- and h^+ and their corresponding arrows on diagrams (a)–(c) indicate the expected mobility of electrons and holes in the ceramic wafers.

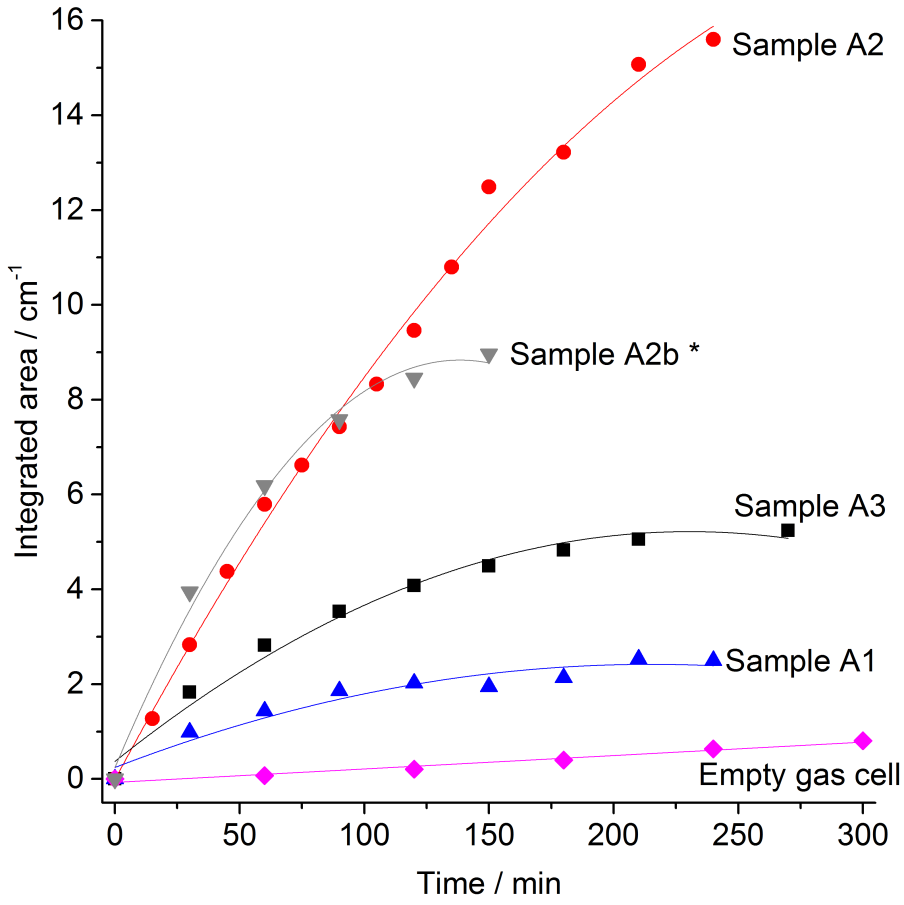

Figure 6.11 CO_2 evolution profile over the course of the degradation of stearic acid on ceramic wafers, under UVA irradiation (2 × 8 W 365 nm) as identified in Figure 6.10. * Sample A2b was coated with 10 µL of 0.05 M stearic acid, to investigate whether the degradation rate was affected by the quantity of stearic acid present.

The data presented in Figure 6.11 can be used to determine the initial formal quantum efficiency (FQE) for the removal of SA, defined as the ratio between the SA molecule degradation rate and incident photon flux. The photon flux for the UVA light source was calculated as 1.09×10^{15} photons cm^{-2} s^{-1}. The average values of the FQE and SA degradation rate are provided in Table 6.1. From the FQE values reported, it is clear that the photocatalytic activity is higher for the TiO_2–WO_3 heterojunction wafers, and

similar findings are reported in the literature, for composite thin films of TiO_2–WO_3 prepared via chemical vapour deposition (Quesada Cabrera et al. 2012).

Table 6.1 Formal quantum efficiency (FQE) and average stearic acid (SA) degradation rate on ceramic wafer samples of TiO_2 and TiO_2–WO_3, as described in Figure 6.11.

Sample	**FQE × 10^{-4} (molecules photon^{-1})**	**Rate × 10^{13} (molecules cm^{-2} min^{-1})**
A1	1.7	1.1
A2	6.7	4.4
A2b	6.9	4.5
A3	2.7	1.8

6.4.3. Ceramic wafer characterisation

The ceramic wafers were analysed by XRD before and after heat treatment. An XRD pattern of the TiO_2 phase (Figure 6.12) confirms that the TiO_2 remained in the anatase (A) structure after heat treatment.

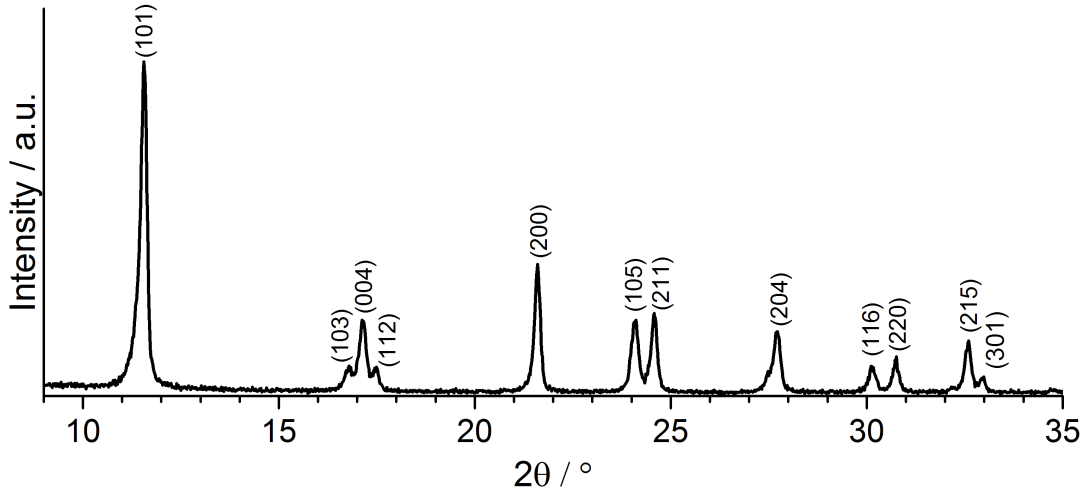

Figure 6.12 X-ray diffraction pattern of the TiO_2 phase of a TiO_2–WO_3 ceramic wafer following heat-treatment (500 °C, 6 h), indexed to the anatase structure of TiO_2. Data collected using Mo-Kα radiation (λ = 0.709 Å).

FE-SEM images are shown in Figure 6.13, where the distinction between the TiO_2 and WO_3 layers is clearly apparent; suggesting the interaction between the layers is a physical, rather than chemical, interaction. Also apparent from the image is the large difference in particle size between the two materials (Figure 6.13(a)-(b)). Despite this difference, the results described in this work demonstrated that electron transfer was still feasible between the particles. The average thickness of the WO_3 layer was measured as 82.2 ± 3.2 μm. Figure 6.13(c) shows an image of the WO_3 layer where loosely bound particles are seen in the area marked *a*. Upon cracking of the ceramic wafer (to enable imaging across the heterojunction interface) the physical interaction between particles may have disrupted, resulting in loosened particles. Conversely, the area marked *b* shows particles in very close contact in the horizontal plane (which was also the direction of compaction), across which it is believed charge transport occurs. Figure 6.13(d) shows an image of the TiO_2 layer, although analysis was limited due to the low resolution of the image.

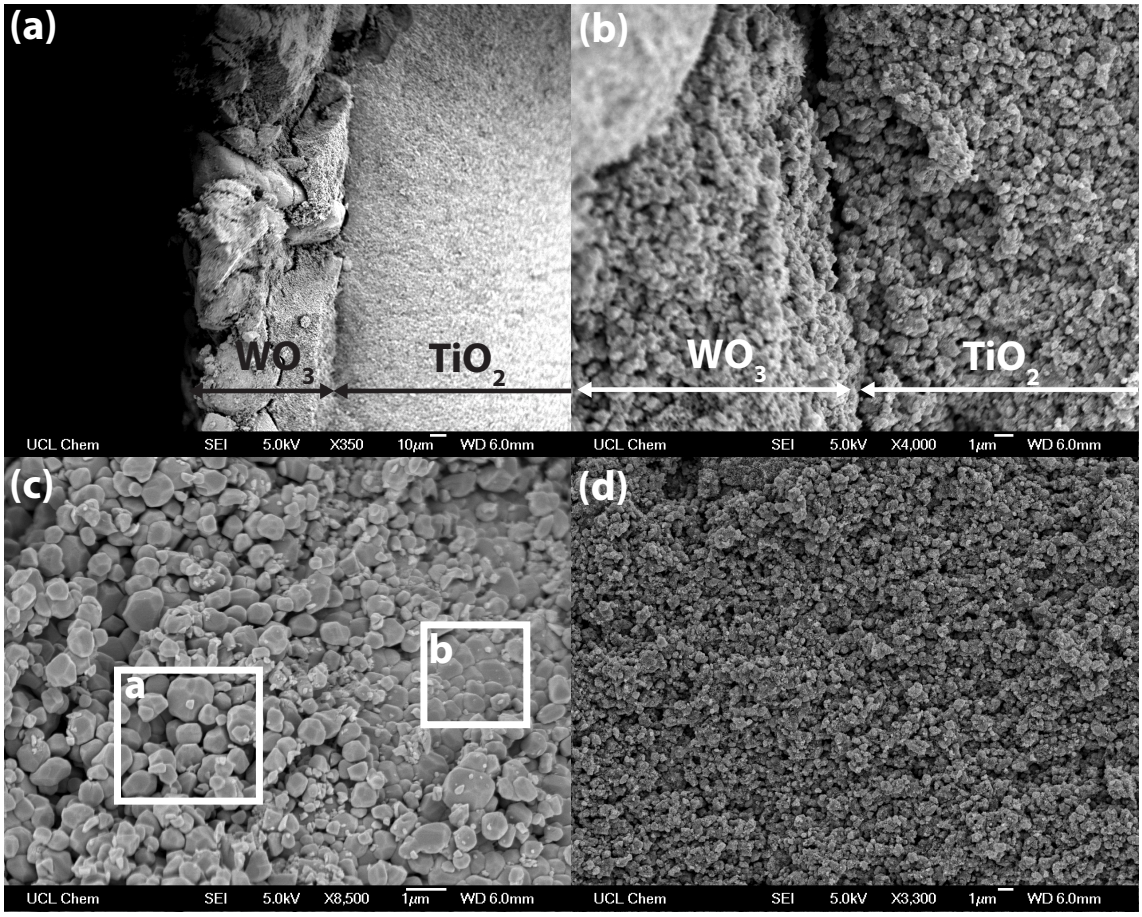

Figure 6.13 FE-SEM images of the TiO_2–WO_3 ceramic wafer heterojunction following preparation. Images (a) and (b) show the distinction between the TiO_2 and WO_3 layers at the physical interface between the two materials. Image (c) shows the WO_3 layer, with the area marked *a* showing loosely bound particles as a result of the disrupted physical interaction when the ceramic wafer was cracked for imaging. The area marked *b* shows particles in very close contact, as a result of the compaction of the powder upon preparation of the ceramic wafer (the compaction occurred in the horizontal plane). Image (d) shows the TiO_2 layer.

6.5. CONCLUSIONS

In closing, the findings presented herein show that simple and robust TiO_2–WO_3 SPH wafers can be prepared using a low-cost method, by pressing the relevant powders together at high pressure, followed by heat treatment to increase their mechanical strength. The wafers were self-supported and therefore did not require a substrate layer. Whilst TiO_2 is known to be an efficient photocatalyst in its own right, the formation of a semiconductor heterojunction with WO_3 provided greater control over, and enhanced,

its photocatalytic activity. One main factor leading to this was the vectorial charge separation and reduction in electron-hole recombination, due to the efficient transfer of photogenerated electrons between the TiO_2 and WO_3 layers. The findings demonstrated that an intimate electronic contact can be developed between different photocatalytic powders through high-pressure pressing only, not requiring multiple (often complex) reaction steps, or taking many hours to complete.

The work presented in this chapter shows that there is considerable potential for improved photocatalytic performance, by using the self-supported heterojunction wafers described, prepared by a simple technique. Whilst the ceramic heterojunction wafers had greater photocatalytic efficiencies than individual semiconductor wafers, the pressing procedure was not optimised. Therefore, there may be potential to further improve their photocatalytic performance by, firstly understanding the nature of charge transfer through the wafer, and secondly, further developing the pressing procedure. Additionally, by carefully selecting appropriate photocatalyst combinations to best exploit band gaps and relative band positions (under suitable conditions), it should be possible to facilitate heterojunctions for a wide range of photocatalytic reactions. Following on from this investigation, Chapter 7 presents further experimental results, focussing on the application of the heterojunction wafers in photocatalytic water disinfection.

Chapter 7. Photocatalytic water disinfection by TiO_2-WO_3 pressed ceramic wafers

7.1. AIMS AND OUTLINE

In this chapter, the heterojunction TiO_2–WO_3 ceramic wafers that were introduced in Chapter 6 are investigated for their ability to photocatalytically disinfect water. In addition to the heterojunction wafers, a single layer pure TiO_2 wafer was also investigated. The aim of this work was to determine the similarities and differences between these two pressed wafer configurations. The wafers were placed in solutions that had been inoculated with bacteria, and their disinfection profile was followed over a given period. The disinfection data was fitted using a bacterial inactivation model-fitting tool, which reported a number of statistical measures to allow meaningful comparison.

7.2. INTRODUCTION

In 2012, the United Nations estimated that nearly 11 % of the world's population did not have access to improved sources of drinking water, with ca. 3.5 million deaths annually attributed to unsafe water supplies, poor sanitation and unsatisfactory hygiene (United-Nations 2012). With ever-increasing populations, there is now an unprecedented demand to improve basic water facilities, particularly in rural regions of less economically developed countries. The ideal solution would be to improve sanitation infrastructure, however, this is often associated with large cost and may not be practical to implement quickly. Short-term solutions that provide clean drinking water at the point-of-use are regularly used, such as boiling and filtration techniques. However, these are not effective at removing all pathogens.

Over the last decade, solar disinfection techniques such as SODIS (SOlar DISinfiection) have been developed and used by over a million people (Ubomba-Jaswa et al. 2008; Ubomba-Jaswa et al. 2009; McGuigan et al. 2012). SODIS typically involves filling a glass or plastic bottle with contaminated water and placing the bottle in direct sunlight (e.g. on a roof) for at least 6 hours, which exposes pathogens to UVA radiation, and

therefore inactivates them. After this exposure, the water is deemed safe to drink. However, while the SODIS technique is simple and easy to implement, it has limitations that can lead to the drinking water being unsafe. Main limitations concern the type of bottle used (a maximum volume of 3 litres), the turbidity of the water (i.e., placing the bottle on a newspaper should allow the headline text to be read through the bottled water), and the shelf-life of the SODIS-cleaned water, that should be consumed within 24 hours (McGuigan et al. 2012). Based on these considerations, the SODIS technique can only be used as a point-of-use intervention, rather than for large-scale water disinfection. Thus, there is a real need to develop simple and inexpensive alternatives to SODIS, which are able to provide larger volumes of clean drinking water.

An alternative approach to SODIS is to use semiconductor photocatalysts to efficiently achieve solar water disinfection, without the limitations of SODIS. In this approach, the semiconductor photocatalyst undergoes a series of photoelectrochemical processes that result in the formation of reactive species, which are able to more rapidly inactivate pathogens. In the first step, illumination of the semiconductor by light of an appropriate wavelength can excite electrons from the valence to the conduction band, leading to the formation of an electron-hole pair. The charge carriers can then either recombine (with no catalytic reaction) or migrate to the semiconductor surface where they can participate in surface reactions to form radicals, typically reactive oxygen species (ROS). These radical species are powerful redox agents that can rapidly destroy organic pollutants and inactivate many pathogens.

Typically, photocatalytic disinfection experiments are conducted with either the photocatalyst suspended in solution or immobilised on a substrate. Although placing the photocatalyst in suspension can yield high efficiencies (Malato et al. 2009), it is often difficult to recover the photocatalyst (Byrne et al. 2011), and therefore photocatalysts immobilised on surfaces are of interest (Dunlop et al. 2002; Fernández et al. 2005; Sichel et al. 2007a; Sichel et al. 2007b; Dunlop et al. 2008; Akhavan et al. 2009; Alrousan et al. 2009; Alrousan et al. 2012; Pablos et al. 2013).

Building on the use of self-supported photocatalytic heterojunction wafers discussed in Chapter 6, the investigations discussed herein focus on addressing the challenges presented in water disinfection applications. Comparisons are made between the

photocatalytic action of a TiO_2–WO_3 heterojunction wafer and a pure TiO_2 wafer, by photoirradiating wafers placed in a saline solution contaminated with the Gram-negative bacterial pathogen, *E. coli* K-12, a widespread infective agent found in water. Photodisinfection using the SPH wafer was highly effective and superior to the pure TiO_2 wafer.

7.3. EXPERIMENTAL METHODS

7.3.1. Chemicals and materials

Escherichia coli (*E. coli*) K-12 (DSM 5210) was obtained from the Deutsche Sammlung von Mikroorganismen und Zellkulturen GmbH, DSMZ (Braunschweig, Germany). Luria Bertani (LB) medium and phosphate buffered saline (PBS) were obtained from Sigma-Aldrich (Dorset, UK). Sodium chloride (NaCl) was obtained from VWR (Leicestershire, UK). Deionised (DI) water (>15 MΩ resistivity) was used for the preparation of all solutions. All chemicals were used as received.

7.3.2. Experimental techniques

Throughout all experiments, it was necessary to ensure a sterile environment was maintained, so as to prevent any external factors affecting bacterial inactivation. All surfaces were wiped with ethanol to ensure there was no contamination from the environment. Equipment that was in direct contact with bacterial samples was autoclaved prior to use. The autoclave provided high-pressure steam at 121 °C for 15 minutes to inactivate bacteria, bacterial spores, viruses and fungi, from equipment surfaces. Autoclave tape was used as an indicator to confirm that the above conditions were reached during any autoclave cycle (the tape would change colour under autoclave conditions). When handling equipment and samples, gloves were always worn (which were wiped clean with ethanol prior to use). Bacterial samples were handled either in a laminar flow hood, or in the presence of a Bunsen flame (to sterilise the surrounding air).

7.3.3. Preparation of agar plates

Agar plates were prepared in a laminar flow hood, which maintained a sterile environment by purifying air through a series of filters, and then passing the purified air uniformly over a bench surface. LB agar powder was mixed with sterile DI water at ≈ 20 g/L and autoclaved. The liquid was then poured in to sterile petri dishes and allowed to cool, upon which it solidified. The lids were placed on the petri dishes and stored in a fridge until further use. The agar plates were stored upside down, to prevent any condensation that may have formed on the internal surface of the lid from dripping down on to the agar.

7.3.4. Initial bacterial cultivation

E. coli was obtained as a freeze-dried pellet consisting of a culture suspension on a protectant/carrier, and stored in a sealed glass ampoule. Under sterile conditions, the inner tube containing the pellet was removed, 500 µL LB was added and the pellet was left to dissolve for 30 min. 10 µL of the resulting solution was dropped on to an agar plate and spread across the surface. This procedure was repeated to obtain a second plate, and both plates were placed in an incubator at 37 °C for 15 hours (Figure 7.1).

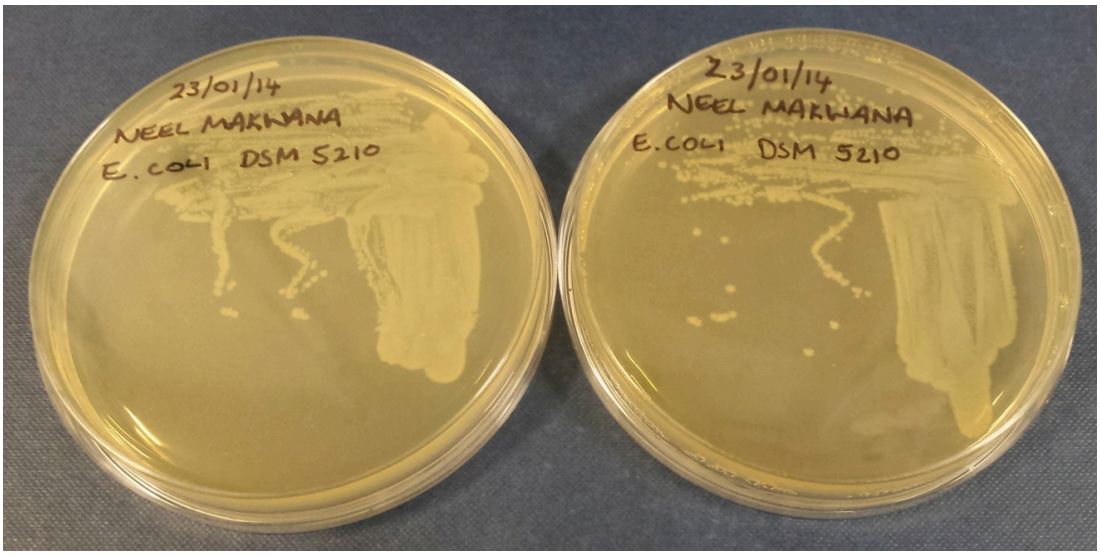

Figure 7.1 Agar plates following cultivation of *E. coli* DSM-5210. Single colonies (known as colony forming units, CFU) are observed as individual spots on the agar plate.

Separately, each of four centrifuge tubes was filled with 10 mL LB. In each tube, 100 µL of the *E. coli* solution was placed, and the tubes were incubated at 37 °C for 15 hours. The tubes were then made up with glycerol and stored at –80 °C as an additional source of the bacteria. The remainder of the *E. coli* solution was placed in a microcentrifuge tube and stored in the fridge for future cultivations, if required.

7.3.5. Determination of stationary phase culture growth conditions

Following cultivation of *E. coli* on agar plates, it was necessary to determine the optimum culture growth conditions to obtain the required quantity of colony forming units per millilitre (CFU/mL), at the stationary phase. Two conditions were chosen: (a) cultivation at 37 °C for 18 hours under an agitation of 250 rpm (sample FT-1), and (b) cultivation at 37 °C for 24 hours under an agitation of 100 rpm (sample FT-2). For each condition, a single colony of *E. coli* from the agar plate was taken and placed in a centrifuge tube containing 10 mL LB. The tubes, along with control tubes containing only 10 mL LB (to ensure sterility of the technique), were placed in an incubator under their respective conditions. Following incubation, the tubes in which a single colony of *E. coli* had been placed developed a cloudy appearance, whilst the control tubes remained transparent (shown in Figure 7.2). The cloudy appearance characterised bacterial growth (Kumar 2012), whilst the transparent appearance of the control tubes confirmed that the LB remained contaminant-free.

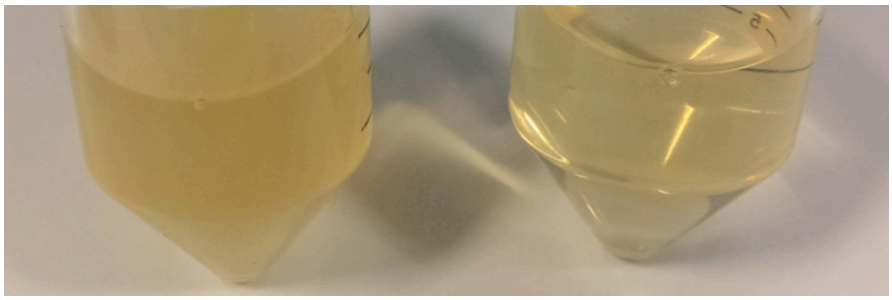

Figure 7.2 Photograph of FT-2 (left) and control (right) following cultivation at 37 °C for 24 hours under 100 rpm agitation. The cloudy appearance of FT-2 is characteristic of a sample containing bacteria, whereas the transparent appearance of the control shows only the presence of LB.

The number of CFU/mL was determined for each of the two samples using the serial dilution technique, illustrated in Figure 7.3. Up to seven microcentrifuge tubes were filled with 900 µL of phosphate buffered saline (PBS); 100 µL of the *E. coli* sample (from either sample FT-1 or FT-2) was then added to the first microcentrifuge tube. The tube was shaken, 100 µL was removed and added to the second tube; this dilution process was repeated until all tubes were filled. It was important to replace the pipette tip after each dilution to prevent contamination. 10 µL from each tube, starting with the highest dilution (most dilute), were removed and a drop placed on an agar plate. For each tube, 3 drops were added to the plate. 3 drops of the neat *E. coli* sample were also added to the plate (as the 0^{th} dilution). After allowing the plates to dry for 20 minutes, they were placed in an incubator at 37 °C for approximately 15 hours.

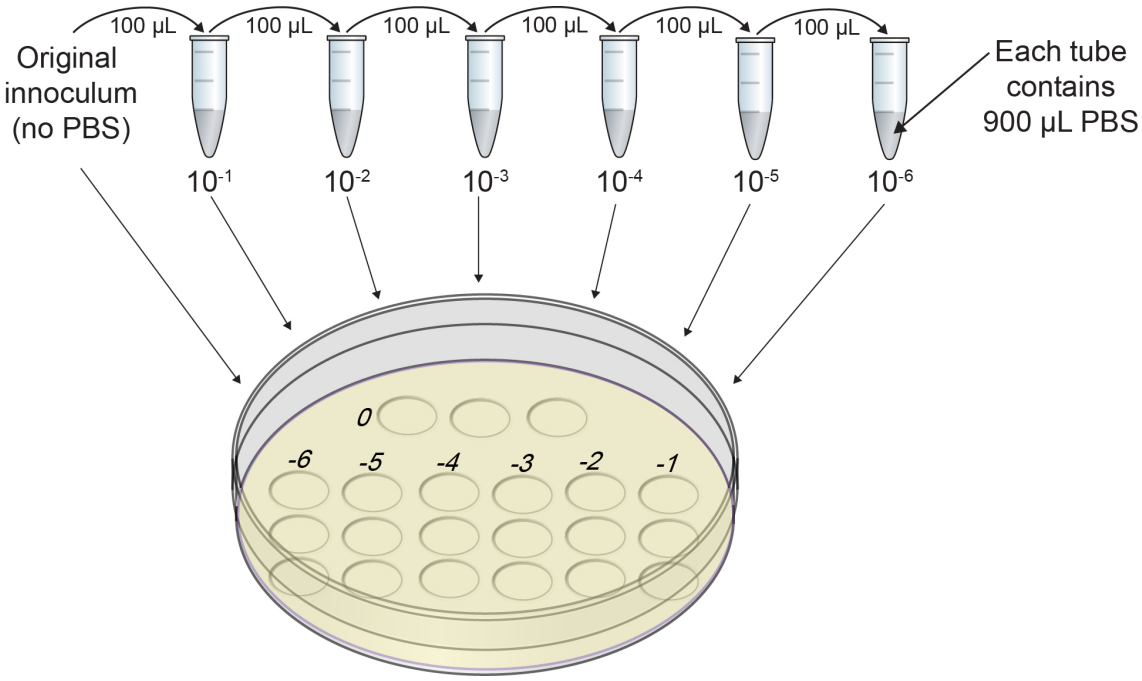

Figure 7.3 Illustration of the serial dilution technique. The original inoculum (100 µL) was placed in a microcentrifuge tube with 900 µL PBS solution (forming the 10^{-1} dilution) and shaken. 100 µL from the first microcentrifuge tube was then transferred to a second microcentrifuge tube (containing 900 µL PBS) and shaken, before 100 µL was transferred to a third microcentrifuge tube. This sequential dilution was repeated until up to seven dilutions

had taken place (i.e. up to 7 microcentrifuge tubes). 3 × 10 µL drops for each dilution and the original inoculum (0th dilution) were placed on an agar plate as shown.[§]

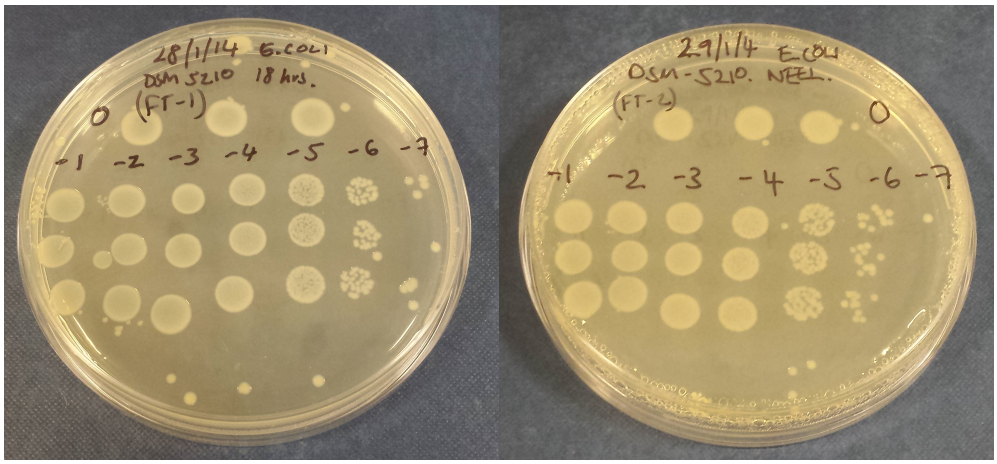

Figure 7.4 Appearance of agar plates (L) FT-1 and (R) FT-2 following the serial dilution technique to determine ideal growth conditions for *E. coli* bacteria. The numbers 0 to -7 indicates the dilution factor, whilst the white spots show *E. coli* growth. At the -6 and -7 dilution, individual spots are observed; each represents one colony forming unit (CFU).

Figure 7.4 shows the appearance of the agar plates following incubation. Sample FT-1 gave a total count of 9 colonies at the -7 dilution, equating to 3×10^9 CFU/mL, and sample FT-2 gave a total of 31 colonies at the -6 dilution, equating to 1×10^9 CFU/mL. For the water disinfection experiments the required concentration was 10^6 CFU/mL, hence both growth conditions gave adequate bacterial concentrations.

7.3.6. Subsequent bacterial cultivation

The procedures described in sections 7.3.4 and 7.3.5 were only conducted once to (a) activate the bacterial strain and (b) determine growth conditions. Subsequent cultivations were performed by taking a sample of *E. coli* from stock (stored at −80 °C) and placing it in 10 mL LB in a centrifuge tube. The tube, along with a control (containing only 10 mL LB) was placed in an incubator at 37 °C for 18 hours under an

[§]Image credit: Microcentrifuge tube illustration provided by http://www.vector.me (file: 'eppendorf_open') and petri dish illustration provided by http://www.clker.com

agitation of 250 rpm. 10 μL of the resulting solution was dropped on to an agar plate and spread across the surface; the plate was then placed in an incubator at 37 °C for 15 hours. Following incubation, a single colony was taken from the agar plate and placed in 10 mL LB for incubation, at 37 °C for 18 hours under an agitation of 250 rpm.

1 mL of the suspension was removed, placed in a microcentrifuge tube and centrifuged at 3000 rpm for 10 minutes. The bacteria consolidated to form a yellow spot at the bottom of the microcentrifuge tube. The supernatant was discarded before re-suspending the bacteria in 1 mL of a 0.9 % sodium chloride (NaCl; saline) solution. The centrifugation was repeated twice more, each time with the supernatant being removed and replaced with fresh saline solution. This process of washing the sample was used to remove traces of LB from the bacteria. Following the final centrifugation, the bacteria were re-suspended in the saline solution, ready to inoculate the test solution.

7.3.7. Preparation of ceramic wafers

Ceramic wafers were prepared following an identical method to that described in Chapters 3 and 6. Briefly, powders (either TiO_2 with WO_3 on top or TiO_2 alone) were placed in a 25 mm diameter stainless steel die (Compacting Tooling Inc., Philadelphia, USA) and levelled to create an even surface. The die assembly was placed in the extraction ram of a non-end-loaded piston cylinder device (Depths of the Earth Co., Arizona, USA), and pressed to a pressure of 200 bar. The ceramic wafers were heat-treated at 500 °C for 6 hours in air to enhance their mechanical strength.

7.3.8. Control experiments

A number of control experiments were conducted, to ensure the sterility of the techniques employed throughout this study was sufficient to prevent the growth of foreign organisms, which may have affected the survivability of the *E. coli* bacteria. Saline solution (60 mL) was placed in a water-cooled (jacketed) glass vessel, and placed under dark and light conditions, separately. After a 3-hour period, a 10 μL sample was placed on an agar plate and spread across the surface. Following an overnight incubation, bacterial growth was not observed in either case, and this confirmed that the sterility of the saline preparation technique was sufficient. Additionally, the control

experiments were repeated in the presence of the photocatalytic wafers; again bacterial growth was not observed.

7.3.9. Disinfection experiments

Each disinfection experiment was conducted in 60 mL saline solution. The solution was inoculated with the *E. coli* suspension (60 µL) prepared in section 7.3.6, which achieved an initial cell density of 10^6 CFU/mL. For experiments conducted under photoirradiation, UV-visible light was provided by a 75 W xenon arc lamp (Photon Technology International, UK) fitted with an AM 1.5G filter (Newport Spectra-Physics Ltd., UK), to simulate solar irradiation. To avoid any thermal effects arising from the xenon lamp, all experiments were conducted in a double-walled glass reactor with cooling water (20 °C) circulated through the outer wall (ThermoHake 75 chiller). The ceramic wafer was suspended in the glass reactor, and aligned such that it was in the direct path of light from the lamp. For experiments conducted under dark conditions, the glass reactor was covered with aluminium foil to prevent any stray light from entering the reactor. During the experiments, samples of the test solution (0.5 mL) were collected from the reactor at regular intervals. Each sample was subjected to a series of 10-fold dilutions in saline solution, following the serial dilution technique (described in section 7.3.5). After the agar plates were incubated, colonies were counted visually to determine the bacterial concentration at each time interval.

7.3.10. Data fitting models

The *E. coli* survivability data were fitted using the Geeraerd and Van Impe Inactivation Model Fitting Tool (GInaFiT, v1.6) (Geeraerd et al. 2005). A number of fitting models were run for each data set; comparison between the fit of each model was possible by assessing the value of the Root Mean Sum of Squared Errors (RMSE). The RMSE is considered the most simple and informative measure of goodness-of-fit, where a smaller value indicates a better data fit (Ratkowsky 2003). For the data presented herein, it was found that the 'log-linear with shoulder', 'Weibull with tail' and 'Weibull' models (Geeraerd et al. 2000; Albert and Mafart 2005) were most appropriate for the SODIS, TiO_2–WO_3 SPH and TiO_2 wafers, respectively. The output fitting curves are shown

along with the bacterial survival data, with the data values presented in section 7.6 for comparison.

7.4. RESULTS AND DISCUSSION

7.4.1. Disinfection control experiments

Once it was confirmed that the sterility of the techniques was adequate, and would not contribute to any bacterial growth, it was necessary to conduct further control experiments to calibrate for any potential effects of the experimental conditions on *E. coli* in the saline solution. Such effects included osmotic and mechanical stresses (imposed by the saline solution and stirring), temperature, pH, and the nature of the surrounding environment. The first control experiments were conducted in the dark, in the presence and absence of the photocatalytic wafers. The results (Figure 7.5) showed that significant decrease in bacterial survivability under these experimental conditions was not observed, where the *E. coli* concentration fluctuated about 10^6 CFU/mL over a 5-hour period.

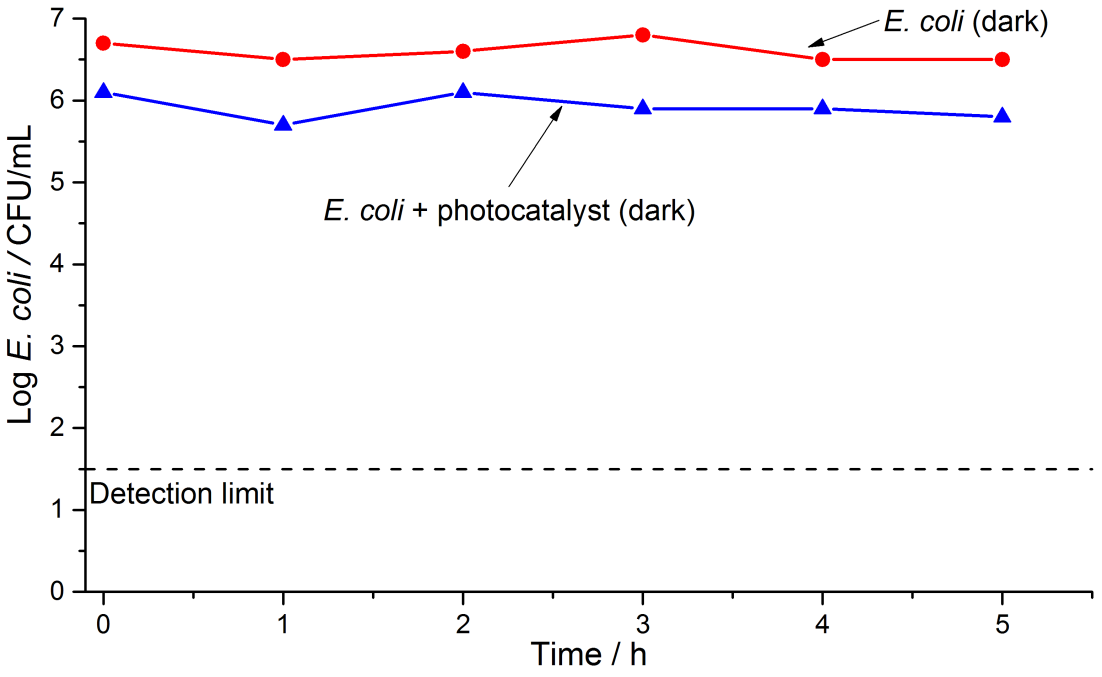

Figure 7.5 *E. coli* inactivation control experiments over a 5-hour period; filled circles [●] show inactivation of *E. coli* in saline solution in the dark and filled triangles [▲] show inactivation in the presence of a TiO_2–WO_3 wafer in the dark.

Subsequent control experiments were conducted with *E. coli* bacteria suspended in saline solution, and placed under photoirradiation (in the absence of the photocatalytic wafers), simulating the SODIS technique of placing contaminated water under direct sunlight. Figure 7.6 shows the appearance of agar plates following the serial dilution technique at each sampling interval (1 hour increments). The corresponding inactivation data is shown in Figure 7.7. A decrease in bacterial survivability was observed after ca. 2 hours of irradiation, demonstrating that the UV light partially and directly inactivated *E. coli*. Similar results have been reported previously using simulated or real solar conditions, with slow *E. coli* inactivation observed in the range ca. 2 to 6 hours (Lonnen et al. 2005; Berney et al. 2006b; Boyle et al. 2008; Ubomba-Jaswa et al. 2008; Ubomba-Jaswa et al. 2009; Alrousan et al. 2012; Agulló-Barceló et al. 2013). These observations are in line with expectations, and demonstrate SODIS water disinfection. The kinetics of the disinfection process is discussed later in section 7.4.3.

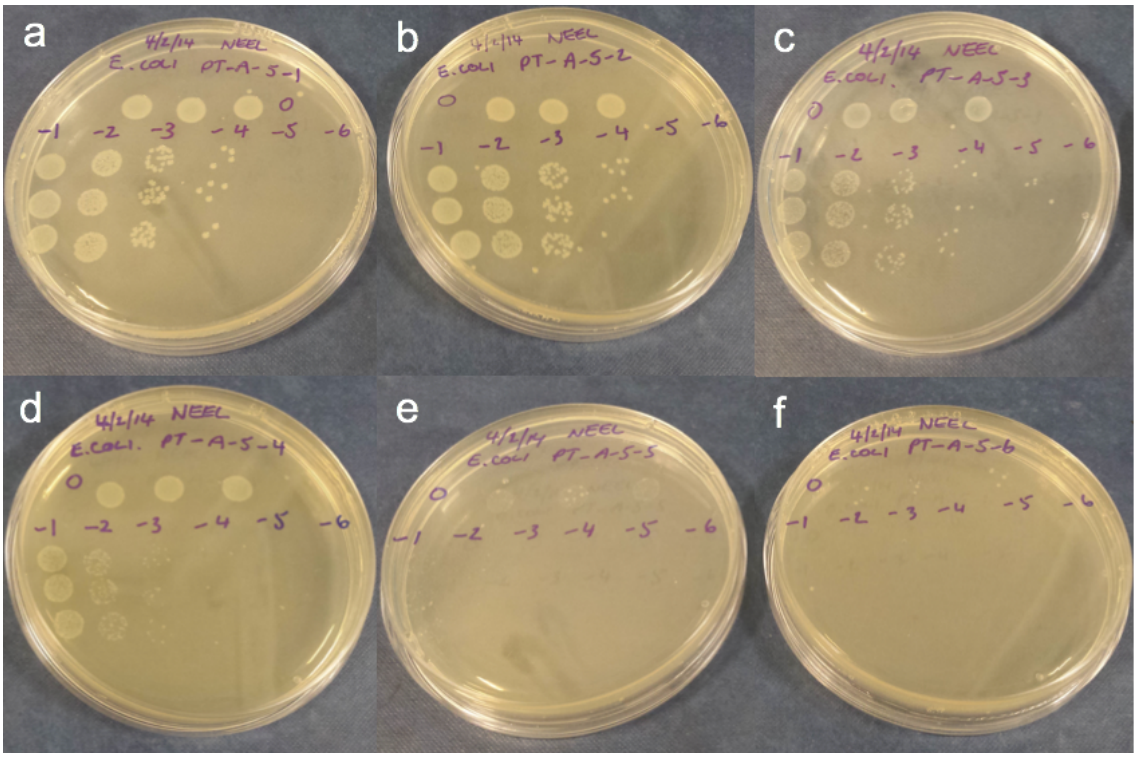

Figure 7.6 Appearance of agar plates following the serial dilution technique conducted following the SODIS experiment. Each photograph shows the *E. coli* growth following incubation of the agar plates for 15 hours at 37 °C at hourly time intervals beginning with (a) 0 hours through to (f) 5 hours.

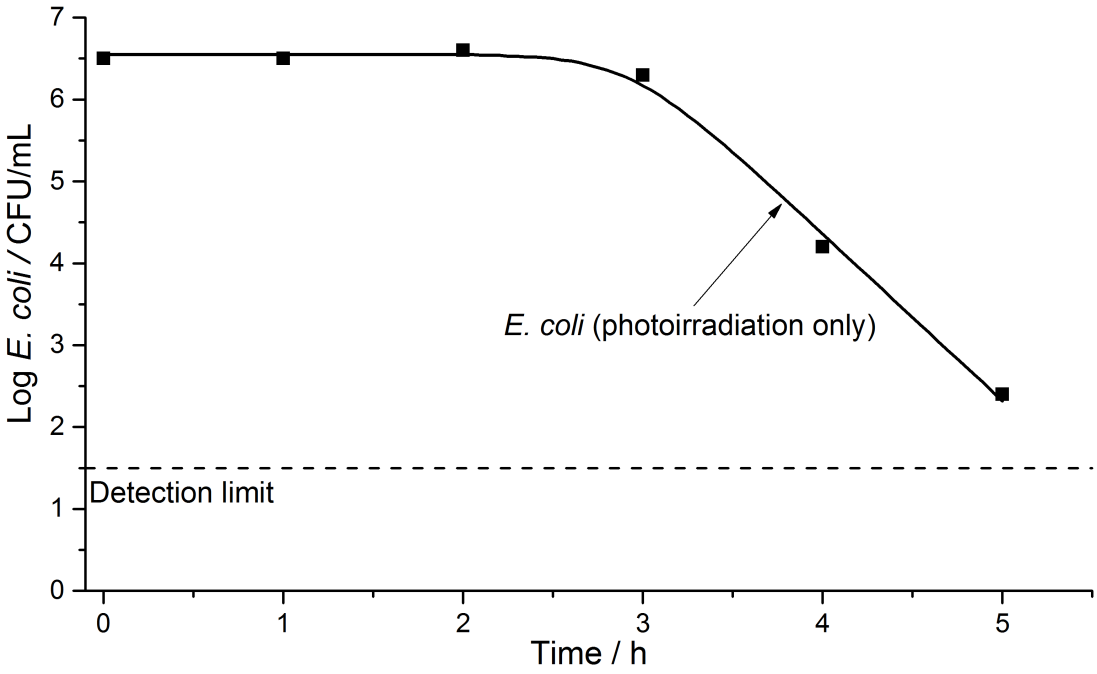

Figure 7.7 Inactivation of *E. coli* in saline solution under direct irradiation from a 75 W xenon lamp (in the absence of a photocatalytic wafer), simulating the SODIS technique. The solid line shows a data fit using the log-linear with shoulder model.

7.4.2. Photocatalytic disinfection of water

Photocatalytic disinfection experiments were conducted with a TiO_2–WO_3 heterojunction wafer and a pure TiO_2 wafer, to determine the similarities and differences in photocatalytic rates between heterojunction and non-heterojunction systems. Figure 7.8 shows the *E. coli* inactivation data obtained for water disinfection in the presence of a TiO_2–WO_3 wafer, over a 5-hour period. Sampling was conducted at hourly intervals. The results show that bacterial inactivation occurred within the first hour, after which the detection limit was reached at each subsequent hour. This suggested that the presence of the TiO_2–WO_3 wafer had a profound effect on the inactivation of *E. coli*. It was not possible to fit the data using the GInaFIT tool because there were too few data points during the time period of interest, i.e. the first hour. To investigate the potential for bacterial re-growth following water disinfection, the last sample (collected at 5 hours) was kept in the dark at room temperature. After a period of 16.5 hours, a plate spread was prepared using 10 µL of this sample, and incubated as described earlier. Bacterial re-growth was not observed, suggesting the photocatalytic

disinfection process was able to completely inactivate *E. coli*. This is in contrast to the SODIS technique, where re-growth has been reported over a period of seven days following SODIS (Gelover et al. 2006). Hence the recommendation that SODIS disinfected water is consumed within 24 hours.

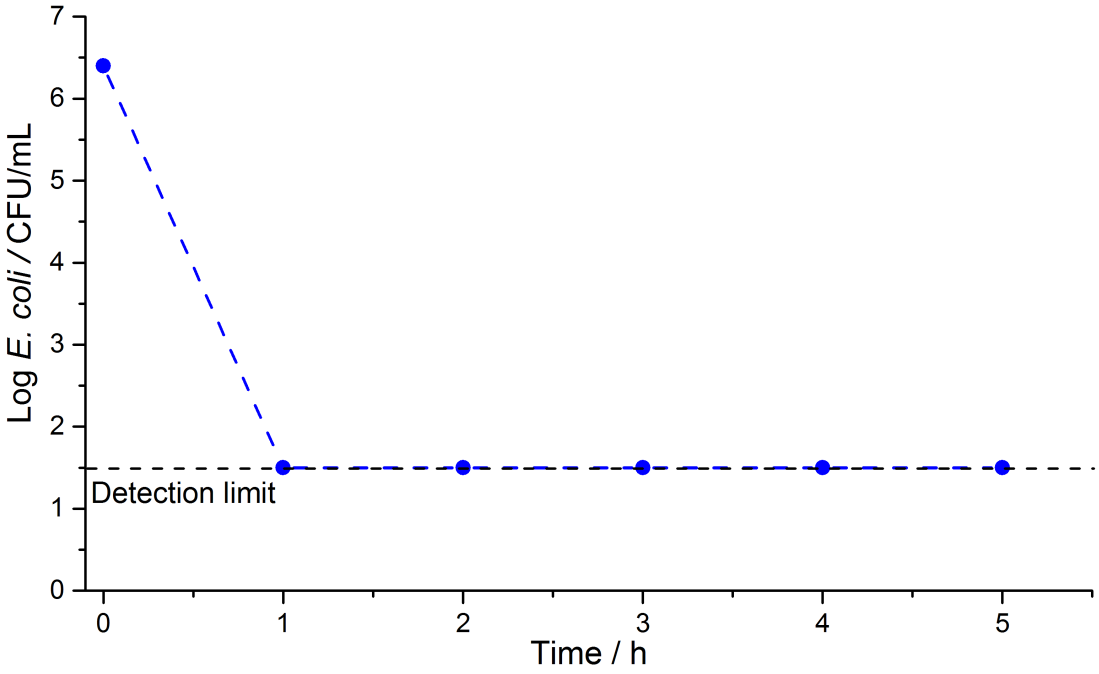

Figure 7.8 *E. coli* inactivation over a 5-hour period under irradiation from a 75 W xenon lamp in the presence of a TiO_2–WO_3 heterojunction ceramic wafer. The dashed line (blue colour) is shown only for clarity and does not constitute a data fit.

The results in Figure 7.8 showed that it was necessary to reduce the sampling interval to determine the disinfection profile occurring within the first hour, during which the detection limit was reached. A subsequent experiment was carried out where sampling was conducted in 15-minute intervals for the first hour, and then at 30-minute intervals for a second hour. The data obtained (not shown) suggested similar results to those already observed – the detection limit was reached within 30 minutes, but it was again not possible to fit the data, because there were only two data points during this time period.

Subsequently, sampling was reduced to 5-minute intervals, with a total sampling period of 30 minutes (data presented in Figure 7.9). The data was fitted with the GInaFIT tool

and it was deduced that the Weibull with tail model provided the most appropriate fit. To provide comparison with a non-heterojunction system, identical disinfection experiments were conducted with a pure TiO_2 ceramic wafer (data presented in Figure 7.10). In this case, the Weibull model provided the best fit to the data. Similarly to the heterojunction wafer, the detection limit was reached within ca. 30 minutes, except the disinfection profiles appeared very different. From these results, it was apparent that the solar disinfection rate in the presence of the SPH or pure TiO_2 wafers was more than 10 times faster than with no photocatalyst present.

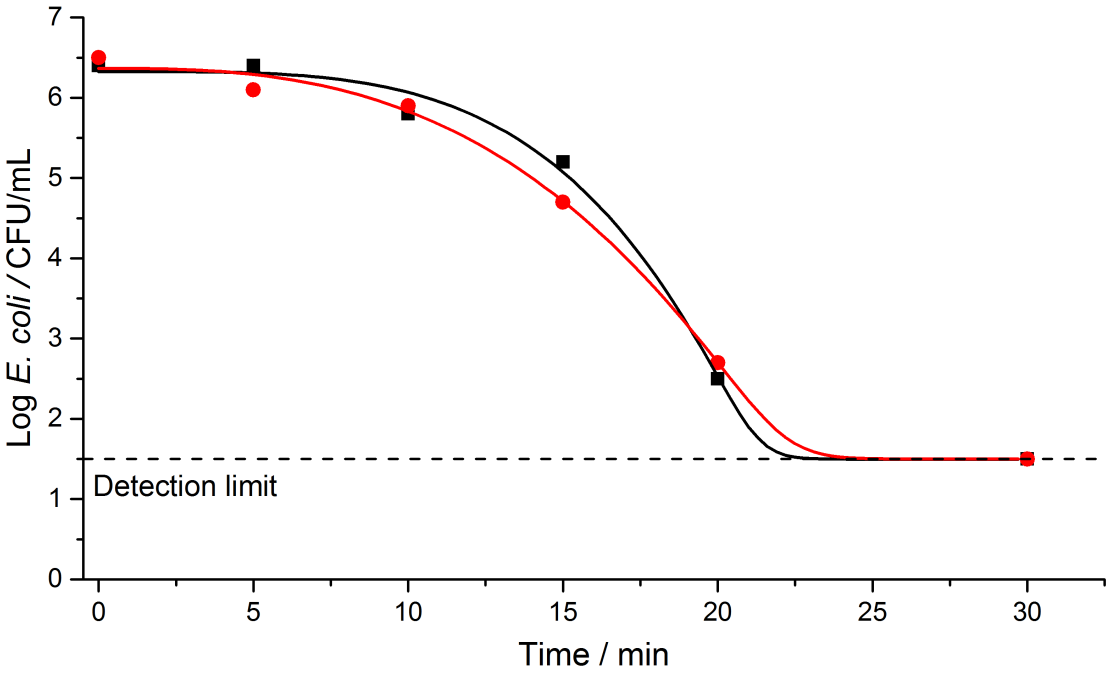

Figure 7.9 *E. coli* inactivation over a 30-minute period under irradiation from a 75 W xenon lamp in the presence of a TiO_2–WO_3 heterojunction ceramic wafer. The filled square [■] and circle [●] symbols are for two duplicate samples conducted simultaneously. The solid lines show data fits using the Weibull with tail model.

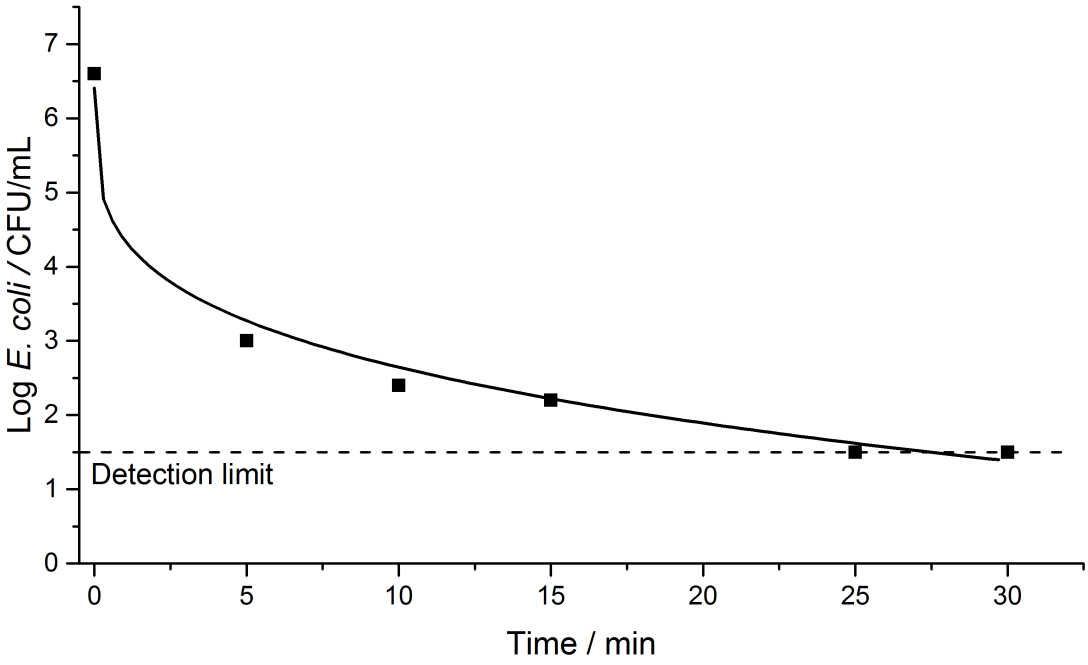

Figure 7.10 *E. coli* inactivation over a 30-minute period under irradiation from a 75 W xenon lamp in the presence of a TiO_2 ceramic wafer. The solid line shows a data fit using the Weibull model.

Comparison between the *E. coli* disinfection profiles of the TiO_2–WO_3 heterojunction and TiO_2 wafers showed a clear difference in the kinetics of the two systems. For the SPH wafer, there was an initial slow reduction in the microbial population, followed by a clear increase in the rate of inactivation. In contrast, for the pure TiO_2 wafer, the initial bacterial reduction was much faster, but was then followed by a gradual decrease in the rate of inactivation. The differences apparent between these two photoactive semiconducting systems can be explained in terms of electron-hole transfer lifetimes. The electron-hole recombination rate was expected to be substantially greater in the pure TiO_2 than the SPH wafer, because the latter incorporated a heterojunction that facilitated efficient vectorial charge separation, and allowed build-up (longer lifetimes) of these charges, which can facilitate the production of ROS for bacterial inactivation.

It is important to note that the differences in the time taken for a significant reduction in the *E. coli* population, occur because different disinfection mechanisms occur in the presence or absence of a photocatalyst. In the SODIS technique, bacterial inactivation results from direct exposure to UVA light and heat, resulting in cellular membrane

damage and a decreased rate of bacterial growth (Hamamoto et al. 2007). Formation of ROS can also occur when photons are absorbed by dissolved oxygen in the water, and these species may also contribute to the SODIS effect. In the presence of a photocatalyst, however, the main disinfection mechanism is believed to arise from cellular attack by ROS species (Byrne et al. 2011). It is suggested that the hydroxyl radical ($OH^{\bullet}$) is primarily responsible for inactivation of microorganisms (Alrousan et al. 2012), while there are also reports that other ROS species, such as superoxide radicals ($O_2^{\bullet-}$), can affect survivability of microorganisms.

Results previously described in Chapter 6 have shown that when the titania side of TiO_2-WO_3 SPH wafers is photoirradiated, electrons can rapidly shuttle to the WO_3 side. Once at the WO_3 surface, these electrons can reduce W^{6+} (to W^{5+}) and O_2 molecules to form $O_2^{\bullet-}$ or H_2O_2, which then undergo reductive decomposition to form $OH^{\bullet}$ radicals (Kim et al. 2010). The holes at the TiO_2 surface can also oxidise species such as surface-adsorbed H_2O, to form $OH^{\bullet}$ radicals with disinfective properties (Quesada Cabrera et al. 2012).

The immobilisation of photocatalysts in solar water disinfection is of importance, particularly in locations where post-filtration may not be available. Previously, Alrousan et al. studied the solar disinfection of water under flow, using TiO_2 immobilised on the internal surface of borosilicate glass tubes. Microorganism inactivation occurred over a period of 5 hours, with no delamination of the TiO_2 coating occurring (Alrousan et al. 2012). Whilst immobilisation of a photocatalyst on a substrate proved effective, the self-supported nature of the pressed wafers presented herein removes the need for a substrate, along with associated production costs. Additionally, scale-up of pressed wafers such as those described, can be readily achieved by using industrial powder processing techniques, to manufacture larger quantities of such self-supported photocatalyst structures.

7.4.3. Evaluation of disinfection kinetics

Since the first reports of photocatalytic water disinfection by Matsunaga et al. (Matsunaga et al. 1985), most kinetic data have been modelled using the Chick-Watson model (Chong et al. 2010), which is applicable to the log-linear bacterial inactivation

phase of the curve. While this region is of most interest, it is also important to model the kinetics occurring in other regions of the bacterial growth cycle, in order to understand the complete disinfection process. In this work, the GInaFIT model (Geeraerd et al. 2005) was used to quantitatively compare the kinetics of bacterial disinfection for experiments conducted under simulated solar irradiation, in the presence or absence of a photocatalyst. The GInaFIT model provides a total of nine potential models that can be applied to bacterial inactivation kinetic data. The suitability of each model can be determined by comparing the root mean square error (RMSE) values obtained for each. Table 7.1 provides the RMSE values for the various models used in this work, that are in the range 0.10 – 0.23. Because it was necessary to allow the bacterial solution to homogenise after each measurement, it was not possible to reduce the sampling interval to less then 5 minutes, and this limited the number of data points that could be obtained to constrain kinetic models.

The curve presented for bacterial inactivation under photoirradiation only (i.e. SODIS; Figure 7.7) began with an initial lag period followed by a bacterial inactivation phase. The initial lag phase is termed a 'shoulder' on the kinetic data, and its presence suggests that the bacteria initially display resistance to solar inactivation (Amin et al. 2014). The presence of the shoulder may be explained in terms of the nature of the organisms.

Bacteria may exist in a group or a clump, where each clump represents a single colony. To inactivate the colony, it is necessary to inactivate all individual cells in that clump, and therefore the length of the shoulder may coincide with the time before all but one organisms in such a clump is inactivated. This is known as the single-hit, multiple target theory (Casolari 1988; Geeraerd et al. 2000; Berney et al. 2006a; Kumar and Pandit 2012). Another theory, known as the multi-hit theory, is based on the assumption that a single target must be hit a number of times before it is inactivated (Berney et al. 2006a; Marugán et al. 2008). Alternatively, bacteria may be able to synthesise a critical component, and inactivation only occurs when the rate of destruction is greater than the rate of synthesis. In this scenario, the shoulder length may represent the time during which the cells are able to synthesise the critical component (Geeraerd et al. 2000). It is likely that a combination of these theories exists in the case of the SODIS bacterial inactivation.

Table 7.1 Kinetic parameters obtained from the GInaFIT tool with the log-linear with shoulder, Weibull with tail, and Weibull models.

Sample	Shoulder length, S_l	Rate constant, k_{max}	Scale parameter, δ	Shape parameter, p (min)	Root mean square error, RMSE
Simulated SODIS	2.9 ± 0.1 hours	4.70 ± 0.11 h^{-1}	–	–	0.1375
TiO_2–WO_3 (1)	–	–	14.15 ± 0.97	3.89 ± 0.73	0.2262
TiO_2–WO_3 (2)	–	–	12.51 ± 0.88	2.79 ± 0.39	0.1708
TiO_2	–	–	0.01 ± 0.01	0.20 ± 0.10	0.1015

The GInaFIT tool allowed quantification and comparison of the model output curves, by providing various parameters depending on the fitting model chosen. For the log-linear with shoulder model (SODIS experiment), the parameters provided were the shoulder length, S_l, and the first order rate constant, k_{max}. The shoulder length was the lag time before the log-linear bacterial inactivation began; for the simulated SODIS experiment shown herein, this is 2.9 ± 0.1 hours (Table 7.1). The first order rate constant for this experiment was 4.7 ± 0.1 $hour^{-1}$.

For the *E. coli* inactivation conducted in the presence of a TiO_2–WO_3 SPH wafer or a pure TiO_2 wafer, the Weibull with tail and Weibull models, respectively, were determined as providing the best fits to the data. In these models, different parameters were defined: a scale parameter δ and a shape parameter p. δ was denoted as the time taken to achieve the first decimal reduction in bacterial population, and p related to the curvature of the fit; for $p>1$, convex curves are obtained, and for $p<1$, concave curves are observed. For these types of curves, first-order kinetics correspond to $p=1$. The disinfection curves for the TiO_2–WO_3 and TiO_2 wafers showed different curvatures; the former fitted well with a convex curve, while the latter fitted with a concave curve. The respective p values correlated well with these observations.

A possible explanation for the different curvatures may be given in terms of the kinetics of the photogeneration of charge carriers, upon irradiation of the wafers. For the TiO_2–WO_3 wafer, upon photoexcitation, electrons would have been transported across the heterojunction into the conduction band of WO_3 (as discussed in Chapter 6), before they were able to react to form ROS species. In comparison, the electron pathway was much shorter in the TiO_2 wafer as electrons only needed to reach the surface. The additional time taken for the electron to transport in the heterojunction wafer may account for the initial slow disinfection rate. However, once electrons had transported, they would have been available to react, and this was observed as an increase in the disinfection rate. For the TiO_2 wafer, the disinfection rate began to decrease after ca. 2 minutes of photoirradiation. This may have been because over the course of the photoirradiation, the frequency of charge recombination may have increased, resulting in fewer electrons and holes available for reaction, to form ROS species.

Comparing both scenarios, it should be noted that the disinfection kinetics for the TiO_2–WO_3 SPH wafer would be beneficial to the overall disinfection rate, since efficient vectorial electron-hole separation across the heterojunction, would sustain the continuous formation of ROS species. This characteristic would be particularly attractive for treating bacterial strains that are typically more resistant to disinfection processes.

7.5. CONCLUSIONS

The findings presented in this chapter demonstrate that mechanically robust ceramic, semiconducting heterojunction wafers, prepared by a simple and low-cost method, are suitable for efficient use in solar disinfection processes. The self-supported nature of the ceramic wafers removes the need for a thin-film substrate, which simplifies their preparation and removes much of the associated cost. Once the disinfection process is completed, the wafers can be easily removed from solution.

In comparison to a pure TiO_2 wafer, the TiO_2–WO_3 SPH wafer promoted efficient and sustained electron-hole separation. Although the initial solar disinfection rate appeared slower for the SPH than for the pure TiO_2 wafer, efficient charge separation across the heterojunction may sustain the overall rate.

The work presented in this chapter supports the results presented in Chapter 6, in that it is demonstrated that there may be considerable potential for improved photocatalytic performance, by utilising heterojunction materials. The use of self-supported heterojunction wafers may be extended to other photocatalytic applications, and optimisation of their preparation may yield further improvements for their photocatalytic performance.

7.6. APPENDIX

Table 7.2 Data table of Log (CFU/mL) values relating to the data presented in the bacterial inactivation curves shown throughout Chapter 7.

	Log (CFU/mL) values			
Time (h)	***E. coli* (dark) [Figure 7.5]**	***E. coli* + photocatalyst (dark) [Figure 7.5]**	***E. coli* (photoirrad. only) [Figure 7.7]**	***E. coli* + photocatalyst [Figure 7.8]**
0	6.7	6.1	6.5	6.4
1	6.5	5.7	6.5	1.5
2	6.6	6.1	6.6	1.5
3	6.8	5.9	6.3	1.5
4	6.5	5.9	4.2	1.5
5	6.5	5.8	2.4	1.5
Time (min)	***E. coli* + photocatalyst (TiO_2–WO_3 wafer)**		***E. coli* + photocatalyst (TiO_2 wafer)**	
	[Figure 7.9]	**[Figure 7.9]**	**[Figure 7.10]**	
0	6.4	6.5	6.6	
5	6.4	6.1	3.0	
10	5.8	5.9	2.4	
15	5.2	4.7	2.2	
20	2.5	2.7	–	
25	–	–	1.5	
30	1.5	1.5	1.5	

Chapter 8. Conclusions and future work

The work presented in this thesis has investigated the synthesis of nanomaterials via a continuous hydrothermal method, and demonstrated the use of semiconductor nanomaterials and heterojunctions in photocatalytic and UV attenuating applications. The hypotheses in Chapter 1 stated that the overall aim of the thesis was to investigate the effects of nanomaterial and heterojunction properties on photocatalytic water splitting, organic degradation and water disinfection, and as polymer coatings for UV attenuation.

The synthesis of boron-doped TiO_2 was attempted via continuous hydrothermal flow synthesis (CHFS). Characterisation of the samples showed that whilst boron doping was not observed, the presence of boric acid in the reagents at increasing concentration (for each sample), affected the pH of the reaction and of the recovered products. As a result, the crystallite size and surface area of the samples varied accordingly.

- The TiO_2 powders were prepared as ceramic wafers, and were evaluated for their ability to photocatalytically evolve hydrogen, in a sacrificial system. It was shown that, where the product slurry was mildly acidic or neutral, the samples had optimum photocatalytic activity, with crystallite sizes in the range 9–12 nm and surface areas 150–200 $m^2 g^{-1}$.
- The study showed that by carefully modifying the reagents that were used for CHFS synthesis, it was possible to affect the pH, and consequently the particle properties.

The unexpected results from this work posed a number of questions, which could be explored further. In the future, it would be interesting to investigate the pH in the CHFS process for the synthesis of TiO_2 (and other materials), and the effects it has on nanoparticle properties. This may be very beneficial for photocatalytic and other applications, because nanoparticle properties are often related to their performance.

- Preparation of boron-doped TiO_2 via CHFS may be further investigated, by altering the reaction conditions within the process, e.g. the reaction temperature and/or the

residence time. Studies may be extended to investigate other dopants, benefitting from the high-throughput capabilities of the CHFS process. The band gap of such materials, to determine whether there is any narrowing, may be deduced via valence band XPS methods. For ease of testing, photocatalysts may be prepared as pressed ceramic wafers, which proved to be a simple, but effective, preparation technique.

- To gain a more detailed understanding of the activity of the TiO_2 photocatalysts, their oxygen evolution capability may also be measured. Whilst the materials investigated in this chapter were not optimised, the work demonstrated the capabilities of the CHFS process, identifying a number of new research directions.

The development of a mini-pilot scale CHFS process was evaluated via the synthesis of ZnO nanomaterials. A mass-based scale up was investigated, similar to that described in the literature, for a pilot scale process. The results showed that the CHFS process was readily scaled, and at precursor concentrations up to 0.5 M, the ZnO particles had similar size and morphology across the two scales.

- At the higher concentrations, rod-like particles were observed, although the degree of growth was larger at the pilot scale. To further evaluate scale up, it would be necessary to conduct similar investigations with other materials; however, this work readily demonstrated the benefits of CHFS as a nanomaterials synthesis technique, particularly from a scale up perspective.
- In this investigation, ZnO average particle sizes were obtained above 50 nm, and were typically observed as agglomerates. As UV attenuating materials in coatings, this was not ideal, since agglomerates can negatively affect optical properties.
- To limit agglomeration for CHFS produced nanoparticles, a modified CHFS process (which employed two confined jet mixers (CJM)) was used to prepare dispersed zinc oxide nanoparticles, in a one-step process. A number of surfactants were evaluated as surface functionalising agents, where particle morphology and dispersibility varied with different surfactants.
- It was found that under the reaction conditions investigated, citric acid was not an appropriate choice of surface functionalising agent for ZnO. The yield of ZnO was severely affected when the citric acid concentration was increased, which is believed to be related to the pH sensitivity of ZnO. The flow of surfactants (or water) in the

second CJM reduced the residence time in the first mixing point, which was sufficient to slightly reduce the average particle size of ZnO materials to 45 nm (the average size was 65 nm without the surfactant/water flow).

To further reduce the average particle size, a novel seeding approach was developed. A pre-prepared TiO_2 sol was employed to provide nucleation sites for ZnO formation. It was found that by increasing the TiO_2 sol concentration, the average particle size of zinc oxide was reduced to below 30 nm.

- Compared to samples prepared without the TiO_2 sol, the UVA absorption profile was enhanced, even though the TiO_2 sol had the effect of reducing particle size.
- When the TiO_2 sol concentration was increased, the absorption profile decreased, which was expected when ZnO particle size decreased, as reported in the literature. However, in all cases, the UV absorption was greater than zinc oxide prepared without the TiO_2 sol.
- A feasibility study was conducted at MacDermid Autotype to evaluate the zinc oxide materials in UV curable polymer coatings. Even at very low concentrations, the zinc oxide provided some UV absorption. Following this study, a larger scale evaluation has been planned for the future.
- Finally, it was found that nano-rods were produced when the TiO_2 sol was used in conjunction with a surfactant, even at low precursor concentrations. The nano-rods had shorter lengths compared to nano-rods observed for ZnO at precursor concentrations > 0.5 M (c.f. Chapter 4), which suggested that the surfactant may have preferentially capped certain facets, allowing growth to only occur in the fast-growth *c* direction of ZnO.

As explained above, there are a number of interesting findings from this study, which can be followed up in future work. For example, further work may be conducted as follows:

- Optimisation of the concentration of surfactants, to improve the dispersion properties of surface functionalised ZnO prepared in a one-step CHFS process.
- The nanoparticle seeding technique may also be extended to other material systems, especially where specific particle sizes are desired.

It was described in Chapter 1, that one method of improving photocatalytic activity was to prepare heterojunctions from two or more photocatalysts. Herein, the procedure used to prepare pressed ceramic wafers in Chapter 3, was extended to prepare bi-layer heterojunction wafers.

- As an example, TiO_2 and WO_3 powders were pressed to form a single wafer. Under photoirradiation of the TiO_2 surface, it was found that the WO_3 side rapidly turned dark blue. When the photoirradiation was repeated on the WO_3 side, only the edges of the WO_3 side turned blue (where there was some exposed TiO_2). XPS studies showed that the blue WO_3 side contained W^{5+} species, whose presence was attributed to the reduction of W^{6+}. Examining the conduction (CB) and valence (VB) band positions of TiO_2 and WO_3 showed that, upon photoirradiation, electrons migrated from the CB of TiO_2 to the CB of WO_3. Since the electrons did not have sufficient energy to reduce water (to evolve hydrogen), they began to reduce W^{6+}. The colour change was a reversible process, taking approximately one week to return to the original colour.
- Electron transfer from TiO_2 to WO_3 was shown to occur approximately normal to the illuminated TiO_2 surface, when photoirradiation was carried out in the presence of a template. Subsequently, the ceramic wafers were evaluated for their ability to photocatalytically degrade stearic acid, where the heterojunction wafers showed faster degradation rates compared to single layer TiO_2 wafers.
- Optimisation of the heterojunction wafer preparation technique may yield higher photocatalytic activities, and it would also be beneficial to fully characterise the heterojunction interface. This may aid in improving charge transfer, thereby increasing charge-carrier lifetimes.

Heterojunction wafers were evaluated for their ability to photocatalytically disinfect water, which was contaminated with *E. coli* bacteria. A single layer TiO_2 wafer was used as a comparison, similar to the photocatalytic stearic acid degradation experiments. The detection limit of *E. coli*, determined via the serial dilution technique, was reached within 30 minutes for both cases i.e. heterojunction (TiO_2–WO_3) and non-

heterojunction (TiO_2) wafers. However, the kinetics of the disinfection process, as modelled by the GInaFIT tool, appeared very different.

- With the single layer TiO_2 wafer, the disinfection process was very fast to begin, but within 2 minutes of photoirradiation, it appeared to slow down considerably. Conversely, the heterojunction wafers showed a slow initial disinfection rate, which increased after approximately 5 minutes. The results suggested that the vectorial charge separation of the heterojunction wafers was beneficial for water disinfection, which may be further investigated by conducting disinfection experiments with other infective agents.
- Applications of the heterojunction ceramic wafers in organic degradation and water disinfection have shown, that the interface that is created upon powder pressing is beneficial for enhanced photocatalytic efficiencies. The TiO_2–WO_3 couple was demonstrated as an example, but the method may be extended to other appropriate photocatalyst combinations. It may also be possible to create larger pressed ceramic heterojunctions, using industrial powder processing techniques. This may allow large-scale photocatalytic evaluation of such samples.
- Where such heterojunction systems may be used in technologies that have direct impact on human life, for example in water disinfection, it would be necessary to conduct toxicity studies, to ensure the materials are safe to use in such applications.

- The photocatalytic experiments that were discussed within this thesis were conducted under simulated solar irradiation. To understand the applications of these materials in real-world scenarios, a future aim may be to evaluate their efficiencies under real solar conditions, for example, at the Plataforma Solar de Almería in Spain.
- Photocatalytic efficiencies may also be improved by investigating visible light activation of photocatalysts, for example, via band engineering (similar to that attempted in Chapter 3 of this thesis). By narrowing the band gap of a semiconductor such at TiO_2, it may be possible to extend light absorption to the visible region, thereby increasing overall efficiency.

Overall, the work presented in this thesis has discussed a number of themes relating to nanomaterials and photocatalysis. In the future, the high-throughput capabilities of the CHFS process may prove beneficial in synthesising a large number of potential photocatalysts, which, if coupled to high-throughput photocatalytic testing, may provide significant advancements towards utilising solar energy.

References

Abe, R. (2010). Recent progress on photocatalytic and photoelectrochemical water splitting under visible light irradiation. *Journal of Photochemistry and Photobiology C: Photochemistry Reviews*, 11, (4) 179-209.

Adschiri, T. (2007). Supercritical Hydrothermal Synthesis of Organic–Inorganic Hybrid Nanoparticles. *Chemistry Letters*, 36, (10) 1188-1193.

Adschiri, T., Hakuta, Y., Kanamura, K. and Arai, K. (2001). Continuous production of $LiCoO_2$ fine crystals for lithium batteries by hydrothermal synthesis under supercritical condition. *High Pressure Research*, 20, (1-6) 373-384.

Adschiri, T., Kanazawa, K. and Arai, K. (1992a). Rapid and continuous hydrothermal crystallization of metal oxide particles in supercritical water. *Journal of the American Ceramic Society*, 75, (4) 1019-1022.

Adschiri, T., Kanazawa, K. and Arai, K. (1992b). Rapid and continuous hydrothermal synthesis of boehmite particles in subcritical and supercritical water. *Journal of the American Ceramic Society*, 75, (9) 2615-2618.

Adschiri, T., Lee, Y.-W., Goto, M. and Takami, S. (2011). Green materials synthesis with supercritical water. *Green Chemistry*, 13, (6) 1380.

Agulló-Barceló, M., Polo-López, M. I., Lucena, F., Jofre, J. and Fernández-Ibáñez, P. (2013). Solar Advanced Oxidation Processes as disinfection tertiary treatments for real wastewater: Implications for water reclamation. *Applied Catalysis B: Environmental*, 136-137, 341-350.

Aimable, A., Aymes, D., Bernard, F. and Le Cras, F. (2009). Characteristics of $LiFePO_4$ obtained through a one step continuous hydrothermal synthesis process working in supercritical water. *Solid State Ionics*, 180, (11-13) 861-866.

Akhavan, O. (2010). Thickness dependent activity of nanostructured TiO_2/ α –Fe_2O_3 photocatalyst thin films. *Applied Surface Science*, 257, (5) 1724-1728.

Akhavan, O., Abdolahad, M., Abdi, Y. and Mohajerzadeh, S. (2009). Synthesis of titania/carbon nanotube heterojunction arrays for photoinactivation of *E. coli* in visible light irradiation. *Carbon*, 47, (14) 3280-3287.

Akiya, N. and Savage, P. E. (2002). Roles of water for chemical reactions in high-temperature water. *Chemical Reviews*, 102, (8) 2725-2750.

Albert, I. and Mafart, P. (2005). A modified Weibull model for bacterial inactivation. *International Journal of Food Microbiology*, 100, (1-3) 197-211.

Alferov, Z. (2000). Double heterostructure lasers: Early days and future perspectives. *IEEE Journal of Selected Topics in Quantum Electronics*, 6, (6) 832-840.

Aloui, F., Ahajji, A., Irmouli, Y., George, B., Charrier, B. and Merlin, A. (2007). Inorganic UV absorbers for the photostabilisation of wood-clearcoating systems: Comparison with organic UV absorbers. *Applied Surface Science*, 253, (8) 3737-3745.

Alrousan, D. M., Dunlop, P. S., McMurray, T. A. and Byrne, J. A. (2009). Photocatalytic inactivation of *E. coli* in surface water using immobilised nanoparticle TiO_2 films. *Water Research*, 43, (1) 47-54.

Alrousan, D. M. A., Polo-Lopez, M. I., Dunlop, P. S. M., Fernandez-Ibanez, P. and Byrne, J. A. (2012). Solar photocatalytic disinfection of water with immobilised titanium dioxide in re-circulating flow CPC reactors. *Applied Catalysis B: Environmental*, 128, 126-134.

Amin, M. T., Nawaz, M., Amin, M. N. and Han, M. (2014). Solar disinfection of Pseudomonas aeruginosa in harvested rainwater: a step towards potability of rainwater. *PLoS One*, 9, (3) e90743.

Anastas, P. T. and Warner, J. C. (1998). Green Chemistry: Theory and Practice. New York, USA, Oxford University Press.

Anpo, M. (2003). The design and development of highly reactive titanium oxide photocatalysts operating under visible light irradiation. *Journal of Catalysis*, 216, (1-2) 505-516.

Ariosa, D., Elhordoy, F., Dalchiele, E. A., Marotti, R. E. and Stari, C. (2011). Texture vs morphology in ZnO nano-rods: On the x-ray diffraction characterization of electrochemically grown samples. *Journal of Applied Physics*, 110, (12) 124901.

Asahi, R., Morikawa, T., Ohwaki, T., Aoki, K. and Taga, Y. (2001). Visible-light photocatalysis in nitrogen-doped titanium oxides. *Science*, 293, (5528) 269-271.

Balachandran, U. and Eror, N. G. (1982). Raman Spectra of Titanium Dioxide. *Journal of Solid State Chemistry*, 42, (3) 276-282.

Balcı, S., Sezgi, N. A. and Eren, E. (2012). Boron Oxide Production Kinetics Using Boric Acid as Raw Material. *Industrial & Engineering Chemistry Research*, 51, (34) 11091-11096.

Banerjee, S., Dionysiou, D. D. and Pillai, S. C. (2015). Self-cleaning applications of TiO_2 by photo-induced hydrophilicity and photocatalysis. *Applied Catalysis B: Environmental*, 176-177, 396-428.

Banerjee, S., Pillai, S. C., Falaras, P., O'Shea, K. E., Byrne, J. A. and Dionysiou, D. D. (2014). New Insights into the Mechanism of Visible Light Photocatalysis. *Journal of Physical Chemistry Letters*, 5, (15) 2543-2554.

Barth, S., Hernandez-Ramirez, F., Holmes, J. D. and Romano-Rodriguez, A. (2010). Synthesis and applications of one-dimensional semiconductors. *Progress in Materials Science*, 55, (6) 563-627.

Baruah, S. and Dutta, J. (2009a). Effect of seeded substrates on hydrothermally grown ZnO nanorods. *Journal of Sol-Gel Science and Technology*, 50, (3) 456-464.

Baruah, S. and Dutta, J. (2009b). Hydrothermal growth of ZnO nanostructures. *Science and Technology of Advanced Materials*, 10, (1) 013001.

Bavykin, D. V., Dubovitskaya, V. P., Vorontsov, A. V. and Parmon, V. N. (2007). Effect of $TiOSO_4$ hydrothermal hydrolysis conditions on TiO_2 morphology and gas-phase oxidative activity. *Research on Chemical Intermediates*, 33, (3-5) 449-464.

Begum, N. S., Farveez Ahmed, H. and Hussain, O. (2008). Characterization and photocatalytic activity of boron-doped TiO_2 thin films prepared by liquid phase deposition technique. *Bulletin of Materials Science*, 31, (5) 741-745.

Berney, M., Weilenmann, H. U., Ihssen, J., Bassin, C. and Egli, T. (2006a). Specific Growth Rate Determines the Sensitivity of *Escherichia coli* to Thermal, UVA, and Solar Disinfection. *Applied and Environmental Microbiology*, 72, (4) 2586-2593.

Berney, M., Weilenmann, H. U., Simonetti, A. and Egli, T. (2006b). Efficacy of solar disinfection of *Escherichia coli*, *Shigella flexneri*, *Salmonella Typhimurium* and *Vibrio cholerae*. *Journal of Applied Microbiology*, 101, (4) 828-836.

Bessekhouad, Y., Robert, D. and Weber, J.-V. (2004). Bi_2S_3/TiO_2 and CdS/TiO_2 heterojunctions as an available configuration for photocatalytic degradation of organic pollutant. *Journal of Photochemistry and Photobiology A: Chemistry*, 163, (3) 569-580.

Bessekhouad, Y., Robert, D. and Weber, J. V. (2005). Photocatalytic activity of Cu_2O/TiO_2, Bi_2O_3/TiO_2 and $ZnMn_2O_4/TiO_2$ heterojunctions. *Catalysis Today*, 101, (3-4) 315-321.

Boldrin, P. (2008). Synthesis and characterisation of nanomaterial catalysts made using continuous hydrothermal flow synthesis. Ph.D., Queen Mary, University of London.

Boyle, M., Sichel, C., Fernández-Ibáñez, P., Arias-Quiroz, G. B., Iriarte-Puna, M., Mercado, A., Ubomba-Jaswa, E. and McGuigan, K. G. (2008). Bactericidal Effect of Solar Water Disinfection under Real Sunlight Conditions. *Applied and Environmental Microbiology*, 74, (10) 2997-3001.

Brunner, G. (2014a). Chapter 1 - Introduction. *Supercritical Fluid Science and Technology*. Brunner, G., Editor, Elsevier. pp. 1-7.

Brunner, G. (2014b). Chapter 2 - Properties of Pure Water. *Supercritical Fluid Science and Technology*. Brunner, G., Editor, Elsevier. pp. 9-93.

Bryan, J. D. and Gamelin, D. R. (2005). Doped Semiconductor Nanocrystals: Synthesis, Characterization, Physical Properties, and Applications. *Progress in Inorganic Chemistry*, John Wiley & Sons, Inc. pp. 47-126.

Byrappa, K. and Adschiri, T. (2007). Hydrothermal technology for nanotechnology. *Progress in Crystal Growth and Characterization of Materials*, 53, (2) 117-166.

Byrappa, K. and Yoshimura, M. (2013). Hydrothermal Technology—Principles and Applications. *Handbook of Hydrothermal Technology (Second Edition)*. Byrappa, K. and Yoshimura, M., Editors. Oxford, UK, William Andrew Publishing. pp. 1-49.

Byrne, J. A., Fernandez-Ibañez, P. A., Dunlop, P. S. M., Alrousan, D. M. A. and Hamilton, J. W. J. (2011). Photocatalytic Enhancement for Solar Disinfection of Water: A Review. *International Journal of Photoenergy*, 2011, (1) 1-12.

Callahan, M. J., Ehrentraut, D., Alexander, M. N. and Wang, B. (2011). Growth Mechanisms and Properties of Hydrothermal ZnO. *Zinc Oxide Materials for Electronic and Optoelectronic Device Applications*. Litton, C. W., Reynolds, D. C. and Collins, T. C., Editors. West Sussex, UK, John Wiley & Sons, Ltd. pp. 189-220.

Calvert, J. G. (1990). Glossary of Atmospheric Chemistry Terms. *Pure and Applied Chemistry*, 62, (11) 2167-2219.

Cao, G. and Wang, Y. (2011). Bottom-Up and Top-Down Approaches. *Nanostructures and Nanomaterials: Synthesis, Properties, and Applications*. Singapore, World Scientific Publishing Co. Pte. Ltd. pp. 8-10.

Cao, J., Xu, B., Lin, H. and Chen, S. (2013). Highly improved visible light photocatalytic activity of BiPO4 through fabricating a novel pâ€“n heterojunction BiOI/BiPO4 nanocomposite. *Chemical Engineering Journal*, 228, (C) 482-488.

Carmichael, P., Hazafy, D., Bhachu, D. S., Mills, A., Darr, J. A. and Parkin, I. P. (2013). Atmospheric pressure chemical vapour deposition of boron doped titanium dioxide for

photocatalytic water reduction and oxidation. *Physical Chemistry Chemical Physics*, 15, (39) 16788-16794.

Carp, O., Huisman, C. L. and Reller, A. (2004). Photoinduced reactivity of titanium dioxide. *Progress in Solid State Chemistry*, 32, (1) 33-177.

Casolari, A. (1988). Microbial Death. *Physiological Models in Microbiology*. Bazin, M. J. and Prosser, J. L., Editors. Boca Raton, FL, CRC Press, Inc. pp. 1-44.

Chapin, D. M., Fuller, C. S. and Pearson, G. L. (1954). A New Silicon p-n Junction Photocell for Converting Solar Radiation into Electrical Power. *Journal of Applied Physics*, 25, (5) 676.

Chatterjee, D. and Dasgupta, S. (2005). Visible light induced photocatalytic degradation of organic pollutants. *Journal of Photochemistry and Photobiology C: Photochemistry Reviews*, 6, (2-3) 186-205.

Chaudhry, A. A., Goodall, J., Vickers, M., Cockcroft, J. K., Rehman, I., Knowles, J. C. and Darr, J. A. (2008). Synthesis and characterisation of magnesium substituted calcium phosphate bioceramic nanoparticles made via continuous hydrothermal flow synthesis. *Journal of Materials Chemistry*, 18, (48) 5900.

Chaudhry, A. A., Haque, S., Kellici, S., Boldrin, P., Rehman, I., Khalid, F. A. and Darr, J. A. (2006). Instant nano-hydroxyapatite: a continuous and rapid hydrothermal synthesis. *Chemical Communications*, (21) 2286-2288.

Chaudhry, A. A., Yan, H., Viola, G., Reece, M. J., Knowles, J. C., Gong, K., Rehman, I. and Darr, J. A. (2012). Phase stability and rapid consolidation of hydroxyapatite-zirconia nano-coprecipitates made using continuous hydrothermal flow synthesis. *J Biomater Appl*, 27, (1) 79-90.

Chen, C., Cheng, J., Yu, S., Che, L. and Meng, Z. (2006). Hydrothermal synthesis of perovskite bismuth ferrite crystallites. *Journal of Crystal Growth*, 291, (1) 135-139.

Chong, M. N., Jin, B., Chow, C. W. and Saint, C. (2010). Recent developments in photocatalytic water treatment technology: a review. *Water Research*, 44, (10) 2997-3027.

Comba, P. and Merbach, A. (1987). The Titanyl Question Revisited. *Inorganic Chemistry*, 26, (8) 1315-1323.

Coronado, J. M. (2013a). A Historical Introduction to Photocatalysis. *Design of Advanced Photocatalytic Materials for Energy and Environmental Applications*. Coronado, J. M., Fresno, F., Hernández-Alonso, M. D. and Portela, R., Editors, Springer London. pp. 1-4.

Coronado, J. M. (2013b). Photons, Electrons and Holes: Fundamentals of Photocatalysis with Semiconductors. *Design of Advanced Photocatalytic Materials for Energy and Environmental Applications*. Coronado, J. M., Fresno, F., Hernàndez-Alonso, M. D. and Portela, R., Editors, Springer London. pp. 5-34.

Cote, L. J., Teja, A. S., Wilkinson, A. P. and Zhang, Z. J. (2002). Continuous hydrothermal synthesis and crystallization of magnetic oxide nanoparticles. *Journal of Materials Research*, 17, (9) 2410-2416.

Cote, L. J., Teja, A. S., Wilkinson, A. P. and Zhang, Z. J. (2003). Continuous hydrothermal synthesis of $CoFe_2O_4$ nanoparticles. *Fluid Phase Equilibria*, 210, (2) 307-317.

Cowan, A. J. and Durrant, J. R. (2013). Long-lived charge separated states in nanostructured semiconductor photoelectrodes for the production of solar fuels. *Chemical Society Reviews*, 42, (6) 2281.

Cundy, C. S. and Cox, P. A. (2003). The Hydrothermal Synthesis of Zeolites: History and Development from the Earliest Days to the Present Time. *Chemical Reviews*, 103, (3) 663-702.

Cundy, C. S. and Cox, P. A. (2005). The hydrothermal synthesis of zeolites: Precursors, intermediates and reaction mechanism. *Microporous and Mesoporous Materials*, 82, (1-2) 1-78.

Cushing, B. L., Kolesnichenko, V. L. and O'Connor, C. J. (2004). Recent Advances in the Liquid-Phase Syntheses of Inorganic Nanoparticles. *Chemical Reviews*, 104, (9) 3893-3946.

Dallinger, D. and Kappe, C. O. (2007). Microwave-Assisted Synthesis in Water as Solvent. *Chemical Reviews*, 107, (6) 2563-2591.

Darr, J. A. and Poliakoff, M. (1999). New Directions in Inorganic and Metal-Organic Coordination Chemistry in Supercritical Fluids. *Chemical Reviews*, 99, (2) 495-542.

Darr, J. A., Tighe, C. J. and Gruar, R. (2011). Co-Current Mixer, Apparatus, Reactor and Method for Precipitating Nanoparticles, World Intellectual Property Organization.

Daschner de Tercero, M., Bruns, M., Martínez, I. G., Türk, M., Fehrenbacher, U., Jennewein, S. and Barner, L. (2013a). Continuous Hydrothermal Synthesis of In Situ Functionalized Iron Oxide Nanoparticles: A General Strategy to Produce Metal Oxide Nanoparticles With Clickable Anchors. *Particle & Particle Systems Characterization*, 30, (3) 229-234.

Daschner de Tercero, M., Gonzáles Martínez, I., Herrmann, M., Bruns, M., Kübel, C., Jennewein, S., Fehrenbacher, U., Barner, L. and Türk, M. (2013b). Synthesis of in situ functionalized iron oxide nanoparticles presenting alkyne groups via a continuous process using near-critical and supercritical water. *The Journal of Supercritical Fluids*, 82, 83-95.

Dem'yanets, L. N., Li, L. E. and Uvarova, T. G. (2006). Zinc oxide: hydrothermal growth of nano- and bulk crystals and their luminescent properties. *Journal of Materials Science*, 41, (5) 1439-1444.

Demianets, L. N. and Kostomarov, D. V. (2001). Mechanism of zinc oxide single crystal growth under hydrothermal conditions. *Annales De Chimie-Science Des Materiaux*, 26, (1) 193-198.

Demianets, L. N., Kostomarov, D. V., Kuz'mina, I. P. and Pushko, S. V. (2002). Mechanism of Growth of ZnO Single Crystals from Hydrothermal Alkali Solutions. *Crystallography Reports*, 47, S86-S98.

Denis, C. J., Tighe, C. J., Gruar, R. I., Makwana, N. M. and Darr, J. A. (2015). Nucleation and Growth of Cobalt Oxide Nanoparticles in a Continuous Hydrothermal Reactor under Laminar and Turbulent Flow. *Crystal Growth & Design*, 15, (9) 4256-4265.

Devi, G. S., Kumar, K. A. S. and Reddy, K. S. (2014). Effect of pH on Synthesis of Single Phase Titania (TiO_2) Nanoparticles and its Characterization. *Particulate Science and Technology*, 33, (3) 219-223.

Djaoued, Y., Balaji, S. and Beaudoin, N. (2013). Sol–gel synthesis of mesoporous WO_3–TiO_2 composite thin films for photochromic devices. *Journal of Sol-Gel Science and Technology*, 65, (3) 374-383.

Djurišić, A. B., Leung, Y. H. and Ng, A. M. C. (2014). Strategies for improving the efficiency of semiconductor metal oxide photocatalysis. *Materials Horizons*, 1, (4) 400-410.

Do, Y. R., Lee, W., Dwight, K. and Wold, A. (1994). The Effect of WO_3 on the Photocatalytic Activity of TiO_2. *Journal of Solid State Chemistry*, 108, (1) 198-201.

Dunlop, P., Byrne, J. A., Manga, N. and Eggins, B. R. (2002). The photocatalytic removal of bacterial pollutants from drinking water. *Journal of Photochemistry and Photobiology A: Chemistry*, 148, (1) 355-363.

Dunlop, P. S. M., McMurray, T. A., Hamilton, J. W. J. and Byrne, J. A. (2008). Photocatalytic inactivation of *Clostridium perfringens* spores on TiO_2 electrodes. *Journal of Photochemistry and Photobiology A: Chemistry*, 196, (1) 113-119.

Dunnill, C. W., Aiken, Z. A., Kafizas, A., Pratten, J., Wilson, M., Morgan, D. J. and Parkin, I. P. (2009). White light induced photocatalytic activity of sulfur-doped TiO_2 thin films and their potential for antibacterial application. *Journal of Materials Chemistry*, 19, (46) 8747.

Dunnill, C. W., Aiken, Z. A., Pratten, J., Wilson, M. and Parkin, I. P. (2010). Sulfur- and Nitrogen-Doped Titania Biomaterials via APCVD. *Chemical Vapor Deposition*, 16, (1-3) 50-54.

Dunnill, C. W., Noimark, S. and Parkin, I. P. (2012). Silver loaded WO_{3-x}/TiO_2 composite multifunctional thin films. *Thin Solid Films*, 520, (17) 5516-5520.

Dunnill, C. W. and Parkin, I. P. (2011). Nitrogen-doped TiO_2 thin films: photocatalytic applications for healthcare environments. *Dalton Transactions*, 40, (8) 1635.

Elouali, S. (2012). Continuous Hydrothermal Flow Synthesis of Semiconductor Nanomaterials for Water Splitting Photochemical Diodes. Ph.D., University College London.

Elouali, S., Bloor, L. G., Binions, R., Parkin, I. P., Carmalt, C. J. and Darr, J. A. (2012). Gas sensing with nano-indium oxides (In_2O_3) prepared via continuous hydrothermal flow synthesis. *Langmuir*, 28, (3) 1879-1885.

Elouali, S., Mills, A., Parkin, I. P., Bailey, E., McMillan, P. F. and Darr, J. A. (2010). Photocatalytic evolution of hydrogen and oxygen from ceramic wafers of commercial titanias. *Journal of Photochemistry and Photobiology A: Chemistry*, 216, (2-3) 110-114.

Fan, Z. and Lu, J. G. (2005). Zinc Oxide Nanostructures: Synthesis and Properties. *Journal of Nanoscience and Nanotechnology*, 5, (10) 1561-1573.

Fang, Z., Assaaoudi, H., Guthrie, R. I. L., Kozinski, J. A. and Butler, I. S. (2007). Continuous Synthesis of Tin and Indium Oxide Nanoparticles in Sub- and Supercritical Water. *Journal of the American Ceramic Society*, 90, (8) 2367-2371.

Feng, S. H. and Xu, R. R. (2001). New Materials in Hydrothermal Synthesis. *Accounts of Chemical Research*, 34, (3) 239-247.

Fernández, P., Blanco, J., Sichel, C. and Malato, S. (2005). Water disinfection by solar photocatalysis using compound parabolic collectors. *Catalysis Today*, 101, (3-4) 345-352.

Fresno, F. (2013). Heterojunctions: Joining Different Semiconductors. *Design of Advanced Photocatalytic Materials for Energy and Environmental Applications*. Coronado, J. M., Fresno, F., Hernández-Alonso, M. D. and Portela, R., Editors, Springer London. pp. 311-327.

Fujishima, A. and Honda, K. (1972). Electrochemical Photolysis of Water at a Semiconductor Electrode. *Nature*, 238, (5358) 37-38.

Fukushima, Y. (2000). Application of Supercritical Fluids. *R&D Review of Toyota CRDL*, 35, (1) 1-9.

Galkin, A. A., Kostyuk, B. G., Lunin, V. V. and Poliakoff, M. (2000). Continuous reactions in supercritical water: A new route to La_2CuO_4 with a high surface area and enhanced oxygen mobility. *Angewandte Chemie International Edition*, 39, (15) 2738-2740.

Galkin, A. A. and Lunin, V. V. (2005). Subcritical and supercritical water: a universal medium for chemical reactions. *Russian Chemical Reviews*, 74, (1) 21-35.

Gasparotto, A., Barreca, D., Maccato, C. and Tondello, E. (2012). Manufacturing of inorganic nanomaterials: concepts and perspectives. *Nanoscale*, 4, (9) 2813-2825.

Geeraerd, A. H., Herremans, C. H. and Van Impe, J. F. (2000). Structural model requirements to describe microbial inactivation during a mild heat treatment. *International Journal of Food Microbiology*, 59, (3) 185-209.

Geeraerd, A. H., Valdramidis, V. P. and Van Impe, J. F. (2005). GInaFiT, a freeware tool to assess non-log-linear microbial survivor curves. *International Journal of Food Microbiology*, 102, (1) 95-105.

Gelover, S., Gómez, L. A., Reyes, K. and Teresa Leal, M. (2006). A practical demonstration of water disinfection using TiO_2 films and sunlight. *Water Research*, 40, (17) 3274-3280.

Goesmann, H. and Feldmann, C. (2010). Nanoparticulate functional materials. *Angewandte Chemie International Edition*, 49, (8) 1362-1395.

Goh, E. G., Xu, X. and McCormick, P. G. (2014). Effect of particle size on the UV absorbance of zinc oxide nanoparticles. *Scripta Materialia*, 78-79, 49-52.

Goodall, J. B., Illsley, D., Lines, R., Makwana, N. M. and Darr, J. A. (2015). Structure-property-composition relationships in doped zinc oxides: enhanced photocatalytic activity with rare Earth dopants. *ACS Combinatorial Science*, 17, (2) 100-112.

Goodall, J. B. M., Kellici, S., Illsley, D., Lines, R., Knowles, J. C. and Darr, J. A. (2014). Optical and photocatalytic behaviours of nanoparticles in the Ti–Zn–O binary system. *RSC Advances*, 4, (60) 31799.

Grabowska, E., Zaleska, A., Sobczak, J. W., Gazda, M. and Hupka, J. (2009). Boron-doped TiO_2: Characteristics and photoactivity under visible light. *Procedia Chemistry*, 1, (2) 1553-1559.

Gruar, R., Tighe, C. J., Reilly, L. M., Sankar, G. and Darr, J. A. (2010). Tunable and rapid crystallisation of phase pure Bi_2MoO_6 (koechlinite) and $Bi_2Mo_3O_{12}$ via continuous hydrothermal synthesis. *Solid State Sciences*, 12, (9) 1683-1686.

Gruar, R. I. (2012). Synthesis and Characterisation of Nanomaterials Produced Using Laboratory and Pilot Scale Continuous Hydrothermal Flow Reactors. Ph.D., University College London.

Gruar, R. I., Tighe, C. J. and Darr, J. A. (2013). Scaling-up a Confined Jet Reactor for the Continuous Hydrothermal Manufacture of Nanomaterials. *Industrial & Engineering Chemistry Research*, 52, (15) 5270-5281.

Gruar, R. I., Tighe, C. J., Muir, J., Kittler, J. T., Wodjak, M., Kenyon, A. J. and Darr, J. A. (2012). Continuous hydrothermal synthesis of surface-functionalised nanophosphors for biological imaging. *RSC Advances*, 2, (26) 10037-10047.

Gruar, R. I., Tighe, C. J., Southern, P., Pankhurst, Q. A. and Darr, J. A. (2015). A Direct and Continuous Supercritical Water Process for the Synthesis of Surface-Functionalized Nanoparticles. *Industrial & Engineering Chemistry Research*, 54, (30) 7436-7451.

Habisreutinger, S. N., Schmidt-Mende, L. and Stolarczyk, J. K. (2013). Photocatalytic Reduction of CO_2 on TiO_2 and Other Semiconductors. *Angewandte Chemie International Edition*, 52, (29) 7372-7408.

Hacham, H., Freeman, S. E., Gange, R. W., Maytum, D. J., Sutherland, J. C. and Sutherland, B. M. (1991). Do pyrimidine dimer yields correlate with erythema induction in human skin irradiated in situ with ultraviolet light (275-365 nm)? *Photochemistry and Photobiology*, 53, (4) 559-563.

Hakuta, Y., Adschiri, T., Suzuki, T., Chida, T., Seino, K. and Arai, K. (1998). Flow method for rapidly producing barium hexaferrite particles in supercritical water. *Journal of the American Ceramic Society*, 81, (9) 2461-2464.

Hakuta, Y., Haganuma, T., Sue, K., Adschiri, T. and Arai, K. (2003). Continuous production of phosphor YAG:Tb nanoparticles by hydrothermal synthesis in supercritical water. *Materials Research Bulletin*, 38, (7) 1257-1265.

Hakuta, Y., Seino, K., Ura, H., Adschiri, T., Takizawa, H. and Arai, K. (1999). Production of phosphor (YAG : Tb) fine particles by hydrothermal synthesis in supercritical water. *Journal of Materials Chemistry*, 9, (10) 2671-2674.

Hakuta, Y., Ura, H., Hayashi, H. and Arai, K. (2005). Continuous Production of $BaTiO_3$ Nanoparticles by Hydrothermal Synthesis. *Industrial & Engineering Chemistry Research*, 44, (4) 840-846.

Hamamoto, A., Mori, M., Takahashi, A., Nakano, M., Wakikawa, N., Akutagawa, M., Ikehara, T., Nakaya, Y. and Kinouchi, Y. (2007). New water disinfection system using UVA light-emitting diodes. *Journal of Applied Microbiology*, 103, (6) 2291-2298.

Hanwha Chemical Co., L. (2013). "Battery Materials." Retrieved 31/08/2015, from:

http://hcc.hanwha.com/eng/business/bus_battery.jsp.

Harvey, A. H. and Friend, D. G. (2004). Chapter 1 - Physical properties of water. *Aqueous Systems at Elevated Temperatures and Pressures*. Palmer, D. A., Fernández-Prini, R. and Harvey, A. H., Editors. London, UK, Elsevier Ltd. pp. 1-27.

Hashimoto, K., Irie, H. and Fujishima, A. (2005). TiO_2 Photocatalysis: A Historical Overview and Future Prospects. *Japanese Journal of Applied Physics*, 44, (12) 8269-8285.

Hayashi, H. and Hakuta, Y. (2010). Hydrothermal Synthesis of Metal Oxide Nanoparticles in Supercritical Water. *Materials*, 3, (7) 3794-3817.

Hayashi, H., Noguchi, T., Islam, N. M., Hakuta, Y., Imai, Y. and Ueno, N. (2010a). Hydrothermal synthesis of $BaTiO_3$ nanoparticles using a supercritical continuous flow reaction system. *Journal of Crystal Growth*, 312, (12-13) 1968-1972.

Hayashi, H., Noguchi, T., Islam, N. M., Hakuta, Y., Imai, Y. and Ueno, N. (2010b). Hydrothermal synthesis of organic hybrid $BaTiO_3$ nanoparticles using a supercritical continuous flow reaction system. *Journal of Crystal Growth*, 312, (24) 3613-3618.

Hayashi, H., Suino, A., Shimoyama, K., Takesue, M., Tooyama, S. and Smith, R. L. (2013). Continuous hydrothermal synthesis of $ZnGa_2O_4$:Mn^{2+} nanoparticles at temperatures of 300–500°C and pressures of 25–35MPa. *The Journal of Supercritical Fluids*, 77, 1-6.

He, T., Ma, Y., Cao, Y., Hu, X. L., Liu, H. M., Zhang, G. J., Yang, W. S. and Yao, J. N. (2002). Photochromism of WO3 colloids combined with TiO2 nanoparticles. *Journal of Physical Chemistry B*, 106, (49) 12670-12676.

He, Y. P., Wu, Z. Y., Fu, L. M., Li, C. R., Miao, Y. M., Cao, L., Fan, H. M. and Zou, B. S. (2003). Photochromism and size effect of WO3 and WO3-TiO2 aqueous sol. *Chemistry of Materials*, 15, (21) 4039-4045.

Heeger, A. J. (2013). 25th Anniversary Article: Bulk Heterojunction Solar Cells: Understanding the Mechanism of Operation. *Advanced Materials*, 26, (1) 10-28.

Henley, S. J., Fryar, J., Jayawardena, K. D. and Silva, S. R. (2010). Laser-assisted hydrothermal growth of size-controlled ZnO nanorods for sensing applications. *Nanotechnology*, 21, (36) 365502.

Hernández-Alonso, M. D. (2013). Shaping Photocatalysts: Morphological Modifications of Semiconductors. *Design of Advanced Photocatalytic Materials for Energy and Environmental Applications*. Coronado, J. M., Fresno, F., Hernández-Alonso, M. D. and Portela, R., Editors, Springer London. pp. 217-244.

Higashimoto, S., Ushiroda, Y. and Azuma, M. (2008). Electrochemically Assisted Photocatalysis of Hybrid WO_3/TiO_2 Films: Effect of the WO_3 Structures on Charge Separation Behavior. *Topics in Catalysis*, 47, (3-4) 148-154.

Hobbs, H., Briddon, S. and Lester, E. (2009). The synthesis and fluorescent properties of nanoparticulate ZrO_2 doped with Eu using continuous hydrothermal synthesis. *Green Chemistry*, 11, (4) 484.

Hoffmann, M. R., Martin, S. T., Choi, W. and Bahnemann, D. W. (1995). Environmental applications of semiconductor photocatalysis. *Chemical Reviews*, 95, (1) 69-96.

Holliday, A. K. and Massey, A. G. (1965). Inorganic Chemistry in Non-Aqueous Solvents. Oxford, UK, Pergamon Press Ltd.

Hong, H. S., Park, K. S., Lee, C. G., Kim, B. S., Kang, L. S. and Jin, Y. H. (2012a). Present Status and Future Prospect of Quantum Dot Technology. *Journal of Korean Powder Metallurgy Institute*, 19, (6) 451-457.

Hong, S.-A., Kim, S. J., Chung, K. Y., Lee, Y.-W., Kim, J. and Sang, B.-I. (2013). Continuous synthesis of lithium iron phosphate nanoparticles in supercritical water: Effect of process parameters. *Chemical Engineering Journal*, 229, 313-323.

Hong, S.-A., Kim, S. J., Kim, J., Lee, B. G., Chung, K. Y. and Lee, Y.-W. (2012b). Carbon coating on lithium iron phosphate ($LiFePO_4$): Comparison between continuous supercritical hydrothermal method and solid-state method. *Chemical Engineering Journal*, 198-199, 318-326.

Hong, S.-A., Nugroho, A., Kim, S. J., Kim, J., Chung, K. Y., Cho, B.-W. and Kang, J. W. (2011). Continuous supercritical hydrothermal synthesis: lithium secondary ion battery applications. *Research on Chemical Intermediates*, 37, (2-5) 429-440.

Hornyak, G. L., Tibbals, H. F., Dutta, J. and Moore, J. J. (2009). Fabrication Methods. *Introduction to Nanoscience & Nanotechnology*. Boca Raton, FL, CRC Press. pp. 177-236.

Hu, S., Li, F. and Fan, Z. (2011). The influence of preparation method, nitrogen source, and post-treatment on the photocatalytic activity and stability of N-doped TiO_2 nanopowder. *Journal of Hazardous Materials*, 196, 248-254.

Huang, H., Wang, S., Tian, N. and Zhang, Y. (2014). A one-step hydrothermal preparation strategy for layered $BiIO_4/Bi_2WO_6$ heterojunctions with enhanced visible light photocatalytic activities. *RSC Advances*, 4, (11) 5561.

Huang, H.-C. and Hsieh, T.-E. (2010). Preparation and characterizations of highly transparent UV-curable ZnO-acrylic nanocomposites. *Ceramics International*, 36, (4) 1245-1251.

Ibrahim, S. A. and Sreekantan, S. (2010). Effect of pH on TiO_2 nanoparticles via sol gel method. X-Ray and Related Techniques in Research & Industry, Aseania Resort Langkawi, Malaysia.

In, J.-H., Lee, H.-C., Yoon, M.-J., Lee, K.-K., Lee, J.-W. and Lee, C.-H. (2007). Synthesis of nano-sized YAG:Eu^{3+} phosphor in continuous supercritical water system. *The Journal of Supercritical Fluids*, 40, (3) 389-396.

Jang, H. D., Kim, S. K. and Kim, S. J. (2001). Effect of particle size and phase composition of titanium dioxide nanoparticles on the photocatalytic properties. *Journal of Nanoparticle Research*, 3, (2-3) 141-147.

Jang, J. S., Kim, H. G. and Lee, J. S. (2012). Heterojunction semiconductors: A strategy to develop efficient photocatalytic materials for visible light water splitting. *Catalysis Today*, 185, (1) 270-277.

Jeon, J.-W., Kim, J.-R. and Ihm, S.-K. (2010). Continuous one-step synthesis of N-doped titania under supercritical and subcritical water conditions for photocatalytic reaction under visible light. *Journal of Physics and Chemistry of Solids*, 71, (4) 608-611.

Jolivet, J.-P., Henry, M. and Livage, J. (2000). Metal Oxide Chemistry and Synthesis: From Solution to Solid State. Chichester, West Sussex, UK, John Wiley & Sons Ltd.

Juzeniene, A. and Moan, J. (2012). Beneficial effects of UV radiation other than via vitamin D production. *Dermato-Endocrinology*, 4, (2) 109-117.

Kalinichev, A. G. and Churakov, S. V. (1999). Size and topology of molecular clusters in supercritical water: a molecular dynamics simulation. *Chemical Physics Letters*, 302, (5–6) 411-417.

Kawai-Nakamura, A., Sato, T., Sue, K., Tanaka, S., Saitoh, K., Aida, K. and Hiaki, T. (2008). Rapid and continuous hydrothermal synthesis of metal and metal oxide

nanoparticles with a microtube-reactor at 523 K and 30 MPa. *Materials Letters*, 62, (19) 3471-3473.

Kawasaki, S., Sue, K., Ookawara, R., Wakashima, Y. and Suzuki, A. (2010a). Development of novel micro swirl mixer for producing fine metal oxide nanoparticles by continuous supercritical hydrothermal method. *Journal of Oleo Science*, 59, (10) 557-562.

Kawasaki, S.-I., Sue, K., Ookawara, R., Wakashima, Y., Suzuki, A., Hakuta, Y. and Arai, K. (2010b). Engineering study of continuous supercritical hydrothermal method using a T-shaped mixer: Experimental synthesis of NiO nanoparticles and CFD simulation. *The Journal of Supercritical Fluids*, 54, (1) 96-102.

Kawasaki, S.-i., Xiuyi, Y., Sue, K., Hakuta, Y., Suzuki, A. and Arai, K. (2009). Continuous supercritical hydrothermal synthesis of controlled size and highly crystalline anatase TiO_2 nanoparticles. *The Journal of Supercritical Fluids*, 50, (3) 276-282.

Keane, D. A., McGuigan, K. G., Ibáñez, P. F., Polo-López, M. I., Byrne, J. A., Dunlop, P. S. M., O'Shea, K., Dionysiou, D. D. and Pillai, S. C. (2014). Solar photocatalysis for water disinfection: materials and reactor design. *Catalysis Science & Technology*, 4, (5) 1211-1226.

Kellici, S., Gong, K., Lin, T., Brown, S., Clark, R. J. H., Vickers, M., Cockcroft, J. K., Middelkoop, V., Barnes, P., Perkins, J. M., Tighe, C. J. and Darr, J. A. (2010). High-throughput continuous hydrothermal flow synthesis of Zn-Ce oxides: unprecedented solubility of Zn in the nanoparticle fluorite lattice. *Philosophical Transactions of the Royal Society A*, 368, (1927) 4331-4349.

Kelly, C. and Howdle, S. (2008). "Supercritical processing." Retrieved 05/09/2015, 2015, from:

http://www.rsc.org/education/eic/issues/2008November/SupercriticalProcessing.asp.

Kerton, F. (2009a). Supercritical Fluids. *Alternative Solvents for Green Chemistry*, The Royal Society of Chemistry. pp. 68-96.

Kerton, F. (2009b). Water. *Alternative Solvents for Green Chemistry*, The Royal Society of Chemistry. pp. 44-67.

Kim, J., Lee, C. W. and Choi, W. (2010). Platinized WO_3 as an Environmental Photocatalyst that Generates OH Radicals under Visible Light. *Environmental Science and Technology*, 44, (17) 6849-6854.

Kim, J.-R., Lee, K.-Y., Suh, M.-J. and Ihm, S.-K. (2012). Ceria–zirconia mixed oxide prepared by continuous hydrothermal synthesis in supercritical water as catalyst support. *Catalysis Today*, 185, (1) 25-34.

Kim, J.-R., Myeong, W.-J. and Ihm, S.-K. (2007). Characteristics in oxygen storage capacity of ceria–zirconia mixed oxides prepared by continuous hydrothermal synthesis in supercritical water. *Applied Catalysis B: Environmental*, 71, (1-2) 57-63.

Kim, J.-R., Myeong, W.-J. and Ihm, S.-K. (2009a). Characteristics of CeO_2–ZrO_2 mixed oxide prepared by continuous hydrothermal synthesis in supercritical water as support of Rh catalyst for catalytic reduction of NO by CO. *Journal of Catalysis*, 263, (1) 123-133.

Kim, K. H., Kim, J. R. and Ihm, S. K. (2009b). Wet oxidation of phenol over transition metal oxide catalysts supported on $Ce_{0.65}Zr_{0.35}O_2$ prepared by continuous hydrothermal synthesis in supercritical water. *J Hazard Mater*, 167, (1-3) 1158-1162.

Koch, C. C. (2003). Top-down Synthesis of Nanostructured Materials: Mechanical and Thermal Processing Methods. *Reviews on Advanced Materials Science*, 5, (2) 91-99.

Kočí, K., Obalová, L., Matějová, L., Plachá, D., Lacný, Z., Jirkovský, J. and Šolcová, O. (2009). Effect of TiO_2 particle size on the photocatalytic reduction of CO_2. *Applied Catalysis B: Environmental*, 89, (3-4) 494-502.

Kockler, J., Oelgemöller, M., Robertson, S. and Glass, B. D. (2012). Photostability of sunscreens. *Journal of Photochemistry and Photobiology C: Photochemistry Reviews*, 13, (1) 91-110.

Kołodziejczak-Radzimska, A. and Jesionowski, T. (2014). Zinc Oxide—From Synthesis to Application: A Review. *Materials*, 7, (4) 2833-2881.

Kruse, A. and Dinjus, E. (2007). Hot compressed water as reaction medium and reactant. *The Journal of Supercritical Fluids*, 39, (3) 362-380.

Kubacka, A., Fernández-García, M. and Colón, G. (2012). Advanced Nanoarchitectures for Solar Photocatalytic Applications. *Chemical Reviews*, 112, (3) 1555-1614.

Kudo, A. and Miseki, Y. (2009). Heterogeneous photocatalyst materials for water splitting. *Chemical Society Reviews*, 38, (1) 253-278.

Kumar, J. K. and Pandit, A. B. (2012). Drinking Water Disinfection Techniques. Boca Raton, CRC Press.

Kumar, S. (2012). Textbook of Microbiology. India, Jaypee Brothers Medical Publishers.

LaMer, V. K. and Dinegar, R. H. (1950). Theory, Production and Mechanism of Formation of Monodispersed Hydrosols. *Journal of the American Chemical Society*, 72, (11) 4847-4854.

Larsen, D. (2015). "Phase Diagrams." ChemWiki: The Dynamic Chemistry Textbook Retrieved 12 August, 2015, from:

http://chemwiki.ucdavis.edu/Wikitexts/UC_Davis/UCD_Chem_2B/UCD_Chem_2B%3A_Larsen/Unit_II%3A_States_of_Matter/Intermolecular_Interactions/11.7%3A_Phase_Diagrams.

Laudise, R. A. and Ballman, A. A. (1960). Hydrothermal Synthesis of Zinc Oxide and Zinc Sulfide. *Journal of Physical Chemistry*, 64, (5) 688-691.

Laumann, A., Bremholm, M., Hald, P., Holzapfel, M., Thomas Fehr, K. and Iversen, B. B. (2012). Rapid Green Continuous Flow Supercritical Synthesis of High Performance $Li_4Ti_5O_{12}$ Nanocrystals for Li Ion Battery Applications. *Journal of The Electrochemical Society*, 159, (2) A166.

Lee, J. S. and Jang, J. (2014). Hetero-structured semiconductor nanomaterials for photocatalytic applications. *Journal of Industrial and Engineering Chemistry*, 20, (2) 363-371.

Lester, E., Blood, P., Denyer, J., Giddings, D., Azzopardi, B. and Poliakoff, M. (2006). Reaction engineering: The supercritical water hydrothermal synthesis of nano-particles. *The Journal of Supercritical Fluids*, 37, (2) 209-214.

Lester, E., Tang, S. V. Y., Khlobystov, A., Rose, V. L., Buttery, L. and Roberts, C. J. (2013). Producing nanotubes of biocompatible hydroxyapatite by continuous hydrothermal synthesis. *CrystEngComm*, 15, (17) 3256.

Lewis, N. S. (2007). Toward cost-effective solar energy use. *Science*, 315, (5813) 798-801.

Li, W. J., Shi, E. W., Zhong, W. Z. and Yin, Z. W. (1999). Growth mechanism and growth habit of oxide crystals. *Journal of Crystal Growth*, 203, (1-2) 186-196.

Li, X., Qiu, Y., Wang, S., Lu, S., Gruar, R. I., Zhang, X., Darr, J. A. and He, T. (2013). Electrophoretically deposited TiO_2 compact layers using aqueous suspension for dye-sensitized solar cells. *Physical Chemistry Chemical Physics*, 15, (35) 14729-14735.

Li, Y. F. and Liu, Z. P. (2011). Particle Size, Shape and Activity for Photocatalysis on Titania Anatase Nanoparticles in Aqueous Surroundings. *Journal of the American Chemical Society*, 133, (39) 15743-15752.

Liang, H., Meng, F., Caban-Acevedo, M., Li, L., Forticaux, A., Xiu, L., Wang, Z. and Jin, S. (2015). Hydrothermal continuous flow synthesis and exfoliation of NiCo layered

double hydroxide nanosheets for enhanced oxygen evolution catalysis. *Nano Letters*, 15, (2) 1421-1427.

Liang, M.-K., Limo, M. J., Sola-Rabada, A., Roe, M. J. and Perry, C. C. (2014). New Insights into the Mechanism of ZnO Formation from Aqueous Solutions of Zinc Acetate and Zinc Nitrate. *Chemistry of Materials*, 26, (14) 4119-4129.

Lin, H., Huang, C., Li, W., Ni, C., Shah, S. and Tseng, Y. (2006). Size dependency of nanocrystalline TiO_2 on its optical property and photocatalytic reactivity exemplified by 2-chlorophenol. *Applied Catalysis B: Environmental*, 68, (1-2) 1-11.

Lin, T., Kellici, S., Gong, K., Thompson, K., Evans, J. R. G., Wang, X. and Darr, J. A. (2010). Rapid Automated Materials Synthesis Instrument: Exploring the Composition and Heat-Treatment of Nanoprecursors Toward Low Temperature Red Phosphors. *Journal of Combinatorial Chemistry*, 12, (3) 383-392.

Liu, G., Wang, L., Yang, H. G., Cheng, H.-M. and Max Lu, G. Q. (2010). Titania-based photocatalysts—crystal growth, doping and heterostructuring. *Journal of Materials Chemistry*, 20, (5) 831.

Liu, Y., Xie, C., Li, J., Zou, T. and Zeng, D. (2012). New insights into the relationship between photocatalytic activity and photocurrent of TiO_2/WO_3 nanocomposite. *Applied Catalysis A*, 433, 81-87.

Livraghi, S., Chierotti, M. R., Giamello, E., Magnacca, G., Paganini, M. C., Cappelletti, G. and Bianchi, C. L. (2008). Nitrogen-Doped Titanium Dioxide Active in Photocatalytic Reactions with Visible Light: A Multi-Technique Characterization of Differently Prepared Materials. *The Journal of Physical Chemistry C*, 112, (44) 17244-17252.

Lonnen, J., Kilvington, S., Kehoe, S. C., Al-Touati, F. and McGuigan, K. G. (2005). Solar and photocatalytic disinfection of protozoan, fungal and bacterial microbes in drinking water. *Water Research*, 39, (5) 877-883.

Lu, J., Minami, K., Takami, S. and Adschiri, T. (2013). Rapid and continuous synthesis of cobalt aluminate nanoparticles under subcritical hydrothermal conditions with in-situ surface modification. *Chemical Engineering Science*, 85, 50-54.

Lu, J., Minami, K., Takami, S., Shibata, M., Kaneko, Y. and Adschiri, T. (2012). Supercritical hydrothermal synthesis and in situ organic modification of indium tin oxide nanoparticles using continuous-flow reaction system. *ACS Applied Materials & Interfaces*, 4, (1) 351-354.

Lu, N., Zhao, H., Li, J., Quan, X. and Chen, S. (2008). Characterization of boron-doped TiO_2 nanotube arrays prepared by electrochemical method and its visible light activity. *Separation and Purification Technology*, 62, (3) 668-673.

Lu, X., Tian, B., Chen, F. and Zhang, J. (2010). Preparation of boron-doped TiO_2 films by autoclaved-sol method at low temperature and study on their photocatalytic activity. *Thin Solid Films*, 519, (1) 111-116.

Lübke, M., Johnson, I., Makwana, N. M., Brett, D., Shearing, P., Liu, Z. and Darr, J. A. (2015a). High power TiO_2 and high capacity Sn-doped TiO_2 nanomaterial anodes for lithium-ion batteries. *Journal of Power Sources*, 294, 94-102.

Lübke, M., Makwana, N. M., Gruar, R., Tighe, C., Brett, D., Shearing, P., Liu, Z. and Darr, J. A. (2015b). High capacity nanocomposite Fe_3O_4/Fe anodes for Li-ion batteries. *Journal of Power Sources*, 291, 102-107.

Maeda, K. (2011). Photocatalytic water splitting using semiconductor particles: History and recent developments. *Journal of Photochemistry and Photobiology C: Photochemistry Reviews*, 12, (4) 237-268.

Maeda, K. (2013). Z-Scheme Water Splitting Using Two Different Semiconductor Photocatalysts. *ACS Catalysis*, 3, (7) 1486-1503.

Mahltig, B., Böttcher, H., Rauch, K., Dieckmann, U., Nitsche, R. and Fritz, T. (2005). Optimized UV protecting coatings by combination of organic and inorganic UV absorbers. *Thin Solid Films*, 485, (1-2) 108-114.

Mahshid, S., Askari, M. and Ghamsari, M. S. (2007). Synthesis of TiO_2 nanoparticles by hydrolysis and peptization of titanium isopropoxide solution. *Journal of Materials Processing Technology*, 189, (1-3) 296-300.

Malato, S., Fernández-Ibáñez, P., Maldonado, M. I., Blanco, J. and Gernjak, W. (2009). Decontamination and disinfection of water by solar photocatalysis: Recent overview and trends. *Catalysis Today*, 147, (1) 1-59.

Malinger, K. A., Maguer, A., Thorel, A., Gaunand, A. and Hochepied, J.-F. (2011). Crystallization of anatase nanoparticles from amorphous precipitate by a continuous hydrothermal process. *Chemical Engineering Journal*, 174, (1) 445-451.

Mani, G. K. and Rayappan, J. B. B. (2014). Impact of annealing duration on spray pyrolysis deposited nanostructured zinc oxide thin films. *Superlattices and Microstructures*, 67, 82-87.

Mao, Y., Banerjee, S. and Wong, S. S. (2003). Hydrothermal synthesis of perovskite nanotubes. *Chemical Communications*, (3) 408-409.

Marschall, R. (2014). Semiconductor Composites: Strategies for Enhancing Charge Carrier Separation to Improve Photocatalytic Activity. *Advanced Functional Materials*, 24, (17) 2421-2440.

Marugán, J., van Grieken, R., Sordo, C. and Cruz, C. (2008). Kinetics of the photocatalytic disinfection of *Escherichia coli* suspensions. *Applied Catalysis B: Environmental*, 82, (1-2) 27-36.

Masuda, Y. and Kato, K. (2008). Morphology control of zinc oxide particles at low temperature. *Crystal Growth & Design*, 8, (8) 2633-2637.

Masuda, Y., Kinoshita, N. and Koumoto, K. (2007). Morphology control of ZnO crystalline particles in aqueous solution. *Electrochimica Acta*, 53, (1) 171-174.

Matsui, K., Noguchi, T., Islam, N. M., Hakuta, Y. and Hayashi, H. (2008). Rapid synthesis of $BaTiO_3$ nanoparticles in supercritical water by continuous hydrothermal flow reaction system. *Journal of Crystal Growth*, 310, (10) 2584-2589.

Matsunaga, T., Tomoda, R., Nakajima, T. and Wake, H. (1985). Photoelectrochemical sterilization of microbial cells by semiconductor powders. *Fems Microbiology Letters*, 29, (1-2) 211-214.

McGuigan, K. G., Conroy, R. M., Mosler, H.-J., du Preez, M., Ubomba-Jaswa, E. and Fernandez-Ibañez, P. (2012). Solar water disinfection (SODIS): A review from bench-top to roof-top. *Journal of Hazardous Materials*, 235-236, 29-46.

McLaren, A., Valdes-Solis, T., Li, G. and Tsang, S. C. (2009). Shape and size effects of ZnO nanocrystals on photocatalytic activity. *Journal of the American Chemical Society*, 131, (35) 12540-12541.

Meissner, D., Memming, R., Kastening, B. and Bahnemann, D. (1986). Fundamental problems of water splitting at cadmium sulfide. *Chemical Physics Letters*, 127, (5) 419-423.

Mi, J.-L., Johnsen, S., Clausen, C., Hald, P., Lock, N., Sø, L. and Iversen, B. B. (2012). Highly controlled crystallite size and crystallinity of pure and iron-doped anatase-TiO_2 nanocrystals by continuous flow supercritical synthesis. *Journal of Materials Research*, 28, (03) 333-339.

Middelkoop, V., Boldrin, P., Peel, M., Buslaps, T., Barnes, P., Darr, J. A. and Jacques, S. D. M. (2009). Imaging the inside of a Continuous Nanoceramic Synthesizer under Supercritical Water Conditions Using High-Energy Synchrotron X-Radiation. *Chemistry of Materials*, 21, (12) 2430-2435.

Mills, A., Davies, R. H. and Worsley, D. (1993). Water purification by semiconductor photocatalysis. *Chemical Society Reviews*, 22, (6) 417.

Mills, A. and Le Hunte, S. (1997). An overview of semiconductor photocatalysis. *Journal of Photochemistry and Photobiology A: Chemistry*, 108, 1-35.

Mills, A., Lepre, A., Elliott, N., Bhopal, S., Parkin, I. P. and O'Neill, S. A. (2003). Characterisation of the photocatalyst Pilkington Activ™: a reference film photocatalyst? *Journal of Photochemistry and Photobiology A: Chemistry*, 160, (3) 213-224.

Mills, A. and Wang, J. (2006). Simultaneous monitoring of the destruction of stearic acid and generation of carbon dioxide by self-cleaning semiconductor photocatalytic films. *Journal of Photochemistry and Photobiology A: Chemistry*, 182, (2) 181-186.

Moan, J. (2001). Visible Light and UV Radiation. *Radiation at Home, Outdoors and in the Workplace*. Brune, D., Hellborg, R., Persson, B. and Pääkkönen, R., Editors. Oslo, Scandanavian Science Publisher. pp. 69-85.

Moniz, S. J. A., Shevlin, S. A., Martin, D. J., Guo, Z.-X. and Tang, J. (2015). Visible-light driven heterojunction photocatalysts for water splitting – a critical review. *Energy & Environmental Science*, 8, (3) 731-759.

Morimoto, T., Tomonaga, H. and Mitani, A. (1999). Ultraviolet ray absorbing coatings on glass for automobiles. *Thin Solid Films*, 351, 61-65.

Naik, A. J. T., Gruar, R., Tighe, C. J., Parkin, I. P., Darr, J. A. and Binions, R. (2015). Environmental sensing semiconducting nanoceramics made using a continuous hydrothermal synthesis pilot plant. *Sensors and Actuators B: Chemical*, 217, 136-145.

Namratha, K. and Byrappa, K. (2012). Novel solution routes of synthesis of metal oxide and hybrid metal oxide nanocrystals. *Progress in Crystal Growth and Characterization of Materials*, 58, (1) 14-42.

Ni, M., Leung, M. K. H., Leung, D. Y. C. and Sumathy, K. (2007). A review and recent developments in photocatalytic water-splitting using TiO_2 for hydrogen production. *Renewable and Sustainable Energy Reviews*, 11, (3) 401-425.

Nicholas, N. J., Franks, G. V. and Ducker, W. A. (2012). The mechanism for hydrothermal growth of zinc oxide. *CrystEngComm*, 14, (4) 1232-1240.

Niederberger, M. and Pinna, N. (2009). Metal Oxide Nanoparticles in Organic Solvents: Synthesis, Formation, Assembly and Application. London, UK, Springer.

Nottingham, U. o. (2013). "shyman: Sustainable Hydrothermal Manufacturing of Nanomaterials." Retrieved 31/08/2015, from:

http://www.shyman.eu.

Nozik, A. J. (1977). Photochemical diodes. *Applied Physics Letters*, 30, (11) 567.

Nugroho, A., Yoon, D., Joo, O.-S., Chung, K. Y. and Kim, J. (2014). Continuous synthesis of $Li_4Ti_5O_{12}$ nanoparticles in supercritical fluids and their electrochemical performance for anode in Li-ion batteries. *Chemical Engineering Journal*, 258, 357-366.

Ohtani, B. (2010). Photocatalysis A to Z - What we know and what we do not know in a scientific sense. *Journal of Photochemistry and Photobiology C: Photochemistry Reviews*, 11, (4) 157-178.

Oskam, G. (2006). Metal oxide nanoparticles: synthesis, characterization and application. *Journal of Sol-Gel Science and Technology*, 37, (3) 161-164.

Osterloh, F. E. (2008). Inorganic Materials as Catalysts for Photochemical Splitting of Water. *Chemistry of Materials*, 20, (1) 35-54.

Pablos, C., van Grieken, R., Marugán, J., Chowdhury, I. and Walker, S. L. (2013). Study of bacterial adhesion onto immobilized TiO_2: Effect on the photocatalytic activity for disinfection applications. *Catalysis Today*, 209, 140-146.

Pandey, R. and Holmes, R. J. (2010). Graded Donor-Acceptor Heterojunctions for Efficient Organic Photovoltaic Cells. *Advanced Materials*, 22, (46) 5301-5305.

Parker, J. E., Thompson, S. P., Cobb, T. M., Yuan, F., Potter, J., Lennie, A. R., Alexander, S., Tighe, C. J., Darr, J. A., Cockcroft, J. C. and Tang, C. C. (2010). High-throughput powder diffraction on beamline I11 at Diamond. *Journal of Applied Crystallography*, 44, (1) 102-110.

Patel, D., Kellici, S. and Saha, B. (2014). Green Process Engineering as the Key to Future Processes. *Processes*, 2, (1) 311-332.

Patera, E. S. and Holloway, J. R. (1978). A non-end-loaded piston-cylinder device for use up to 40 kbar. *Eos, Transactions, American Geophysical Union*, 59, (12) 1217-1218.

Piegari, A. and Polato, P. (2003). Wideband optical coatings for protecting artwork from ultraviolet and infrared radiation damage. *Journal of Optics a-Pure and Applied Optics*, 5, (5) S152-S156.

Prasad Yadav, T., Manohar Yadav, R. and Pratap Singh, D. (2012). Mechanical Milling: a Top Down Approach for the Synthesis of Nanomaterials and Nanocomposites. *Nanoscience and Nanotechnology*, 2, (3) 22-48.

Quesada Cabrera, R., Latimer, E. R., Kafizas, A., Blackman, C. S., Carmalt, C. J. and Parkin, I. P. (2012). Photocatalytic activity of needle-like TiO_2/WO_{3-x} thin films prepared by chemical vapour deposition. *Journal of Photochemistry and Photobiology A: Chemistry*, 239, 60-64.

Quesada-Cabrera, R., Weng, X., Hyet, G., Clark, R. J. H., Wang, X. Z. and Darr, J. A. (2013). High-Throughput Continuous Hydrothermal Synthesis of Nanomaterials (Part II): Unveiling the As-Prepared $Ce_xZr_yY_zO_{2-\delta}$ Phase Diagram. *ACS Combinatorial Science*, 15, (9) 458-463.

Ratkowsky, D. A. (2003). Model fitting and uncertainty. *Modeling Microbial Responses in Foods*. McKellar, R. and Lu, X., Editors. Boca Raton, CRC Press. pp. 151-196.

Rawal, S. B., Bera, S., Lee, D., Jang, D.-J. and Lee, W. I. (2013). Design of visible-light photocatalysts by coupling of narrow bandgap semiconductors and TiO_2: effect of their relative energy band positions on the photocatalytic efficiency. *Catalysis Science & Technology*, 3, (7) 1822.

Roduner, E. (2006). Size matters: why nanomaterials are different. *Chemical Society Reviews*, 35, (7) 583-592.

Rohde, R. A. (2007). Solar Spectrum, Global Warming Art.

Sahoo, Y., Goodarzi, A., Swihart, M. T., Ohulchanskyy, T. Y., Kaur, N., Furlani, E. P. and Prasad, P. N. (2005). Aqueous ferrofluid of magnetite nanoparticles: Fluorescence labeling and magnetophoretic control. *Journal of Physical Chemistry B*, 109, (9) 3879-3885.

Sasaki, T., Ohara, S., Naka, T., Vejpravova, J., Sechovsky, V., Umetsu, M., Takami, S., Jeyadevan, B. and Adschiri, T. (2010). Continuous synthesis of fine $MgFe_2O_4$ nanoparticles by supercritical hydrothermal reaction. *The Journal of Supercritical Fluids*, 53, (1-3) 92-94.

Scanlon, D. O., Dunnill, C. W., Buckeridge, J., Shevlin, S. A., Logsdail, A. J., Woodley, S. M., Catlow, C. R. A., Powell, M. J., Palgrave, R. G., Parkin, I. P., Watson, G. W., Keal, T. W., Sherwood, P., Walsh, A. and Sokol, A. A. (2013). Band alignment of rutile and anatase TiO_2. *Nature Materials*, 12, (9) 798-801.

Scholes, G. D., Fleming, G. R., Olaya-Castro, A. and van Grondelle, R. (2011). Lessons from nature about solar light harvesting. *Nature Chemistry*, 3, (10) 763-774.

Sebastian, V., Arruebo, M. and Santamaria, J. (2014). Reaction engineering strategies for the production of inorganic nanomaterials. *Small*, 10, (5) 835-853.

Serpone, N., Borgarello, E. and Grätzel, M. (1984). Visible Light Induced Generation of Hydrogen from H_2S in Mixed Semiconductor Dispersions; Improved Efficiency through Inter-particle Electron Transfer. *Journal of the Chemical Society, Chemical Communications*, (6) 342-344.

Serpone, N., Dondi, D. and Albini, A. (2007). Inorganic and organic UV filters: Their role and efficacy in sunscreens and suncare products. *Inorganica Chimica Acta*, 360, (3) 794-802.

Shi, L., Naik, A. J., Goodall, J. B., Tighe, C., Gruar, R., Binions, R., Parkin, I. and Darr, J. (2013). Highly sensitive ZnO nanorod- and nanoprism-based NO_2 gas sensors: size and shape control using a continuous hydrothermal pilot plant. *Langmuir*, 29, (33) 10603-10609.

Shibuki, K., Takesue, M., Aida, T. M., Watanabe, M., Hayashi, H. and Smith, R. L. (2010). Continuous synthesis of Zn_2SiO_4:Mn^{2+} fine particles in supercritical water at temperatures of 400–500°C and pressures of 30–35MPa. *The Journal of Supercritical Fluids*, 54, (2) 266-271.

Shin, Y. H., Koo, S.-M., Kim, D. S., Lee, Y.-H., Veriansyah, B., Kim, J. and Lee, Y.-W. (2009). Continuous hydrothermal synthesis of HT-$LiCoO_2$ in supercritical water. *The Journal of Supercritical Fluids*, 50, (3) 250-256.

Sichel, C., Blanco, J., Malato, S. and Fernández-Ibáñez, P. (2007a). Effects of experimental conditions on *E. coli* survival during solar photocatalytic water disinfection. *Journal of Photochemistry and Photobiology A: Chemistry*, 189, (2-3) 239-246.

Sichel, C., Tello, J., de Cara, M. and Fernández-Ibáñez, P. (2007b). Effect of UV solar intensity and dose on the photocatalytic disinfection of bacteria and fungi. *Catalysis Today*, 129, (1-2) 152-160.

Smijs, T. G. and Pavel, S. (2011). Titanium dioxide and zinc oxide nanoparticles in sunscreens: focus on their safety and effectiveness. *Nanotechnology, Science and Applications*, 4, 95-112.

Sue, K., Kawasaki, S.-i., Suzuki, M., Hakuta, Y., Hayashi, H., Arai, K., Takebayashi, Y., Yoda, S. and Furuya, T. (2011). Continuous hydrothermal synthesis of Fe_2O_3, NiO, and CuO nanoparticles by superrapid heating using a T-type micro mixer at 673K and 30MPa. *Chemical Engineering Journal*, 166, (3) 947-953.

Sue, K., Sato, T., Kawasaki, S.-i., Takebayashi, Y., Yoda, S., Furuya, T. and Hiaki, T. (2010). Continuous Hydrothermal Synthesis of Fe_2O_3 Nanoparticles Using a Central Collision-Type Micromixer for Rapid and Homogeneous Nucleation at 673 K and 30 MPa. *Industrial & Engineering Chemistry Research*, 49, (18) 8841-8846.

Thanh, N. T., Maclean, N. and Mahiddine, S. (2014). Mechanisms of nucleation and growth of nanoparticles in solution. *Chemical Reviews*, 114, (15) 7610-7630.

Thanh, N. T. K. and Green, L. A. W. (2010). Functionalisation of nanoparticles for biomedical applications. *Nano Today*, 5, (3) 213-230.

Thompson, K., Goodall, J., Kellici, S., Mattinson, J. A., Egerton, T. A., Rehman, I. and Darr, J. A. (2009). Screening tests for the evaluation of nanoparticle titania photocatalysts. *Journal of Chemical Technology and Biotechnology*, 84, (11) 1717-1725.

Tighe, C. J., Cabrera, R. Q., Gruar, R. I. and Darr, J. A. (2013). Scale Up Production of Nanoparticles: Continuous Supercritical Water Synthesis of Ce–Zn Oxides. *Industrial & Engineering Chemistry Research*, 52, (16) 5522-5528.

Tighe, C. J., Gruar, R. I., Ma, C. Y., Mahmud, T., Wang, X. Z. and Darr, J. A. (2012). Investigation of counter-current mixing in a continuous hydrothermal flow reactor. *The Journal of Supercritical Fluids*, 62, 165-172.

Tompsett, G. A., Bowmaker, G. A., Cooney, R. P., Metson, J. B., Rodgers, K. A. and Seakins, J. M. (1995). The Raman Spectrum of Brookite, TiO_2 (*Pbca*, $Z = 8$). *Journal of Raman Spectroscopy*, 26, 57-62.

Tsuzuki, T. (2009). Commercial scale production of inorganic nanoparticles. *International Journal of Nanotechnology*, 6, (5/6) 567.

Ubomba-Jaswa, E., Boyle, M. A. R. and McGuigan, K. G. (2008). Inactivation of enteropathogenic *E. coli* by solar disinfection (SODIS) under simulated sunlight conditions. *Journal of Physics: Conference Series*, 101, 012003.

Ubomba-Jaswa, E., Navntoft, C., Polo-Lopez, M. I., Fernandez-Ibanez, P. and McGuigan, K. G. (2009). Solar disinfection of drinking water (SODIS): an investigation of the effect of UV-A dose on inactivation efficiency. *Photochemical & Photobiological Sciences*, 8, (5) 587-595.

Umebayashi, T., Yamaki, T., Itoh, H. and Asai, K. (2002). Band gap narrowing of titanium dioxide by sulfur doping. *Applied Physics Letters*, 81, (3) 454.

United-Nations (2012). Millennium Development Goals Report 2012. New York.

Venkatasubbu, G. D., Ramakrishnan, V., Sasirekha, V., Ramasamy, S. and Kumar, J. (2012). Influence of particle size on the phonon confinement of TiO_2 nanoparticles. *Journal of Experimental Nanoscience*, 9, (7) 661-668.

Wallen, S. L., Palmer, B. J. and Fulton, J. L. (1998). The ion pairing and hydration structure of Ni^{2+} in supercritical water at 425 °C determined by x-ray absorption fine structure and molecular dynamics studies. *The Journal of Chemical Physics*, 108, (10) 4039.

Wang, F., Chen, X., Hu, X., Wong, K. S. and Yu, J. C. (2012). WO_3/TiO_2 microstructures for enhanced photocatalytic oxidation. *Separation and Purification Technology*, 91, (C) 67-72.

Wang, H., Zhang, L., Chen, Z., Hu, J., Li, S., Wang, Z., Liu, J. and Wang, X. (2014). Semiconductor heterojunction photocatalysts: design, construction, and photocatalytic performances. *Chemical Society Reviews*, 43, (15) 5234-5244.

Wang, Y., Wang, Q., Zhan, X., Wang, F., Safdar, M. and He, J. (2013). Visible light driven type II heterostructures and their enhanced photocatalysis properties: a review. *Nanoscale*, 5, (18) 8326.

Wang, Y., Xu, G., Ren, Z., Wei, X., Weng, W., Du, P., Shen, G. and Han, G. (2007). Mineralizer-Assisted Hydrothermal Synthesis and Characterization of $BiFeO_3$ Nanoparticles. *Journal of the American Ceramic Society*, 90, (8) 2615-2617.

Wang, Z. L. (2004). Zinc oxide nanostructures: growth, properties and applications. *Journal of Physics: Condensed Matter*, 16, (25) R829-R858.

Wei, W., Keh, C. C. K., Li, C.-J. and Varma, R. S. (2004). Water as a reaction medium for clean chemical processes. *Clean Technologies and Environmental Policy*, 6, (4) 250-257.

Weingartner, H. and Franck, E. U. (2005). Supercritical water as a solvent. *Angewandte Chemie International Edition*, 44, (18) 2672-2692.

Weng, X., Cockcroft, J. K., Hyett, G., Vickers, M., Boldrin, P., Tang, C. C., Thompson, S. P., Parker, J. E., Knowles, J. C., Rehman, I., Parkin, I., Evans, J. R. G. and Darr, J. A. (2009a). High-Throughput Continuous Hydrothermal Synthesis of an Entire Nanoceramic Phase Diagram. *Journal of Combinatorial Chemistry*, 11, (5) 829-834.

Weng, X., Perston, B., Wang, X. Z., Abrahams, I., Lin, T., Yang, S., Evans, J. R. G., Morgan, D. J., Carley, A. F., Bowker, M., Knowles, J. C., Rehman, I. and Darr, J. A. (2009b). Synthesis and characterization of doped nano-sized ceria–zirconia solid solutions. *Applied Catalysis, B: Environmental*, 90, (3-4) 405-415.

Weng, X., Zhang, J., Wu, Z. and Liu, Y. (2011a). Continuous hydrothermal flow syntheses of transition metal oxide doped Ce_xTiO_2 nanopowders for catalytic oxidation of toluene. *Catalysis Today*, 175, (1) 386-392.

Weng, X., Zhang, J., Wu, Z., Liu, Y., Wang, H. and Darr, J. A. (2011b). Continuous hydrothermal syntheses of highly active composite nanocatalysts. *Green Chemistry*, 13, (4) 850.

Weng, X., Zhang, J., Wu, Z., Liu, Y., Wang, H. and Darr, J. A. (2011c). Continuous syntheses of highly dispersed composite nanocatalysts via simultaneous co-precipitation in supercritical water. *Applied Catalysis B: Environmental*, 103, (3-4) 453-461.

Wofford, W. T., Gloyna, E. F. and Johnston, K. P. (1998). Boric Acid Equilibria in Near-Critical and Supercritical Water. *Industrial & Engineering Chemistry Research*, 37, (5) 2045-2051.

Wong, T. and Orton, D. (2011). Sunscreen allergy and its investigation. *Clinics in Dermatology*, 29, (3) 306-310.

Wu, W., He, Q. and Jiang, C. (2008). Magnetic iron oxide nanoparticles: synthesis and surface functionalization strategies. *Nanoscale Research Letters*, 3, (11) 397-415.

Xu, C., Lee, J. and Teja, A. S. (2008). Continuous hydrothermal synthesis of lithium iron phosphate particles in subcritical and supercritical water. *The Journal of Supercritical Fluids*, 44, (1) 92-97.

Xu, H., Ouyang, S., Liu, L., Reunchan, P., Umezawa, N. and Ye, J. (2014). Recent advances in TiO_2-based photocatalysis. *Journal of Materials Chemistry A*, 2, (32) 12642.

Xu, J., Ao, Y., Chen, M. and Fu, D. (2009). Low-temperature preparation of Boron-doped titania by hydrothermal method and its photocatalytic activity. *Journal of Alloys and Compounds*, 484, (1-2) 73-79.

Yakaboylu, O., Harinck, J., Gerton Smit, K. G. and de Jong, W. (2013). Supercritical water gasification of manure: A thermodynamic equilibrium modeling approach. *Biomass and Bioenergy*, 59, 253-263.

Yin, L., Zhang, L., Li, F. and Yu, M. (2005). ZnO single crystals: Synthesis and characterization. *Materials Research Bulletin*, 40, (12) 2219-2224.

Yu, H. D., Regulacio, M. D., Ye, E. and Han, M. Y. (2013). Chemical routes to top-down nanofabrication. *Chemical Society Reviews*, 42, (14) 6006-6018.

Yu, J., Low, J., Xiao, W., Zhou, P. and Jaroniec, M. (2014). Enhanced photocatalytic CO_2-reduction activity of anatase TiO_2 by coexposed {001} and {101} facets. *Journal of the American Chemical Society*, 136, (25) 8839-8842.

Yuan, Y. P., Ruan, L. W., Barber, J., Loo, S. C. J. and Xue, C. (2014). Hetero-nanostructured suspended photocatalysts for solar-to-fuel conversion. *Energy & Environmental Science*, 7, (12) 3934-3951.

Zaleska, A. (2008). Doped-TiO_2: A Review. *Recent Patents on Engineering*, 2, (3) 157-164.

Zanganeh, S., Kajbafvala, A., Zanganeh, N., Molaei, R., Bayati, M. R., Zargar, H. R. and Sadrnezhaad, S. K. (2011). Hydrothermal synthesis and characterization of TiO_2 nanostructures using LiOH as a solvent. *Advanced Powder Technology*, 22, (3) 336-339.

Zayat, M., Garcia-Parejo, P. and Levy, D. (2007). Preventing UV-light damage of light sensitive materials using a highly protective UV-absorbing coating. *Chemical Society Reviews*, 36, (8) 1270-1281.

Zhang, S., Yao, S., Li, J., Zhao, L., Wang, J. and Boughton, R. I. (2011). Growth habit control of ZnO single crystals in molten hydrous alkali solutions. *Journal of Crystal Growth*, 336, (1) 56-59.

Zhang, Z., Brown, S., Goodall, J. B. M., Weng, X., Thompson, K., Gong, K., Kellici, S., Clark, R. J. H., Evans, J. R. G. and Darr, J. A. (2009a). Direct continuous hydrothermal synthesis of high surface area nanosized titania. *Journal of Alloys and Compounds*, 476, (1-2) 451-456.

Zhang, Z., Goodall, J. B. M., Morgan, D. J., Brown, S., Clark, R. J. H., Knowles, J. C., Mordan, N. J., Evans, J. R. G., Carley, A. F., Bowker, M. and Darr, J. A. (2009b). Photocatalytic activities of N-doped nano-titanias and titanium nitride. *Journal of the European Ceramic Society*, 29, (11) 2343-2353.

Zhao, H., Liu, L., Andino, J. M. and Li, Y. (2013). Bicrystalline TiO_2 with controllable anatase–brookite phase content for enhanced CO_2 photoreduction to fuels. *Journal of Materials Chemistry A*, 1, (28) 8209.

Zhu, K.-R., Zhang, M.-S., Chen, Q. and Yin, Z. (2005). Size and phonon-confinement effects on low-frequency Raman mode of anatase TiO_2 nanocrystal. *Physics Letters A*, 340, (1-4) 220-227.